Micromechanical modelling of voided FCC and HCP polycrystals in inelastic regime

PhD thesis by

mgr inż. Saketh Virupakshi

Supervisor:

prof. dr hab. inż. Katarzyna Kowalczyk-Gajewska

Auxiliary supervisor:

dr inż. Karol Frydrych

Instytut Podstawowych Problemów Techniki Polskiej Akademii Nauk

02-106 Warszawa, ul. Adolfa Pawinskiego 5B

2025

Acknowledgements

I would like to express my profound gratitude to my supervisor, **prof. dr hab. inż. Katarzyna Kowalczyk-Gajewska**, and auxiliary supervisor, **dr inż. Karol Frydrych**, for their invaluable support, sharing their extensive knowledge, skills, and experience. Their immense dedication and effort have been instrumental in guiding me through the preparation of this dissertation.

I would also like to express my sincere gratitude to **prof. dr hab. inż. Stanisław Stupkiewicz** for his invaluable assistance in implementing the crystal plasticity model within the AceGen/AceFEM environment, as well as for his inspiring ideas shared through his lectures on contact mechanics. Additionally, I extend my thanks to **dr inż. Mohsen Rezaee Hajidehi** for the insightful discussions and support with finite element implementations.

I would also like to extend my heartfelt thanks to my parents, wife, son, and all others who may not be mentioned individually for their unwavering support and words of encouragement throughout the preparation of this dissertation. My gratitude also goes to my colleagues from the doctoral program and the employees of IPPT for all the assistance they have provided.

I would also like to express my gratitude for the financial support received from the National Science Centre under grant 2021/41/B/ST8/03345.

My gratitude would be incomplete without acknowledging God, who endowed me with the strength and determination to complete my thesis, reinforcing my conviction that I am exactly where I need to be.

Abstract

High specific strength metals and alloys with face centered cubic (FCC) and hexagonal close packed (HCP) lattice symmetry are gaining significant interest in the transport and aerospace sectors because of their excellent strength-to-weight ratios and improved durability at high temperatures. However, the widespread application of such materials is sometimes impeded by their low ductility and poor fracture toughness. These constraints stem from the distinct crystallographic characteristics, which for HCP crystals limit the availability of easy slip systems and leads to activity of twinning. Moreover, for some alloys with FCC symmetry, despite their high lattice symmetry, the initiation of twinning results in low ductility and fracture toughness. A better understanding of the void growth failure mechanism in these highly anisotropic metallic materials will facilitate the reduction of the aforementioned limitations. Therefore, this thesis focuses on exploring and elucidating the connection between crystal anisotropy and the processes of void growth and coalescence that lead to ductile damage in polycrystalline metals, utilizing numerical analyses and micromechanical models.

Numerical full-field calculations are employed to investigate porous FCC and HCP crystal structures, using both 2D plane strain unit cells with cylindrical voids and 3D unit cells with spherical voids. This method allows for an in-depth analysis of how boundary conditions, crystal orientations, and initial void volume fractions impact void evolution and stress or strain heterogeneity in these materials. To achieve this goal, a rate-dependent crystal plasticity constitutive theory is considered. The theory incorporates slip and twinning mechanisms, accounting for their mutual interactions in terms of hardening laws and the lattice reorientation effects due to twinning.

To predict the macroscopic behavior of porous polycrystals, a micromechanical mean-field model is formulated. At the single porous crystal level, an additive Mori-Tanaka scheme is employed to capture the elasto-viscoplastic response. In the second step, an additive self-consistent scheme is implemented to estimate the overall behavior of the porous polycrystal. The numerical implementation of this model at both stages is detailed, offering a comprehensive framework for its application. Predictions from the mean-field model are validated and analyzed against full-field numerical computations. Moreover, a novel GTN-type yield criterion for porous crystals is formulated using a micromechanical approach, with model tuning parameters calibrated via full-field unit cell calculations. Comparisons are drawn between the newly proposed model and existing models in the literature. The findings from this research hold significant potential for predicting the performance of porous polycrystalline materials across various loading scenarios.

Streszczenie

Metale i stopy o wysokiej wytrzymałości właściwej o sieci krystalicznej regularnej ściennie centrowanej (A1, ang. FCC – face centered cubic) i heksagonalnej zwartej (A3, ang. HCP – hexagonal close packed) zyskują duże zainteresowanie w sektorach transportu i lotnictwa ze względu na doskonały stosunek masy do wytrzymałości i zwiększoną trwałość w wysokich temperaturach. Z drugiej strony szerokie zastosowanie takich materiałów jest utrudnione przez ich niską ciągliwość i słabą odporność na pękanie. Ograniczenia te wynikają ze szczególnych cech struktury krystalograficznej, która ogranicza dostępność łatwych systemów poślizgu i wywołuje aktywność bliźniakowania. Co więcej, w przypadku niektórych stopów o symetrii FCC, pomimo ich wysokiej symetrii sieci, inicjacja bliźniakowania skutkuje niską ciągliwością i odpornością na pękanie. Lepsze zrozumienie mechanizmu uszkodzenia na skutek wzrostu pustek w tych wysoce anizotropowych materiałach metalicznych ułatwi redukcję wyżej wymienionych ograniczeń. Dlatego też, niniejsza praca skupia się na badaniu i wyjaśnianiu związku między anizotropią kryształów a procesami wzrostu i łączenia pustek, które prowadzą do ciągliwego uszkodzenia w metalach polikrystalicznych, wykorzystując analizy numeryczne i modele mikromechaniczne.

Obliczenia numeryczne metodą elementów skończonych (MES) są stosowane do badania porowatych struktur krystalicznych FCC i HCP, wykorzystując zarówno dwuwymiarowe komórki jednostkowe z cylindrycznymi pustkami w płaskim stanie odkształcenia, jak i trójwymiarowe komórki jednostkowe z kulistymi pustkami. Ta metoda umożliwia dogłębną analizę tego, w jaki sposób warunki brzegowe, orientacje kryształów i początkowe udziały objętościowe pustek wpływają na ich ewolucję, jak również niejednorodność naprężenia w tych materiałach. Aby osiągnąć ten cel, zastosowana jest teoria plastyczności kryształów wrażliwa na prędkość odkształcenia. Teoria ta obejmuje mechanizmy poślizgu i bliźniakowania, uwzględniając ich wzajemne oddziaływania pod względem praw umocnienia i skutków reorientacji sieci spowodowanej bliźniakowaniem.

Aby przewidzieć makroskopowe zachowanie porowatych polikryształów, sformułowano model mikromechaniczny. Na poziomie pojedynczego porowatego kryształu, do uchwycenia odpowiedzi sprężysto-lepkoplastycznej stosuje się addytywny schemat Mori-Tanaki. W drugim kroku, implementuje się addytywny schemat wewnętrznie zgodny, aby oszacować ogólne zachowanie porowatego polikryształu. Szczegółowo opisano numeryczną implementację tego modelu na obu etapach, co pozwala na jego dalsze zastosowanie. Przewidywania modelu mikromechanicznego są weryfikowane i analizowane w stosunku do obliczeń numerycznych MES. Dodatkowo, zostało sformułowane nowe kryterium uplastycznienia typu Gurson-Tvergaard-Needleman (GTN) dla kryształów porowatych

przy użyciu podejścia mikromechanicznego, z parametrami modelu skalibrowanymi za pomocą symulacji MES dla reprezentatywnych komórek jednostkowych. Przeprowadzono porównania między nowo zaproponowanym modelem a istniejącymi modelami w literaturze. Wyniki tych badań mają znaczny potencjał do przewidywania odpowiedzi porowatych materiałów polikrystalicznych w różnych scenariuszach obciążenia.

Contents

List of Figures

List of Tables

CHAPTER 1

Introduction

1.1 Motivation

This thesis focuses on modeling ductile failure, including void growth and coalescence, in polycrystalline materials with strong anisotropy in terms of plastic properties, such as Zn, Mg, and Ti alloys with a hexagonal close-packed (HCP) crystal structure or metals and alloys of FCC crystal structure deforming by slip and twinning. Despite the advantageous mechanical properties, such metals and alloys often exhibit deficiencies such as low ductility, fracture toughness, and formability, restricting their potential numerous industrial applications, cf. Appel and Wagner (1998); Proust et al. (2007); Agnew et al. (2001); Mróz (2006). The mechanical response of these materials are significantly influenced by their microstructure. Developing a reliable, physically based description of their behavior under loading is crucial to mitigate the risk associated with unexpected failures in designs utilizing these materials.

Metals and alloys characterized by strong anisotropy, demonstrate the following advantageous properties: cf. (Kowalczyk-Gajewska, 2011):

- low density,
- exceptional specific strength and stiffness, even under elevated temperatures,
- robust corrosion resistance ranging from good to excellent.

A more profound understanding of the correlation between microstructure characteristics, active plastic deformation mechanisms, and the void growth leading to ductile failure in single crystals or polycrystalline metal and alloys is crucial for the effective utilization of innovative multifunctional materials like advanced steels, magnesium, zirconium, or titanium alloys in commercial applications. The increasing adoption of novel hexagonal close-packed (HCP) alloys is notable. These alloys are gaining momentum in a wide array of applications, spanning various fields such as:

- The aerospace and automotive sectors are exploring solutions to reduce fuel consumption, such as incorporating Ti and Ti-Al alloys in the structural components of aircraft engines and using Mg alloys in powertrain and various automotive components.
- Biomedical applications involve the utilization of Ti alloys for hip and dental implants, with the potential consideration of Zn alloys as a replacement due to their improved biocompatibility.
- In the nuclear energy industry, Zr alloys are employed in nuclear reactor fuel claddings.
- Additionally, in the electronics field, lightweight Mg alloys are employed in mobile electronic devices.

The optimal utilization of the materials under consideration encounters specific challenges:

- Restricted ductility and formability at room temperature, particularly evident in Mg alloys.
- Elevated processing costs due to the necessity of integrating advanced technological processes, notably in the case of Ti and Zr alloys.
- Elevated sensitivity of properties to the material's microstructure, marked by strong anisotropy induced by crystallographic texture.

It is evident that employing advanced multi-scale analysis to study void growth and coalescence in elasto-viscoplastic crystals with multiple deformation modes is crucial for understanding the complex relationship between structure, fabrication process, and properties, especially in a large strain regime. Specifically, this approach will enable a comprehensive exploration of the connection between the evolving void volume and its coalescence on one hand and the local plastic anisotropy of a single crystal on the other hand, accounting for the applied loading conditions. Furthermore, the study will delve into the intricate mutual interactions between void growth and microstructural changes in the surrounding material. Determining such interrelations is a pivotal aspect in the realm of engineering sciences at the intersection of material science and mechanics of materials.

1.2 State of the art

Over the past seven decades, extensive research has been carried out on the fracture micro-mechanisms in ductile porous solids. Those research encompasses numerous

experiments, development of micromechanical theories, and numerical models. The ongoing interest in this field is evident through innovative techniques, diverse perspectives, and philosophies adopted by scientists and engineers to understand the micro-mechanisms of ductile fracture in materials. The initial part of this literature review provides a brief exploration of experimental observations regarding ductile failure in materials at both macro and micro scales. Subsequently, attention shifts to the mathematical description (phenomenological models) of ductile failure at the macroscopic level. The review then delves into a detailed analysis of numerical approaches applied to porous unit cell models, spanning both macro and micro perspectives. Following this, the focus narrows down to recent developments in proposing new models for porous single crystals, with a specific emphasis on their implementation within finite element frameworks.

1.2.1 Experimental research on ductile fracture.

Scenarios of void initiation, growth and coalescence in polycrystalline metallic materials and metal matrix composites. The literature contains fairly comprehensive documentation on the ductile fracture of porous materials (Das, 2021; Wciślik and Lipiec, 2022). From a macroscopic perspective, voids typically originate in the central region of the sample, initiating crack propagation perpendicular to the sample loading axis in the neck area. As the crack approaches the surface, reduced constraints cause the trajectory to shift, resulting in a cup-and-cone fracture pattern (Wciślik and Lipiec, 2022). At the microscopic level, ductile failure is characterized by the initiation, growth and coalescence of microscopic voids. The ductile fracture micromechanisms, along with various microstructural and fracture features under tensile deformation, are schematically represented in Fig. 1.1a. Example of the experimental evidence of void nucleation caused by fragmentation of TiN particles, along with a fracture surface showing dimples in IF steels, is shown in Fig. 1.1b. It is observed that the complex process of micro-void nucleation, growth, and coalescence typically begins at or beyond the ultimate tensile strength up on induced plastic strain and stress triaxiality.

Voids typically originate through either decohesion or the cracking of second phase particles / inclusions (Tipper, 1949; Rogers, 1960; Gurland and Plateau, 1963; León-García et al., 2010; Chen et al., 2018), at the intersection of the slip bands (Chan and Davidson, 1999) and at the grain boundaries (Gardner et al., 1977). Some observations concerning these phenomena are discussed below.

In materials containing second-phase particles, initiation of voids can take place through either the separation of the particle/matrix interface or the cracking of particles. The

manifestation of either of the two specified mechanisms is significantly influenced by the mechanical characteristics of both the matrix and the particle and the strength of the matrix-particle interface. Typically, particle separation tends to occur predominantly in relatively soft and ductile matrices. Nevertheless, a matrix with high yield stress, hardening exponent, and particle stiffness enhances the occurrence of the particle cracking. The interactions between slip and a second phase particle, typically less deformable than the matrix, results in regions with highly localized stress, leading to cracking of particles or interface decohesion (Bluhm and Morrissey, 1965; Gladman et al., 1971; Gurland, 1972).

Cox and Low (1974) emphasize the significance of non-metallic inclusion sizes in determining the fracture resistance of AISI 4340 and maraging steels. In maraging alloys, plastic fracture occurs through the initiation of voids resulting from the fracture of titanium carbo-nitride inclusions. The subsequent growth of these voids leads to coalescence and final fracture. In contrast, AISI 4340 steels experience fracture through the nucleation and growth of voids formed by the fracture of the interface between manganese sulfide inclusions and the matrix. The growth of these inclusion-nucleated voids is halted before coalescence, as void sheets composed of small voids nucleated by cementite precipitates connect these neighboring sulfide-nucleated voids. Controlling the sizes of these inclusions is crucial for enhancing fracture resistance.

The involvement of dislocations in the formation of voids is demonstrated by Gardner et al. (1977). He observed the transformation of dislocation structures into cells in iron and beryllium crystals under high strains. The boundaries between these cells, characterized by ample surface energy, initiated voids without requiring additional internal stress concentrators like precipitates or second phase particles. In the Nb-Cr-Ti alloy, slip band decohesion and potential void nucleation occur through an intersecting slip process, with the decohered slip bands serving as void nuclei for further growth and coalescence, ultimately leading to dimpled fracture (Chan and Davidson, 1999). Utilizing advanced research techniques such as high-angle annular dark-field scanning transmission electron microscopy (HAADF-STEM), the study by Noell et al. (2020) explores the fracture mechanism of copper with copper oxide particles. The investigation reveals that voids initially nucleate at the nanoscale within the diffuse neck of a deformed specimen, often unrelated to the presence of second-phase particles. Only a select few of these void nuclei grow from the nano to microscale, ultimately leading to failure. The initial stages of void growth from the nanoscale to the microscale seem to be primarily influenced by the location of void nuclei. Specifically, dislocation structures play a crucial role in controlling the early phases of void growth, both for particle-free voids and those associated with particles.

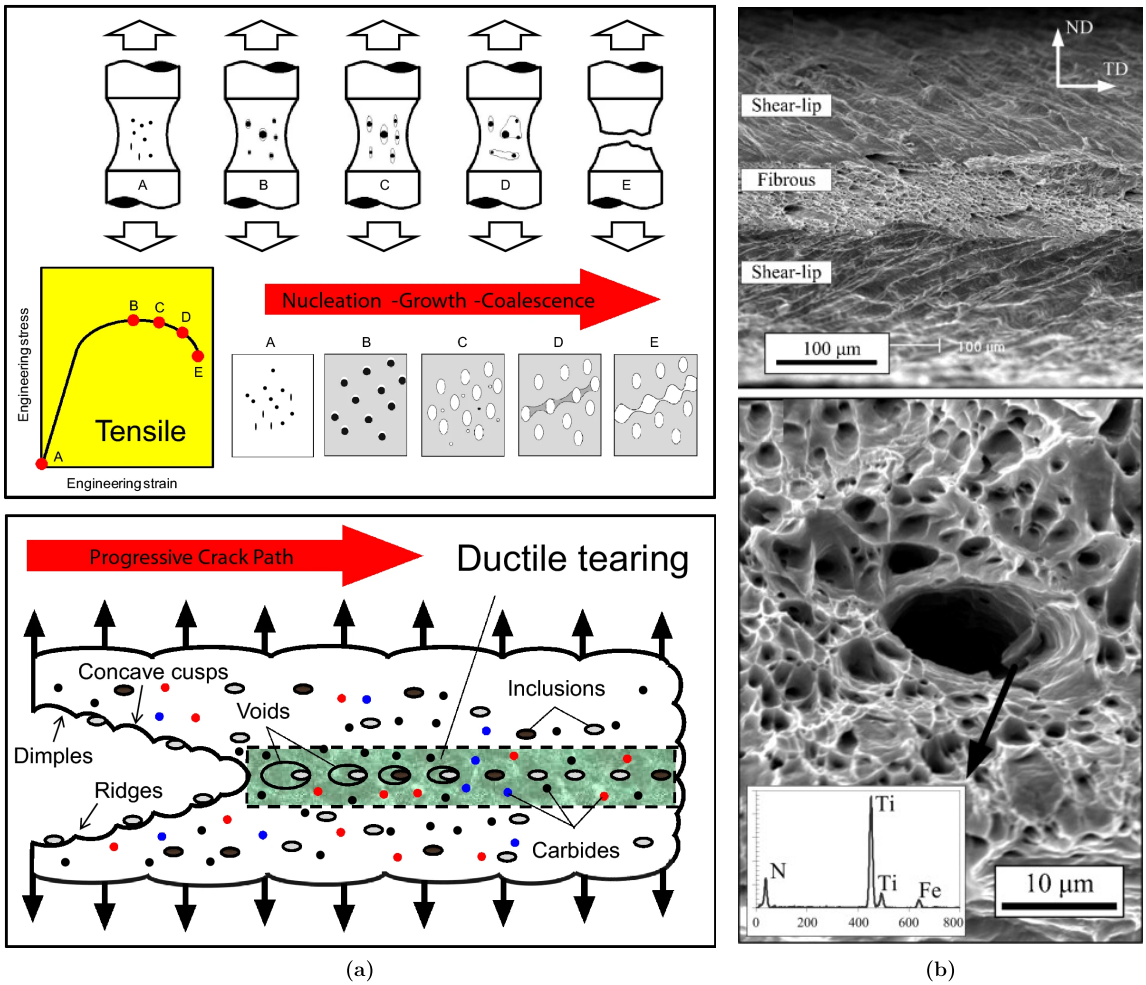

FIGURE 1.1 a) Schematic representation of ductile fracture micro-mechanisms, illustrating various fracture features observed during the failure process.(reprinted from Das (2021) with permission from Springer Nature) b) Fracture surface of an IF steel tensile specimen showing a TiN particle in a dimple of the fibrous zone. (reprinted from León-García et al. (2010) with permission from Elsevier).

The work by Thompson and Williams (1977) delves into the distinction in failure mechanisms between single-phase and two-phase Ti alloys. In two-phase Ti alloys, ductile failure initiates at interphase interfaces, while in single-phase alloys due to lacking of second-phase particles, void nucleation occurs through blocked slip bands. Similarly, Van Stone et al. (1978) focuses on the failure mechanisms of Ti alloys at cryogenic temperatures. Metallographic sections of specimens deformed under cryogenic conditions reveal elongated dimples nucleating as cigar-shaped voids at offsets in twin boundaries or grain boundaries, resulting from the intersection of intense slip bands or deformation twins with those boundaries.

There is also a lot of experimental observation concerning the stage of the void growth and in general, damage evolution. The experiments conducted by Poole and Charras (2005) involved generating varying levels of initial damage in the Al–Si model composite, which was then tested with the matrix heat treated under identical conditions. The findings unambiguously demonstrate that pre-existing damage reduces the overall flow strength of the materials and enhances the strain to necking. Thus, the decisive factor influencing tensile fracture is not the extent of damage but rather the rate of damage evolution and its impact on the overall work-hardening behavior.

Regarding failure in DP steels, the fracture of martensite plays a pivotal role. The detailed analysis of microdamage development in DP1000 steel under tension was conducted by Alharbi et al. (2015). Strength tests were performed within the scanning electron microscope (SEM) chamber, capturing the microstructure of the material in the chosen area at regular intervals. Cracking of the particles was observed at a relatively small overall strain, around 2%. Upon further strain increase, the martensite phase eventually cracked. The increase of deformation caused the crack to transform into a void, acting as a stress concentrator and it becomes the cause for crack propagation in the ferrite. The substantial intensity of this phenomenon underscores its predominant role in the failure of DP1000 steel. Similar conclusions were drawn by the authors of Santos et al. (2019). Investigation into the microdamage development in DP600 and DP800 steels under uniaxial tension revealed that at low strain, the globular aluminum oxide inclusions acted as void initiators. However, with higher deformations, voids were observed to form near the ferrite–martensite interfaces, within the ferrite matrix, and close to martensite islands.

In a recent study, Pathak et al. (2020) extensively explored the impact of stress state on void nucleation in DP780 and CP800 steels through various strength tests, including simple shear, hole tension, v-bending, and biaxial tension. Microtomography was employed to capture the material microstructure in the region of interest during each test, and nucleation intensity was quantified as the average number of nucleated voids per 1 mm^3 of material in the process zone. Biaxial tension tests exhibited the highest void nucleation, with approximately 30,000 voids/mm^3 at failure. In contrast, hole tension tests recorded a lower nucleation intensity, ranging from about 9,500 to 18,000, depending on the material. Shearing tests showed the lowest nucleation intensity, with values between 3,000 and 4,000 voids/mm^3 at failure. Han et al. (2022) conducted experimental investigations on the mechanical damage induced during the shearing process of QP980 steel. They identified two distinct types of microvoids based on the nucleation site. Numerous microvoids with small sizes (≤5 μm) were formed at phase interfaces, while a few larger microvoids originated from inclusions, exceeding 5 μm. The evolution of a V-shape microcrack from

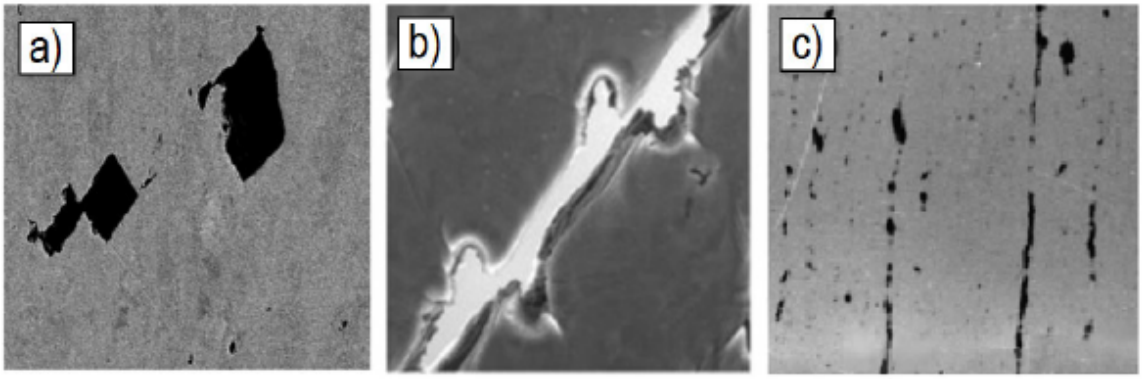

FIGURE 1.2 Modes of void coalescence (observed in steels) a) Internal necking, b) Internal shearing, and c) necklace coalescence (reprinted from Pineau et al. (2016) with permission from Elsevier).

the microvoids distributed on the sheared surface emerged as a critical factor, as it could lead to edge failure in subsequent forming processes.

In AA2024-T3 under shear loading, as studied by Tancogne-Dejean et al. (2021), pre-existing voids rotate and elongate with mechanical loading, while intermetallic particles fail early in a brittle manner, leading to void nucleation. The newly-formed voids grow, hindered by fragmented particles, leading to micro-cracks. The process ends with the observation of strain localization bands and void-sheet failure.

Experimental observation concerning the last stage of ductile damage, i.e., void coalescence and/or strain localization are also numerous. Microvoids, once initiated, undergo growth within a plastically deformed solid matrix. This growth is influenced by plastic strain and hydrostatic stresses, with a connection to weak dependence on the spatial distribution of microvoids (Benzerga and Keralavarma, 2009). Various numerical and constitutive models proposed by scientists related to void growth will be discussed after an experimental literature review. Stable void growth is characterized by relatively uniform plastic strain distribution, but beyond a certain point, *strain localization occurs between adjacent voids*, limiting material ductility. Although the void volume fraction is a crucial parameter in the study of microvoid growth, various factors beyond void volume fraction also significantly influence the processes of void growth and strain localization. Material softening can occur through various mechanisms such as microstructural changes, thermal interactions, and damage evolution. This leads to a localized degradation of the material's load-carrying capacity, causing strain localization in a thin band (Fressengeas and Molinari, 1985).

The initiation of strain localization is influenced by factors like stress state, material

properties, and material porosity (Needleman and Rice, 1978). *Strain localization can also occur through void coalescence*, a critical mechanism in the failure of ductile materials. This phenomenon exhibits various modes influenced by microstructural factors, loading conditions, and plastic flow characteristics, categorized into three main modes (Pineau et al., 2016). The first mode involves coalescence by internal necking of the intervoid ligament (Fig. 1.2a), initially discussed by Argon et al. (1975). The second mode is coalescence by internal shearing of the intervoid ligament (Fig. 1.2b), already discussed above (Cox and Low, 1974), where localized shear can lead to void sheeting and local failure. The third mode is necklace coalescence (Fig. 1.2c), where voids link up along their length, observed in steels with elongated inclusions. Necklace coalescence is regarded as a crucial mechanism in the development of ductile delamination cracking (Pala and Dzioba, 2018).

In a recent investigation by Naragani et al. (2020), the void coalescence and ductile failure in IN718 were explored using high-energy synchrotron X-ray tomography and diffraction. The study characterized the initial porosity and its evolution under tensile loading through micro-tomography. Two distinct mechanisms of ductile failure emerged: intervoid shearing, associated with grains exhibiting low stress triaxiality, and intervoid necking, linked to grains with high stress triaxiality. Notably, despite the prevalence of high stress triaxiality in many grains, the research revealed that factors like plasticity and stress heterogeneity within the lattice of the grains between voids play pivotal roles in predicting the onset of intervoid necking-based failure.

The ongoing discussion, based on experimental findings, has been focused on exploring void nucleation sites and coalescence mechanisms across various polycrystalline materials. In view of the presented review, it is evident that voids nucleate due to decohesion and cracking of different kinds precipitates (intermetallics, second phase particles), the separation of the particle/matrix interfaces as well as at the intersection of slip bands and other dislocation structures, with the stress condition and the stiffness difference between the particle and matrix being noted as playing a role. Additionally, voids can emerge at grain and twin boundaries, particularly noticeable in HCP alloys. Once formed, voids are growing within the plastically deformed matrix, influenced by their location and the prevailing stress state. Eventually, stable void growth leads to strain localization, thereby limiting material ductility. Three primary mechanisms of void coalescence have been identified: internal necking, void sheeting, and necklace coalescence.

Role of material microstructure on void initiation, growth in FCC and HCP lattice structures. The forthcoming literature study places greater emphasis on experimental investigations pertaining to metals with FCC and HCP lattice structures, encompassing

both macro and single crystal levels.

In their study, Barrioz et al. (2019) investigated the role of dislocation channeling in void growth within FCC crystals, focusing on Solution Annealed 304L austenitic stainless steel. Through experiments and simulations, they highlight significant interactions between voids and dislocation channels, especially under irradiated conditions, revealing distinct localization patterns. As the applied strain increases, deformation becomes more homogeneous at the void scale through the activation of secondary channels. The research emphasizes the importance of these dynamics for ductile fracture modeling.

The interaction of lattice dislocations with grain boundaries in proton- and ion-irradiated austenitic stainless steels was examined by Cui et al. (2014). The importance of the local resolved shear stress in determining the ability of dislocations to propagate through grain boundaries and the role of strain energy density minimization in slip transmission prediction was emphasized. When the grain boundary cannot facilitate slip, alternative relief methods such as out-of-plane displacement and crack nucleation on the grain boundary are observed; however, in the experiments conducted, it was not possible to determine the sequence of these events. These observations suggest implications for the modeling of mechanical properties in irradiated metals.

In the experimental study by Furukimi et al. (2017), void nucleation behavior in single crystal iron during tensile tests was investigated, emphasizing the influence of specimen size and slip systems. It was determined that void nucleation in single crystal iron requires the presence of multiple slips. While the smaller specimen manifested single slip, the larger one demonstrated multiple slip systems, resulting in voids with diameters ranging from 50-100 nm along slip bands. Accumulation of dislocations across various slip planes in the larger specimen corroborated the presence of multiple slip systems, where voids were distinctly observed.

In the research by Perez-Bergquist et al. (2011), a detailed quantitative characterization of damage and substructural evolution in bicrystal copper is presented. Upon examining the shocked bicrystals using optical microscopy, widespread void formation was observed, both at grain boundaries and within individual crystals. The occurrence of voids was notably influenced by crystallographic orientation, with a pronounced number appearing in the [1 0 0] grain. While most of each grain retained its orientation post-spalling, notable misorientations were found near grain boundaries. Additionally, defects with up to 18° misorientations adjacent to void/matrix interfaces emphasized the significance of substructural changes in void formation during dynamic loading.

The fracture behavior of a rolled AA7075-T651 aluminum plate under quasi-static loading was investigated by Fourmeau et al. (2013), emphasizing the influence of stress

state and plastic anisotropy. They found that strain to failure in in-plane uniaxial tension varied significantly with direction and ductility, resulting in cup-and-cone or shear mode fractures. Notched tensile specimens exhibited reduced strain to failure due to increased stress triaxiality, while in-plane upsetting tests consistently surpassed uniaxial tension tests, likely due to lower stress triaxiality. Through-thickness tests showed limited ductility, with fractures inclined at a 45° angle to the loading axis.

Experimental observations on ductile failure mechanisms in FCC crystals have revealed a range of phenomena across different materials. Annealed steels exhibit void growth influenced by dislocation channeling, while austenitic stainless steels show cracks initiated by the interaction of lattice dislocations with grain boundaries. In aluminum specimens, the stress state and anisotropy play a significant role, leading to various failure modes such as in-plane cup and cone failure transitioning to shear failure. Void nucleation in Fe single crystals depends on the activity of multiple slip systems, while in Nickel superalloys, void growth is driven by dislocations.

Microscopic damage mechanisms in hot-rolled magnesium alloy AZ31B were examined under both uniaxial and controlled triaxial loadings by Kondori and Benzerga (2014). It was determined that magnesium alloys with void-forming second phase particles might exhibit enhanced tolerance to ductile damage accumulation over the one commonly reported for uniaxial loading scenarios. When subjected to moderately triaxial loading, AZ31B displayed increased ductility, marked by the activation of multiple deformation systems. This led to a shift from twinning-controlled fracture to microvoid coalescence (microscale). The strain to failure decreases with increasing stress triaxiality, indicating pronounced void growth activity. Nevertheless, the presence of shallow dimples on fracture surfaces under high triaxialities implied premature coalescence of initiated microcracks. Fig. 1.3a illustrates a twin-sized void located near the tip of the macroscopic slanted crack. The arrow marks in the Fig. 1.3b indicates the varying sizes of twin related microcracks under uniaxial loading. The influence of void volume fraction on the growth and linkage of pre-drilled holes in pure magnesium was investigated by Nemcko et al. (2016). It was determined that the effects of the void fraction were overshadowed by the heterogeneous deformation associated with the local microstructure. Notably, strain concentrations at twin and grain boundaries were identified to be significantly higher than macroscopic strain levels. Such boundaries are believed to have a critical strain threshold for fracture initiation, ultimately resulting in the premature linkage of holes.

In the research conducted by Nemcko and Wilkinson (2016), the processes of nucleation, growth, and linkage of microvoids in commercially pure magnesium were investigated using x-ray computed microtomography. It was observed that flat penny-shaped voids

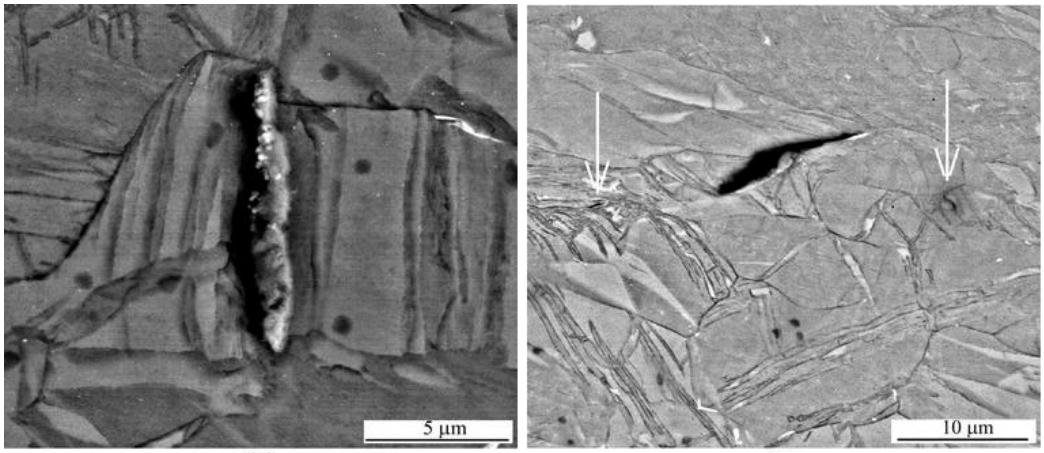

FIGURE 1.3 SEM micrograph of the longitudinal section of a uniaxial tensile specimen from the Mg alloy AZ31B, halted at the onset of macroscopic crack formation. The image highlights (a) a twin-sized void positioned near the tip of the slanted macroscopic crack and (b) several twin-related microcracks of varying sizes located near the primary crack.(reprinted from (Kondori and Benzerga, 2014) with permission from Springer Nature).

predominantly nucleated early in the deformation process, especially at twin and grain boundaries. As deformation progressed, void growth accelerated, with a preference for expansion along these boundaries, resulting in irregular flat void shapes. Ultimately, voids linked via the void sheeting mechanism, leading to a widespread shearing failure throughout the material. The distinctive faceted fracture patterns in magnesium were attributed to the failure of twin boundaries.

The study by Basu et al. (2017) demonstrated that plastic anisotropy can be altered to aid ductility in Mg alloys, as evidenced by comparing samples of different textures produced by severe plastic deformation. It provides insights into the correlation between anisotropy and ductility. The study proposes a simple micromechanical model to understand the complex relationship between plastic anisotropy and ductility by introducing the anisotropy effect on ductility (AED) index, which can be tuned through processing to enhance ductility at comparable strength levels.

In the experimental study by Kondori et al. (2018), synchrotron radiation laminography revealed diffuse damage in Mg alloy AZ31, indicative of its ductile behavior. Void formation and coalescence were widespread, originating as flat voids that varied in blunting based on factors such as spatial location, overall triaxiality, and local strain levels. The transition from damage to fracture was marked by macroscopic cracks, primarily from void coalescence in the plate's rolling direction, evolving into a corrugated crack pattern.

In addition to microstructural features, the shape of voids and the orientation of void

bands also influence the mechanical response of both FCC and HCP crystals. In their research, Fadida et al. (2020) explored the mechanical response of Ti6Al4V specimens with artificial voids under varying strain rates and shear stress states. They observed that void shape notably influences failure displacement in shear compression specimens under quasi-static conditions. Additionally, an increased number of voids at a constant volume fraction decreases this displacement. Across both quasi-static and dynamic loadings, the presence of voids consistently reduced the displacement to failure, while void spacing and orientation showed minimal impact on the mechanical behavior of specimens.

The influence of void band orientation and crystallographic anisotropy on void growth and linkage in magnesium and copper sheets was explored by Nemcko et al. (2016). For copper, as the void band orientation angle increases from 0° to 45° relative to the tensile axis, the mechanism shifts from internal necking to shear localization. This shows the significant impact of void band orientation on the growth and linkage of holes in copper. Conversely, in magnesium, void band orientation does not significantly impact the growth and linkage processes. The interruption in hole growth is attributed to failures at twin and grain boundaries, with the local microstructure prevailing over void band orientation effects.

In summary, the experimental observations of ductile failure in HCP materials, encompassing pure Mg, Mg alloys, Ti, and Zr alloys, uncovers various underlying mechanisms. In pure Mg, stress concentrations at twin and grain boundaries initiate the formation of penny-shaped voids, which gradually grow and eventually merge through void sheeting. In Mg alloys, damage initiation occurs at second phase particles and deformation twins. Factors such as spatial location and strain levels lead to void blunting. Notably, AZ31B Mg alloys demonstrate enhanced ductility under moderate triaxialities due to activity of multiple deformation systems, transitioning from twinning failure to microvoid coalescence under differing stress conditions. In titanium samples, the presence and shape of voids significantly influence failure, especially under shear compression, with crystal orientation further impacting void growth. Additionally, in Mg sheets the role of void band orientation dictates the failure. These observations highlight the intricate relationship between microstructure, stress conditions, and deformation mechanisms in HCP materials, particularly during ductile failure.

1.2.2 Macroscopic models for porous ductile materials

In this part, classical mechanical models of ductile failure will be discussed which are set in the macroscopic phenomenological plasticity or viscoplasticity. The pioneering

work on void growth in nonlinear solids was conducted by F. A. McClintock (McClintock, 1968). It was observed in the experiments that long, roughly cylindrical voids frequently form in the neck of a tension bar when subjected to significant deformation. Based on these observations, a fracture criterion was formulated to describe fracture through the growth and coalescence of preexisting holes in plastic materials. This criterion was formulated by extrapolating the existing solution for *elliptical holes* in viscous materials under both varying and constant stress ratios. In addition to that, the classical closed-form solution of relationship between the void growth rate and remote stress value for circular hole in von Mises plastic material is presented. The criterion demonstrates a strong inverse dependence of fracture strain on transverse tensile stress, as well as anisotropic fracture behavior due to the shape and spacing of the holes. Next, an approximate relation to depict the growth of a *spherical void* within a rigid, infinite, perfectly plastic material subjected to a uniform remote strain field was given by Rice and Tracey (1969). It was found that the rate of void enlargement was enhanced over the remote strain rate by a factor that exponentially increases with the ratio of mean normal stress to the yield stress. The findings further indicated a pronounced decrease in fracture ductility as hydrostatic tension increased. In the seminal work of Gurson (1977), limit analysis was applied to derive the homogenized macroscopic yield potential for the voided material which depends on the macro-stresses and the volume fraction of voids. According to this outcome the macroscopic plastic flow becomes pressure sensitive and a homogenized solid is compressible even though the respective matrix is governed by the incompressible Huber-Mises plasticity.

One of the first finite element models of a porous material in terms of a unit cell representing a doubly periodic square array of circular cylindrical voids within an elastic-plastic medium under plane-strain conditions was presented by Needleman (1972). A variational principle was employed as the basis for implementing the finite-element analysis. The research yielded insights into change in void shape and size as the overall strain increases, the tensile behavior of material in the presence of voids, and the evolution of the plastic zone surrounding a void. By comparing the results with an original Gurson model it was found by Tvergaard (1981, 1982) that the tuning parameters q_1 and q_2 need to be introduced to refine the predictions of the constitutive Gurson model into closer-agreement with the comprehensive numerical analyses of a periodic array of voids. Tvergaard and Needleman (1984) investigated necking and failure in a round tensile test specimen. They utilized elastic-plastic constitutive relations that take into account the initiation and growth of micro-voids. An equivalent damage parameter function was introduced by them to substitute the real volume fraction of voids in the initial Gurson model, addressing the consequences of abrupt void coalescence during failure. In this way

the widely used GTN model came to existence. The yield criterion has the following form:

$$\Phi = \left(\frac{\sigma_{eq}}{\sigma_y}\right)^2 + 2q_1 f \cosh\left(\frac{3q_2\sigma_m}{2\sigma_y}\right) - (1 + q_1 f^2) = 0, \tag{1.1}$$

where σ_{eq} is the equivalent Huber-Mises stress, σ_y is the flow stress of the matrix material, f is the void volume fraction, σ_m is the hydrostatic mean stress, and q_1, and q_2 are tuning parameters (when $q_1 = q_2 = 1$ the original Gurson model is recovered).

Since the introduction of the GTN model, many subsequent studies have validated it under various loading conditions and extended the approach to account for different void shapes, anisotropy, and other factors. Koplik and Needleman (1988) investigated the parameter dependence of void growth and coalescence by simulating a periodic array of spherical voids within an isotropically hardening elastic-viscoplastic matrix. The numerical outcomes were related to the rate-sensitive version of the Gurson model. A transition from a generalized axisymmetric deformation state to a mode of uniaxial straining was demonstrated, resulting in accelerated void growth and coalescence within porous plastic materials. Gologanu et al. (1993, 1994) extended the classical Gurson analysis to ellipsoidal volumes containing confocal ellipsoidal cavities. A two-field estimation of the overall yield criterion was presented, which was further approximated to a Gurson-like criterion dependent on the "shape parameter" of the cavity.

Finite deformation constitutive relations for plastically dilatant materials, encompassing ductile fracture damage, were formulated by Rousselier (1981). These relations, which characterize the ductile fracture of metals, were deduced from a macroscopic perspective, based on the existence of the quasi-potential of dissipation and the normality rule for plastic strain rate and internal variable rates. An exponential correlation between ductile fracture damage and stress triaxiality was demonstrated by the model. The yield function has the following form, different from the Gurson model:

$$\Phi = \frac{\sigma_{eq}}{\rho} + 0.57\sigma_y f \exp\left(\frac{3\sigma_m}{2\rho\sigma_y}\right) - \psi^1(\alpha) = 0, \tag{1.2}$$

where ρ is the density of the material, and $\psi^1(\alpha)$ characterizes the hardening curve of the material.

A three-dimensional model for ductile fracture in metals was introduced by Thomason (1985), encompassing the influences of volumetric growth and shape change of microvoids within triaxial stress fields. The condition marking the plastic limit-load failure of the intervoid matrix at the onset of void coalescence was outlined by this model. Theoretical predictions of ductile fracture strains derived from this model were found to align well

with experimental observations. This approach to micro void coalescence, has gained substantial attention in recent times.

Leblond et al. (1994) proposed approximate macroscopic potentials for the viscoplastic solids containing cavities of cylindrical or spherical shape, based on the exact form of overall potential of a porous viscoplastic volume element. Pardoen and Hutchinson (2000) introduced the enhanced Gurson approach for spheroidal voids by heuristically extending the existing Gologanu-Leblond-Devaux model, addressing void shape effects, and the Thomason model for the initiation of void coalescence. This new framework considers both material flow characteristics and void dimensions. The efficacy of the proposed framework was subsequently evaluated using void cell computations.

Extension of the Gurson approach to the anisotropic Hill quadratic yield function for the metal matrix was done by Benzerga and Besson (2001). It was demonstrated that the anisotropy of the metal matrix impacts void evolution through a single scalar parameter, which serves as an invariant of the IVth order plastic anisotropy tensor, defining the Hill criterion. The criterion has the following form:

$$\Phi = \frac{3\boldsymbol{\sigma}' : \mathbb{H} : \boldsymbol{\sigma}'}{2\sigma_y^2} + 2f\cosh\left(\frac{3\sigma_m}{h\sigma_y}\right) - (1+f^2) = 0, \tag{1.3}$$

where $\boldsymbol{\sigma}'$ is the stress deviator, $\mathbb{H}$ is the fourth-order material dependent macroscopic anisotropy tensor, Σ_m is the mean stress, and h is the anisotropic factor. For isotropic matrix i.e, $\mathbb{H} = \mathbb{I}^s$, $h = 2$, the criterion reduces to Gurson yield criterion (Eq. (1.1)).

As will be discussed below, these seminal works laid the foundation for numerous studies that extend the results by incorporating additional features of matrix microstructure, pore geometry, and specific loading conditions, as well as their evolution during the deformation process. Monchiet et al. (2008), Keralavarma and Benzerga (2010) formulated plastic constitutive relations for anisotropic porous materials with spheroidal voids oriented arbitrarily with respect to the surrounding orthotropic matrix using nonlinear homogenization theory. Similarly, Morin et al. (2015) extended these criteria for spheroidal voids and the criterion by Madou and Leblond (2012a,b) regarding general ellipsoidal cavities within plastically isotropic matrices to arbitrary ellipsoidal voids in anisotropic matrix.

Nahshon and Hutchinson (2008) introduced a modification to the Gurson Model, incorporating the third stress invariant to account for damage growth during low triaxiality straining in shear-dominated situations. Meanwhile, Stewart and Cazacu (2011) put forth a macroscopic anisotropic yield criterion tailored for porous materials, characterized by an incompressible and anisotropic matrix that exhibits tension-compression asymmetry. This yield criterion is derived from micromechanical considerations and non-linear

homogenization, and it accommodates strength-differential effects. The developed criterion reduces to the yield criterion proposed by Benzerga and Besson (2001) (Eq. (1.3)) if the matrix material does not exhibit tension-compression asymmetry. The yield surfaces obtained using the anisotropic yield criterion proposed by Stewart and Cazacu (2011) are compared with those from the full-field dilatational viscoplastic fast Fourier transform (FFT) analyses for porous polycrystals undergoing twinning at the single-crystal level. Both methods demonstrate a pronounced sensitivity to the third invariant of the stress deviator, which is linked to the anisotropy and tension-compression asymmetry in the plastic behavior of the matrix as indicated by Lebensohn and Cazacu (2012).

Agoras and Ponte Castañeda (2014) introduced a finite strain constitutive model of macroscopic behavior of porous viscoplastic solids, considering changes in void size, shape, and distribution due to deformation. Utilizing the 'iterated variational linear comparison' procedure of Agoras and Ponte Castañeda (2013), the model employs consistent homogenization estimates to describe both the instantaneous effective behavior of the porous material and the development of its inherent microstructure.

The effects of stress triaxiality, Lode parameter, and initial void volume fraction on the behavior of void collapse and void coalescence were investigated by Liu et al. (2016) through micromechanical modeling, focusing on the energy perspective (specifically change in elastic energy relative to the plastic work). The numerical results revealed that the loci of strain-to-onset of void collapse and void coalescence were found to be discontinuous functions of stress triaxiality, with a transition zone separating the two behaviors. Within this region, characterized by low triaxiality, there exists an interplay between void collapse and coalescence.

Morin et al. (2017) proposed a Gurson-type model for ductile porous materials, incorporating both isotropic and kinematic hardening. This model is based on a "sequential limit-analysis" of a hollow sphere made from a rigid-hardenable material. The influence of the heterogeneous distribution of microscopic hardening parameters near the voids is comprehensively addressed in the model.

Srivastava et al. (2017) introduced the approach for characterizing the creep response of porous cubic single crystals which is based on the orthotropic potential proposed by Stewart and Cazacu (2011). This phenomenological model accounts for the impact of crystal orientation and the applied stress state on the evolution of both creep strain and porosity in porous cubic single crystals. When compared to results from three-dimensional finite deformation unit cell analyses (Srivastava and Needleman, 2015), the phenomenological model not only reproduces similar trends but also exhibits notable quantitative agreement in certain cases.

A micromechanical modeling approach for a rigid plastic Huber-Mises matrix material with spherical voids, incorporating the coupling of mean-field homogenization with Gurson's single cavity stress-strain solution, was proposed by El Ghezal and Doghri (2018). Alternative microstructures (rigid plastic inclusions embedded in the homogeneous Gurson material) are homogenized using the generalized self-consistent (GSC) and Mori-Tanaka (MT) models. Numerical predictions of effective yield surfaces are then compared against full-field finite element (FE) and analytical results for a range of porosities.

Torki (2019) proposed a unified model for the description of void growth and coalescence under combined tension and shear. This model was formulated through limit analysis applied to a cylindrical elementary cell that encompasses a coaxial cylindrical void. Sartori et al. (2019) developed analytical expressions for mechanical fields, such as macroscopic stress, effective equivalent plastic strain rate in the matrix, and plastic multiplier, while characterizing porous materials with either the Gologanu et al. (1997) or Gurson (1977) yield surfaces. This approach is suitable for thermo-viscoplastic materials that show strain hardening and is not confined to materials that behave perfectly plastic. A plastic instability criterion for porous plastic solids was derived by Keralavarma et al. (2020). The failure criterion is contingent upon the stress triaxiality, Lode parameter, porosity, and the strain hardening characteristics of the material. It distinctly indicates that failure arises due to the interplay between strain hardening and softening induced by void growth within the coalescence band.

The distinctive mechanical behaviors of the GTN and Rousselier models were discussed by Rousselier (2021). The Rousselier model demonstrates the capability to achieve strain localization in a plane at all stress triaxialities, while the GTN model is limited to pointwise localization for the ultimate mechanical state, a constraint that can be alleviated through finite element discretization. Due to its analytical form, the Rousselier model was incorporated by the author into the multiscale framework of self-consistent polycrystalline plasticity, allowing for the modeling of various mechanisms related to plasticity and ductile fracture at the slip system scale.

An isotropic multi-surface model, which incorporates inhomogeneous yielding, was formulated by Torki et al. (2021). This model was employed to explore the influence of the third stress invariant on ductile failure. The effective yield surface of a material containing voids is influenced by all stress invariants, including the third stress invariant. The influence of the third stress invariant is particularly prominent at low stress triaxiality and is attributable to the occurrence of inhomogeneous yielding.

In this section, various phenomenological macroscopic models addressing ductile failure in porous materials are reviewed. Initial analytical solutions for void growth were

provided by McClintock (1968); Rice and Tracey (1969). Models were then formulated using thermodynamic principles, kinematic limit analysis, or variational homogenization theory. The classical Gurson model, derived from kinematic analysis for the Huber-Mises material, was extended in multiple ways, including the incorporation of tuning parameters from unit cell FE computations to enhance model predictions, the inclusion of the third stress invariant, hardening, tension-compression asymmetry, and general ellipsoidal shape of voids with their distribution. Similarly, models for viscoplastic porous solids were extended. Additionally, a GTN-type criterion was developed for anisotropic matrices following the orthotropic Hill criterion and the similar extensions are proposed to this model as those applied to the Gurson model. Most of these formulations are validated with respect to FE computations.

1.2.3 Macroscopic finite element models for porous ductile materials

In this section, computational finite element (FE) models used to study ductile failure in porous materials will be discussed. Recalling that the GTN model was validated through numerical unit cell analyses in terms of yield point prediction, porosity growth, and evolution of macroscopic response of porous materials, attention will now be directed towards the FE approaches applied to further investigate ductile failure mechanisms.

The computational cell model, as employed by Faleskog et al. (1998), has demonstrated successful application in predicting the nonlinear fracture behavior of low and moderately hardening materials. Moreover, its adaptability extends to high hardening materials through a two-step calibration procedure that encompasses the calibration of GTN and cell fracture parameters. When appropriately calibrated, the cell model proves capable of accurately capturing the load, displacement, and crack growth histories under various loading conditions for high hardening materials. Barsoum and Faleskog (2011) explored the influence of the Lode parameter on the failure of ductile materials, focusing on deformation concentration in a narrow band with voids. They used a micromechanical model with a 3D unit cell (Fig. 1.4a) containing a single void and found that the third invariant of stress impacts void shape evolution, and the growth rate increases as stress triaxiality decreases. At moderate triaxiality, the Lode parameter strongly influences the behavior of the voided band. However, in shear-dominant stress states, the localization criterion does not predict material failure, suggesting a need for a micromechanical-based coalescence criterion in such conditions. Using unit cell micromechanics, Wong and Guo (2015) investigated tensile and shear void coalescence in ductile materials from an energetics perspective. Analyses were conducted for general triaxial stress states under imposed periodic, homogeneous

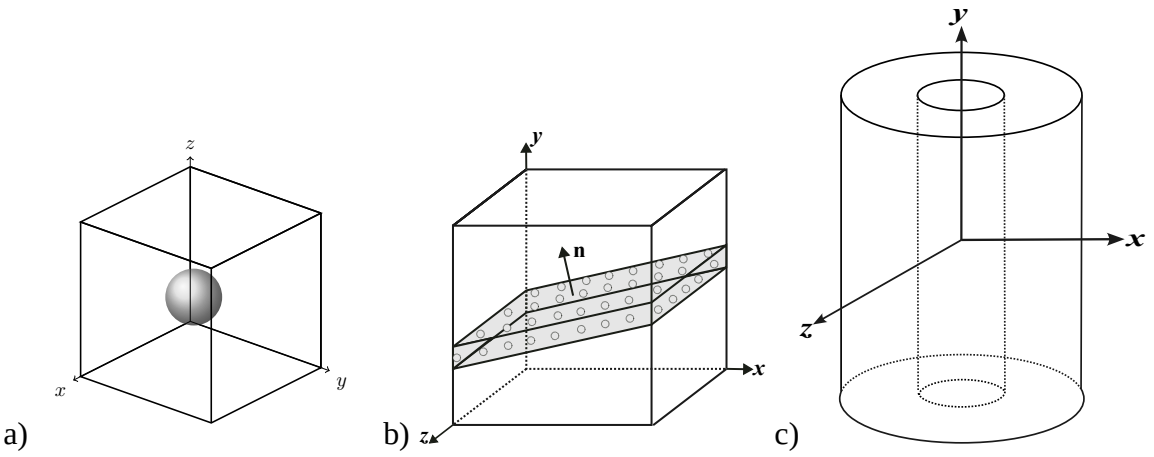

FIGURE 1.4 Schematic representation of various cell models used in computational studies of ductile failure. (a) Unit cell with a spherical void, (b) void band cell inclined at an arbitrary angle, (c) long cylindrical cell with a cylindrical void, where a slice can be cut and treated as a plane strain model for analysis.

and symmetric boundary conditions, considering the presence and absence of shear stress as dictated by stress triaxiality and Lode parameter. Shear stress was found to have a significant impact on lowering the effective strains at the beginning and end of void coalescence, based on the total elastic and plastic energies of the cell.

The impact of stage III and IV hardening on void expansion and coalescence was evaluated by Lecarme et al. (2011) using FE unit cell calculations and a Kocks-Mecking type hardening law. It was found that stage IV hardening can greatly delay void coalescence while increasing ductility. Subsequently, the Kocks-Mecking rule was incorporated into the Gologanu-Leblond-Devaux (GLD) porous plasticity model, and damage model predictions were compared to FE results.

Tekoğlu et al. (2015) employed a FE 3D model (Fig. 1.4b), incorporating a porous band with a doubly periodic array of spherical voids, to explore two distinct mechanisms of strain localization: macroscopic localization driven by void growth and localization resulting from void coalescence. It was observed that simultaneous occurrence is evident at low triaxialities, while a clear distinction is notable at high triaxialities. In a similar manner, Guo and Wong (2018) applied the 3D void-sheet model to clarify the differences in the onset of macroscopic strain localization and void coalescence, emphasizing that macroscopic strain localization precedes void coalescence.

For a three-dimensional non-periodic void cluster, Trejo Navas et al. (2018) conducted a parametric study to investigate void growth and coalescence. The simulations show non-uniform and rapid void growth close to the plastic localization band. The coalescence mechanism observed between voids involves internal necking, underscoring the significance

of considering intervoid interactions. Using unit cell finite element computations, Reboul et al. (2020) examined the impact of strain rate sensitivity on the onset of strain localization and void coalescence in porous ductile materials. It was found that the applied stress triaxiality and the strain rate sensitivity had a significant impact on both the critical porosity and strain.

1.2.4 Crystal plasticity FE models for porous crystals

Recently, there has been a growing interest in characterizing void growth at the single crystal level within the context of crystal plasticity framework. In this context, numerical investigations involving 2D and 3D unit cells containing cylindrical or spherical voids embedded within the single crystal matrix have been performed. Firstly, finite deformation and rate-dependent crystal plasticity theory within the framework of 2D planar strain models were employed by O'Regan et al. (1997) and Potirniche et al. (2006) to investigate the growth and coalescence of microvoids in single crystals under in-plane strain-driven boundary conditions. In a similar fashion, Liu et al. (2007) utilized numerical analysis on a 3D unit cell containing a spherical void to investigate the behavior of void growth and coalescence in FCC single crystals employing 3D rate-dependent crystal plasticity theory. The results show that the growth patterns and shape of voids are strongly influenced by the crystallographic orientation, especially under loading with a small strain biaxiality. Additionally, Liu et al. (2007) presented results concerning microstructure evolution in the presence of voids. Their focus lies on texture evolution within the unit cell and the heterogeneity of deformation, assessed through the misorientation angle with respect to the average orientation. It was concluded that the areas around the void exhibit concentrated lattice rotation heterogeneity. Gan et al. (2006) compared results from the proposed anisotropic slip line theory (Kysar et al., 2005) with experimental and finite element findings concerning deformation around a cylindrical void in FCC single crystals. The investigation involved in-plane uniaxial compression of a single crystal along the [001] direction, with the cylindrical void axis aligned along the [110]. As elucidated in detail by Gan et al. (2006), the application of the anisotropic rigid-plastic slip line theory in this configuration ensures a plane strain condition in the [001] - [110] crystal plane under the influence of compressive or tensile loading, incorporating three effective in-plane slip systems. The study demonstrated that the measurements of lattice rotation agrees well with the numerical results, particularly in illustrating the deformation sectors around the void.

The effect of stress triaxialities, crystallographic orientations, and initial void volume

fractions on void growth and coalescence in FCC single crystals was examined by Ha and Kim (2010) through the incorporation of rate-dependent single crystal plasticity into a 3D finite element framework. It was demonstrated that the void growth is primarily dictated by the crystallographic orientation at low stress triaxiality, while the impact of stress triaxiality becomes more pronounced at higher values. The void undergoes a transformation into prolate and oblate shapes influenced by stress triaxiality, and the formation of corners was observed for specific crystallographic orientations. The growth rate of voids is more rapid for smaller initial void volume fractions in comparison to larger ones. In a similar manner, Yerra et al. (2010) employed 3D finite element calculations to study void formation and coalescence in BCC single crystals. Furthermore, the Thomason void coalescence criterion was utilized to investigate the onset of void coalescence. Using a crystal plasticity constitutive model that considers self and latent hardening, Zhang et al. (2009) investigated the effects of strain rate sensitivity, hardening, and the initial orientation of the loading axis on necking under tensile loading of aluminum single crystals. The results demonstrated that each of these parameters influences the localization strain. The influence of the creep exponent, void spacing, initial void fraction, and Lode parameter under fixed triaxiality on the dynamics of void growth and collapse in FCC single crystals was investigated by Srivastava and Needleman (2013) using the unit cell FE methodology. In a similar fashion Srivastava and Needleman (2015) analyzed the impact of crystal orientation, stress triaxiality, and the third invariant of stress on void evolution in FCC single crystals using a rate-dependent crystal plasticity framework. The study revealed that, for higher triaxialities and asymmetric orientations, the Lode parameter has a significant impact on both porous and creep strain evolution.

Concerning HCP crystals, only a few studies have been found in the literature. HCP materials undergoing deformation through slip and twinning were exclusively investigated by Prasad et al. (2015) in the case of cylindrical voids and by Selvarajou et al. (2019) for spherical voids. An unexpected effect of twin-related reorientation was observed on void growth, resulting in a substantial decrease in porosity under uniaxial c-axis loading. Additionally, lattice reorientation due to twinning exhibited spatial non-uniformity within the cell, leading to the formation of twin-matrix and twin-twin boundaries. The intersections of these boundaries with the void became hotspots of strain concentration, resulting in facet formation and the development of complex quasi-polyhedral shapes for evolving cavities.

Beyond single crystal case, Liu et al. (2009) and Dakshinamurthy et al. (2021) explored void growth at grain boundaries using a bi-crystal unit cell model. The void shape in bi-crystals is affected by triaxiality, Lode parameter, and the initial orientation of each grain. Due to the heterogeneity of slip activity at higher triaxialities, voids tend to grow faster

in soft orientations, while they collapse in hard orientation crystals. Furthermore, around the void, heterogeneity of lattice rotation is observed, leading to grain fragmentation. Additionally, Jeong et al. (2018) conducted CPFEM simulations on Representative Volume Elements (RVE) of BCC single, bi, and tri-crystals, incorporating voids within the grains, grain boundaries, and tri-junctions. The study indicated that the anisotropic expansion of voids located at grain borders is impacted by inter-grain orientations. Frodal et al. (2021) integrated damage evolution with a single crystal plasticity model to predict failure in polycrystalline materials. The outcomes from this coupled model effectively replicated the experimental responses of both smooth and notched tensile specimens with a high level of accuracy.

In spite of predominant FE simulations, the fast Fourier transform (FFT) method, dislocation dynamics or molecular dynamics calculations were used to study the void initiation and growth in crystalline materials. Let us mention a few examples. Bringa et al. (2010) examined the influence of the loading direction on void initiation in FCC nano-crystalline metals through molecular dynamics simulations. The simulations revealed that distinctive dislocation loops, originating at the surface of nanoscale voids, played a crucial role in the outward growth of the voids and the formation and interaction of these loops were found to be contingent on the loading orientation of the material. In a similar manner, the impact of size effect on void growth in FCC single crystals was demonstrated by Chang et al. (2015) using three-dimensional dislocation dynamics. A dislocation-density-based evolution formulation was incorporated into a crystal plasticity model by Shanthraj and Zikry (2012) to examine the mechanisms governing plastic strain localization and void interactions in crystalline materials. Anisotropic dislocation interactions, including junction formation and annihilation in FCC crystals, can lead to significant variations in microstructural evolution and void interaction behavior based on crystal orientation.

Lebensohn et al. (2013) introduced an FFT-based full-field formulation for calculating void growth in porous polycrystalline materials. This formulation involves the integration of polycrystal plasticity and dilatational plasticity. Subsequently, the obtained results were compared with unit cell finite element calculations.

1.2.5 Crystal plasticity phenomenological models for porous crystals

Regarding the analytical description of porous crystals, there are limited contributions. A micromechanical two-level homogenization approach for modeling ductile damage in polycrystalline materials with hard intracrystalline particles was proposed by Bonfoh

et al. (2004). At the single crystal level (micro-meso transition) with hard particles, they proposed a novel hardening law that considers particle and dislocation interactions. Additionally, the formation of cavities at the Particle–Crystal interface was predicted based on the comparison of elastic energy of the particle and surface energy formation. For meso-macro transition to polycrystal level self-consistent approach was used.

Han et al. (2013) proposed a phenomenological extension of the Schmid multisurface to incorporate porosity in FCC single crystals. This extension was developed using the micromechanical variational homogenization method introduced by DeBotton and Ponte Castañeda (1995). It is noteworthy that the original outcome of this method was a quadratic criterion in terms of the void volume fraction and dilatational stress. Subsequently, this criterion was adapted to a Gurson-type model through the use of a power expansion of the $\cosh(\mathrm{x})$ function. Furthermore, three tuning parameters were introduced based on the Tvergaard-Needleman concept, and these parameters were calibrated using unit cell calculations. Ling et al. (2016) proposed an elasto-viscoplastic model for porous single crystals at finite strains, extending the yield function developed by Han et al. (2013) for porous single crystals at infinitesimal strains to include finite strains. The porosity evolution and strain hardening of the single crystal matrix is incorporated in the model. Furthermore, the proposed GTN-type framework has been integrated into the large strain constitutive model and implemented in the finite element code. Preliminary FEM results are provided for uniaxial tension tests conducted on notched single crystal specimens.

Models relying on the Schmid criterion (as the Han et al. (2013) yield criterion) are recognized to encounter challenges in the distinct selection of active slip systems, necessitating special procedures in the finite element implementation of the model. This difficulty can be circumvented by employing the regularized Schmid law of 2n degree (Arminjon and Bacroix, 1991; Gambin, 1991; Kowalczyk and Gambin, 2004). Following this observation, Paux et al. (2015); Paux et al. (2018) formulated a GTN-type model based on the regularized law. Notably, the resulting yield condition comprises only two fitting parameters, compared to the three parameters present in the proposal by Han et al. (2013). This condition was derived by initially assuming n = 1 and following the methodology of kinematic limit-analysis applied to a hollow sphere made of an anisotropic Hill matrix, as outlined by Benzerga and Besson (2001). Subsequently, the result was ad-hoc generalized to n > 1. It is important to highlight that one of the tuning parameters in the development process is referred to as the anisotropy coefficient.

There is also a family of analytical models, which are formulated by means of the variational homogenization approach. Idiart and Ponte Castañeda (2007) derived variational bounds on effective potentials based on the generalized linear comparison method for

non-linear composites with crystalline constituents. This application was specifically focused on a two-phase porous crystalline material, which consists of a viscoplastic single crystal phase and isotropically and randomly distributed cylindrical pores. Applying similar methodology, constitutive models for nonlinear voided polycrystals, incorporating dilatational viscoplastic behavior, were developed by Lebensohn et al. (2011); Lebensohn et al. (2012) using the variational linear comparison approach. The model predictions were subsequently compared to results from full-field numerical simulations, employing FFT method, to investigate the influence of various microstructural parameters such as overall porosity and matrix phase texture.

Mbiakop et al. (2015b) proposed a rate-dependent constitutive model for porous single crystals with elliptical voids under plane strain conditions for arbitrary slip systems. The model is based on Ponte Castañenda (1991) variational nonlinear homogenization approach and Danas and Aravas (2012) modified variational method. The model was validated using full-field FE simulations of periodic unit cells, which took into account numerous parameters such as crystal anisotropy, void shapes and orientations, creep exponents, and loading conditions. Similarly, Mbiakop et al. (2015a) extended the model to three dimensions, specifically addressing porous single crystals with ellipsoidal voids with arbitrary crystal anisotropy.

A generalized iterated variational homogenization (IVH) method was developed by Song and Ponte Castañeda (2017b) based on the combination of the nonlinear variational homogenization method and the iterated homogenization procedure introduced by Agoras and Ponte Castañeda (2013). This method was utilized to estimate the effective flow potential of high anisotropic, low lattice symmetry HCP porous viscoplastic single crystals. The macroscopic response of porous HCP crystals to axisymmetric loadings was examined, and it was shown that porosity, void shape, and crystal anisotropy all influence the overall size, shape, and orientation of the macroscopic gauge surfaces, which is defined as the single equi-potential surface in stress space to represent effective behavior of the porous single crystal. Similarly, a finite-strain constitutive model for the macroscopic response of porous viscoplastic single crystals was developed by Song and Ponte Castañeda (2017a), utilizing the fully optimized second-order (FOSO) variational method of Ponte Castañeda (2015), in conjunction with an appropriate generalization of the iterated homogenization procedure by Agoras and Ponte Castañeda (2013). This fully optimized second-order (FOSO) variational approach was used by Song and Ponte Castañeda (2018a,b) to derive finite-strain constitutive models for the macroscopic response of porous polycrystals with huge pores randomly scattered across a fine-grained polycrystalline matrix.

Das et al. (2021) developed a constitutive model for porous polycrystals with

pressurized pores, taking into account the evolution of pore pressure, shape, and matrix texture with deformation. This was accomplished using an iterative second-order variational homogenization approach proposed by Song and Ponte Castañeda (2018a) for vacuous pores. The porous polycrystal is thought of as a three-scale composite, and the model was used to study the macroscopic response of porous ice-type HCP polycrystals. The existence of pressured pores can cause solid polycrystal-like behavior and have a major hardening influence on the overall response.

A reduced micromorphic crystal plasticity model at finite deformations was formulated by Ling et al. (2018), based on a single scalar variable known as microslip. This proposed model was subsequently utilized to investigate strain localization phenomena, as well as void growth and coalescence, in FCC single crystals. The investigation of viscoplastic behavior in voided cubic crystals under hydrostatic loading was explored in a micromechanical study by Joëssel et al. (2018). Three distinct methodologies were utilized, encompassing a Gurson-type estimate treating crystals as hollow sphere assemblies, a sequential laminate approach of infinite rank, and a complex unit cell representation of a periodic medium. Results revealed consistent agreement among the approaches under weak plastic anisotropy conditions. However, discrepancies arose under conditions of strong plastic anisotropy.

Scherer et al. (2019) derived closed-form analytical solutions for single slip under conditions of positive, zero, and negative strain hardening within a periodic unit cell subjected to simple shear. These solutions were subsequently employed to validate the finite element implementation. Additionally, they proposed an enhanced model incorporating non-linear saturating softening behavior, which was applied to investigate the interaction between voids and slip bands.

A crystal plasticity based constitutive model for porous single crystals was proposed by Siddiq (2019), accounting for damage resulting from void growth and coalescence. A detailed parametric assessment has been conducted to explore the impact of various parameters on material response. Subsequently, the proposed model has been implemented in a finite element framework. A coalescence criterion for porous single crystals with periodic arrays of voids was proposed by Hure (2019), based on limit-analysis, homogenization, and crystal plasticity. Good agreement with numerical results for various configurations has been demonstrated. The criterion considers crystal orientation, void lattice, and their interactions.

A ductile damage model was proposed by Kong et al. (2023), which integrates classical porous plasticity and the Coulomb-Rousselier-Luo (CRL) model at the slip system scale into a mean-field polycrystalline framework. The proposed model was applied to sheet specimens made of an anisotropic aluminum alloy under non-proportional loading.

In addition to the literature mentioned above, it should be noted here that some recent review papers have been published, which encompass profound literature pertaining to ductile failure. Pineau et al. (2016) provided an overview of metal failure, focusing on brittle and ductile fracture under monotonic loads. The local approach to fracture was discussed, which included the integration of microstructure, physical mechanisms, and overall fracture properties. Das (2021) undertook a thorough literature study on the fracture micro-mechanisms of ductile porous solids, emphasizing the intricate interplay between engineering/metallurgical variables. The research history, status, importance, and potential gaps in ductile fracture research were discussed.

1.3 Scientific goal and scope of the thesis

The scientific aim of this thesis is *to comprehend and elucidate, through numerical analyses and micromechanical modeling, the relationship between crystal anisotropy and the processes of void growth and coalescence that result in ductile damage in polycrystalline metals and alloys characterized by FCC and HCP symmetry, especially when they deform by slip and twinning*. As discussed in the preceding Section 1.1, materials with high plastic anisotropy, such as magnesium, zirconium, or zinc alloys with a HCP lattice, are known to exhibit reduced ductility and fracture toughness. These limitations stem from a scarcity of easily deformable slip systems and the occurrence of twinning. The failure mechanism linked to void growth under conditions of locally constrained plastic deformation within a crystallite and the markedly heterogeneous stress field in a polycrystalline volume element is not yet fully understood and incorporated into validated constitutive models. Micromechanics, describing the connection of the macroscopic response of heterogeneous materials with the local properties and microstructure geometry through properly selected micro-macro transition schemes, is considered a well-suited tool to address the current problem and fill this gap. In analogy to the seminal results by Gurson, Tvergaard, and Needleman (the so-called GTN model of ductile damage), the applied approach is expected to yield macroscopic elasto-(visco)plastic models for porous crystals and polycrystals of specified lattice symmetry. These models can then be utilized as material models in large-scale finite element (FE) calculations.

The effectiveness of the proposed micromechanical approach in making accurate predictions depends on two critical factors: i. the accurate identification of the phenomena influencing crystal behavior at the local observation level, and ii. the judicious selection of an appropriate micro-macro transition scheme. In the context of metals with HCP lattice symmetry, the local constitutive rule must consider the mutual interactions between different

slip modes and twinning, altering hardening laws for material parameters like critical resolved shear stresses (Sahoo et al., 2019; Frydrych et al., 2020). Furthermore, twinning, in contrast to slip, possesses a polar character and results in a sudden lattice reorientation within a part of the observed grain. This transformation turns a single grain into a bi- or multi-crystal, comprising parent and twin orientations. Consequently, this process induces heterogeneous plastic flow within the volume element, leading to the development of local internal stresses and grain refinement. Experimental observations (Nemcko et al., 2016; Kondori et al., 2018) confirm that all these phenomena, especially the twin-matrix boundaries significantly impact void growth and coalescence. Therefore, they will be integrated into the local crystal plasticity model employed within the micromechanical framework.

Concerning the micro-macro transition, the primary challenge lies in the pronounced non-linearity and anisotropy of local behavior. Established micro-macro transition schemes, such as the Mori-Tanaka method, the self-consistent method, the generalized self-consistent model, and the differential and incremental schemes (Nemat-Nasser and Hori, 1999) were originally formulated assuming a linear constitutive law. To adapt these concepts to cases involving physical nonlinearity, some form of linearization scheme must be applied (Kanouté et al., 2009). The formulation of such a scheme is not trivial, particularly when dealing with an elasto-viscoplastic medium, as demonstrated by Mercier et al. (2019). In the present work, the so-called sequential linearization method will be applied in this regard (Kowalczyk-Gajewska and Petryk, 2011; Girard et al., 2021) and its applicability to porous polycrystalline materials will be verified.

In this study, while the primary focus is on porous polycrystalline materials with HCP lattice symmetry, the analysis encompasses comprehensive numerical studies and detailed application of micromechanical theories to FCC porous polycrystalline materials as well. The investigation initiates with an in-depth examination of void growth and coalescence scenarios in unit cells of porous single crystal, employing the crystal plasticity finite element method (CPFEM) for both FCC and HCP crystal structures. Subsequently, the research moves to formulation of micromechanical models, addressing both porous single and polycrystals characterized by FCC and HCP symmetry.

After detailed discussion of the state of the art in terms of ductile failure in metals and alloys presented in previous subsections, the next chapters present own research focusing on numerical and analytical micromechanical modeling of these phenomena in single and polycrystalline metals and alloys. The thesis is organized as follows:

In Chapter 2, a crystal plasticity model that accounts for both slip and twin systems is presented. This model is implemented within a finite element framework to perform unit

cell calculations in both 2D and 3D cases for HCP and FCC porous single crystals. In Chapter 3, the finite element implementation and the various boundary conditions applied to the unit cell models are discussed in detail.

In Chapter 4, the crystal plasticity finite element method (CPFEM) is employed to investigate cylindrical void growth or collapse in FCC crystals, as well as accompanied microstructure evolution, using a 2D plane strain model. This study compares displacement-controlled and stress-controlled boundary conditions, and examines the anisotropic response of porous crystals under different crystal orientations. In Chapter 5, the similar analysis is conducted for HCP crystals. A 2D plane strain model with a cylindrical void under prismatic and c-axis loading is studied across different biaxial loading scenarios, with the results compared to the work of Prasad et al. (2015). Subsequently, a 3D unit cell with a spherical void under uniaxial loading is considered. In this study, the loading direction is varied while the crystal orientation remains fixed. The obtained results are then compared with the work of Selvarajou et al. (2019).

In Chapter 6, a theoretical formulation of a novel micromechanical mean field model for porous polycrystals is presented. At the level of crystal with a void, the additive Mori-Tanaka scheme is employed to determine the overall response of the porous single crystal, while the additive self-consistent scheme is used to find the overall response of the porous polycrystals. The numerical implementation of this model, for both single and polycrystals, is discussed in Chapter 7. In addition, the mean field model predictions are validated against unit cell FE computations for both porous single and polycrystals.

Finally, in Chapter 8, a new GTN-type yield criterion for porous single crystals is proposed, based on the micromechanical approach discussed in Chapter 6. The tuning parameters of the model are calibrated using unit cell FE computations. The predictions of the model are then compared with the proposals of Han et al. (2013) and Paux et al. (2018) for FCC single crystals. Additionally, for HCP crystals, the extension of Paux et al. (2018) yield criterion that account for twinning is proposed and calibrated. The calibrated anisotropic parameter, based on optimization employing differential evolutionary algorithm, is compared with the results obtained using kinematic limit analysis under hydrostatic loading. The thesis concludes with a brief summary and suggestions for future work.

The results from Chapter 4 have already been published in the article Virupakshi and Kowalczyk-Gajewska (2023). As the content of this article aligns with the material included in this chapter, its certain sections reproduce parts of this publication. Additionally, in the remaining sections of the thesis, the content that overlaps with the article has been expanded upon to different extent.

CHAPTER 2

Crystal plasticity model

In this chapter, the crystal plasticity formulation accounting for slip and twinning is presented. This formulation is utilized in the unit cell finite element calculations for FCC and HCP crystal systems, which will be discussed in the subsequent chapters. Initially, the slip and twin systems considered for both crystal systems throughout the work are presented, followed by a description of kinematics and constitutive equations. The proposed model incorporates the polarized character of twinning, the emergence of new twin-related orientations (via reorientation scheme), and the impact of the slip-twin coupling on the hardening phenomenon and the lattice rotations during deformation.

2.1 Notation

Throughout the work, the "tensor" notation is used. When needed, certain expressions are also presented in indicial notation, utilizing tensor components within an orthonormal basis and the summation convention over the repeated indices. The following notation conventions apply:

- Scalars are represented in italics or roman typeface, for example, $\dot{\gamma}^r, E, \tau^r_{cr}$, Σ_{m}, $\log(\mathrm{L}_0)$.
- Vectors and second-order tensors are denoted by boldface English or Greek alphabets, both in small and capital letters, for eg., $\mathbf{m}, \mathbf{n}, \mathbf{F}, \boldsymbol{\sigma}, \boldsymbol{\Sigma}$.
- The double-struck letters are used to represent fourth-order tensors. e.g., $\mathbb{S}, \mathbb{P}, \mathbb{L}, \mathbb{M}$

The second-order and fourth-order identity tensors are denoted as $\mathbf{I}$ and $\mathbb{I}$, respectively. Their components in any orthonormal basis are expressed as δ_{ij} and $\delta_{ik}\delta_{jl}$, respectively. In the subspace of symmetric second-order tensors, the identity operation is achieved through the symmetrized $\mathbb{I}$, represented as $\mathbb{I}^S$, with components $\frac{1}{2}(\delta_{ik}\delta_{jl} + \delta_{il}\delta_{kj})$. The notation

TABLE 2.1 Notation used for tensor operations.

Tensor Notation	Indicial Notation
$\mathbf{m}\cdot\mathbf{n}, \mathbf{T}\cdot\mathbf{F}, \mathbb{P}\cdot\mathbb{L}$	$m_i n_i, T_{ij}F_{ij}, P_{ijkl}L_{ijkl}$
$\mathbf{F}\cdot\mathbf{n}, \mathbb{P}\cdot\mathbf{n}, \mathbb{P}\cdot\mathbf{F}$ $\mathbf{n}\cdot\mathbf{F}, \mathbf{n}\cdot\mathbb{P}, \mathbf{F}\cdot\mathbb{P}$	$F_{ij}n_j, P_{ijkl}n_l, P_{ijkl}F_{kl}$ $n_iF_{ij}, n_iP_{ijkl}, F_{ij}P_{ijkl}$
$\mathbf{m}\otimes\mathbf{n}, \mathbf{T}\otimes\mathbf{F}, \mathbb{P}\otimes\mathbb{L}$ $\mathbf{F}\otimes\mathbf{n}, \mathbb{P}\otimes\mathbf{n}, \mathbb{P}\otimes\mathbf{F}$	$m_i n_j, T_{ij}F_{kl}, P_{ijkl}L_{pqrs}$ $F_{ij}n_k, P_{ijkl}n_p, P_{ijkl}F_{pq}$
$\mathbf{TF}, \mathbb{P}\circ\mathbb{L}, \mathbf{T}:\mathbf{F}$	$T_{ij}F_{jk}, P_{ijkl}L_{klmn}, T_{ij}F_{ji}$
$\nabla\mathbf{v}, div\mathbf{v}, rot\mathbf{v}$ $\nabla\mathbf{T}, div\mathbf{T}$	$v_{i,j}, v_{i,i}, \epsilon_{ijk}v_{k,j}$ (where ϵ_{ijk} is a permutation tensor) $T_{ij,k}, T_{ij,j}$

employed for various operations involving tensors of different orders is summarized in Tab. 2.1. The second-order tensor $\mathbf{F}$ with components F_{ij} is represented by $\mathbf{F}^T$ when transposed, indicating a tensor with components F_{ji}, while the fourth-order tensor $\mathbb{P}$ with components P_{ijkl} is denoted by $\mathbb{P}^T$ when transposed, representing a tensor with components P_{klij}. Inverses of second- and fourth-order tensors are denoted as $\mathbf{F}^{-1}$ and $\mathbb{P}^{-1}$, respectively.

2.2 Abbreviations

Below are the defined abbreviations used throughout the entire text:

- FCC - Face Centered Cubic
- FFT - Fast Fourier Transforms
- FEM - Finite Element Method
- CPFEM - Crystal Plasticity Finite Element Method
- HCP - Hexagonal Close Packed
- VPSC - ViscoPlatic Self Consistent
- PTVC - Probabilistic Twin Volume Consistent
- CRSS - Critical Resolved Shear Stress

- MFP - Mean Free Path
- RVE - Representative Volume Element
- RPP - Representative Porous PolyCrystal
- HPPC - Homogenized Porous PolyCrystal
- RPSC - Representative Porous Single Crystal
- HPSC - Homogenized Porous Single Crystal
- HEM - Homogenous Equivalent Medium
- EVPSC - Elasto-Visco Plastic Self-Consistent
- MFM - Mean Field Model
- IPF - Inverse Pole Figure
- SFE - Stacking Fault Energy
- GTN - Gurson-Tvergaard-Needleman

2.3 Crystal lattice symmetry

In this section, the independent components of the elastic stiffness tensor, as well as the slip and twin systems considered throughout the work for FCC and HCP single crystals, are discussed. For FCC crystals with cubic symmetry, the elastic stiffness tensor $\mathbb{L}_e$ has three independent components in anisotropy axes, namely $L_{1111} = L_{2222} = L_{3333}$, $L_{1122} = L_{1133} = L_{2233}$, and $L_{1212} = L_{1313} = L_{2323}$. However, for Mg and Ti HCP crystals with transverse isotropic symmetry, which have their third axis ($\mathbf{c} = \mathbf{e}_3$) coaxial with the main axis of symmetry, there are five independent components in the anisotropy axes: L_{1111}, L_{1122}, L_{1133}, L_{3333}, and L_{1313}. It is important to note that due to material symmetry, there are additional non-zero components, such as $L_{2222} = L_{1111}$, $L_{2233} = L_{1133}$, $L_{2323} = L_{1313}$, and $L_{1212} = L_{1111} - L_{1122}$.

The symmetry of the crystal influences the slip and twin systems that apply to the material being examined. The slip planes and directions are specified within the crystal frame, utilizing Miller indices. In this representation, the slip plane is identified by its normal vector (refer Kocks et al. (2000)).

TABLE 2.2 Slip & twin systems considered for FCC crystals.

1	2	3	4	5	6	7	8	9	10	11	12
Slip plane											
(111)	(111)	(111)	$(11\bar{1})$	$(11\bar{1})$	$(11\bar{1})$	$(1\bar{1}1)$	$(1\bar{1}1)$	$(1\bar{1}1)$	$(\bar{1}11)$	$(\bar{1}11)$	$(\bar{1}11)$
Slip direction											
$[1\bar{1}0]$	$[10\bar{1}]$	$[01\bar{1}]$	$[1\bar{1}0]$	$[101]$	$[011]$	$[110]$	$[10\bar{1}]$	$[011]$	$[110]$	$[101]$	$[01\bar{1}]$
Twin plane											
(111)	(111)	(111)	$(\bar{1}11)$	$(\bar{1}11)$	$(\bar{1}11)$	$(\bar{1}\bar{1}1)$	$(\bar{1}\bar{1}1)$	$(\bar{1}\bar{1}1)$	$(1\bar{1}1)$	$(1\bar{1}1)$	$(1\bar{1}1)$
Twin direction											
$[\bar{2}11]$	$[1\bar{2}1]$	$[11\bar{2}]$	$[211]$	$[\bar{1}\bar{2}1]$	$[\bar{1}1\bar{2}]$	$[2\bar{1}1]$	$[\bar{1}21]$	$[\bar{1}\bar{1}\bar{2}]$	$[\bar{2}\bar{1}1]$	$[121]$	$[1\bar{1}\bar{2}]$

TABLE 2.3 Slip & twin systems considered for HCP crystals.

	Slip/twin plane	Slip/twin direction
Basal slip	(0001)	$[11\bar{2}0]$
	(0001)	$[\bar{2}110]$
	(0001)	$[1\bar{2}10]$
Prismatic $\langle a \rangle$ slip	$(10\bar{1}0)$	$[1\bar{2}10]$
	$(01\bar{1}0)$	$[2\bar{1}\bar{1}0]$
	$(\bar{1}100)$	$[1120]$
Pyramidal $\langle c+a \rangle$ slip	$(11\bar{2}2)$	$[\bar{1}\bar{1}23]$
	$(\bar{1}2\bar{1}2)$	$[1\bar{2}1\bar{3}]$
	$(\bar{2}112)$	$[2\bar{1}\bar{1}3]$
	$(\bar{1}\bar{1}22)$	$[11\bar{2}3]$
	$(1\bar{2}12)$	$[\bar{1}2\bar{1}3]$
	$(2\bar{1}\bar{1}2)$	$[\bar{2}1\bar{1}3]$
Tensile twinning (TT)	$(10\bar{1}2)$	$[\bar{1}011]$
	$(\bar{1}012)$	$[10\bar{1}1]$
	$(1\bar{1}02)$	$[\bar{1}101]$
	$(\bar{1}102)$	$[1\bar{1}01]$
	$(01\bar{1}2)$	$[0\bar{1}11]$
	$(0\bar{1}12)$	$[01\bar{1}1]$

- In FCC crystals, plastic deformation predominantly occurs along the $\{111\}\langle 110\rangle$ family of slip systems and the $\{111\}\langle\bar{2}11\rangle$ family of twin systems. As a result, a total of 12 slip and 12 twin systems are considered in this study, each of which is

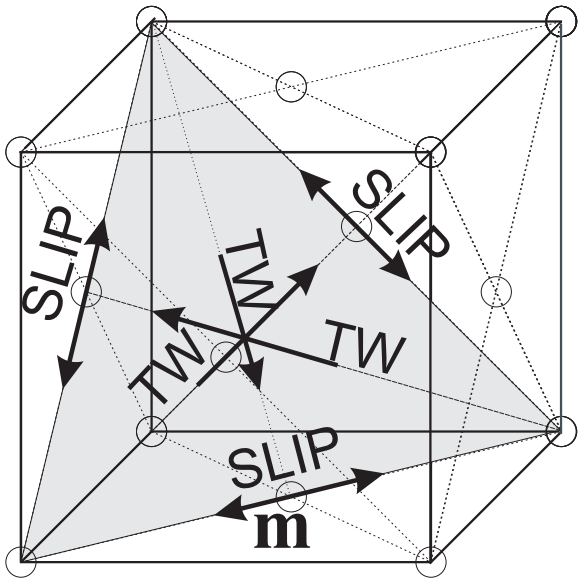

FIGURE 2.1 Geometry of slip and twin systems considered for FCC crystals (Kowalczyk-Gajewska, 2011).

detailed in Tab. 2.2. Furthermore, Fig. 2.1 illustrates a schematic representation of the FCC crystal structure, highlighting potential slip and twin systems.

- In HCP crystals, considered in the present thesis, characterized by low lattice symmetry in terms of plastic deformation, the slip systems are categorized into three families: three basal slip systems denoted as $\{0001\}\langle 11\bar{2}0\rangle$, three prismatic slip systems represented by $\{1100\}\langle 11\bar{2}0\rangle$, and six pyramidal slip systems indicated by $\langle c+a\rangle$ $\{1122\}\langle 11\bar{2}3\rangle$. Additionally, based on the lattice parameter c/a ratio, one family of tensile twin systems is identified, namely $\{10\bar{1}2\}\langle 10\bar{1}1\rangle$. Tab. 2.3 provides a comprehensive description of all the slip and twin systems examined in this study, utilizing the conventional notation of four Miller indices. Additionally, these systems are schematically depicted in Fig. 2.2. Although the present set of slip and twin systems is most commonly considered for Mg or Ti HCP alloys, other families of slip and twinning systems are sometimes considered in other works. While the use of four indices notation in the hexagonal system is common for describing HCP crystal symmetries, the non-orthogonality of this system necessitates its transformation into an orthonormal basis to ensure an accurate description of lattice orientation. In the current study, the x-axis is aligned parallel to the a_1 axis, as illustrated in Fig. 2.2. The orthonormal basis is denoted by $(x-y-z)$. An alternative approach is to orient the y-axis along the a_2 direction (refer to Frydrych and Kowalczyk-Gajewska (2018)).

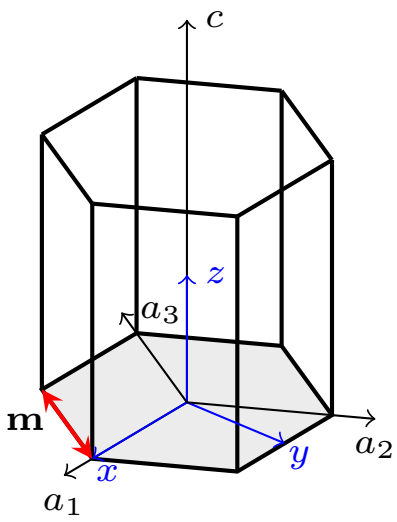

Basal slip

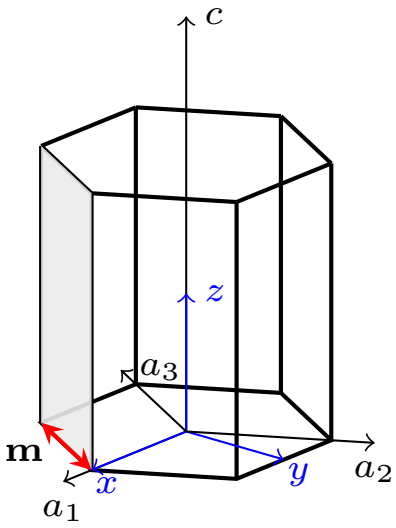

Prismatic $\langle a \rangle$ slip

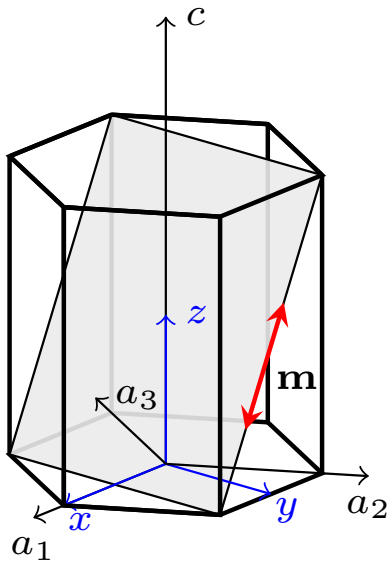

Pyramidal $\langle c+a \rangle$ slip

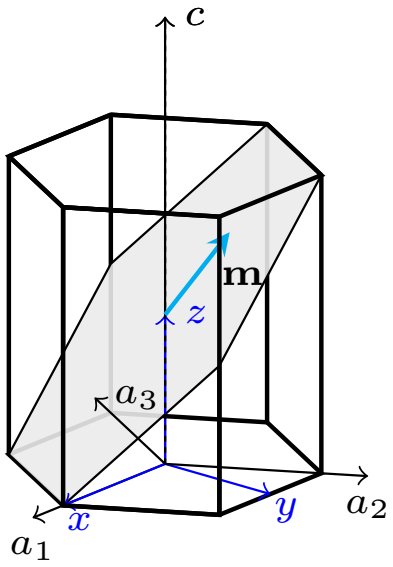

Tensile twinning

FIGURE 2.2 Geometry of slip and twin systems considered for HCP crystals.

2.4 Rate-dependent crystal plasticity formulation

Various proposals exist in the literature concerning crystal plasticity formulation, encompassing both full-field FEM, FFT-based models, and micromechanical mean-field models at both small strain and large strain regimes. Additionally, consideration is given to both elastic and viscoplastic components of deformation in some models, whereas others focus solely on the viscoplastic part, keeping only elastic rotations, while disregarding stretches due to their negligible contribution. Furthermore, various hardening models exist regarding the coupling between slip and twinning. Here, a brief description is provided for the various models existing in the literature, while the displacement-based model in the Lagrangian framework, utilized in the present work, is presented in detail, encompassing the consideration of twinning and the reorientation scheme within the model.

In the domain of finite strain elasto-viscoplasticity of crystals, two types of models are prevalent. The first class of models is based on the velocity-based method, which uses an additive decomposition of the velocity gradient ($\mathbf{L}$) and the hypoelastic law. For example, Frodal et al. (2021, 2023) proposed a coupled damage crystal plasticity model using a hypoelastic corotational formulation and objective stress rates. The second kind of models is based on an incremental displacement-based framework and a multiplicative decomposition of the deformation gradient ($\mathbf{F}$) utilizing the hyperelastic law. The hyperelastic law is formulated using conjugated stress and strain measures. If the elastic component is small, the law can be approximated as linear. Regarding micromechanical mean field models, a VPSC formulation was proposed by Lebensohn and Tomé (1993) to simulate plastic deformation in polycrystals. This formulation is based on an additive decomposition of the velocity gradient. In this model, the contributions to deformation from the elasticity part are considered small compared to plastic deformation by slip, hence they are neglected. The crystal lattice is updated using an elastic spin tensor ($\mathbf{W}^e$), and the model is formulated based on stress and strain rate tensors utilizing inclusion problem and various linearization schemes due to the rate-dependent nonlinear power law. This model has been employed in one of our recent publications (Frydrych et al., 2021) for finding optimal crystal plasticity parameters by comparing experimental textures with the simulated textures.

A crystal plasticity model for pure Mg, encompassing slip and deformation twinning, was proposed by Zhang and Joshi (2012) based on the framework of Kalidindi (1998). Drawing from experimental observations, they developed constitutive descriptions for the evolution of slip and twinning, as well as their hardening interactions. Additionally, they integrated lattice reorientation resulting from twinning into their model. Moreover, in a more recent work, a finite-strain phase-field model that integrates deformation twinning

and crystal plasticity was introduced by Rezaee-Hajidehi et al. (2022). Within this model, twinning is regarded as a displacive transformation distinguished by a volume-preserving stretch, as opposed to a simple shear considered in the standard approach. In the following sections, the displacement-based formulation utilized in the current work will be presented.

2.4.1 Kinematics

The initial step in the model formulation involves describing the kinematics. In terms of kinematic description, the model adheres to classical contributions (Hill and Rice, 1972; Asaro and Rice, 1977; Asaro and Needleman, 1985). The deformation gradient $\mathbf{F}$ is multiplicatively decomposed into two parts:

$$\mathbf{F} = \mathbf{F}_e \mathbf{F}_p, \tag{2.1}$$

where $\mathbf{F}_e$ and $\mathbf{F}_p$ denote the elastic and plastic components, respectively. The evolution of the plastic part of the deformation gradient is governed by the equations:

$$\dot{\mathbf{F}}_p = \hat{\mathbf{L}}_p \mathbf{F}_p, \tag{2.2}$$

where the dot over the quantity denotes its material time derivative.

When it comes to twinning, a mechanism akin to slip takes place (see Fig. 2.3). However, in this scenario, only a segment of a matrix grain experiences shearing along the designated twin plane and in the specified twin direction, resulting in a particular amount of shear referred to as γ^{TW}, which is dependent on lattice geometry. Consequently, a twinned sub-grain is created. In contrast to the slip mechanism, twinning operates unidirectionally, as outlined by Fischer et al. (2003). This phenomenon is attributed to the lattice geometry, which demands significantly more energy to displace an atom in the reverse direction. With a specified lattice orientation relative to the matrix grain, the twinned volume fraction exhibits a distinct orientation, determined by the following relation:

$$\begin{aligned} \mathbf{a}_0^{\mathrm{TW}} &= \mathbf{R}^{\mathrm{TW}} \mathbf{a}_0^{\mathrm{M}}, \\ \mathbf{R}^{\mathrm{TW}} &= 2\mathbf{n}_0^{\mathrm{TW}} \otimes \mathbf{n}_0^{\mathrm{TW}} - \mathbf{I}, \end{aligned} \tag{2.3}$$

here, $\mathbf{a}_0^{\mathrm{TW}}$ represents the crystallographic direction in the twinned portion of the grain, while $\mathbf{a}_0^{\mathrm{M}}$ denotes the crystallographic direction within the matrix grain defined in the initial configuration. Additionally, $\mathbf{n}_0^{\mathrm{TW}}$ signifies the unit vector perpendicular to the twinned plane in the initial configuration. The conventional approach, as employed by Chin et al.

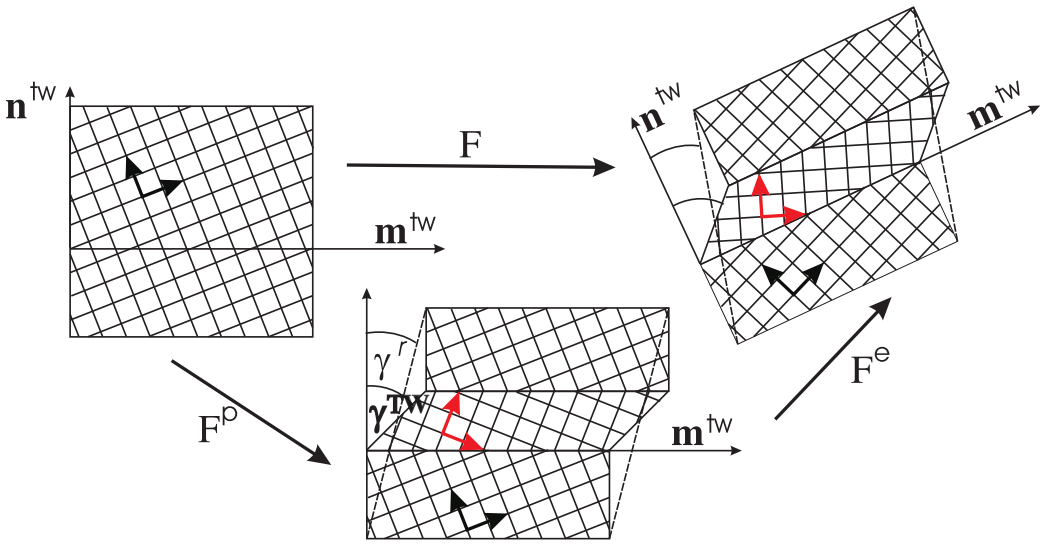

FIGURE 2.3 Single crystal deformation by twinning (Kowalczyk-Gajewska, 2011).

(1969); Kalidindi (1998); Staroselsky and Anand (1998), incorporates twinning into the crystal plasticity model. Twinning is regarded as a form of unidirectional slip mechanism. The rate of pseudo slip $\dot{\gamma}^l_{(t)}$ is correlated with the rate of volume fraction $\dot{f}^l$ of the twinned portion generated by the twin system l, according to the formula:

$$\dot{\gamma}^l_{(t)} = \gamma^{\mathrm{TW}} \dot{f}^l, \tag{2.4}$$

where γ^{TW} is the characteristic twin shear which depends on the geometry of the crystal. The plastic part of the velocity gradient $\hat{\mathbf{L}}_p$ is described as follows:

$$\hat{\mathbf{L}}_p = \sum_{k=1}^{2M} \dot{\gamma}^k_{(s)} \mathbf{m}^k_0 \otimes \mathbf{n}^k_0 + \sum_{l=1}^{N} \dot{\gamma}^l_{(t)} \mathbf{m}^l_0 \otimes \mathbf{n}^l_0 = \sum_{r=1}^{2M+N} \dot{\gamma}^r \mathbf{m}^r_0 \otimes \mathbf{n}^r_0, \tag{2.5}$$

where $\mathbf{m}^r_0$ and $\mathbf{n}^r_0$ denote, respectively, the slip direction and slip plane normal defined in the initial configuration. To unify the description of slip and twinning in the above formula the slip in the $\mathbf{m}_0$ direction is distinguished from the slip in $-\mathbf{m}_0$ direction, and $\dot{\gamma}^r$ denotes the rate of shear in the r-th deformation mode. M denotes the number of slip systems and N the number of twinning systems respectively; so $M, N = 12$ for FCC and $M = 12, N = 6$ for HCP crystals (see Tabs. 2.2 and 2.3). The total volume fraction of twins generated within the matrix grain across all twin systems must not exceed unity, i.e.,

$$f^{\mathrm{TW}} = \sum_{l=1}^{N} f^l = \frac{1}{\gamma^{\mathrm{TW}}} \sum_{l=1}^{N} \gamma^l_{(t)} \leq 1. \tag{2.6}$$

2.4.2 Twin reorientation scheme

One challenge associated with modeling twinning in the context of texture evolution is addressing the emergence of new orientations related to twinning. Several researchers have tackled the modeling of the emergence of new twin-related orientations. The first to address this was Van Houtte (1978), who introduced a probabilistic twin reorientation condition. This condition is based on determining whether the maximum increment in the volume fraction of twins accumulated across all potential twin systems in the given strain increment exceeds a certain threshold value. Staroselsky and Anand (1998) modified the Van-Houtte method by incorporating the maximum of the total volume fractions of twins accumulated over the entire deformation process up to the current time step. It is crucial to emphasize that each grain possesses a distinct orientation, either corresponding to the matrix orientation or to the twin-related orientation. This distinction helps to mitigate the ambiguity associated with the increase in the number of orientations.

Another two approaches to address twin-related orientations were introduced by Tomé et al. (1991). The first strategy, termed Predominant Twin Reorientation (PTR) scheme, substitutes the probabilistic reorientation condition with a deterministic one. In this scheme, the threshold value in the reorientation condition will depend on the total volume fraction of twins accumulated throughout the deformation process in the entire polycrystalline element. The second approach, referred to as the Volume Fraction Transfer scheme, maintains a fixed set of orientations throughout the deformation process, allowing the associated volume fractions to evolve. It is important to highlight that both of these schemes require an analysis of the entire polycrystalline aggregate to determine reorientation, making them impractical for implementation in a finite element (FE) model of a polycrystal. All the models, including their details and limitations, were thoroughly discussed in Kowalczyk-Gajewska (2013). In the present formulation, the probabilistic twin volume consistent (PTVC) reorientation scheme developed by Kowalczyk-Gajewska (2010, 2011, 2013) is utilized to address lattice reorientation resulting from twinning. It ensures the consistency between the twin volume fraction and the proportion of reoriented domains within the sample. When the reorientation criterion is met, a crystal lattice is reoriented to the twin-related orientation. It is important to note that only the information available at the specific point (in FEM calculations precisely at Gauss point) is required to validate this reorientation criterion. The condition is as follows:

$$\text{if} \quad \Delta f^{\mathrm{TW}} > \xi \quad \text{or} \quad f^{\mathrm{TW}} > f^{crit} \quad \rightarrow \quad \mathbf{a}^{new} = \mathbf{R}^{\mathrm{TW}} \mathbf{a}^{old} \quad \text{and} \quad \tau_0^{c,twinned} = \mu \tau_0^c,$$

where Δf^{TW} is increment of twin volume for a given time step, ξ is a number randomly

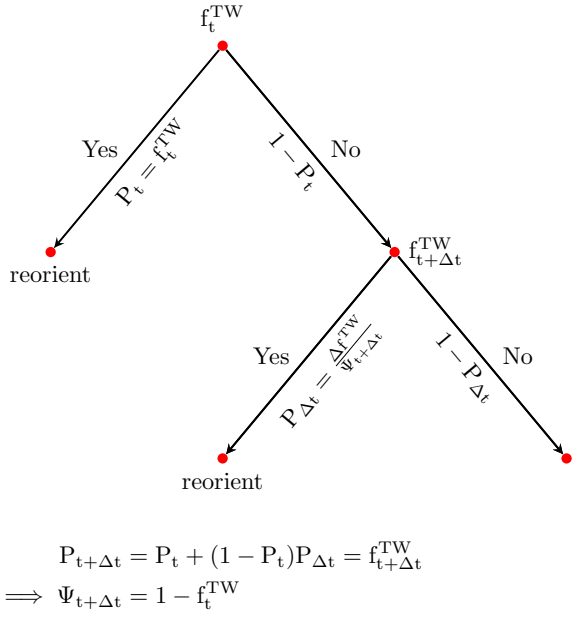

FIGURE 2.4 Schematic representation of Probabilistic Twin Volume Consistent (PTVC) reorientation scheme and the way of finding the current size of $\Psi_{t+\Delta t}$. $\mathrm{P_t}$ and $\mathrm{P_{t+\Delta t}}$ denote probability of reorientation up to time t and $\mathrm{t} + \Delta\mathrm{t}$ respectively, while $\mathrm{P_{\Delta t}}$ probability of reorientation at the time step $\Delta\mathrm{t}$.

generated from the set $(0, \Psi_{t+\Delta t})$, while f^{crit} is a value of twin volume fraction for which the reorientation is always performed. $\mathbf{R}^{\mathrm{TW}}$ is the rotation tensor as shown in the Eq. (2.3). In rotation tensor $\mathbf{R}^{\mathrm{TW}}$, $\mathbf{n}_0^{\mathrm{TW}}$ represents the unit normal to the twin plane of the twin system l, where $\gamma_{(t)}^{l} = \gamma^{\mathrm{TW}} f^{l}$ is maximized among twin systems at the current time step. The current size of the set $\Psi_{\mathrm{t+\Delta t}}$ changes along the deformation process to ensure consistency. It is important to highlight that this condition is inherently probabilistic, so the formation of twin matrix laminate or distinct twin lamellae is not typically observed in the calculations. The intricate details of this scheme are elucidated in Fig. 2.4.

2.4.3 Rate-dependent constitutive law

The rate of shearing on a given slip or twinning system r is calculated using the visco-plastic power law (Hutchinson, 1976; Asaro and Needleman, 1985):

$$\dot{\gamma}^r = \dot{\gamma}_0 \left(\frac{\tau^r}{\tau_{cr}^r} \right)^n , \tag{2.7}$$

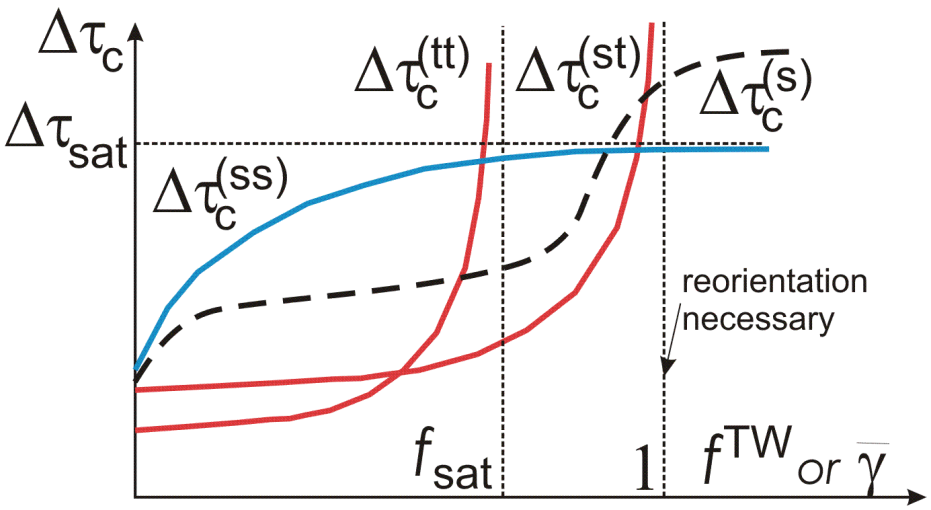

FIGURE 2.5 Illustrative depiction of the evolution of critical shear stress τ_{cr} resulting from slip activity and twin activity.

where $\dot{\gamma}_0$ is the reference shear rate, n is a rate-sensitivity parameter. As $n \to \infty$ the model approaches the rate insensitive limit. In the rate-insensitive limit, the power law Eq. (2.7) with a high value of n is frequently regarded as a viscoplastic regularization of rate-independent plasticity.

The resolved shear stress (RSS) is the projection of the Mandel stress tensor $\mathbf{M}_e$ on the direction $\mathbf{m}_0^r$ and plane of slip $\mathbf{n}_0^r$:

$$\tau^r = < \mathbf{m}_0^r \cdot \mathbf{M}_e \cdot \mathbf{n}_0^r > \geq 0, \quad \mathbf{M}_e = \mathbf{F}_e^T \mathbf{S} \mathbf{F}_p^T = \mathbf{F}_e^T \boldsymbol{\tau} \mathbf{F}_e^{-T}, \tag{2.8}$$

where $< \cdot > \equiv \frac{1}{2}((\cdot) + |\cdot|)$, $\mathbf{S}$ is the first Piola-Kirchhoff stress and $\boldsymbol{\tau}$ is the Kirchhoff stress. The Mandel stress tensor is obtained using a hyper-elastic law:

$$\mathbf{M}_e = 2\mathbf{C}_e \frac{\partial \Psi}{\partial \mathbf{C}_e}, \tag{2.9}$$

where $\mathbf{C}_e = \mathbf{F}_e^T \mathbf{F}_e$ is the right elastic Cauchy-Green tensor and

$$\Psi = \frac{1}{2} \mathbf{E}_e \cdot \mathbb{L}^e \cdot \mathbf{E}_e \tag{2.10}$$

is the Kirchhoff-type function of free energy density per unit volume in the reference configuration, $\mathbb{L}^e$ is the anisotropic stiffness tensor of single crystal and $\mathbf{E}_e = \frac{1}{2}(\mathbf{C}_e - \mathbf{I})$ is the elastic Lagrangian strain tensor.

2.4.4 Hardening laws

In the following subsection, the evolution of the critical resolved shear stress (CRSS) τ_{cr}^{r}, which is influenced by the interaction of different slip and twin systems is presented (Kowalczyk-Gajewska, 2010, 2011; Frydrych et al., 2020). The development of the hardening laws was based on experimental observations. The consequence of impeding the movement of dislocations due to other dislocations, particles of foreign phases, and grain boundaries results is the strengthening of the material. However, at a certain point, the density of dislocations in the material saturates, halting further strengthening. Various mechanisms were outlined in the literature where twinning also contributes to the strengthening of the material (Salem et al., 2006; Sahoo et al., 2019). Hardening is a crucial phenomenon in plastic deformation processes. Therefore, modeling the hardening phenomenon accurately is essential for predicting material behavior and for designing metal forming processes effectively.

In the context of crystal plasticity, the proposed hardening law is as follows:

$$\dot{\tau}_{cr}^{r} = \dot{\tau}_{cr}^{r+M} = H_{(ss)}^{r} \sum_{q=1}^{M} h_{rq}^{(ss)} \dot{\bar{\gamma}}^{q} + H_{(st)}^{r} \sum_{q=2M+1}^{2M+N} h_{rq}^{(st)} \dot{\gamma}^{q} \,, \text{where } r \leq M \tag{2.11}$$

$$\dot{\tau}_{cr}^{r} = H_{(ts)}^{r} \sum_{q=1}^{M} h_{rq}^{(ts)} \dot{\bar{\gamma}}^{q} + H_{(tt)}^{r} \sum_{q=2M+1}^{2M+N} h_{rq}^{(tt)} \dot{\gamma}^{q} \,, \text{where } r > 2M \tag{2.12}$$

and $\dot{\bar{\gamma}}^{q} = \dot{\gamma}^{q} + \dot{\gamma}^{q+M}$. Eq. (2.11) represents the increase of CRSS of slip systems due to slip and twinning activity whereas the increase of CRSS of twin systems due to slip and twin systems is given by Eq. (2.12). The latent hardening on a given system α due to activity on system β is described using the submatrices. These matrices have the following form (Asaro and Needleman, 1985):

$$h_{rq}^{(\alpha\beta)} = q^{(\alpha\beta)} + (1 - q^{(\alpha\beta)}) |\mathbf{n}_0^r \cdot \mathbf{n}_0^q| \,, \tag{2.13}$$

where $q^{(\alpha\beta)}$ are the corresponding latent hardening ratios and the term $|\mathbf{n}_0^r \cdot \mathbf{n}_0^q|$ is responsible for considering the influence of coplanarity of systems. The functions $H_{(\alpha\beta)}^{r}$ depict the hardening of the r-th slip system or the r-th twin system resulting from the activity of other slip or twin systems. These hardening laws are assumed based on experimental observations as follows. To describe the hardening of the r-th slip system or r-th twin system resulting from the activity of slip systems, the Voce-type law with saturation, in the form utilized by Kalidindi et al. (1992) to which a separate linear term is added, is

employed.

$$H^r_{(\alpha s)} = h_0^{\alpha s}\left(1 - \frac{\tau^r_{cr}}{\tau^r_{sat}}\right)^{\beta} + h_1^{\alpha s}. \tag{2.14}$$

The depicted law is illustrated schematically in Fig. 2.5. From the figure, it is evident that initially there is a rapid increase in critical stress, indicating strengthening due to the increase of dislocation densities within the material. As strain increases, the rate of strengthening diminishes owing to dynamic recovery, resulting in a reduction in dislocation density. Thus, the model accommodates both athermal statistical storage of moving dislocations and dynamic recovery. As the CRSS value approaches τ_{sat}, stress growth nearly halts and the critical shear stress grows linearly with the modulus $h_1^{\alpha s}$, representing the attainment of equilibrium between dislocation density increase from slips and dynamic recovery. The parameters $\tau^r_{sat}, h_0^{\alpha s}$, $h_1^{\alpha s}$, and β are material constants. When β equals to 1 and $h_1 = 0$, the exponential Voce hardening function is obtained. In the present work, for FCC crystals without twinning, the evolution of the critical value of the resolved shear stress adheres to the exponential Voce law. This law is employed in the material model, and the results will be detailed in the subsequent chapter. The equation representing this law is as follows:

$$H^{(r)}_{ss}(\Gamma) = \frac{\mathrm{d}\tau^{\mathrm{r}}_{\mathrm{cr}}(\Gamma)}{\mathrm{d}\Gamma},\ \tau^r_{cr}(\Gamma) = \tau^r_0 + (\tau^r_{sat} + h_1^{ss}\Gamma)\left(1 - \exp\left(-\Gamma\frac{h_0^{ss}}{\tau^r_{sat}}\right)\right), \tag{2.15}$$

$$\Gamma = \int \dot{\Gamma}\mathrm{d}t,\ \ \dot{\Gamma} = \sum_r |\dot{\gamma}^r|. \tag{2.16}$$

The parameters $\tau^r_{sat}, h_0^{ss}, h_1^{ss}$ are hardening parameters. Similarly, in the current study of HCP materials with twinning, a similar form of hardening law is employed:

$$H^r_{(\alpha s)} = h_1^{\alpha s} + h_0^{\alpha s}\exp\left(\frac{-h_0^{\alpha s}}{\tau^r_{sat}}\Gamma^s\right), \tag{2.17}$$

$$\Gamma^s = \int \dot{\Gamma}\mathrm{d}t,\ \ \dot{\Gamma} = \sum_{r=1}^{2M} |\dot{\gamma}^r|. \tag{2.18}$$

The values of hardening parameters will be outlined in the subsequent chapters. For describing the hardening of the r-th slip or r-th twin system as a result of twinning activity, the following law is assumed based on the concept of Karaman et al. (2000):

$$H^r_{(\alpha t)} = \frac{h_0^{\alpha t} f_{sat}^{\alpha t}}{(f_{sat}^{\alpha t} - f^{\mathrm{TW}})^2}. \tag{2.19}$$

In this model, the hardening effect of twins is considered through a term proportional to $\frac{1}{f_{sat}^{\alpha t} - f^{\mathrm{TW}}}$, where f^{TW} represents the current volume fraction of twins. Consequently, the

CRSS undergoes variation with an increase in the twin volume fraction (f^{TW}). However, by adjusting $f_{sat}^{\alpha t}$ to be less than 1 instead of 1, the saturation of the volume fraction of twins occurs below unity (refer to Fig. 2.5). Unlike the proposals of Karaman et al. (2000), explicit length-scale parameters are not included in this model. Thus, material parameters like $h_0^{\alpha t}$ and initial values of τ_{cr}^{r} may rely on the grain size, for instance, following the Hall-Petch relation.

The subsequent step is to decide whether slip and secondary twinning could occur in the grains reoriented by twinning and assessing the level of slip and twin resistances following the reorientation. Thus, in the event that the reorientation condition is true for a given point, and the crystal lattice at this point has been reoriented owing to twinning, the newly formed crystal is assumed to be described by the same material model with different material parameters. It accounts for the fact that the mechanical characteristics of twins differ from those of the parent grain mainly due to conversion of glissile dislocations into the sessile ones due to the twinning shear transformation of the lattice (Basinski's-type hardening Basinski et al. (1997); Sahoo et al. (2019)). Experimental results on low stacking fault energy (SFE) material (Asgari et al., 1997) indicate that twinning and slip within twinned regions are more difficult than in untwinned regions. Slip within twinned regions may be largely limited to planes that are co-planar with the matrix-twin border. Thus the increased resistance observed in twinned material can be also attributed to the Hall-Petch type effects stemming from the directional reduction of the mean free path (MFP) within twin lamellae (Mahajan and Chin, 1973). Based on these observations in the present calculations we assumed that the twinning is no more possible in reoriented parts, while the initial critical shear stress τ_0 for slip and the hardening parameters: h_0^{ss}, h_1^{ss} and τ_{sat}^{ss} are modified.

CHAPTER 3

FE implementation and boundary conditions

In this chapter, the aspects of finite element implementation of crystal plasticity model, construction of the unit cell models, and boundary conditions applied in the performed numerical analyses are presented and discussed. Throughout the study, both 2D plane strain and 3D unit cell models featuring cylindrical and spherical voids are considered to investigate the effects of crystal orientation, and loading conditions on void growth and deformation heterogeneity in porous single crystals and polycrystals. Additionally, the unit cell calculations are used to calibrate the yield surfaces proposed for both FCC and HCP single crystals in the Chapters 4 and 5. Fully displacement-controlled or mixed boundary conditions are utilized.

3.1 FE implementation

The standard procedures developed for the FE implementation of finite strain elasto-plasticity in the fully Lagrangian displacement-based setting are followed (Simo and Hughes, 1998). In particular, incremental constitutive equations have been obtained by applying the implicit backward-Euler time integration scheme and the relation (Eq. (2.2)) is integrated using the exponential map,

$$\mathbf{F}_p(t+\Delta t) = \exp(\Delta t \hat{\mathbf{L}}_p)\mathbf{F}_p(t). \tag{3.1}$$

The implementation has been performed using AceGen code generator (Korelc, 2002). It combines the symbolic algebra capabilities of Wolfram Mathematica with automatic differentiation and advanced techniques of expression optimization. The package enables straightforward derivation of an algorithmic consistent tangent that leads to a quadratic

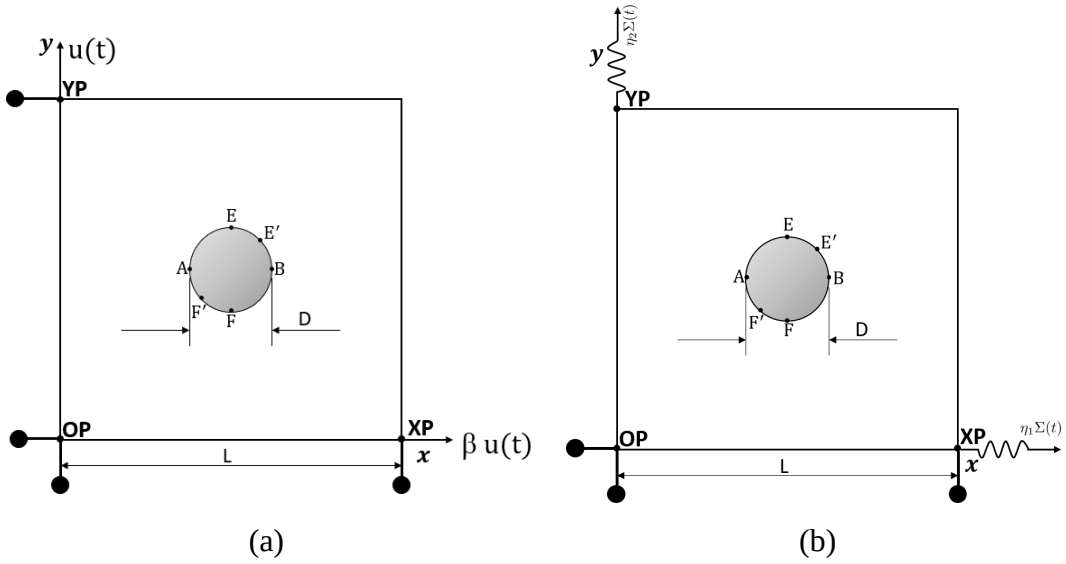

FIGURE 3.1 Schematic representation of the 2D unit cell with two types of boundary conditions:(a) displacement controlled, (b) stress controlled. In the figure D/L= 0.2 which is corresponding to 0.0314 void volume fraction.

convergence rate. Computations were performed using the AceFEM package. In the calculations, 4-noded linear quadrilateral elements with 4 integration points (i.e., "Q1" element topology as per AceGen convention, "CPE4R" as per ABAQUS convention) are used for the 2D plane strain unit cell. For the 3D unit cell with a spherical void, both 8-noded linear and 20-noded hexahedral elements with 2*2*2 integration points are employed (i.e., "H1" for the 8-noded hexahedral element and "H2S" for the 20-noded hexahedral element as per AceGen convention, "C3D8","C3D20R" respectively as per ABAQUS convention). The H2S element with reduced integration (2*2*2) is used for some of the computations to determine yield points for calibrating the proposed yield surface for porous single crystals as discussed in Chapter 8. Additionally, the F-bar method (de Souza Neto et al., 1996) is applied to 2D plane strain with "Q1" and 3D unit cell with "H1" elements in order to have a robust implementation, enabling the enforcement of nearly incompressible material behavior in the geometrically non-linear regime.

The three-dimensional nature of the crystal plasticity model, specifically the geometry of slip systems, is fully considered for the 2D plane strain problem. At each Gauss point the material displacement gradient $\mathbf{H} = \mathbf{F} - \mathbf{I}$ is assumed for which components $H_{i3} = H_{3i} = 0$ $(i = 1, 2, 3)$ and '3' denotes the direction perpendicular to the plane.

In micromechanics, the concept of a unit cell serves as a crucial bridge between the microstructure of a material and its macroscopic properties, enabling efficient analysis and prediction of material behavior. The unit cell is defined as the smallest representative

volume element (RVE) of a heterogeneous material that captures its essential microstructural features, allowing the determination of the effective properties of the material. It is a simplified model that incorporates key components of the microstructure of the material-such as the matrix, inclusions, voids, and interfaces arranged in a way that represents the overall composition and structure.

In the present study, a unit cell with a void, representing the microstructure of a porous crystal, is used to perform finite element (FE) computations. These computations aim to predict the evolution of porosity and the mechanisms leading to ductile failure. For such unit cell, the connection between macroscopic stress and strain measures (for example deformation gradient ($\overline{\mathbf{F}}$) and first Piola-Kirchhoff stress ($\overline{\mathbf{S}}$)) and respective local fields within the unit cell are given by so called averaging relations (Nemat-Nasser (1999)), specified in the reference configuration:

$$\begin{aligned} \overline{\mathbf{F}}(t) &= \frac{1}{V}\int_V \mathbf{F}(\mathbf{X},t)dV, \\ \overline{\mathbf{S}}(t) &= \frac{1}{V}\int_V \mathbf{S}(\mathbf{X},t)dV. \end{aligned} \tag{3.2}$$

3.2 Unit cell model and boundary conditions

3.2.1 2D & 3D cell model

A 2D plane strain unit cell with one cylindrical void is employed for analyzing the cylindrical void growth in Chapter 4. Cartesian coordinate system ($x-y$) is used and the origin of the coordinate frame is placed at the node OP, see Fig. 3.1. The following notation is used interchangeably for $x-1, y-2, z-3$ and vice versa in both 2D and 3D model. The initial diameter of the void is D and the square plate has a side length of L. The ratio of D/L is used to define the void volume fraction: $f = \pi/4(D/L)^2$. Nodes OP, XP, and YP are used to prescribe the periodic boundary conditions. In this study, two types of boundary conditions are considered for FCC crystals, namely stress-controlled and displacement controlled, as depicted in Fig. 3.1, while for the HCP 2D plane strain model, only stress-controlled boundary conditions are utilized.

As depicted in Fig. 3.2, a 3D cubic unit cell with a spherical void is employed, utilizing the Cartesian coordinate system (x-y-z), with the origin of the coordinate frame located at node **OP**. The initial diameter of the void is represented by D, while the side length of the cube is denoted as L. The void volume fraction is defined by the ratio D/L. Nodes OP, XP, YP, and ZP are utilized to impose periodic boundary conditions and to apply different

stress ratios. The present investigation utilizes a 3D unit cell methodology to determine the yield points, which will subsequently be used to calibrate the proposed yield surface for both FCC and HCP crystals with spherical voids in Chapter 8. Additionally, this unit cell is employed to investigate the mechanics of porous evolution, the effect of crystal orientation, and the activity of different slip and twin systems in HCP crystals with a spherical void in Chapter 5.

3.2.2 Periodic boundary conditions for both 2D and 3D unit cells

During deformation, rather than confining the sides of the unit cell to remain planar, which can over-constrain the model and lead to the development of high stresses for some orientations, periodic boundary conditions are applied. Accordingly, the displacement of corresponding nodes on opposite sides of the unit cell in each direction is connected by periodic boundary conditions, given by:

$$\mathbf{u_2} - \mathbf{u_1} = \overline{\mathbf{H}}(\mathbf{X_2} - \mathbf{X_1}), \tag{3.3}$$

where $\overline{\mathbf{H}}$ is the overall (averaged) material displacement gradient tensor of the unit cell and its relation with macroscopic deformation gradient is $\overline{\mathbf{H}} = \overline{\mathbf{F}} - \mathbf{I}$, $\mathbf{u_1}, \mathbf{u_2}$ represent the displacement of corresponding nodes on opposite sides and $\mathbf{X_1}, \mathbf{X_2}$ represent the corresponding nodal position vectors at the reference configuration.

Following Koplik and Needleman (1988) studies for phenomenological plasticity, several studies were carried out by Han et al. (2013); Srivastava and Needleman (2013, 2015) on unit cells with single crystal containing voids imposed with constant stress triaxiality ratio (ratio of the mean stress to the von Mises stress) boundary conditions. On the other hand, strain-controlled boundary conditions were considered by Schacht et al. (2003); Potirniche et al. (2006). In the subsequent chapters, both kinds of boundary conditions are employed in order to compare and quantify the influence of strain and stress ratios on the void growth and coalescence under overall loading. The way in which they are imposed is described in the next subsections.

3.2.3 Imposing stress controlled boundary conditions

In the present study, various constant macroscopic stress triaxiality (T) values are imposed to investigate the mechanics of void evolution. Triaxiality is defined as the ratio of hydrostatic stress Σ_m to the equivalent stress Σ_{eq} of the macroscopic Cauchy stress $\mathbf{\Sigma}$. This is achieved using a special spring element method based on the work of Ling et al.

(2016). The same methodology is applicable to 2D plane strain cells as well, but here the general case of the 3D framework is presented.

The macroscopic Cauchy stress tensor is defined in terms of stress ratios (η_1, η_2) as follows, with z considered as the primary loading direction.

$$[\Sigma_{ij}] = \begin{bmatrix} \Sigma_{11} & 0 & 0 \\ 0 & \Sigma_{22} & 0 \\ 0 & 0 & \Sigma_{33} \end{bmatrix} = \Sigma_{33}(t) \begin{bmatrix} \eta_1 & 0 & 0 \\ 0 & \eta_2 & 0 \\ 0 & 0 & 1 \end{bmatrix} \rightarrow \mathbf{\Sigma} = \Sigma_{33}(t)\mathbf{N}, \tag{3.4}$$

such that the triaxiality and Lode parameter in terms of η_1, η_2 are as follows:

$$\mathrm{T} = \frac{\Sigma_m}{\Sigma_{eq}} = \frac{1+\eta_1+\eta_2}{3\sqrt{1-\eta_1-\eta_2-\eta_1\eta_2+\eta_1^2+\eta_2^2}} \text{ and } \mathrm{L} = \frac{2\eta_2-\eta_1-1}{1-\eta_1}, \tag{3.5}$$

where the stress state is taken to be such that $\Sigma_{33} \geq \Sigma_{22} \geq \Sigma_{11} \Leftrightarrow \eta_1 \leq \eta_2 \leq 1$. It is important to note that if the main direction of loading changes to the x or y direction, the equations will change accordingly. Similarly, for the calculation of the Lode parameter, the principal stress components are ordered accordingly. For the axisymmetric loading case, $\eta_1 = \eta_2 = \eta$, the Lode value is -1, and the triaxiality is:

$$\mathrm{T} = \frac{1+2\eta}{3(1-\eta)}. \tag{3.6}$$

In order to impose constant $\mathbf{N}$ direction in Eq. (3.4) along the deformations process, a special spring element aligned with the main loading direction (i.e., the z direction) is considered. It has only one degree of freedom ($\tilde{\mathrm{F}}_{33}$) at the far end of the spring, which is used to impose displacement. The near end of the spring has nine degrees of freedom and is connected to the unit cell in such a way that these components correspond to the nine components of the macroscopic deformation gradient of the unit cell (i.e., $\bar{\mathrm{F}}_{ij}$, where $i, j = 1, 2, 3$). Therefore, this element functions as a spring in the primary loading direction in the following manner:

$$\tilde{\mathrm{S}}_{33} = K(\tilde{\mathrm{F}}_{33} - \overline{\mathrm{F}}_{33}), \tag{3.7}$$

where K is the element stiffness and $\tilde{\mathrm{S}}_{33}$ is the component of the first Piola-Kirchhoff stress tensor in the spring loading direction. The corresponding macroscopic first Piola-Kirchhoff stress tensor of the unit cell can be written as:

$$\overline{\mathbf{S}} = \bar{J}\mathbf{\Sigma}\overline{\mathbf{F}}^{-T} = \bar{J}\Sigma_{33}(t)\mathbf{N}\overline{\mathbf{F}}^{-T} = \Sigma_{33}(t)\hat{\mathbf{M}}(\overline{\mathrm{F}}_{ij}, \eta_1, \eta_2), \tag{3.8}$$

where $\hat{\mathbf{M}} = \bar{J}\mathbf{N}\overline{\mathbf{F}}^{-\mathrm{T}}$. Due to the connection between the unit cell and the spring element at the near end, by using $\tilde{\mathrm{S}}_{33} = \overline{\mathrm{S}}_{33} = \Sigma_{33}(t)\hat{\mathrm{M}}_{33}$ and the Eq. (3.7), $\Sigma_{33}(t)$ can be written as:

$$\Sigma_{33}(t) = \frac{K(\tilde{\mathrm{F}}_{33} - \overline{\mathrm{F}}_{33})}{\hat{\mathrm{M}}_{33}}. \tag{3.9}$$

Consequently, the macroscopic first Piola-Kirchhoff stress is applied to the unit cell via the spring element to maintain constant stress triaxiality as defined in Eq. (3.5).

In the subsequent chapter, the implementation of spring elements for the HCP unit cell under uniaxial loading will be slightly modified. Here, the crystal orientation is kept fixed while the stress direction is varied to impose the uniaxial loading. The uniaxial loading state can be written in the following form:

$$\boldsymbol{\Sigma} = \Sigma(t)\mathbf{n} \otimes \mathbf{n}, \tag{3.10}$$

where $\Sigma(t)$ is the magnitude of stress (which can be found from the solution of global problem by energy minimization), $\mathbf{n}$ is the direction of loading, represented using the angles u and v as follows: $[\cos(u)\sin(v), \sin(u)\sin(v), \cos(v)]$. Thus, the components of overall stress tensor $\boldsymbol{\Sigma}$ under uniaxial loading can be written as follows:

$$[\Sigma_{ij}] = \Sigma(t)\begin{bmatrix} \eta_1(u,v) & \eta_4(u,v) & \eta_5(u,v) \\ & \eta_2(u,v) & \eta_6(u,v) \\ \text{sym.} & & \eta_3(u,v) \end{bmatrix}. \tag{3.11}$$

Similar to Eq. (3.9), $\Sigma(t)$ can be determined using the following equation:

$$\Sigma(t) = \frac{K(\tilde{\mathrm{F}}_{33} - \mathbf{n}\cdot\overline{\mathbf{F}}\cdot\mathbf{n})}{\mathbf{n}\cdot\hat{\mathbf{M}}\cdot\mathbf{n}}, \tag{3.12}$$

where $\mathbf{n}\cdot\overline{\mathbf{F}}\cdot\mathbf{n}$ and $\mathbf{n}\cdot\hat{\mathbf{M}}\cdot\mathbf{n}$ are the components of $\overline{\mathbf{F}}, \hat{\mathbf{M}}$ in the uniaxial loading direction.

3.2.4 In-plane displacement controlled boundary conditions for 2D plane strain unit cell

For the displacement controlled boundary conditions, a displacement biaxiality factor β is set, which is defined as the ratio of the displacement in the x direction to the displacement in the y direction, namely $\beta = u_x(\mathrm{XP})/\mathrm{u_y}(\mathrm{YP}) = \mathrm{const}$. Therefore, the following displacement boundary conditions along with the periodic boundary conditions

Eq. (3.3), are imposed at the reference configuration as shown in Fig. 3.1b:

- at node OP, $u_x = u_y = 0$,
- at node XP, $u_x = \beta u(t), u_y = 0$,
- at node YP, $u_x = 0, u_y = u(t)$,

which result in the following components of the displacement gradient $\overline{\mathbf{H}}$ in Eq. (3.3):

$$[\overline{\mathrm{H}}_{kl}] = \frac{u(t)}{L} \begin{bmatrix} \beta & 0 & 0 \\ 0 & 1 & 0 \\ 0 & 0 & 0 \end{bmatrix}.$$

Note that all components of $\overline{\mathbf{H}}$ are known for this loading scenario. For the uniaxial tension/compression case in the y-direction of the sample, the following displacement boundary conditions are imposed:

- at node OP, $u_x = u_y = 0$
- at node XP, $u_y = 0$
- at node YP, $u_y = u(t)$,

which result in the following components of the displacement gradient $\overline{\mathbf{H}}$ in Eq. (3.3):

$$[\overline{\mathrm{H}}_{kl}] = \frac{u(t)}{L} \begin{bmatrix} \star & \star & 0 \\ 0 & 1 & 0 \\ 0 & 0 & 0 \end{bmatrix}, \tag{3.13}$$

where by $\star$ we denoted unknown components of $\overline{\mathbf{H}}$. By energy minimization, this leads to the averaged Cauchy stress for which $\Sigma_{xy} = \Sigma_{xx} = 0$, so the stress biaxiality factor $\eta = \Sigma_{xx}/\Sigma_{yy} = 0$. Note that this case is not equivalent to the 3D uniaxial tension case since, in general all Σ_{kz}, $k = x, y, z$ are not necessarily zero for anisotropic material under plane strain conditions.

3.2.5 In-plane stress controlled boundary conditions for 2D plane strain unit cell

For controlling the in-plane stress biaxiality factor η, the formulation based on the proposal by Ling et al. (2016), as discussed in the Subsection 3.2.3 is employed. A

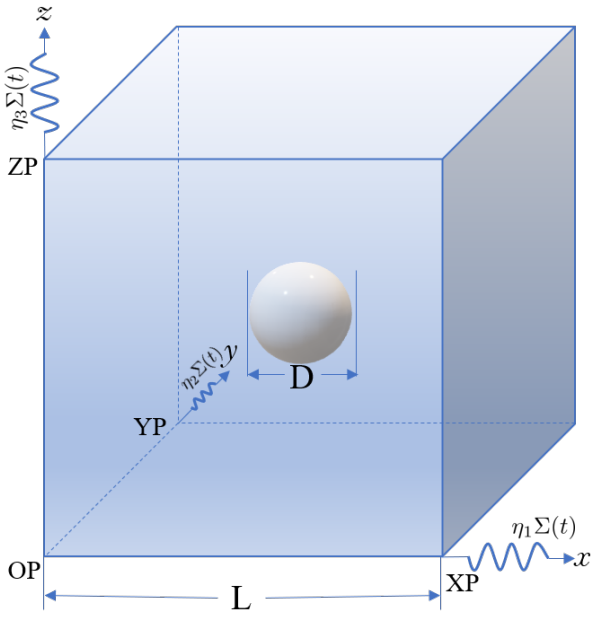

FIGURE 3.2 Schematic representation of the 3D porous unit cell with geometric parameters and imposed stress controlled boundary conditions.

special spring element oriented in the direction of principal loading is employed to regulate displacement at the nodes XP and YP in order to maintain the constant stress ratio. Node OP is fixed and the displacement of node XP in the y direction is disabled to remove rigid motion as shown in the Fig. 3.1a. In-plane stress biaxiality η, which is defined as the ratio of the Cauchy's stress normal components along x direction to y direction, namely $\eta = \Sigma_{xx}/\Sigma_{yy} = \text{const}$ is kept constant to study the void growth. Application of the element results in the averaged Cauchy stress for the unit cell of the form:

$$[\Sigma_{kl}] = \Sigma_{yy}(t) \begin{bmatrix} \eta & 0 & \star \\ & 1 & \star \\ \text{sym.} & & \star \end{bmatrix}, \tag{3.14}$$

where by $\star$ we denote unknown components of $\boldsymbol{\Sigma}$. Note that $\Sigma_{yy}(t)$ is also unknown, while via the spring element, displacement $u_y(\text{YP})$ is imposed.

3.2.6 Stress controlled boundary conditions for 3D unit cell

As discussed in Subsection 3.2.3, maintaining constant triaxiality is achieved using a spring element. In the current study focusing on calibrating the yield surface for FCC

crystals, the x direction serves as the primary loading direction. To ensure constant stress triaxiality, a specialized spring element oriented in the direction of principal loading is utilized, controlling displacements at nodes XP, YP, and ZP as shown in Fig. 3.2. Node OP is fixed, and displacements of node XP in the y and z directions are restricted, along with the z-direction displacement at node YP, to eliminate rigid rotation of the unit cell. Stress ratios η_2 and η_3 are kept constant to enforce constant triaxiality, and these values are adjusted to calibrate the yield surface of the single crystal. The imposition of these boundary conditions leads to the following representation of the overall Cauchy stress tensor and the macroscopic deformation gradient:

$$[\Sigma_{kl}] = \Sigma_{xx}(t) \begin{bmatrix} 1 & 0 & 0 \\ & \eta_2 & 0 \\ \text{sym.} & & \eta_3 \end{bmatrix}, [\bar{H}_{kl}] = \frac{u_x(t)}{L} \begin{bmatrix} 1 & \star & \star \\ 0 & \star & \star \\ 0 & 0 & \star \end{bmatrix}. \tag{3.15}$$

The unknown components of $\mathbf{H}$ are denoted by $\star$. It should be noted that $\Sigma_{xx}(t)$ (refer Eq. (3.9)) is also unknown, while the displacement $u_x(t)$ is imposed via the spring element. Similarly, in the unit cell calculations for the calibration of the yield surface for an HCP single crystal, the z direction is taken as the primary loading direction. Node OP is fixed, and the displacement along the x and y directions for node ZP and along the x direction for node YP is constrained to remove rigid rotation, resulting in the following representation of the overall Cauchy stress tensor and the macroscopic deformation gradient.

$$[\Sigma_{kl}] = \Sigma_{zz}(t) \begin{bmatrix} \eta_1 & 0 & 0 \\ & \eta_2 & 0 \\ \text{sym.} & & 1 \end{bmatrix}, [\bar{H}_{kl}] = \frac{u_z(t)}{L} \begin{bmatrix} \star & 0 & 0 \\ \star & \star & 0 \\ \star & \star & 1 \end{bmatrix}, \tag{3.16}$$

where $\Sigma_{zz}(t)$ (refer Eq. (3.9)) is unknown and the displacement component $u_z(t)$ is imposed via the spring element.

Regarding the HCP crystal with a spherical void under uniaxial tension, the crystal orientation is fixed with the x-axis parallel to the $[10\bar{1}0]$ direction and the z-axis parallel to the c-axis, i.e., $[0001]$. The loading direction is varied in this configuration. The current study examines five uniaxial loading scenarios in the YZ plane, which result in Eq. (3.11) taking the following form:

$$\mathbf{\Sigma} = \Sigma(t)\mathbf{n} \otimes \mathbf{n} \rightarrow [\Sigma_{kl}] = \Sigma(t) \begin{bmatrix} 0 & 0 & 0 \\ & \eta_2(v) & \eta_6(v) \\ \text{sym.} & & \eta_3(v) \end{bmatrix}, \tag{3.17}$$

where $\mathbf{n}$ is the direction of loading and it is has following components in sample frame [0, $\cos[v]$, $\sin[v]$]. The angle v will be varied from 0° to 90° in the YZ plane. 0° corresponds to prismatic loading, while 90° corresponds to c-axis loading. $\Sigma_{zz}(t)$ is unknown and can be found from the Eq. (3.12). Similar to previous cases, node OP is fixed. In these analyses to remove rigid rotation, additional constraint equations is solved which ensure that the macroscopic deformation gradient $\overline{\mathbf{F}}$ is symmetric.

3.3 Finite element geometry and mesh

Two commercial software packages are utilized in this study. The 2D plane strain and 3D unit cell model geometry and mesh are generated using the commercial CAE software ABAQUS (version 6.13), as shown in Figs. 3.3 and 3.4. The mesh data is then imported into the symbolic and algebraic system Wolfram Mathematica, as specified in Section 3.1, for finite element calculations and post-processing using the AceFEM package.

For the 2D plane strain model, the ratio of the void diameter to the side length in the XY plane is set as $D/L = 0.2$, resulting in an initial void volume fraction of $f = 0.0314$. A 2D mesh consisting of 1168 elements of type CPE4R ("Q1" element topology as per AceGen convention) is employed. Similarly, for the study of void evolution in the HCP unit cell under uniaxial tension, the ratio of the void diameter to the side length in the XY plane is taken as $D/L = 0.2673$, leading to an initial void volume fraction of $f = 1\%$. A 3D mesh comprising 6128 elements of type C3D8R ("H1" element topology as per AceGen convention) is employed. For the calibration of the yield surface using unit cell calculations for both FCC and HCP crystals, a similar mesh with 6128 elements of type C3D8R (both "H1" and "H2S" element topologies as per AceGen convention) is used. The applied mesh density was established based on the mesh convergence tests. They were carried out on a number of unit cells with different mesh sizes. Convergence was evaluated by determining the evolution of the relative void volume fraction with the overall effective strain.

Results of numerical analyses are presented/discussed mainly in terms of the macroscopic stress-strain curves, evolution of the relative void volume fraction, averaged accumulated slip and twin and the averaged current relative activity of slip systems. Those quantities are established as described below. Similarly to other studies (see e.g. (Ling et al., 2016)), the overall Cauchy stress $\boldsymbol{\Sigma} = \frac{1}{\bar{J}}\overline{\mathbf{S}}\ \overline{\mathbf{F}}^{\mathrm{T}}$ ($\bar{J} = \det\overline{\mathbf{F}}$) is calculated based on the volume averaged first Piola-Kirchhoff stress $\overline{\mathbf{S}}$ (Eq. (3.2)) which for zero stress in the void is reduced to:

$$\overline{\mathbf{S}} = \frac{1}{V}\int_V \mathbf{S}(\mathbf{X})dV = \frac{1-f}{V_m}\int_V \mathbf{S}(\mathbf{X})dV_m\,, \tag{3.18}$$

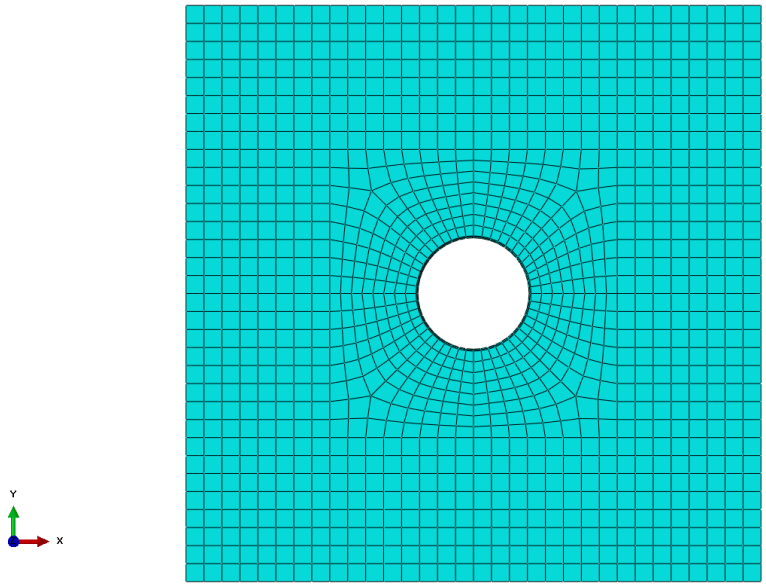

FIGURE 3.3 Finite element mesh of 2D plane strain unit cell.

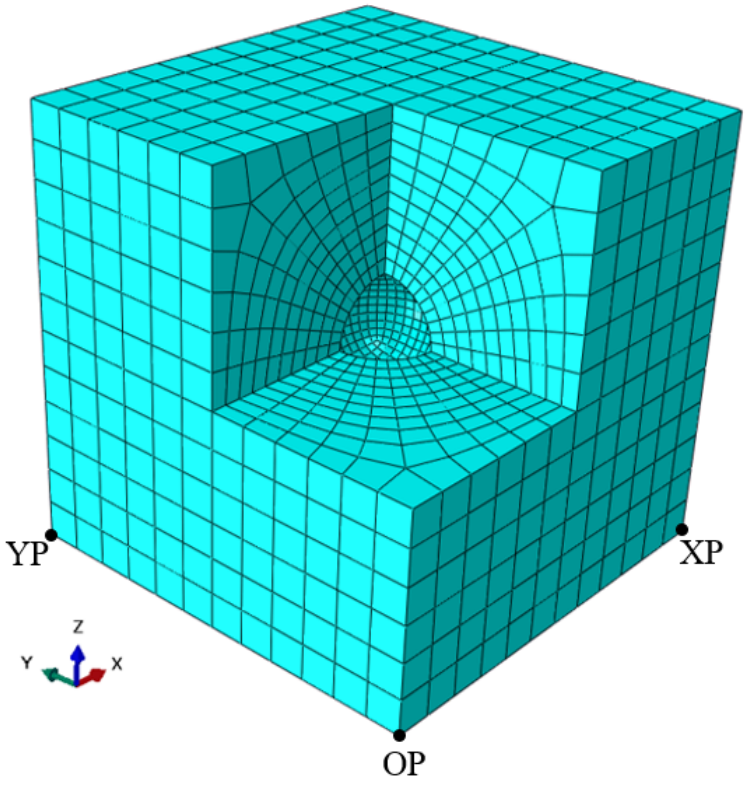

FIGURE 3.4 Finite element discretization of 3D unit cell with spherical void used for yield surface calibration and study the mechanics of porous evolution in HCP single crystals.

where V_m is the bulk crystal volume and the integration is performed numerically in the reference configuration. For 3D unit cell, unknown components of the overall deformation gradient $\bar{\mathbf{F}} = \mathbf{I} + \bar{\mathbf{H}}$ are calculated based on the relation (Eq. (3.3)) using the current displacement vectors at nodes XP, YP and ZP and the initial lengths L_x, L_y, L_z of unit cell edges along x, y, z direction, namely

$$\begin{aligned}
\bar{F}_{11} &= 1 + \frac{u_x(\mathrm{XP})}{L_x}, & \bar{F}_{12} &= \frac{u_x(\mathrm{YP})}{L_y}, & \bar{F}_{13} &= \frac{u_x(\mathrm{ZP})}{L_z}, \\
\bar{F}_{21} &= \frac{u_y(\mathrm{XP})}{L_x}, & \bar{F}_{22} &= 1 + \frac{u_y(\mathrm{YP})}{L_y}, & \bar{F}_{23} &= \frac{u_y(\mathrm{ZP})}{L_z}, \\
\bar{F}_{31} &= \frac{u_z(\mathrm{XP})}{L_x}, & \bar{F}_{32} &= \frac{u_z(\mathrm{YP})}{L_y}, & \bar{F}_{33} &= 1 + \frac{u_z(\mathrm{ZP})}{L_z}.
\end{aligned} \tag{3.19}$$

Similarly, for the 2D plane strain case, the unknown components of the deformation gradient are calculated as follows.

$$\begin{aligned}
\bar{F}_{11} &= 1 + \frac{u_x(\mathrm{XP})}{L_x}, & \bar{F}_{12} &= \frac{u_x(\mathrm{YP})}{L_y}, \\
\bar{F}_{21} &= \frac{u_y(\mathrm{XP})}{L_x}, & \bar{F}_{22} &= 1 + \frac{u_y(\mathrm{YP})}{L_y}.
\end{aligned} \tag{3.20}$$

The current normalized void volume fraction is defined as the ratio of the current void volume fraction (f) to the initial void volume fraction (f_0). f is calculated as follows:

$$f = \frac{v_{cell}(t) - v_m(t)}{v_{cell}(t)}, \tag{3.21}$$

where $v_{cell}(t)$ and $v_m(t)$ denote current cell and matrix volume respectively, which are :

$$v_{cell}(t) = \det \overline{\mathbf{F}} V_0,$$

and

$$v_m(t) = \int_{V_m} \det \mathbf{F}(\mathbf{x}, t) dV_m = \sum_g \det \mathbf{F}(\mathbf{X}_g, t) w_g,$$

where $\mathbf{X}_g$ and w_g are the position and the weight of the Gauss point g respectively . The volume averaged accumulated slip and twin volume fraction are defined as:

$$\bar{\Gamma} = \sum_i \frac{\Gamma_i V_i}{V_{sample}}, \quad \bar{f}^{\mathrm{TW}} = \sum_i \frac{f_i^{\mathrm{TW}} V_i}{V_{sample}}, \tag{3.22}$$

where summing is applied over all Gauss points in the sample volume over which the

averaging is performed. Here V_i denotes the volume represented by i^{th} Gauss point. Γ_i is the accumulated slip and f_i^{TW} the twin volume fraction at that Gauss point (if reorientation was performed at the given Gauss point the twin volume fraction for this point equals one). The volume averaged relative activity $\bar{\xi}$ of a slip or twin system (α) is defined as:

$$\bar{\xi} = \frac{\sum_{\mathrm{i}} \Delta\gamma_{\mathrm{i}}^{\alpha} \mathrm{V_i}}{\sum_{\mathrm{j}} \Delta\Gamma_{\mathrm{j}} \mathrm{V_j}}, \tag{3.23}$$

where summing is applied over all Gauss points in the volume over which the averaging is performed. Eq. (3.23) quantifies the activity of the particular mechanism compared to the others over a given time step. Here V_l denotes the volume represented by l^{th} Gauss point. $\Delta\gamma_l^{\alpha}$ is the increment in plastic strain on the α^{th} system and $\Delta\Gamma_l = \sum_{\alpha=1}^{2M+N} \Delta\gamma_l^{\alpha}$ is the incremental cumulative plastic strain on all N deformation (slip + twin) systems at that Gauss point.

CHAPTER 4

Cylindrical void growth vs grain fragmentation in FCC single crystals

In this chapter, the CPFEM detailed in Chapter 2, Section 2.4 is employed to investigate the interaction between cylindrical void growth or collapse and grain refinement in face-centered cubic (FCC) single crystals deforming by slip only. A 2D plane strain model, as shown in Fig. 3.1, with a single void, is utilized. The impacts of crystallographic orientation and various boundary conditions on void growth or coalescence, as well as grain refinement due to heterogeneous lattice rotation, in a 2D plane strain unit cell, are examined. First, in-plane uniaxial compression and tension, simulated using the displacement-controlled scenario (Eq. (3.13)), are performed to demonstrate the void-induced heterogeneous slip activity, which subsequently leads to spatial variation in lattice rotation. This example also explores the effect of loading direction with respect to crystal axes and loading 'sign' (tension vs. compression). Moreover, the analysis preliminary verifies the model predictions with available experimental findings provided in (Gan et al., 2006). Next, various in-plane biaxial processes are examined to understand the impact of plastic anisotropy on void growth in an FCC single crystal. The results and discussion presented in this chapter have already been published in the paper Virupakshi and Kowalczyk-Gajewska (2023).

4.1 Material parameters, crystal orientations and loading cases considered

The parameters of the hardening model, elastic constants of the material, and the value of n used are shown in the Tab. 4.1. The latent hardening parameter on both coplanar and non-coplanar systems is the same, but in general, it could have been taken as different. Plastic deformation in FCC crystals occurs along the $\{111\}\langle 110\rangle$ family of slip systems.

TABLE 4.1 Elastic constants (C_{11}, C_{12}, C_{44}) (Potirniche et al., 2006), initial critical resolved shear stress (τ_0), and hardening model parameters ($\tau_{sat}, h_0, h_1, q, q_0$), exponent in the power law (n) and reference shear rate (v_0).

C_{11} GPa	C_{12} GPa	C_{44} GPa	τ_0 GPa	τ_{sat} GPa	h_0 GPa	h_1 GPa	q	q_0	n	$\dot{\gamma}_0$
150	75	37.5	0.02	0.097	0.18	0.0×10^{-3}	1.4	1.4	20	0.001

TABLE 4.2 Crystal orientations considered with respective global coordinate axes.

Crystal Orientation	Lateral direction (x)	Primary loading direction (y)	Lateral direction (z)
Orientation O	$[\bar{1}10]$	[001]	[110]
Orientation A	[111]	$[\bar{2}11]$	$[0\bar{1}1]$
Orientation B	[100]	[010]	[001]
Orientation C	[110]	$[\bar{1}10]$	[001]

Thus, in the computations 12 possibly active slip systems are considered (see Tab. 2.2).

Four initial orientations of the crystalline lattice relative to the sample axes are considered to study the impact of plastic anisotropy on evolution of porosity, as summarized in Tab. 4.2. Various types of boundary conditions have already been explained in Chapter 3, and those conditions are applied here (refer to Subsections 3.2.2, 3.2.4 and 3.2.5).

Throughout the discussion, the displacement-controlled boundary condition will be referred to as the β loading case (refer Subsection 3.2.4), and the stress-controlled boundary condition will be referred to as the η loading case (refer Subsection 3.2.5). In the current study, seven loading scenarios with β equal to -0.5, 0, and 1 as well as η equal to -0.5, 0, 0.8, and 1 are analyzed. The scenario $\eta = 0.8$ is selected due to its approximate equivalence to the $\beta = 0$ case. Note that the state of in-plane uni-axial tension or compression is represented by η = 0.

4.2 Microstructure evolution and void growth in in-plane uniaxial tension and compression

Gan et al. (2006) examined in-plane uniaxial compression of a single crystal along the [001] direction with a cylindrical void axis along the [110] (orientation O in Tab. 4.2). As discussed in detail by Gan et al. (2006), by applying the anisotropic rigid-plastic slip line theory, this configuration ensures a plane strain condition in the [001] - $[\bar{1}10]$ crystal

TABLE 4.3 Set of active slip systems for the specified in-plane uniaxial loading of Orientation O (no void) according to the rigid-plastic crystal plasticity model. $\pm\gamma$ denotes the magnitude of the slip on the specified system and its sign at the same level of the true strain in the given loading direction.

Loading	Slip system			
	$(1\bar{1}1)[10\bar{1}]$	$(1\bar{1}1)[011]$	$(\bar{1}11)[101]$	$(\bar{1}11)[01\bar{1}]$
Tension [001]	$-\gamma$	γ	γ	$-\gamma$
Compression [001]	γ	$-\gamma$	$-\gamma$	γ
Tension $[\bar{1}10]$	γ	$-\gamma$	$-\gamma$	γ
Compression $[\bar{1}10]$	$-\gamma$	γ	γ	$-\gamma$

plane under the action of the compressive or tensile loading with three effective in-plane slip systems. For the pristine crystal they are results of equal activity of four systems (see Tab. 4.3), which act in opposite directions (i.e. $\mathbf{m}$ and $-\mathbf{m}$) for tensile and compressive loading in the plane. It could be also verified that when the direction of loading is changed to [001], under a plane strain condition, the same set of slip systems will be active, again in the opposite sense. Thus, as far as plastic deformation by dislocation motion is considered, in-plane compression (cor. tension) in [001] is equivalent to in-plane tension (cor. compression) in $[\bar{1}10]$.

For the sample with a cylindrical void, under the same loading conditions, the formation of regions of unequal slip activity of potentially active systems around the void is observed, which leads to the lattice rotation heterogeneity and crystal fragmentation into subgrains. These theoretical predictions were verified by Gan et al. (2006) experimentally, for the [001] compression case, by EBSD measurements. Note that for the crystal without the void, no lattice rotation is predicted by the model, and slip activity is homogeneous, so the grain is not fragmented.

The purpose of the study is to investigate the differences between void evolution and grain fragmentation using four loading scenarios, namely tension/compression in the $[\bar{1}10]$ and [001] directions, even though the same active slip systems are expected for all cases in a pristine rigid-plastic crystal (as indicated in Tab. 4.3). It is obvious that the overall stress biaxiality factor η is equal to 0 in each case.

First, we have used this example to verify the predictive capabilities of the present numerical model. As shown in Gan et al. (2006) and confirmed in our study, one of three effective in-plane slip systems dominates in three different angular slip sectors which are centered at the middle of the void, as marked by dashed lines in Fig. 4.1b. This results in different lattice rotations in respective domains. In Fig. 4.1b, we present misorientation

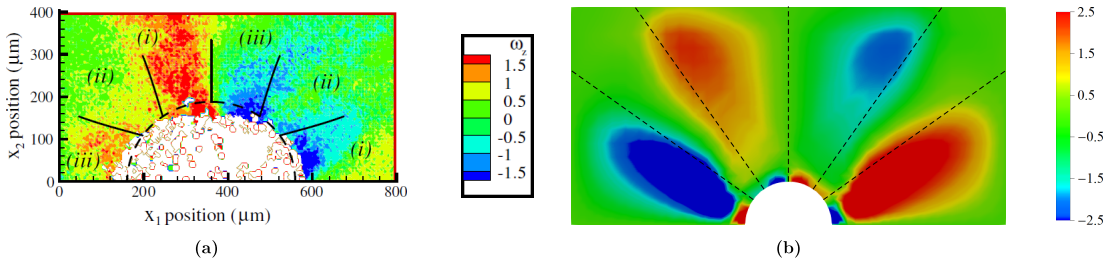

FIGURE 4.1 a) In-plane lattice rotation angle obtained using EBSD measurement (reprinted from (Gan et al., 2006) with permission from Elsevier) and b) misorientation angle map plotted found by the CPFEM method for a 5% compression strain. The dashed line represents the slip sectors at an angle of 35.3°, 54.7°, and 90° respectively.

angle distribution[1] for the compression strain of 5%. Qualitatively similar subdivision is seen in experimental data quoted in Fig. 4.1 after Gan et al. (2006). There are some differences concerning the direction of rotation in the lateral domains, however, a full quantitative comparison is not possible due to the lack of the detailed experiment geometry and boundary condition data in (Gan et al., 2006).

Next, the same sample configuration is used to explore the effect of loading direction and its sign (i.e. in plane tension vs. compression) on the void evolution and grain refinement. To this end, four loading cases enlisted in Tab. 4.3 are studied numerically. In Fig. 4.2a, we compare the overall in-plane mean stress variation vs. magnitude of the true strain in the loading direction. It is seen that initially, the response in terms of the magnitude of the in-plane mean stress ($\sigma_{\text{mean}} = 1/2(\Sigma_{xx} + \Sigma_{yy})$) is the same for all cases and does not show visible tension-compression asymmetry. However, as the deformation proceeds, the difference starts to increase due to differences in the lattice rotation and void evolution. In each case, the stress level is smaller for the porous crystal than for the pristine one. The evolution of the normalized void volume fraction (f/f_0) is presented in Fig. 4.2b. It is observed that, as expected, the void volume fraction increases for tension and decreases for compression, however, there are important differences between the two loading directions. While for tension in [001] void grows monotonically, for tension in $[\bar{1}10]$ after initial increase void volume stabilizes at some, relatively small, constant value ($f/f_0 \sim 1.13$), at least for the demonstrated strain regime[2]. On the other hand, for compression in $[\bar{1}10]$ void volume decreases monotonically and void starts to close

[1] See definition (4.1), which is in the present case equipped with the sign to indicate the in-plane rotation direction. Sign $+$ denotes clockwise and $-$ anticlockwise rotation of [001] axis

[2] It has been verified that for both these loading cases, the void volume starts to increase with accelerating rate and softening is observed for in-plane mean stress at larger strain, which events eventually lead to void coalescence, see Fig. 4.5.

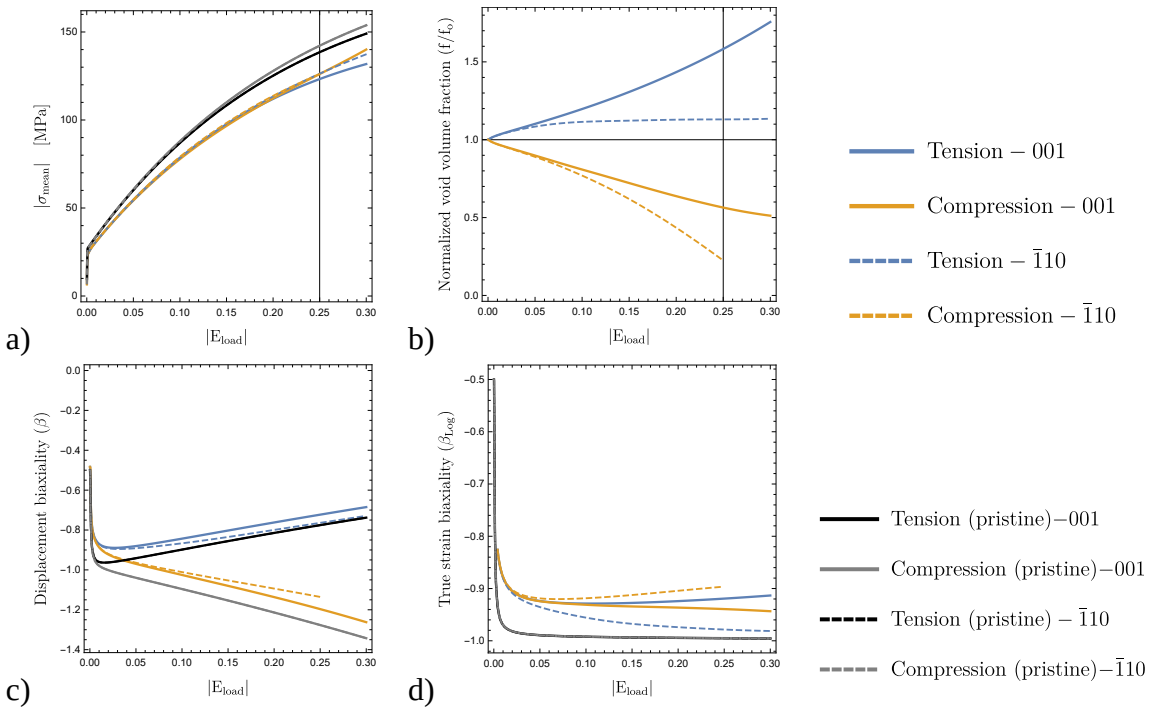

FIGURE 4.2 Comparison of a) absolute value of in-plane mean stress (σ_{mean})b) normalized void volume fraction c) displacement biaxiality factor (β), d) true strain biaxiality factor ($\beta_{\log}$) for four loading cases between pristine and voided single crystal. Evolution of quantities is presented as a function of the absolute value of $E_{\text{load}} = \ln(1 + u/L)$, where u is the displacement in the loading direction.

at a relatively small true strain level (~ 0.25)[3], and for compression in [001] after initial important decrease the void collapse is postponed to higher strain values. It should be stressed that the overall stress triaxiality value, calculated accounting for the 3D character of the stress field (note that Σ_{zz} is not zero for all analyzed cases), is approximately equal to 0.5 for both tension loadings and -0.5 for compression. Only small variations in the Lode parameter calculated for the overall stress are detected for four loading cases (its value is around 0.32-0.33). Displacement biaxiality ratio β, calculated here as the inverse ratio of in-plane displacements in loading direction with respect to the lateral one, is seen in Fig. 4.2c, while the in-plane true strain biaxiality $\beta_{\log}$, calculated as the corresponding ratio of in-plane components of true strain measure (e.g. for tension/compression in [001] it is $\beta_{\log} = E_{xx}/E_{yy} = \ln(F_{xx})/\ln(F_{yy})$) is shown in Fig. 4.2d. Their variation with strain is compared for all four cases and pristine and voided crystals. As expected, it is observed that for a crystal without a void for all cases the evolution of $\beta_{\log}$ is the same: it starts with

[3]Calculations were stopped at the moment when the void opposite boundaries were first in contact since the material overlapping was not prevented in calculations.

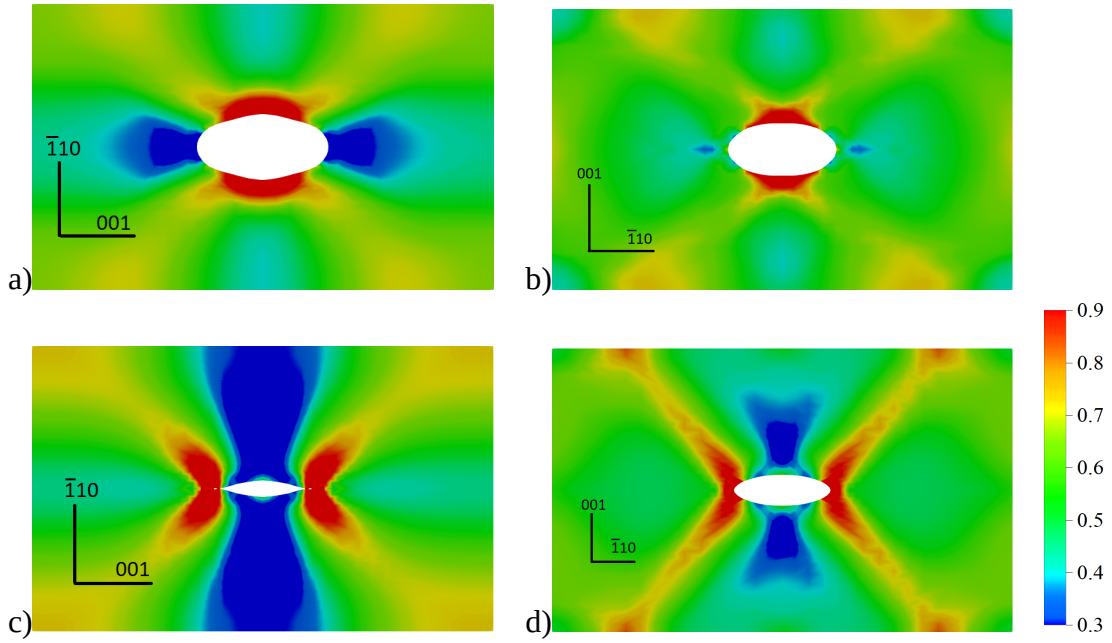

FIGURE 4.3 Space distribution of accumulated shear at true strain $|E_{\text{load}}|$ level 0.25. a) Tension[001] b) Tension [$\bar{1}$10] c) Compression [$\bar{1}$10], d) Compression [001]. Initial orientation of crystallographic directions [001] and [$\bar{1}$10] was marked on the plots.

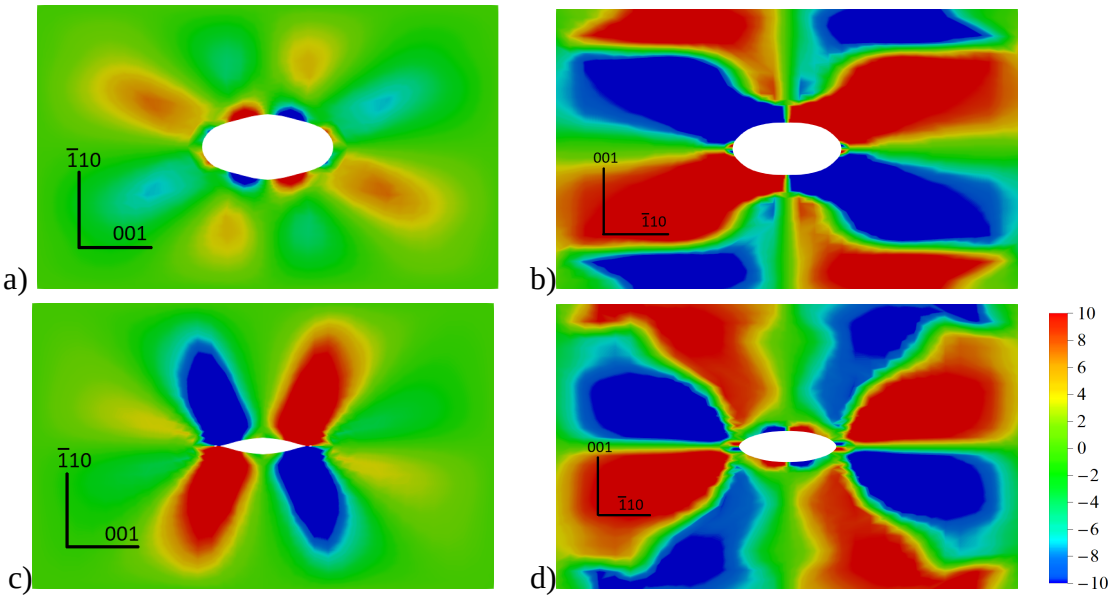

FIGURE 4.4 Local lattice rotation angle at true strain $|E_{load}|$ level of 0.25 in the loading direction. a) Tension [001] b) Tension [$\bar{1}$10] c) Compression [$\bar{1}$10], d) Compression [001]. Initial orientation of crystallographic directions [001] and [$\bar{1}$10] was marked on the plots.

the value of -0.5 in the elastic regime and reaches -1.0 for well-developed plastic flow, which marks incompressible deformation in that regime. On the other hand, for voided

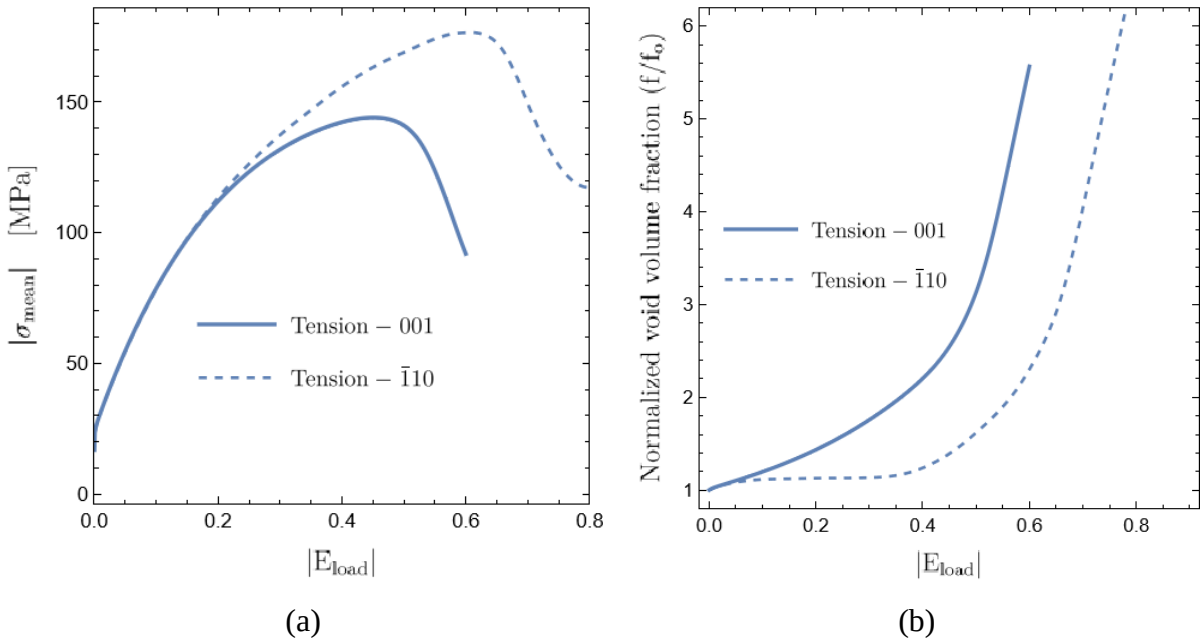

FIGURE 4.5 Uniaxial tension in 001 and $\bar{1}10$ directions under plane strain conditions for the advanced strain: (a) mean in-plane stress evolution (b) normalized void volume fraction.

crystals, the value of -1 is approached only for tension in [$\bar{1}$10], which is related to the stabilization of the void growth. For the remaining processes, the value does not drop below -0.95 indicating the compressibility of voided crystal.

Differences in the void growth or closing for two loading directions concern also the developed void shape as seen in Figs 4.3 and 4.4. While the ellipsoidal shape of the void is observed for tension in [$\bar{1}$10] and compression in [001] (equivalent in terms of slip activity pattern in pristine crystal), the polygonal shapes are the results of compression in [$\bar{1}$10] and tension in [001] directions. Accumulated shear maps also show the failure mode for each case. In compression cases the failure proceeds by accumulated shear localization in two intersecting bands. For tension, although at the initial stage two bands are also visible, the void coalescence takes place, much later for $[\bar{1}10]$ than for $[100]$ case (see footnote 2 and Fig. 4.5).

Fig. 4.4 shows an interesting interplay between the void evolution and the grain fragmentation phenomenon. It is seen that for the two cases for which the void growth/collapse is halted or retarded (tension in [$\bar{1}$10] and compression in [001], respectively) the clear checker-board-type subdivision of initial grain into subgrains, misoriented with respect to each other by the angle as large as $\sim 20^o$ at the true strain level 0.25, is found. On the other hand, for two other processes, the significant lattice rotation is seen only in the domains of intensive strain. These latter results confirm microstructure evolution as an

important effect accompanying the deformation of voided crystalline materials.

The analysis showcased in this section illustrates that both in-plane stress biaxiality and stress triaxiality, as well as displacement or strain biaxiality, alone are inadequate in determining the growth of voids. This is particularly true when anisotropic materials are analyzed. It is important to note that microstructure evolution plays a substantial role in this process. Fragmentation of bulk crystal surrounding the void into subgrains may lead to significant impediment of the void volume changes.

4.3 Void growth and microstructure evolution in in-plane biaxial loading processes

In this subsection, to further explore factors differentiating the void growth and accompanying grain fragmentation in FCC crystals, in-plane biaxial processes are considered, for three orientations A, B, and C defined in Tab. 4.2. Orientations were selected following Potirniche et al. (2006). In order to investigate and differentiate the effect of stress and strain biaxiality seven loading scenarios with β equal to -0.5, 0, and 1 as well as η equal to -0.5, 0, 0.8, and 1 are analyzed. Let us remark that orientation A, contrary to B and C, is non-symmetric with respect to the loading axes, thus shear strain component E_{xy} (cor. shear stress component Σ_{xy}) may be observed for η (cor. β) loading cases even for a pristine crystal sample.

4.3.1 Overall response of voided crystal

Stress biaxiality ratio. The stress biaxiality ratio for seven loading scenarios is shown in Fig. 4.6a. To start with, as it is evident, the stress biaxiality ratio for the η loading case is maintained constant for all crystal orientations during the deformation process, which verifies the validity of the finite element procedure used for imposing a constant stress biaxiality ratio. On the other hand, in general, for displacement controlled processes (with constant β) stress biaxiality ratio η changes during the deformation process. For crystal orientations A and C, under the $\beta = -0.5$ loading case, the stress biaxiality is larger than zero; it initially rises, then progressively drops, and ultimately approaches the uniaxial loading case at the end of loading. Although the biaxiality ratio is marginally more than $\eta = 0$ for orientation B at the end of loading, apparently, it would reach the uniaxial loading state if the deformation would have proceeded. For $\beta = 0$, the magnitude of η steadily rises until it approaches $\eta = 1$ at the end of loading. For this case, on average the value of stress biaxiality for three orientations is close to $\eta = 0.8$ that is why for

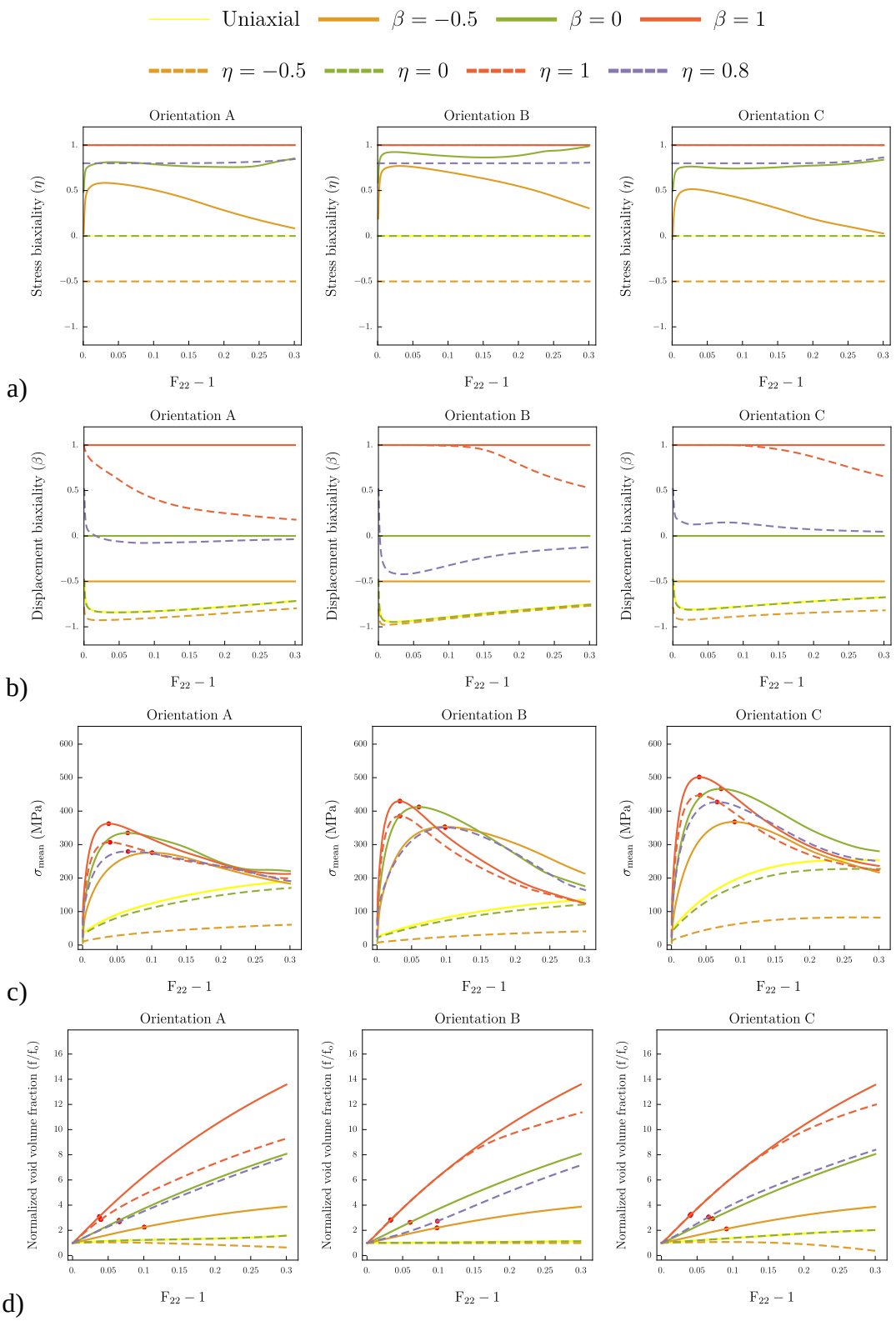

FIGURE 4.6 Variation of a) stress biaxiality ratio, b) displacement biaxiality ratio, c) overall mean stress $(1/2\ (\Sigma_{xx} + \Sigma_{yy}))$ (The peak stress is indicated by •), and d) normalized void volume fraction under various loading cases.

comparison purposes such stress controlled scenario is also selected for analysis. Finally, for the $\beta = 1$ case, the stress biaxiality ratio is kept constant just as it does for the $\eta = 1$ case. Those graphs in conjunction with displacement biaxiality plots in Fig. 4.6b are important for analyzing the growth of the void and the stress response. The softening stress response is evident in Fig. 4.6c when the stress biaxiality ratio increases and void growth is significant, resulting in coalescence.

Additionally, yellow lines are denoted as 'uniaxial' in Fig. 4.6, show the results obtained for the in-plane uniaxial tension process without the employment of a special spring element but using the displacement-controlled conditions with $\mathbf{H}$ described by Eq. (3.13). Calculations are performed for verification purposes and are in good agreement with the predictions obtained with the use of the spring element (marked as $\eta = 0$ in figures).

Displacement biaxiality ratio. The displacement biaxiality under various loading instances is depicted in Fig. 4.6b. Similar to the situation of stress biaxiality, the displacement biaxiality ratio β is kept constant during the β-type process, which verifies the finite element procedure. On the contrary, in general, for stress ratio controlled processes (with constant η), the displacement biaxiality ratio varies in the course of deformation. The displacement biaxiality is kept below -0.5 for $\eta = 0$ (in-plane uniaxial tension) and $\eta = -0.5$ loading cases. For asymmetric orientation A, under the $\eta = 1$ loading scenario, the ratio initially follows the $\beta = 1$ case, but as deformation proceeds the curve steadily falls and approaches the $\beta = 0$ case. For orientations B and C, the ratio remains constant until halfway through the deformation, after which it steadily drops. For $\eta = 0.8$ as expected, the strain biaxiality oscillates around $\beta = 0$, although differently for each of the three orientations. For orientation A it is almost constant and close to zero, for orientation B it is negative, initially being close to -0.5 and increasing towards the uniaxial straining mode, while for orientation C it starts with a positive value and next decreases to zero. These plots are again valuable for studying in conjunction with the contour plots of accumulated shear in Subsection 4.3.2, void evolution (Fig. 4.6d) and stress response (Fig. 4.6c).

Overall mean stress response. Fig. 4.6c illustrates the in-plane overall mean stress response for the various loading scenarios and the given crystallographic orientation. When all loading scenarios are compared, $\beta = 1$ exhibits the stiffest response in the initial deformation phase, whereas $\eta = -0.5$ demonstrates the softest stress response for all crystal orientations. For the $\eta = 0$ loading scenario, the stress response increases monotonically in all orientations. Fig. 4.6a shows that the stress biaxiality ratio is greater than 0 (positive) for β = -0.5, 0 and 1, and η =0.8 and 1 loading cases. As a result,

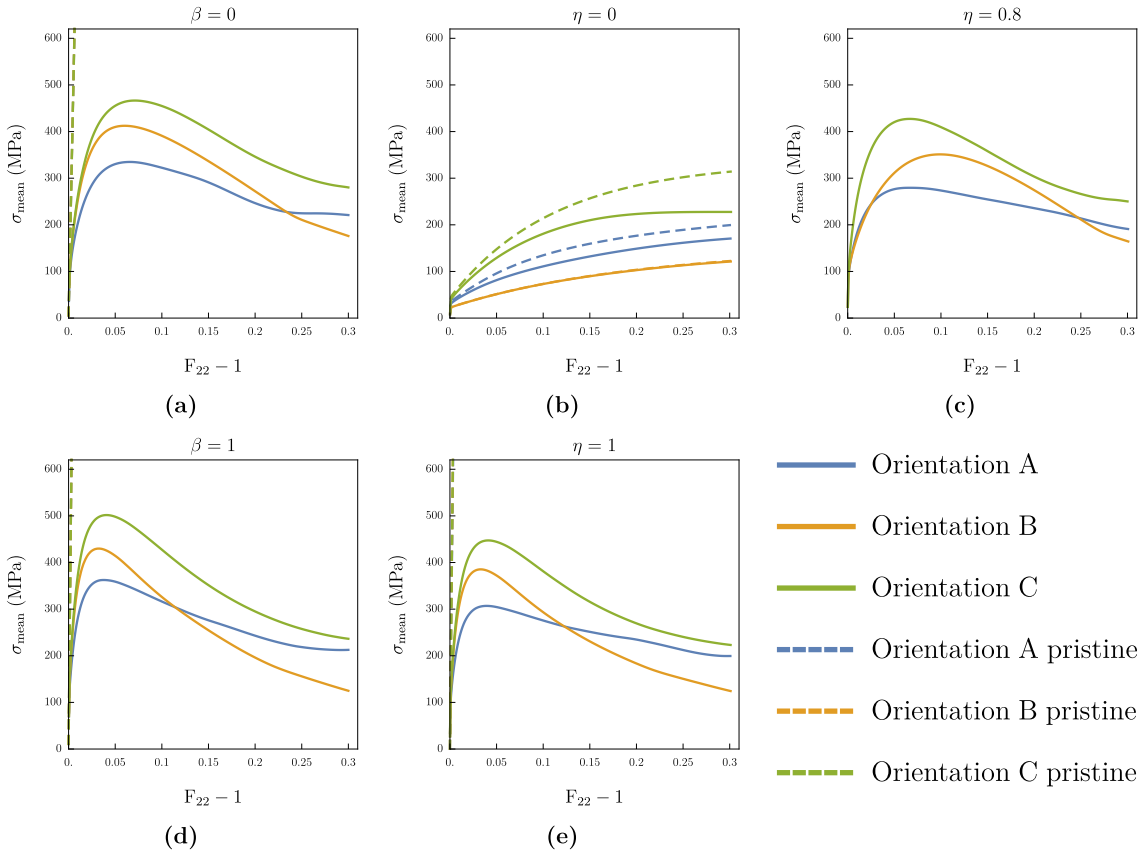

FIGURE 4.7 Overall mean stress response ($\sigma_{\text{mean}} = 1/2\ (\Sigma_{xx} + \Sigma_{yy})$) for different crystal orientations and for the loading case: a) $\beta = 0$, (b) $\eta = 0$, (c) $\eta = 0.8$ (d) $\beta = 1$ (e) $\eta = 1$.

in the initial deformation stage, a stiffer stress response is observed, followed by a softening response due to significant void expansion in the crystal, which cannot be further compensated by an increase of average stress in the bulk crystal. When the magnitude of peak stress for the different orientations is compared, orientation C has the largest peak stress, and orientation A has the lowest peak stress for β =1 loading case. Furthermore, the evolution of the overall mean stress in Fig. 4.6c correlates well with the displacement biaxiality ratio β shown in Fig. 4.6b. In particular, the higher β value the more stiff the initial response is and the sooner (in terms of the value of $F_{22} - 1$) the peak stress is achieved for the given process.

Fig. 4.7 depicts the overall mean stress response in both pristine and porous unit cells for various crystal orientations and the specified loading scenario. Five loading scenarios where β and η are both equal to 0 and 1 are analyzed, together with scenario $\eta = 0.8$ which approximately corresponds to $\beta = 0$ case as discussed before. It is evident that all loading

cases exhibit the anisotropic response. Also, it is apparent that the response of the porous crystal differs substantially from that of the pristine crystal. With the exception of $\eta = 0$ (uniaxial loading condition), the pristine crystal response is almost/nearly elastic. In the case of $\eta = 0$ loading, the pristine crystal displays a stiffer response than the porous crystal for orientations A and C; however, for orientation B, the response is almost the same for both the pristine and porous crystal. The response of orientation C is the stiffest in each of the loading conditions. For loading scenarios, $\beta = 0, 1$, and $\eta = 0.8, 1$, orientation A initially displays the softest response, whereas orientation B exhibits the softest response by the end of the deformation process. When the loading scenarios $\beta = 0$ and $\eta = 0$ are compared, the substantially higher stress biaxiality in the $\beta = 0$ loading case (refer to Fig. 4.6a) causes a more stiff response during an early deformation stage, followed by a softening due to significant void expansion in the crystal. On the contrary, a monotonic stress increase is observed for the $\eta = 0$ loading scenario. Instead, as expected, the stress response for $\beta = 0$ case is close to $\eta = 0.8$ loading conditions. Due to the highest stress biaxiality, a similar response was observed for $\beta = \eta = 1$.

Normalized void volume fraction evolution. Fig. 4.6d compares the evolution of the normalized void volume fraction for various loading conditions and the specified orientation. These evolution plots are in good agreement with displacement biaxiality ratio plots in Fig. 4.6a. For all orientations, the void growth rate increases as the displacement biaxiality ratio increases. The void is collapsing for the $\eta = -0.5$ loading case, and this behavior is the most pronounced in orientation C. Confirmation of the phenomenon can be seen in contour plots of accumulated shear for orientation C which are shown in Fig. 4.15. Under $\eta = 0$ loading case, the void grows very slowly as compared to higher stress biaxiality cases. If the displacement biaxiality ratio is less than -0.5, softening behavior is not observed, since not much void growth is seen. The void growth increases at first with $\beta = -0.5$ but subsequently stabilizes for all orientations. The evolution of the void volume fraction under the β and $\eta = 1$ loading scenarios correlates with the evolution of the displacement biaxiality ratio (Fig 4.6b). The curves of void evolution start to deviate from each other at the same moment when the value of β for $\eta = 1$ case drops below one.

Qualitative differences are observed in the curves shown in Fig. 4.6d for η-cases, which can be explained by the accompanied variation of displacement biaxility ratio. As it is seen, for the high stress biaxiality ratio: $\eta = 1$, initially for all three orientations the displacement biaxiality β is equal to 1, so the cell is under the conditions beneficial for the void expansion. Accordingly, at this stage, the void is growing in all directions (compare Figs. 4.10f, 4.12f, and 4.14f). However, as deformation proceeds *the displacement biaxiality ratio is* ***decreasing towards zero***, which effectively ***slows down*** *the void growth* since its growth

starts to be limited to one direction in the plane. Nevertheless, the void volume fraction is still growing on the cost of bulk crystal, and the achieved values are high. This causes a decrease of the overall in-plane mean stress as an increase of average stress in the bulk crystal is not able to compensate for the void expansion, Fig. 4.6c. On the contrary, for smaller stress biaxiality ratio: $\eta = 0$, the initial displacement biaxiality is negative, so even though the net change of void volume fraction is positive, in this scenario the void diameter is growing only in one direction while decreasing in the perpendicular one (compare Figs. 4.10e, 4.12e, and 4.14e). For this case, as the deformation proceeds *the displacement biaxiality ratio* ***increases towards zero***, which in this case leads to ***accelerated*** *void growth* because the reduction of void size in one of the directions is halted, while it is still growing in another one. For all three orientations for the considered deformation range, the increase in the void volume fraction is not yet sufficient to overcome the overall mean stress increase due to the strain hardening in bulk crystal. However, with increasing deformation one may expect softening which will be accompanied by an accelerated void growth rate. Interestingly, for the $\eta = 0.8$ case the former and latter scenarios of void growth are observed for orientations C and B, respectively (see also Fig. 4.8c). Orientation A exhibits here some limit case with the almost constant rate of void volume fraction.

Fig. 4.8 compares the evolution of the void volume fraction for different crystal orientations and the selected loading conditions. Five loading cases, the same as in mean stress response plots shown in Fig. 4.7 are illustrated. For $\eta = 0$ (in-plane uniaxial loading case), the anisotropic response is observed. Void growth in orientation C is the highest, followed by orientations A and B. But for $\beta = 0$ and 1 loading cases, due to relatively large strain biaxiality, the void growth is significant and the effect of crystal orientation diminishes. It has been verified that the latter observation is true also for other processes in which β value is kept constant. The same observation is reported in (Potirniche et al., 2006) under displacement controlled boundary conditions. The void growth for orientations C and B are nearly identical for $\eta = 1$ loading. However, the void growth rate is slower in asymmetric orientation A than in orientations B and C. For the same η and β values, the void expansion under $\beta = 0$ is substantially faster than the $\eta = 0$ loading situation, since, as already mentioned, this case corresponds approximately to $\eta = 0.8$ case, so a much higher stress biaxiality ratio. Similarity between $\eta = 0.8$ and $\beta = 0$ case is also seen when comparing the contour plots in (b) parts of figures in Subsection 4.3.2 with respective maps in Fig. 4.16.

Unlike in (Prasad et al., 2015) the void coalescence criterion is not formulated in the present study. Nevertheless, in order to closely observe this phenomenon, Fig. 4.9 it is demonstrated how the void size is changing in three different directions: AB, EF,

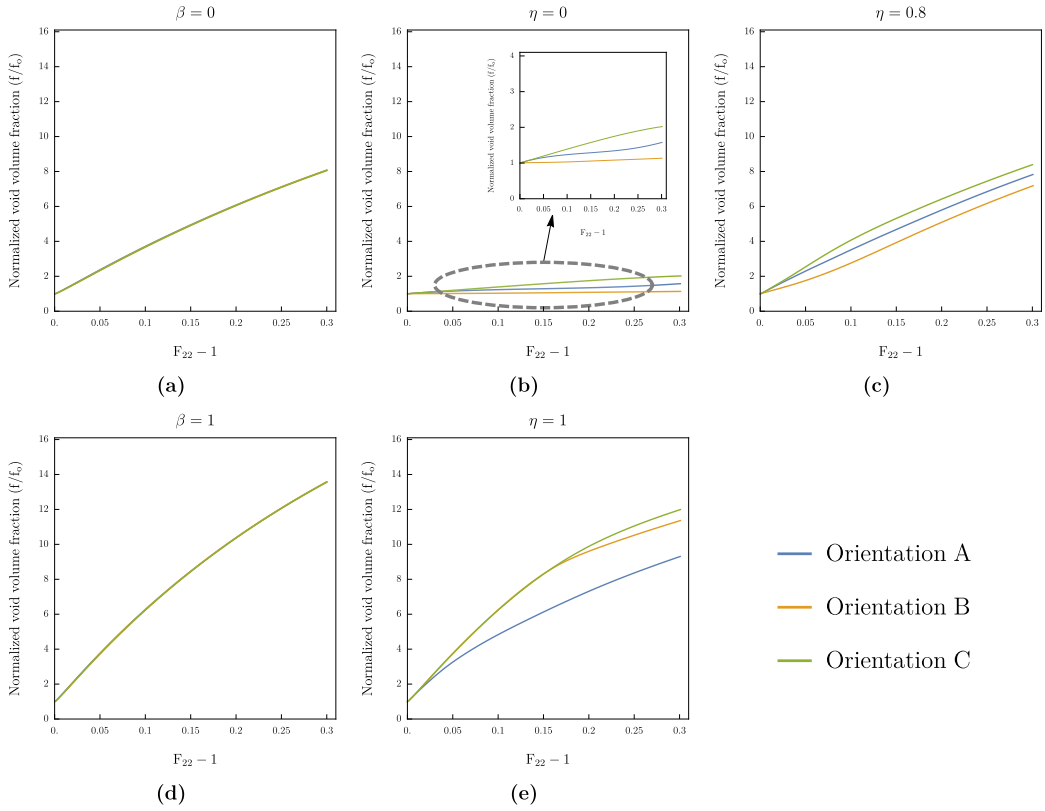

FIGURE 4.8 Normalized void volume fraction evolution for different crystal orientations and for the loading case: (a) $\beta = 0$ (b) $\eta = 0$ (c) $\eta = 0.8$ (d) $\beta = 1$ (e) $\eta = 1$.

E'F' marked in Fig. 3.1 for two selected loading cases: $\beta = 1$ and $\eta = 1$. The figure presents the evolution of the value of $\log(L/|\mathbf{x}_{\text{right}} - \mathbf{x}_{\text{left}}|)$ where $\mathbf{x}_{\text{right}}$ and $\mathbf{x}_{\text{left}}$ denote current locations of nodes at the right and left end of the respective diameter and L is the current cell size in a relevant direction. When this value is tending to zero the coalescence is approached. It is seen that for the case $\beta = 1$ and symmetric orientations B and C the coalescence state is attained in two perpendicular bands along X and Y directions. Additionally, the void is loosing its spherical shape, more importantly for orientation B than C. For other cases the coalescence is approached mainly in X direction and this state is attained visibly sooner for orientations A and B than for orientation C. Fig. 4.9 shows that, although the orientation effect is not seen in the normalized void evolution plots shown in Fig. 4.8 under the same value of displacement biaxiality, it manifests in the developed void shape and thus may influence the coalescence strain and, in general, the failure mode.

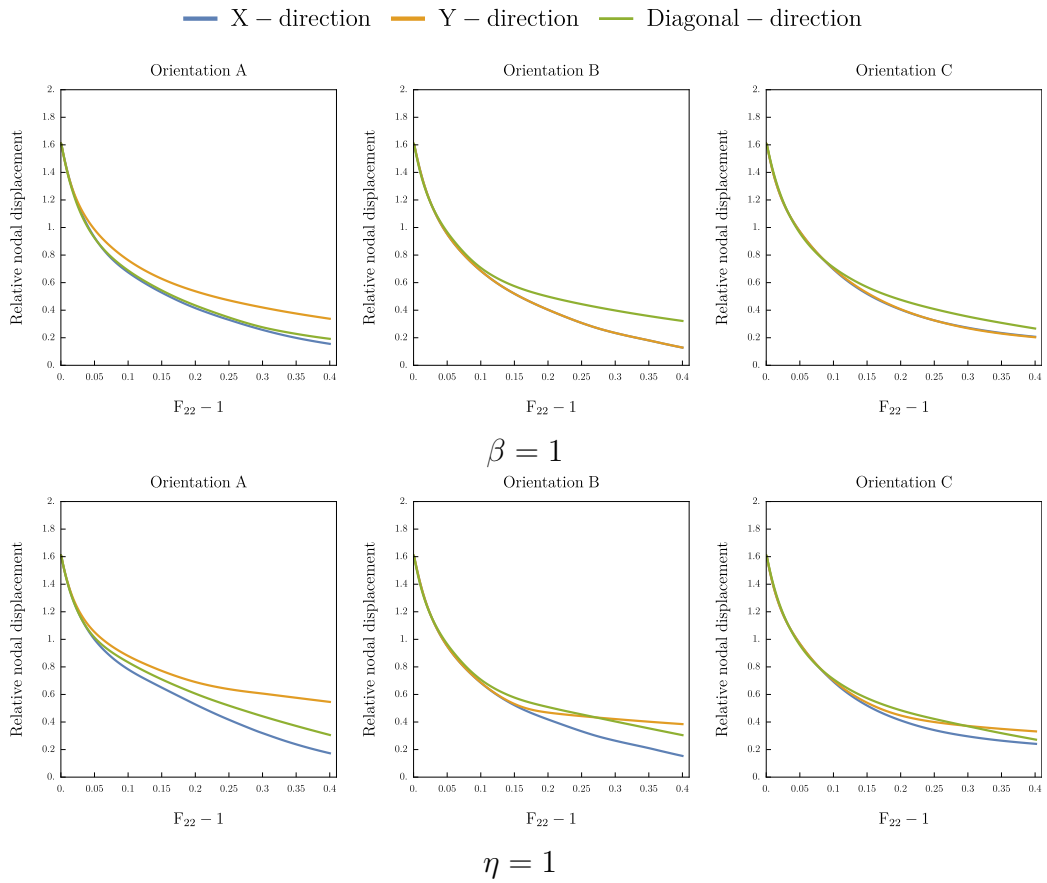

FIGURE 4.9 The change of the void diameters along X (AB), Y (EF) and diagonal (E'F') directions (see Fig. 3.1) for three orientations and two loading cases: $\beta = 1$ (top) and $\eta = 1$ (bottom). The curves present the value of $\log(L/|\mathbf{x}_{\text{right}} - \mathbf{x}_{\text{left}}|)$ where $\mathbf{x}_{\text{right}}$ and $\mathbf{x}_{\text{left}}$ denote current locations of nodes at the right and the left end of the respective diameter marked in Fig. 3.1 while L is the current cell size in a relevant direction.

4.3.2 Local sample response

Local distribution of accumulated shear. First, in order to show the possible failure mode, contour plots of accumulated shear are presented at the end of the deformation process at strain level 0.3 for six considered loading scenarios in Figs. 4.11, 4.13 and 4.15, for three crystallographic orientations A, B, and C listed in Tab. 4.2, respectively. Since the strain level along the principal loading direction is the same for all the cases, one is able to observe relative variation in a shape change of the cell as a whole and the void for all six loading scenarios. Additionally, to illustrate the strain localization process, the contour plots are presented for $F_{22} - 1 = 0.15$, so at the intermediate stage of the deformation (refer Figs. 4.10, 4.12 and 4.14)

Part (a) of Figs. 4.10–4.15 shows the contour plots of accumulated shear under $\beta = -0.5$

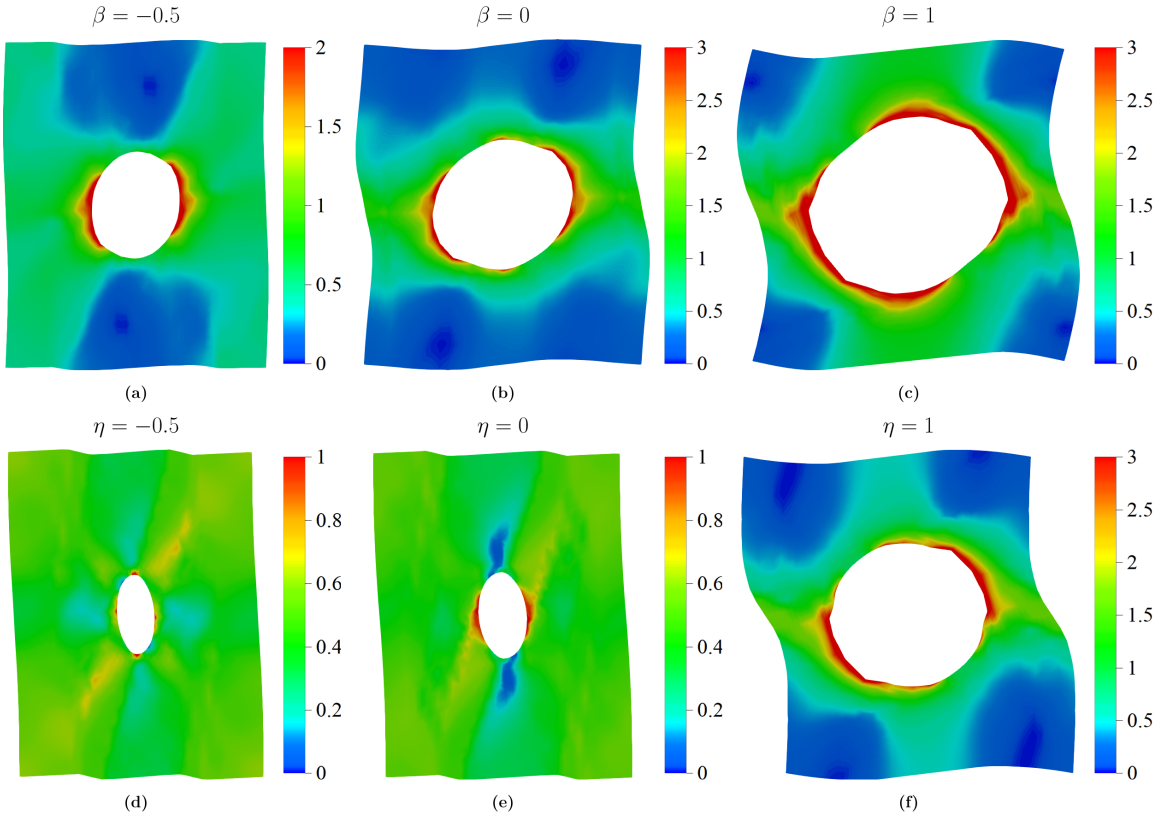

FIGURE 4.10 Contour plots of accumulated shear Γ for the asymmetric orientation A under various loading conditions at the strain level of $F_{22} - 1 = 0.15$.

loading. For all orientations, shear begins to accumulate on the transverse sides of the voids at the intermediate strain level of 0.15. Due to the symmetry of crystal orientations B and C with respect to the loading direction, the symmetrical distribution of accumulated slip is observed, whereas for asymmetrical orientation A alternate bands of severe deformation and no deformation are developing. Because of the relatively high stress biaxiality ratio in the $\beta = -0.5$ scenario, void growth is rapid as deformation progresses (refer to Fig. 4.6(a, d)). The unit cell is deformed substantially at strain level 0.3, with the maximum shear accumulating on the transverse sides of the void. For orientations A and B, the transverse ligament is the origin of void coalescence. In orientation A, the void rotates, and the strain concentration is observed on the transverse sides along the inclined direction. Moreover, at the strain level 0.3 a slight trace of the shear band is seen. Because of the asymmetric orientation, the unit cell edges do not remain straight and are deformed. For orientation B, a polygonal void shape is noticed. For orientation C, inclined shear bands clearly form, and the shear accumulates along the transverse sides of the void. The mode of failure

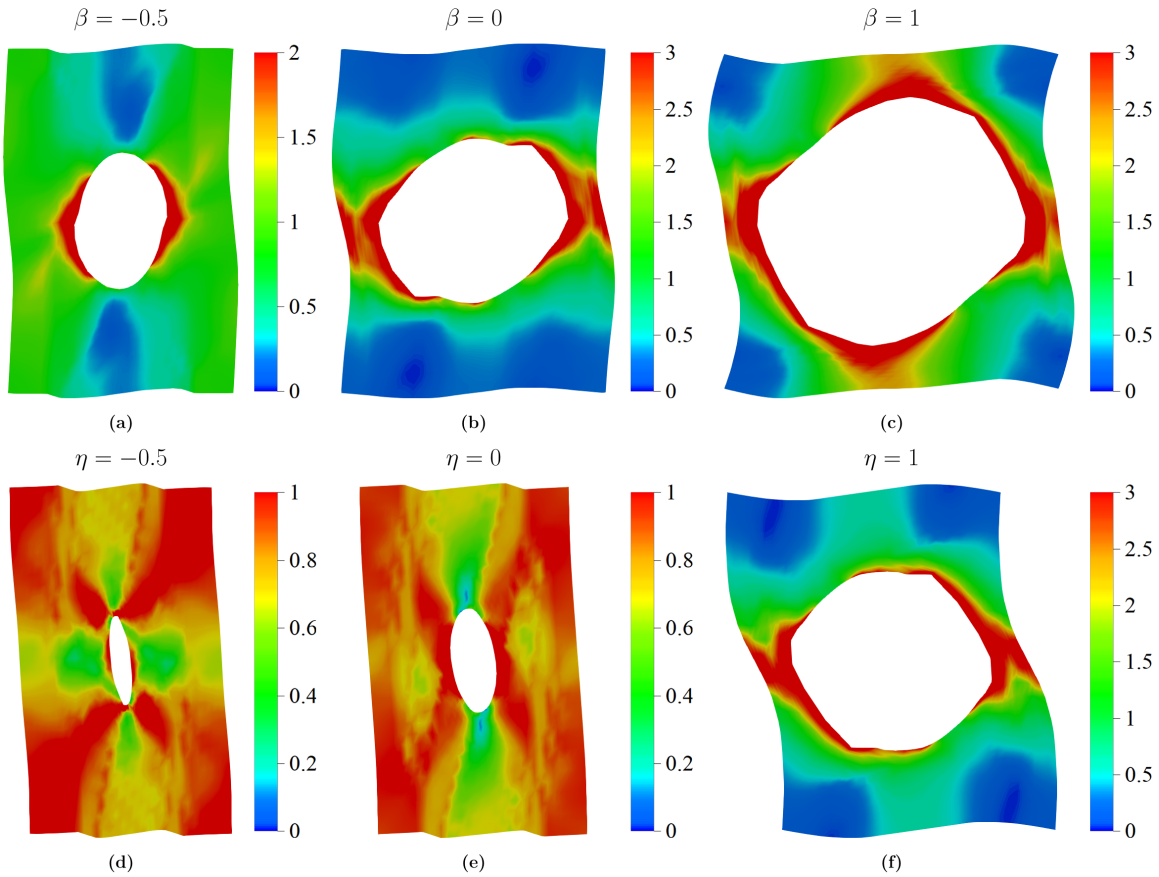

FIGURE 4.11 Contour plots of accumulated shear Γ for the asymmetric orientation A under various loading conditions at the strain level of $F_{22} - 1 = 0.3$.

in this case is through these inclined shear bands. In addition, the void elongates in the loading direction, resulting in an ellipsoidal void shape.

Part (b) of Figs. 4.10–4.15 displays the contour plots of accumulated shear under $\beta = 0$ loading. The void growth is substantially faster due to the high stress biaxiality ($0.5 < \eta < 1$, refer to Fig. 4.6a) and is evident even at the intermediate strain level of 0.15. At this strain level, shear begins to accumulate around the void and the void starts to grow significantly in the transverse direction for all three orientations. Additionally, the void rotates for orientation A. More shear is accumulated in the transverse ligament for orientation C than for orientations A and B. The symmetric distribution of contours is found again for symmetric orientations B and C. As the deformation process proceeds, rapid void growth is observed in all crystal orientations, and coalescence occurs along the transverse sides of the void. The void is substantially rotated for orientation A, and a zigzag pattern of strain localization bands is seen along the transverse direction of the

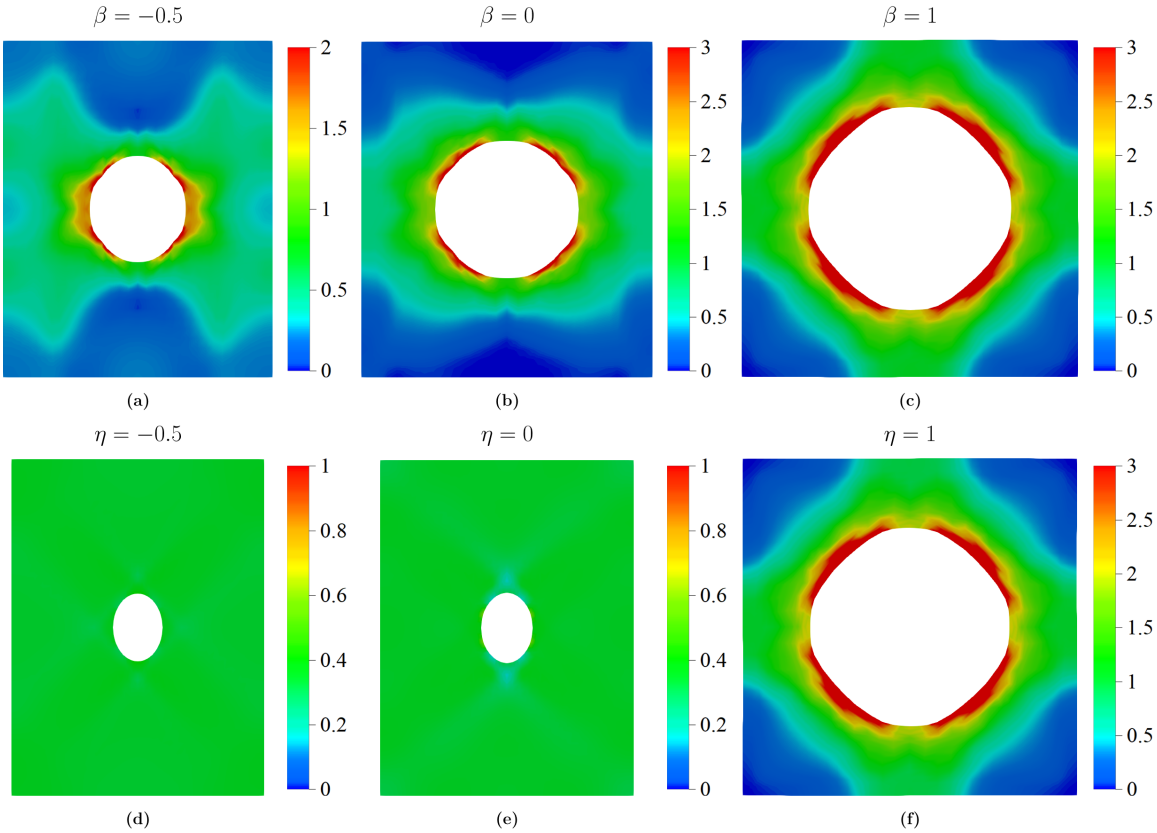

FIGURE 4.12 Contour plots of accumulated shear Γ for the symmetric orientation B under various loading conditions at the strain level of $F_{22} - 1 = 0.15$.

void. Similarly, in orientation B, void expansion in the transverse direction is quick, and a polygonal form of the void is clearly developed. On the other hand, the void shape in orientation C is nearly circular, and accumulated shear is seen in the transverse ligament.

Part (c) of Figs. 4.10–4.15 present the accumulated shear distribution under $\beta = 1$ loading. The contour plots resemble those from the preceding loading scenario, i.e. β = 0, however, the void growth is quick in both longitudinal and transverse directions due to the strong stress biaxiality. When compared to the previous loading instance β =0, the void expansion and accumulation of shear is significantly more severe at the intermediate strain level of 0.15. The void is rotated for asymmetric orientation A, as in prior loading scenarios. Due to the high stress biaxiality, the void form is much more circular for orientations B and C at the strain of 0.15. In contrast to prior loading examples, coalescence is observed in both directions at the final strain level of 0.3 for orientations B and C. In addition, for orientations B and C, a polygonal void shape with rounded corners is observed. Similar behavior was reported in (Srivastava and Needleman, 2015) at high stress triaxialities.

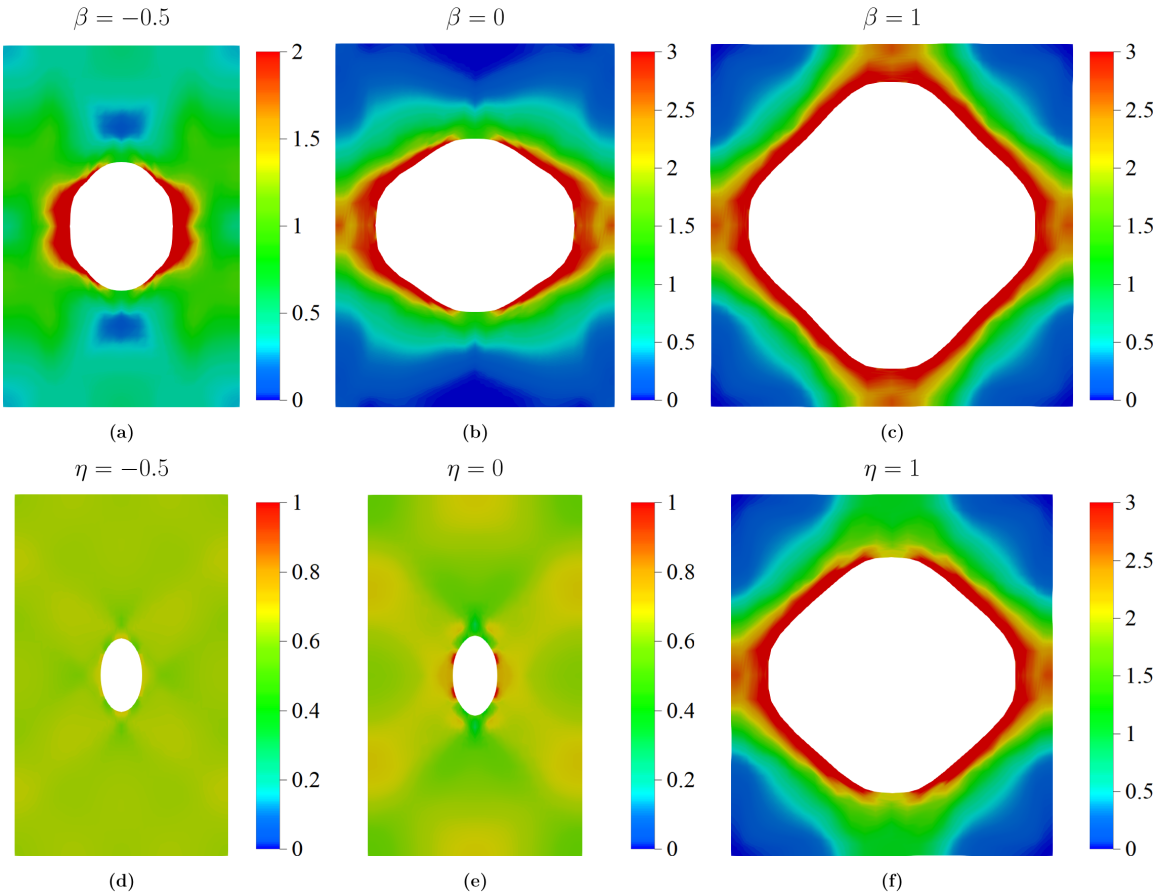

FIGURE 4.13 Contour plots of accumulated shear Γ for the symmetric orientation B under various loading conditions at the strain level of $F_{22} - 1 = 0.3$.

Furthermore, for both orientations, substantial shear accumulation is seen around the void. The void rotates even further in asymmetric orientation A, but its shape is not perfectly circular or polygonal. The same rapid void growth is clearly observed in normalized void volume fractions plots for this β loading case and three orientations (refer Fig. 4.6d).

Now, let us move to the $\eta = \text{const}$ loading scenarios. Subfigures (d) of Figs. 4.10–4.15 show the contour plots of accumulated shear under the $\eta = -0.5$ loading scenario. In comparison to the $\beta = -0.5$ loading condition, void growth is not significant under this loading configuration. This is because the stress biaxiality ratio is low. Also, as previously discussed on the basis of the void evolution plots, void expansion is not detected when the displacement biaxiality ratio β is lower than -0.5. At the intermediate strain level of 0.15, inclined shear bands begin to form for orientation A, whereas shear bands for orientation C are at 45° with the main loading direction. However, in orientation B, the deformation is almost homogeneous and there is no void growth. For orientations A and

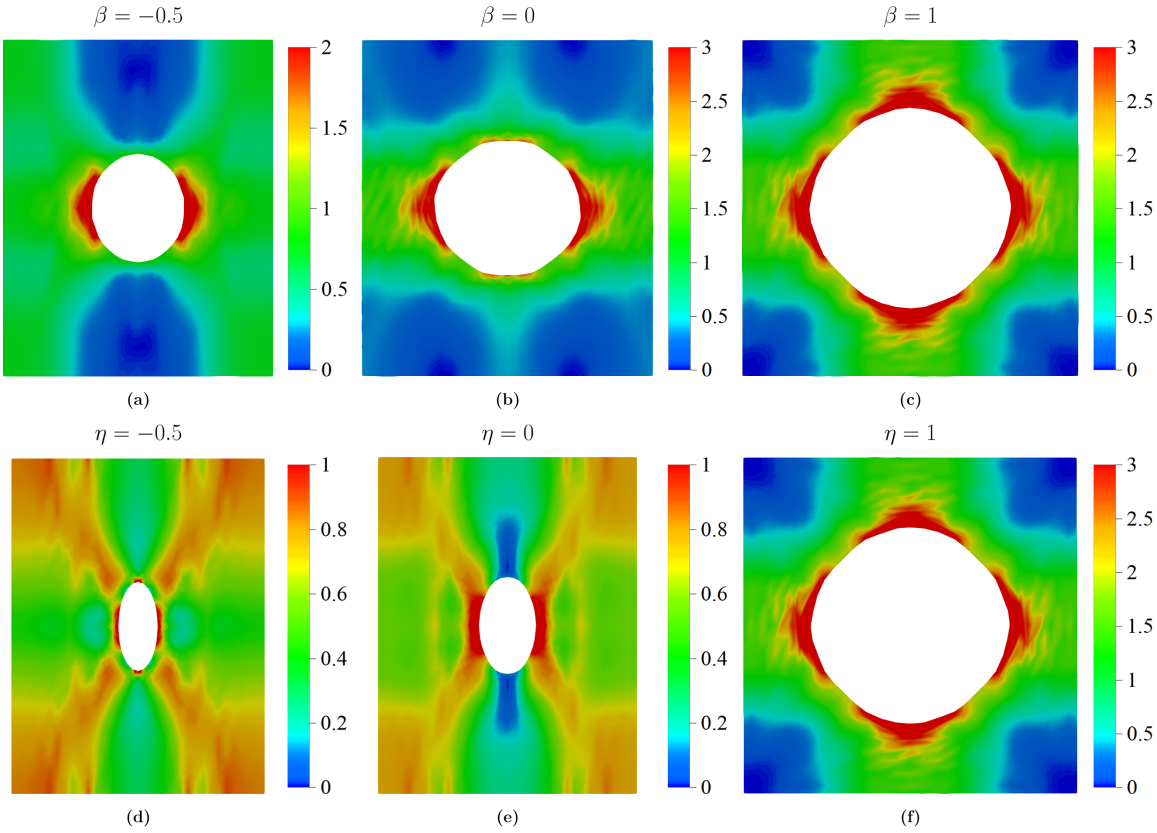

FIGURE 4.14 Contour plots of accumulated shear Γ for the symmetric orientation C under various loading conditions at the strain level of $F_{22} - 1 = 0.15$.

C, the void collapses at a strain level of 0.3. Normalized void volume fraction plots confirm the observation. The void in orientation C is collapsing like a penny shaped crack. Furthermore, shear accumulates the most at the tip of the severely elongated void. For orientation B, still, almost homogeneous deformation is seen, with no void expansion.

Part (e) of Figs. 4.10–4.15 displays the contour plots of accumulated shear in accordance with the $\eta = 0$ (uniaxial) loading scenario. The response is quite similar to the loading case with $\eta = -0.5$. At the strain level of 0.15, for asymmetric orientation A, the shear starts to accumulate on the transverse sides of the void and the formation of one family of inclined shear bands is observed whereas for orientation B almost homogeneous deformation is observed with no shear localization. The formation of two families of the inclined deformation bands and accumulation of slip on transverse sides of the void is seen for orientation C. For orientation A, a noticeable formation of another family of inclined deformation bands is observed at a strain level of 0.3, and the unit cell is distorted whereas for orientation B some heterogeneity of deformation is observed, but not much

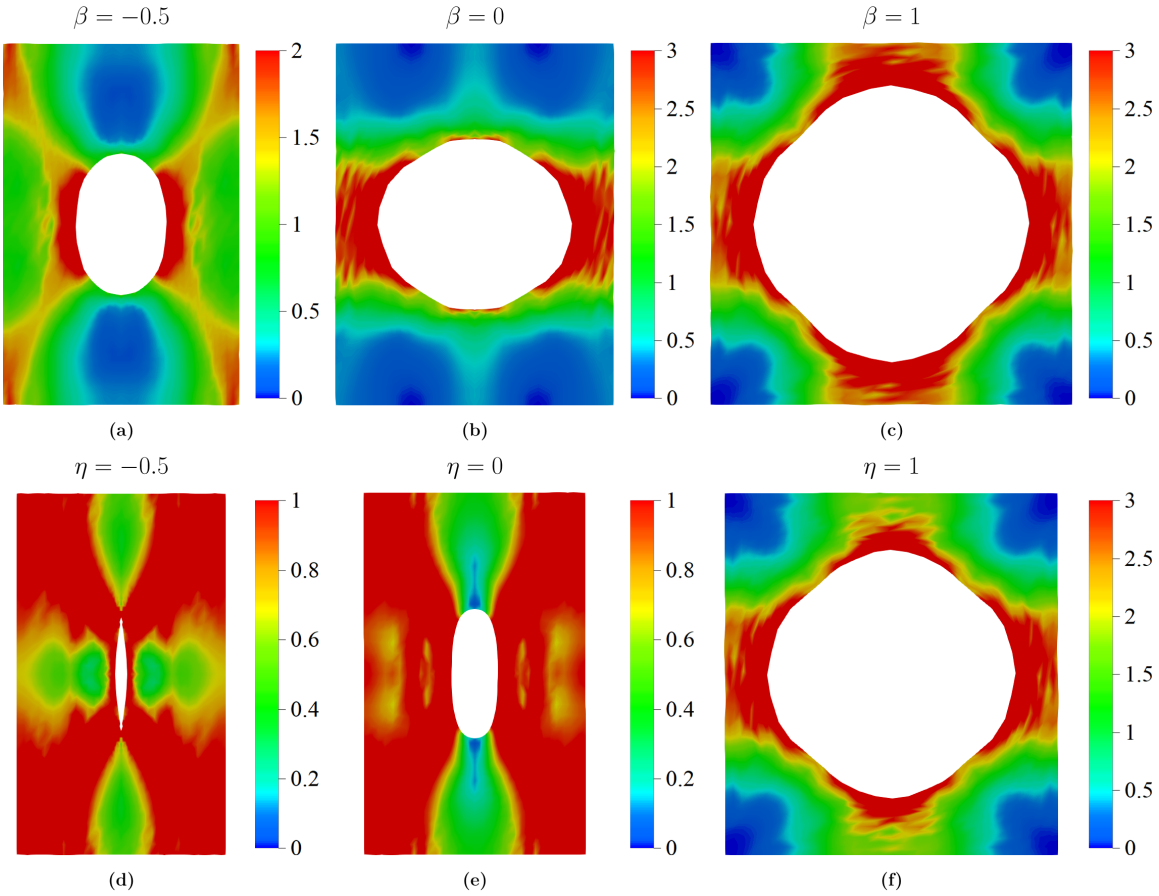

FIGURE 4.15 Contour plots of accumulated shear Γ for the symmetric orientation C under various loading conditions at the strain level of $F_{22} - 1 = 0.3$.

void expansion. For orientation C, slip shear accumulates on both sides of the void, causing the void to elongate along the loading direction, resulting in an ellipsoidal shape. When compared to orientations A and B, void expansion is substantially more prominent for orientation C. Overall, when comparing responses of three orientations with the respective $\beta = 0$ loading case, the void growth is not significant due to low stress and negative displacement biaxiality ratios. On the other hand, as already discussed, the $\beta = 0$ case is approximately equivalent to the $\eta = 0.8$ case for which the respective accumulated shear maps are shown in Fig. 4.16. Those contour plots are very similar to the maps shown in (b) subfigures included in this subsection.

Finally, part (f) of Figs. 4.10–4.15 depicts the accumulated shear contour plots under the $\eta = 1$ loading scenario. Similarly to the $\beta = 1$ loading scenario, void growth is accelerated due to high stress and displacement biaxiality. The displacement biaxiality ratio plot (Fig. 4.6b) explains the slight deviations from the $\beta = 1$ loading condition. For

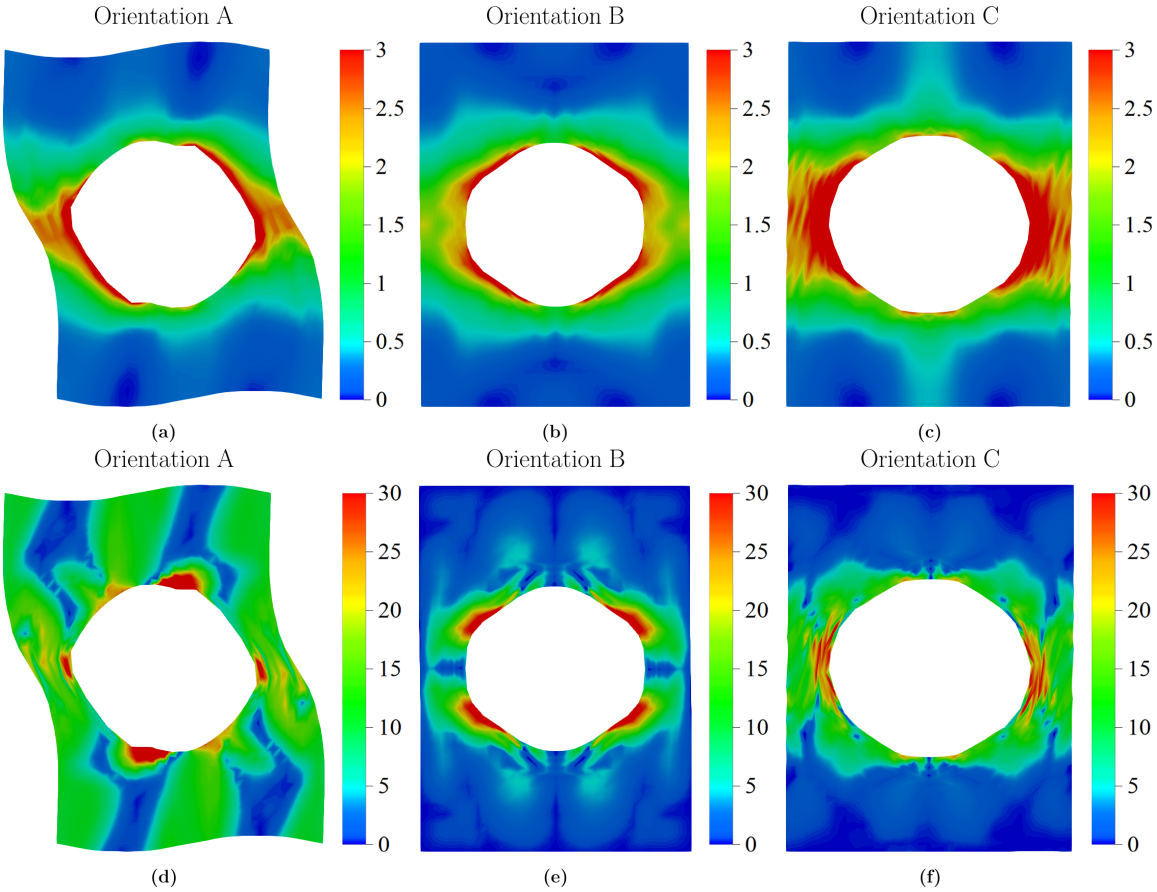

FIGURE 4.16 Contour plots of accumulated shear Γ (a-c) and lattice rotation angle in degrees (d-f) for orientations A, B and C at $F_{22} - 1 = 0.3$ for $\eta = 0.8$ case.

orientations B and C, the void growth is rapid even at the strain level of 0.15, which is identical to the $\beta = 1$ loading situation. However, there is some deviation in the strain accumulation as compared to $\beta = 1$ case for asymmetric orientation A, which can be correlated with differences seen in the displacement biaxiality ratio curves in Fig. 4.6b for these cases. A polygonal void shape with rounded corners is seen for orientations B and C at the strain level of 0.3, which is identical to the $\beta = 1$ loading situation. The void growth is slightly reduced since the displacement biaxiality ratio is less than 1 (refer to Fig. 4.6d). The primary difference is that in the $\beta = 1$ loading situation, void coalescence occurs in both loading directions, but in the $\eta = 1$ loading instance, void coalescence happens only in the transverse ligament. Displacement biaxiality plots (Fig. 4.6b) clearly show the origin of this disparity. In addition, the maximum shear accumulates around the void for all orientations.

Local distribution of lattice rotation. The influence of void evolution and loading conditions on new grain formation is now studied on the basis of contour plots of the lattice rotation angle. We concentrate on, somewhat opposite, cases of orientation A and B, and present only selected results for orientation C.

The lattice rotation angle $\Psi \in (0, \pi)$, presented in the plots, is defined as:

$$\Psi = \arccos\left(\frac{\mathrm{tr}(\Delta\mathbf{R}(\mathrm{t})) - 1}{2}\right) \tag{4.1}$$

where $\Delta\mathbf{R}(t)$ is calculated based on the initial orientation tensor $\mathbf{R}(0)$ and current orientation tensor $\mathbf{R}(t)$, respectively, as

$$\Delta\mathbf{R}(t) = \mathbf{R}(t)\mathbf{R}(0)^{\intercal}\,. \tag{4.2}$$

Orientation tensor $\mathbf{R}(t)$ is constructed based on the current orientation of lattice direction $\mathbf{a}$ with the Miller indices $[100]$ and lattice plane normal $\mathbf{b}$ with $\{001\}$, respectively. The change of their orientation during the deformation process is governed by the elastic part of the deformation gradient $\mathbf{F}_e$, so that $\mathbf{a}(t) = \mathbf{F}_e(t)\mathbf{a}(0)$ and $\mathbf{b}(t) = \mathbf{F}_e^{-T}(t)\mathbf{b}(0)$.

In each loading case, we observe rotation angle heterogeneity, which results in the development of a new microstructure. The presence of a void causes heterogeneity of strain, which results in heterogeneity of lattice rotation. However, we notice that the distribution of the rotation angle does not follow perfectly the distribution of accumulated shear Γ, as was already seen in Section 4.2 for uniaxial loading cases.

The lattice rotation angle plots for asymmetric orientation A are shown in Fig. 4.17. Because orientation A is not stable under prescribed loading conditions, we observe uniform lattice rotation even in pristine crystals. For example, the calculated lattice rotation angle for loading case $\eta = 0$ at $F_{22} - 1 = 0.3$ for a crystal without a void is $11°$. For voided crystal and $\eta = 0$ case, we observe bands with rotation angles of $30°$, whereas the remaining portion of the cell rotates at a smaller angle of about $10°$, which roughly corresponds to the lattice rotation which would be seen in pristine crystals. In the unit cell, new grains are formed as a result of the different rotation angles. Under the η = -0.5 loading scenario, a similar response is observed. Two inclined bands are forming in this case. The evolution of the void volume fraction has an effect on the evolution of the microstructure. For η = -0.5, we see that the new subgrains with larger rotation angle correlate with the zones of increased accumulation of shear. For β =0, β =1, and η = 1 loading cases, the formation of new grains takes place around the void, as well as alternate domains of no rotation (blue domain) and moderate rotation outside of the void

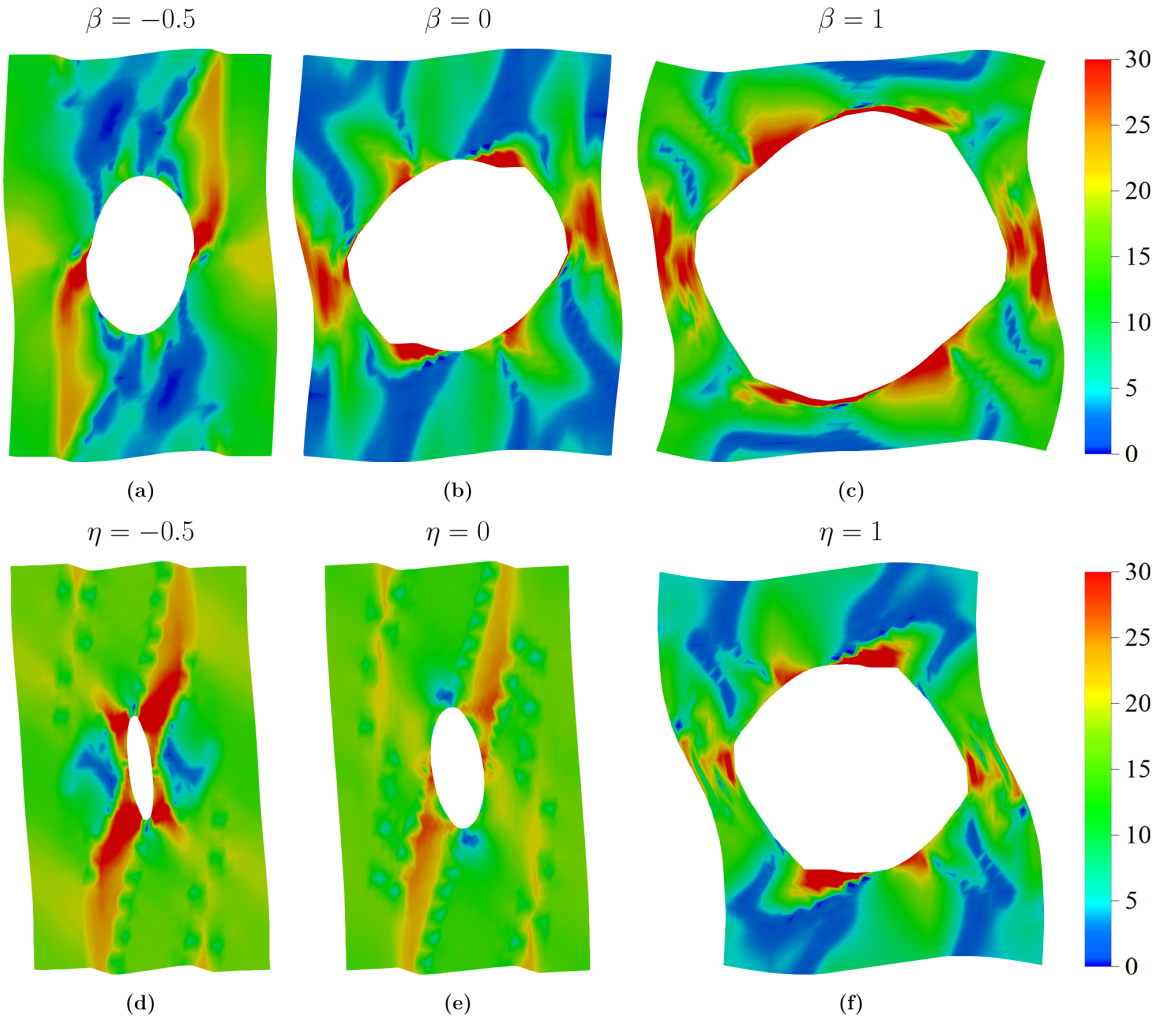

FIGURE 4.17 Contour plots of lattice rotation angle (Ψ) in (**degrees**) for the asymmetric orientation A at the strain level of $F_{22} - 1$ = 0.3.

is observed. All of these factors contribute to the formation of multigrain microstructures, particularly at high strain or stress biaxiality values. For the β = -0.5 loading case (and for the approximately equivalent $\eta = 0.8$ case as seen in the Fig. 4.16), the combination of effects found for other loading cases is seen. We observe the formation of a band with high lattice rotation, which starts at the lateral sides of the void and then is parallel to the main direction of loading, as well as alternating bands of no and medium rotation angles in the middle vertical portion of the unit cell.

Fig. 4.18 depicts the lattice rotation angle plots for orientation B. Due to the symmetry of orientation with respect to the loading conditions, the developed microstructure preserves this symmetry. Because orientation B is stable under prescribed loading conditions, we

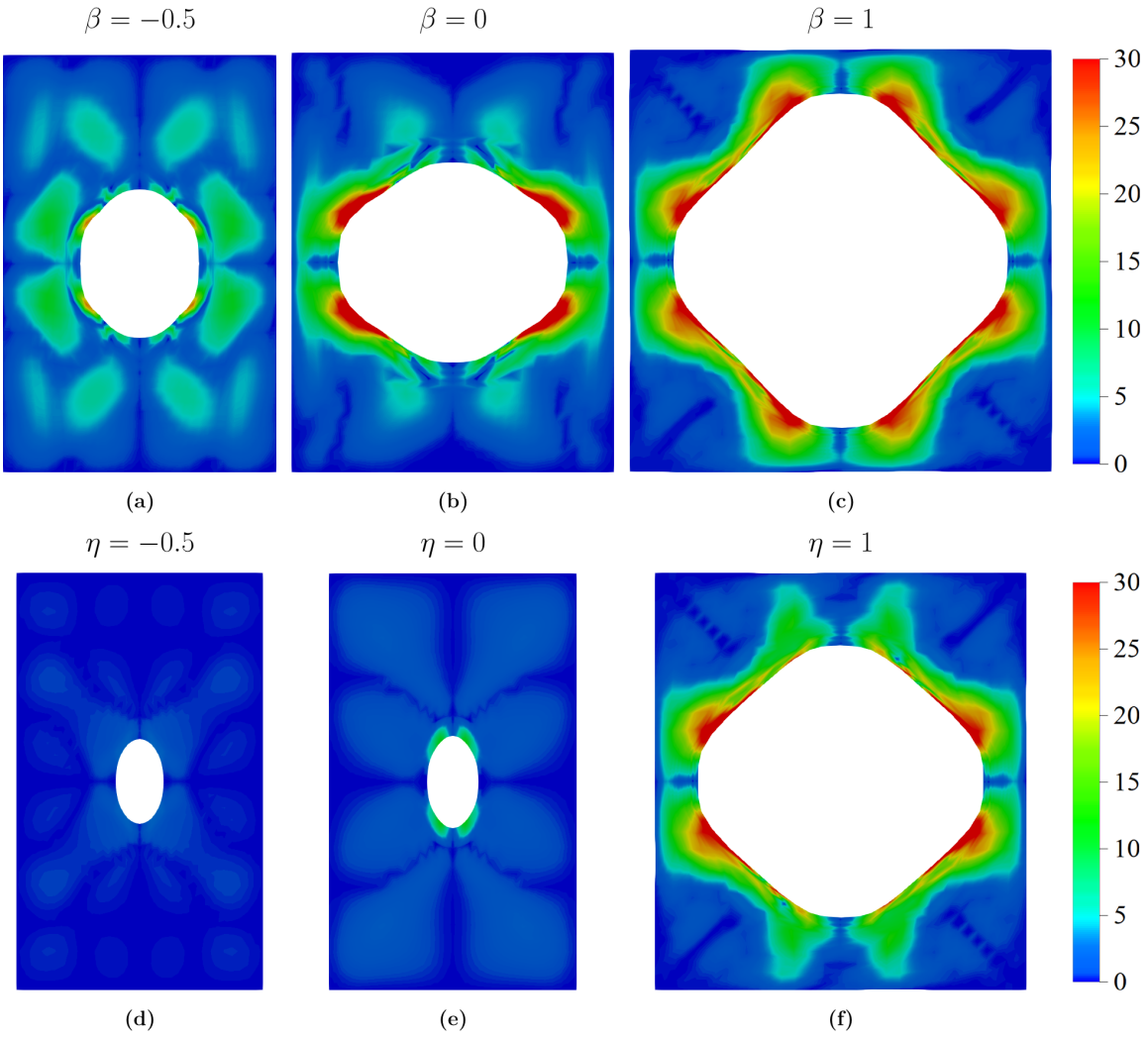

FIGURE 4.18 Contour plots of lattice rotation angle (Ψ) in (**degrees**) for the symmetric orientation B at the strain level of $F_{22} - 1$ = 0.3.

do not observe lattice rotation for pristine crystal. For a voided crystal, for $\eta = 0$ and $\eta = -0.5$ loading cases, the heterogeneity of lattice rotation angle is very small, which is less than 5°, following homogeneity of deformation seen in Fig. 4.13(d, e). Around the void, a few small domains with 5–10° of lattice rotation are present. The formation of new grains around the void is observed for higher biaxiality loading cases where $\beta = 0$, 1 and $\eta = 1$, and the crystal domain in a larger distance from the void does not rotate significantly. Under $\beta = -0.5$ and $\eta = 0.8$ loadings, the response is somewhere in between the two scenarios discussed before.

In order to further illustrate the effects related to grain refinement, Figs. 4.19 and 4.20 present histograms of the lattice rotation angle generated based on the data in

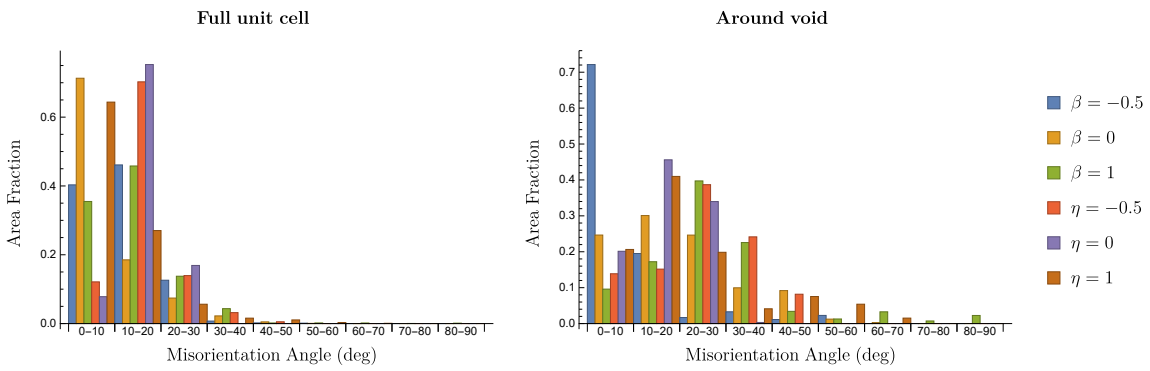

FIGURE 4.19 Histogram plots of lattice rotation angle Ψ in **degrees** for the asymmetric orientation A at the strain level of $F_{22} - 1 = 0.3$. (Area fraction is calculated in reference configuration).

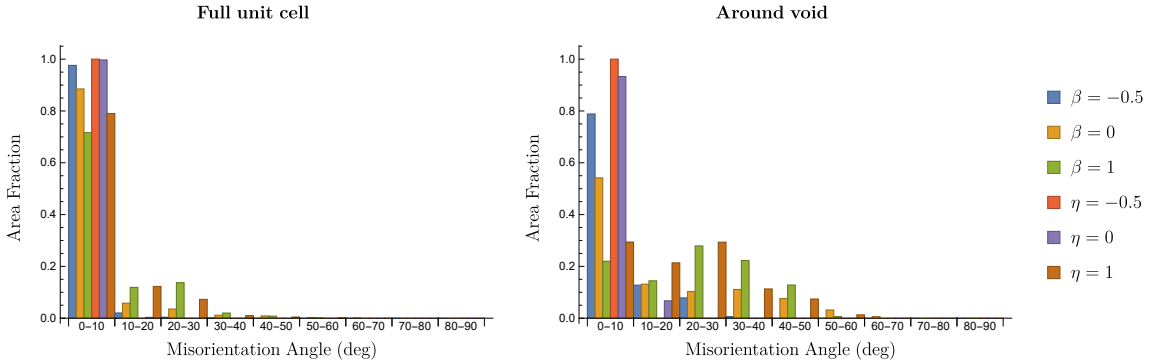

FIGURE 4.20 Histogram plots of lattice rotation angle Ψ in **degrees** for the symmetric orientation B at the strain level of $F_{22} - 1 = 0.3$. (Area fraction is calculated in reference configuration).

Figs. 4.17 and 4.18, respectively. The histogram plot on the left displays the entire unit cell, while the histogram plot on the right shows the area surrounding the void. For the purpose of the latter plot, we employed two layers of finite elements which surround the void (refer to Fig. 3.3). Different colors of bars correspond to different loading conditions. When we compare the results for asymmetric orientation A and symmetric orientation B, we observe that orientation A has a substantially larger orientation spread than orientation B. This is because most of the elements rotate less than 10° in orientation B. When we consider the area around the void for both orientations, the orientation spread widens significantly, especially for $\eta = 1$ and $\beta = 1$ loading cases.

In order to quantify more directly observed differences for each case mean value and standard deviation of rotation angle were calculated and collected in Tab. 4.4, which includes also the respective values found for orientation C. As expected, for all loading

TABLE 4.4 Mean (M) and standard deviation (SD) of misorientation angles (degrees) for two orientations under different loading scenarios.

Loading Case		$\beta = -0.5$	$\beta = 0$	$\beta = 1$	$\eta = -0.5$	$\eta = 0$	$\eta = 0.8$	$\eta = 1$
Orientation A	M	11.656	8.593	13.605	16.804	16.034	9.1274	9.308
	SD	7.302	7.997	9.114	6.390	4.569	6.91265	8.223
Orientation B	M	3.179	4.446	7.548	0.255	0.808	4.08305	5.702
	SD	2.938	7.605	9.837	0.321	0.956	6.87856	8.125
Orientation C	M	5.188	4.490	6.502	7.103	6.445	4.68702	5.727
	SD	5.278	6.808	7.576	8.595	6.451	7.06543	6.737

conditions the highest mean value is obtained for orientation A, which is connected with lack of symmetry for this configuration. Considering the results for the same orientation but different loading conditions, we see that the highest mean misorientation angle is found for the case $\eta = -0.5$ and 0 for orientation A, and for $\beta = 1$ for orientation B and C (refer to Tab. 4.4). The standard deviation is used to illustrate lattice rotation heterogeneity. High biaxiality factors η and $\beta = 1$ correspondingly showed the highest lattice rotation heterogeneity for orientation A. However, for other stress and strain biaxiality factors, the variation in lattice rotation is not significantly lower. The smallest heterogeneity is observed for the $\eta = 0$ case (around $4.5°$). As a result, in the presence of a void, orientation A is prone to grain fragmentation. For orientations B and C, the disparities in lattice rotation heterogeneity are larger. Again, β and $\eta = 1$ had the highest values. However, no heterogeneity is evident for $\eta = -0.5$ and $\eta = 0$ for orientation B, as shown by contour plots (Fig. 4.18). This observation is not true for orientation C, which can be correlated with important strain heterogeneity for those two cases seen in Fig. 4.15. On overall, the level of orientation spread appears to be more influenced by loading conditions in the case of symmetric orientations.

4.4 Summary and conclusions

In this chapter, using the crystal plasticity theory combined with the finite element method, we have investigated the effects of initial crystallographic orientation, stress, and displacement controlled loading conditions on the void and microstructure evolution in a 2D plane strain unit cell. Uniaxial and biaxial loading cases have been studied.

For uniaxial loading cases a special configuration, which enforces an equivalent pattern of plastic deformation in the pristine crystal, has been selected in order to investigate the

mutual interactions between the evolving void and the lattice rotation heterogeneity. It has been found that neither macroscopic in-plane stress biaxiality nor displacement/strain biaxiality, are sufficient to fully decide about the void growth, especially when anisotropic materials are considered, and that a significant role in this process is played by microstructure evolution. Fragmentation of bulk crystal surrounding the void into subgrains may lead to significant disturbance of the void volume changes. Note that a similar observation, about the importance of the microstructure changes, was made by Prasad et al. (2015) for HCP crystal in which the appearance of domains with new twin related orientation strongly affected void growth and coalescence.

Next, biaxial loading cases have been considered for three crystal orientations, one of which is not symmetric with respect to loading directions. It has been analyzed how stress or strain biaxiality factors and initial lattice orientation influence the void evolution in terms of its size and shape. Overall, seven cases with three displacement controlled loading scenarios ($\beta = \{-0.5, 0, 1\}$) and four stress controlled loading scenarios ($\eta = \{-0.5, 0, 0.8, 1\}$) have been considered. The following are the key conclusions of the study:

1) It seems that the primary driving factor for void growth and coalescence is the displacement biaxiality factor β. A clearer correlation is found between variations in displacement biaxiality ratio and normalized void volume fraction evolution plots, as well as the resulting void shape and coalescence pattern.

2) Softening stress response is evident for large displacement biaxiality factors when the stress biaxiality ratio η increases. The void volume fraction increase in such cases is significant, resulting in void coalescence. The effect of crystal orientation is then diminished. Similar findings were reported in other studies (Potirniche et al., 2006). The coalescence is observed in both directions for displacement biaxiality β =1, but only in the transverse ligament for stress biaxiality η =1. For advanced plastic deformation, particularly at high stress and displacement biaxiality $\eta = \beta = 1$, voids evolve into polygonal forms. Similar findings have been reported by Srivastava and Needleman (2015).

3) For stress controlled processes, the starting point can be described as a biaxial straining process which under the void growth is approaching an uniaxial straining mode. The way by which the void growth proceeds is governed by the variation of the displacement biaxiality factor β. When initially β is positive the obtained void volume fractions are larger (softening is observed earlier), while the void growth rate will be decreasing when the uniaxial straining mode is approached. On the

other hand, when initially β is negative then the obtained void volume fractions are smaller (softening is observed later), while the void growth rate will be increasing when the uniaxial straining mode is approached.

4) For lower stress η and displacement β biaxiality values, an anisotropic response is observed, and the strain-stress response is dependent on crystallographic orientation. For the lowest value of stress biaxiality $\eta = -0.5$, void closure has been observed, particularly in the non-symmetric orientation A and orientation C, as well as the formation of strain localization bands.

5) In general, the heterogeneity of plastic deformation is the largest for non-symmetric orientation A. This results in lattice rotation heterogeneity and the formation of grain fragmentation in each loading case. For other orientations heterogeneity of lattice rotation is concentrated around the void, especially for higher stress and displacement biaxiality ratios ($\beta = \{0, 1\}$ & $\eta = \{0.8, 1\}$). On the other hand, for small or negative values of both biaxiality factors, void evolution, and lattice rotation heterogeneity is greatly influenced by initial crystal orientation and substantially differ for the same value of stress and strain biaxiality factor, while the grain refinement encompasses a larger crystal volume.

CHAPTER 5

Finite element analyses of HCP crystals with voids

In this chapter, the growth and coalescence of voids in HCP single crystals deforming through slip and twinning are examined using CPFEM, by employing a unit cell methodology, similarly as in the previous chapter. A 2D plane strain unit cell with a cylindrical void and a 3D unit cell with a spherical void are considered (see Figs. 3.1b and 3.2). A rate-dependent crystal plasticity model that includes slip, twinning, and PTVC reorientation scheme is used; the formulation details are thoroughly explained in Chapter 2, Section 2.4. For a better understanding of the impact of stress state on void growth, simulations were conducted using constant stress ratio controlled boundary conditions imposed through a specific special spring element. This approach is already discussed in Chapter 3, Subsection 3.2.3. In the first part, the growth of a cylindrical void in a 2D plane strain cell under various stress biaxiality ratios is discussed. In the second part, the anisotropic growth of a spherical void under uniaxial tension in five different direction with respect to crystal axes is examined.

5.1 Numerical analyses of a 2D plane strain unit cell with cylindrical void

A 2D plane strain unit cell with one cylindrical void is employed (refer schematic Fig. 3.1b and for FE mesh Fig. 3.3). Three basal, three prismatic, six pyramidal slip systems, and six tensile twinning systems are considered as potential plastic deformation modes for HCP crystals (refer to Tab. 2.3), taking into account the three-dimensional nature of crystal slip and twin systems. As already mentioned, regarding boundary conditions, to control in-plane stress biaxiality, stress controlled boundary conditions are imposed as

TABLE 5.1 Crystal orientations considered with respective global coordinate axes.

Case	In-plane lateral loading direction (x)	Primary loading direction (y)	Out-of-plane lateral direction (z)
Prismatic (Orientation A)	$[10\bar{1}0]$	$[1\bar{2}10]$	$[0001]$
C -axis (Orientation B)	$[1\bar{2}10]$	[0001]	$[10\bar{1}0]$

TABLE 5.2 Elastic constants and some other parameters for Mg alloy AZ31B (Frydrych, 2017).

C_{11} [GPa]	C_{12} [GPa]	C_{13} [GPa]	C_{33} [GPa]	C_{44} [GPa]	γ^{TW}	c/a	n	$\dot{\gamma}_0$
59.3	25.7	21.4	61.5	16.4	0.129	1.624	20	0.001

TABLE 5.3 Hardening parameters for Mg alloy AZ31B (Frydrych, 2017).

System	Interaction	τ_0 [GPa]	h_0 [GPa]	h_1 [GPa]	τ_{sat}/f_{sat} [GPa]/–	μ –	q basal	prism.	pyr. <c+a>
								twin	
Basal	slip-slip	0.0029	0.03016	0.0	0.0783	1.0	1.0	1.0	0.0
	slip-twin	—	0.00001	—	0.9	—		1.6	
Prism.	slip-slip	0.1122	0.989	0.0	0.1057	1.2	1.0	1.0	1.0
	slip-twin	—	0.00001	—	1.0	—		1.6	
Pyr. <c+a>	slip-slip	0.135	1.585	0.0	0.135	2.0	1.0	1.0	1.0
	slip-twin	—	0.0002	—	1.0	—		1.4	
Tensile twin	twin-slip	—	0	72.5	0.01	—	0.0	0.0	1.0
	twin-twin	0.0649	0.001	—	0.95	100.0		1.4	

outlined in Subsection 3.2.5. In the calculations, the sample direction is fixed with y axis denoting principal loading axis. The crystal lattice is oriented along this direction using a rotation matrix defined by Euler angles.

5.1.1 Crystal orientations, material parameters and loading cases considered

The material and hardening parameters representing the Mg alloy AZ31B, as shown in Tabs. 5.2 and 5.3, were used in the calculations. These parameters were identified in (Frydrych, 2017) based on the experimental results of Proust et al. (2009). The elastic response of Mg is transversely isotropic, and the elastic constants are defined in Tab. 5.2. In the following section, the analysis focuses on the influence of crystal orientation on texture development, void evolution, stress-strain response, and deformation mechanisms. Two crystal orientations are considered, as presented in Tab. 5.1. It should be noted that

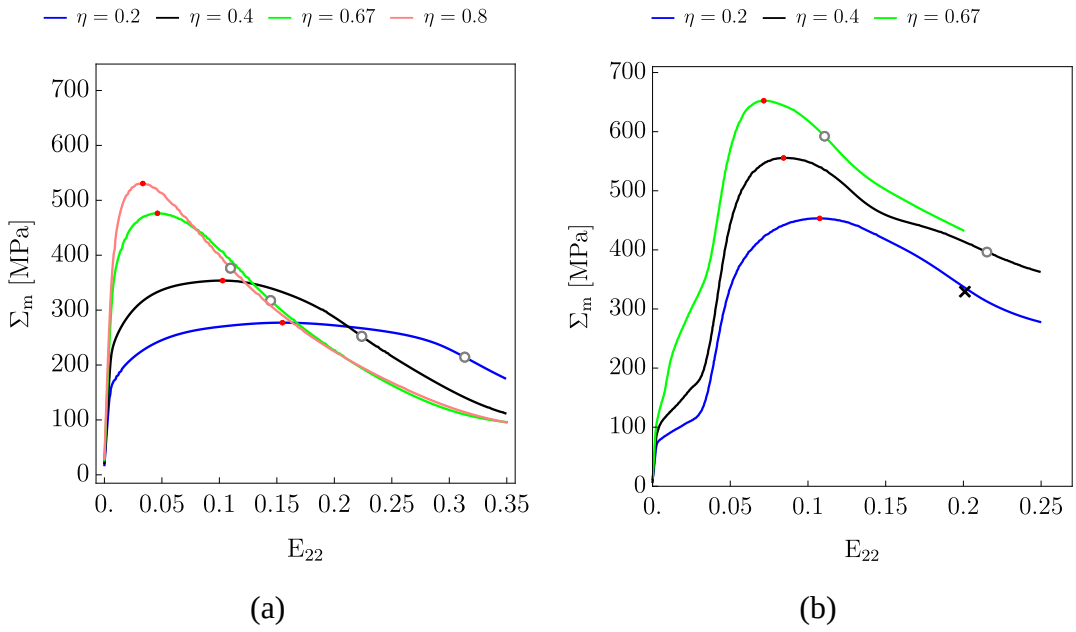

FIGURE 5.1 Variation of macroscopic mean stress (Σ_{m}) with macroscopic strain (E_{22}) for (a) orientation A and (b) orientation B corresponding to initial void volume fraction of 0.031. The peak stress is indicated by • where as onset of void coalescence is indicated by ∘ & ×.

in the prismatic loading scenario (orientation A), the c-axis is oriented perpendicular to primary loading direction while for Orientation B c-axis is parallel to primary loading direction. Each orientation is studied under four loading conditions with stress biaxiality (η) values of 0.2, 0.4, 0.67, and 0.8, encompassing a wide range of in-plane mean stress levels. Both orientations are symmetric under such loading conditions, so the overall deformation gradient in 3D is approximately diagonal,

$$\mathrm{F}_{ij} = \begin{bmatrix} \mathrm{F}_{11} & 0 & 0 \\ 0 & \mathrm{F}_{22} & 0 \\ 0 & 0 & 1 \end{bmatrix}$$

so is the Hencky logarithmic strain: $\mathbf{E} = \log \mathbf{U} = \log \mathbf{F}$.

5.1.2 Macroscopic response of voided crystal

In Fig. 5.1(a, b), the changes in in-plane macroscopic mean stress Σ_{m} with E_{22} (defined as $\log[\mathrm{F}_{22}]$) are illustrated for orientations A and B, respectively. The stress-strain response differs qualitatively between the two orientations as a result of activation of different set of deformation modes. Fig. 5.2 shows the volume-averaged relative activity plot of all

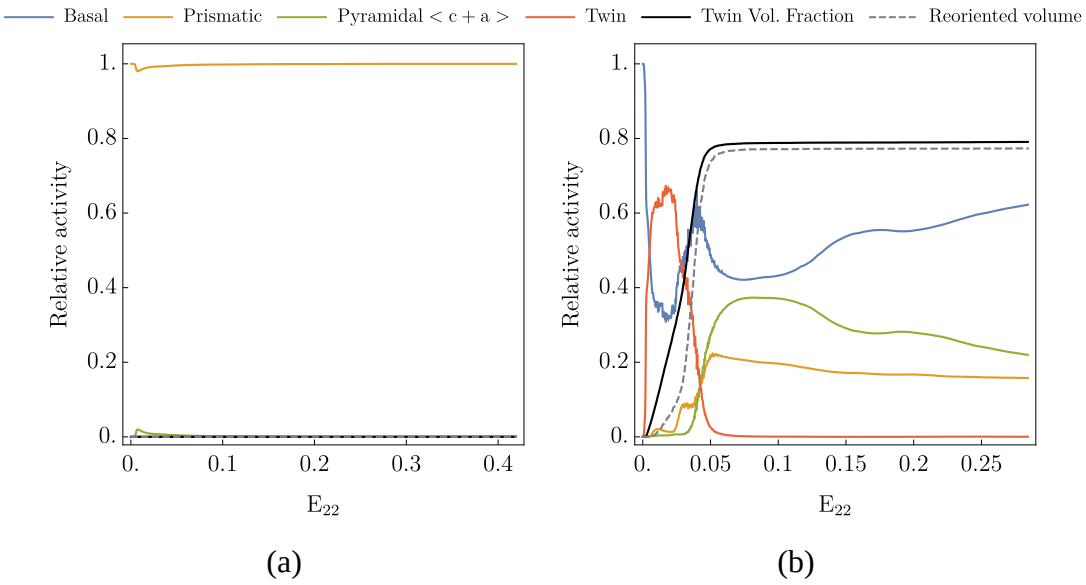

FIGURE 5.2 Relative activity plots, $\bar{\xi}$ (refer Section 3.3), of deformation mechanisms (a) orientation A and (b) orientation B with $\eta = 0.4$.

possible slip and twin mechanisms under the loading case $\eta = 0.4$. Similar results are observed for other η loading cases. This plot is utilized to analyze an impact of deformation mechanisms on the averaged (macroscopic) and local mechanical response of a unit cell.

In Fig. 5.1a, it is shown that for orientation A, mean stress initially increases linearly with E_{22} and then begins to saturate due to plastic yielding in the cell and void expansion at low stress ratios of $\eta = 0.4$ and 0.2. When strain hardening in a single crystal cannot compensate for the expansion of the void, the macroscopic stress reaches a peak and then starts to decline. This peak occurs at higher levels of E_{22} for low stress ratios of $\eta = 0.4$ and 0.2 due to the slow expansion of the void and significant accumulation of plastic deformation, as seen in Fig. 5.1a. For high stress ratios $\eta = 0.8$ and 0.67, this behavior occurs at lower E_{22} values, shortly after the macroscopic mean stress versus strain curves deviate from linearity due to the rapid growth of the void. Additionally, it can be observed that as the stress ratio η decreases, the peak macroscopic mean stress values decrease. This behavior is qualitatively similar to the behavior of the FCC unit cell discussed in the previous chapter (compare Fig. 4.6c) as only (prismatic) slip modes are active for this orientation (Fig. 5.2a) for all values of η.

In comparison to Fig. 5.1a, the macroscopic mean stress Σ_{m} vs. E_{22} curves for orientation B in Fig. 5.1b exhibit a distinct pattern which results from the activity of different set of slip systems and in particular, twinning. In this scenario, Σ_{m} initially increases gradually with E_{22} (up to $E_{22} \approx 0.04$). During this phase, twin formation

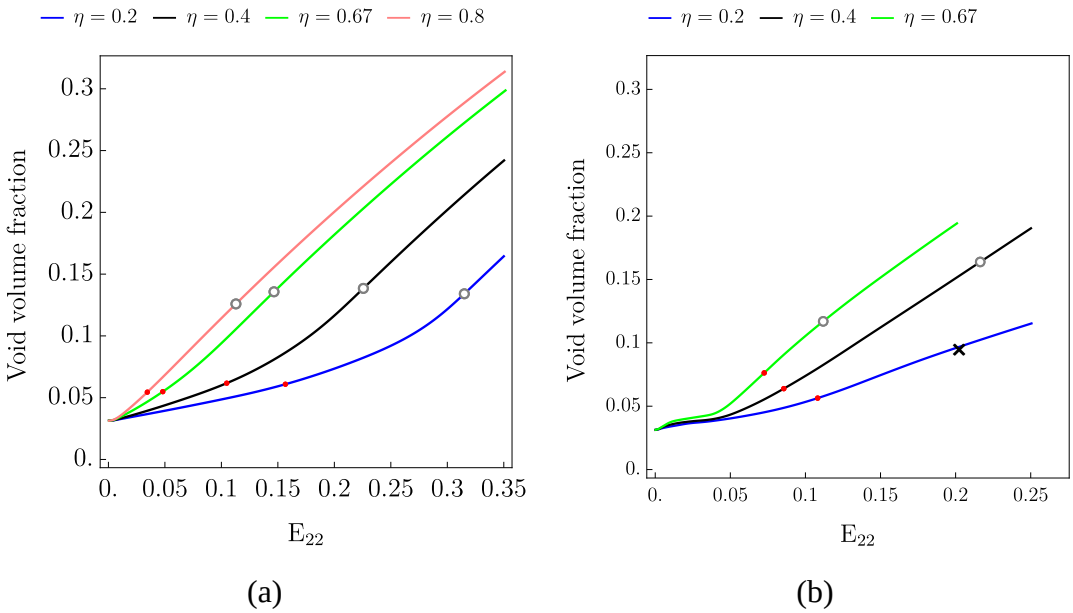

FIGURE 5.3 Evolution of void volume fraction with macroscopic strain (E_{22}) for (a) orientation A and (b) orientation B corresponding to initial void volume fraction of 0.031. The peak stress is indicated by • where as onset of void coalescence is indicated by ∘ & ×.

occurs in the cell for low stress ratios of $\eta = 0.4$ and 0.2, as observed in the relative activity plot (Fig. 5.2b). More details will be given when presenting the local response. After lattice reorients throughout a large section of the cell, Σ_{m} increases significantly, as seen in Fig. 5.1b. Multiple slip mechanisms become active after this stage especially in reoriented domains of the cell, as observed in Fig. 5.2b, resulting in rapid increase of the mean stress. As the material hardens volumetric deformation is concentrated in the void. With the void continuing to expand rapidly, the macroscopic mean stress decreases after reaching the peak stress. Similar to orientation A, peak macroscopic mean stress values decrease as the stress ratios decrease. Due to the increased hardening induced by lattice reorientation from tensile twinning, the levels of peak macroscopic mean stress Σ_{m} are higher for orientation B than for orientation A for the same η.

5.1.3 Void growth and coalescence

Fig. 5.3(a, b) depicts the evolution of the void volume fraction with E_{22} for orientations A and B, respectively, for various stress ratios (η). The void volume fraction is defined as the ratio of the area enclosed by the void to the area of the unit cell. Fig. 5.3a reveals that as η decreases from 0.8 to 0.67, the void volume fraction declines very little at a fixed value of E_{22} for orientation A. This trend is consistent with the plastic slip developing

within the unit cell in a similar manner (refer to Subsection 5.1.4). Furthermore, as η is reduced further from 0.67 to 0.2, a significant delay in the evolution of the void volume fraction with E_{22} is observed for both orientations A and B. This delay can be attributed to a substantial drop in macroscopic mean stress (Σ_{m}) and increased evolution of plastic slip in the cell (orientations A & B). Consequently, for Mg single crystals, the level of in-plane mean stress is crucial in controlling the evolution of the void volume fraction with macroscopic strain. There is an interplay between void growth and development of plastic deformation in the material.

By observing Fig. 5.3b, a kink is visible on the curves for all stress ratios at $E_{22} \approx 0.04$ for orientation B. This stage is characterized by a significant rise in macroscopic stress due to the completion of the reorientation caused by tensile twinning and saturation of the activity of this mechanism throughout a large portion of the cell. The void growth rate accelerates significantly after this stage due to the activation of several difficult-to-proceed slip mechanisms in the reoriented area (refer to Fig. 5.2b). Consequently, mean stress reaches a peak shortly after this transition due to rapid void growth, as seen in Fig. 5.1b. At high stress ratios, the void growth rate for orientation B is slower in comparison to orientation A due to tensile twinning before reorientation is completed in the cell, as shown in Fig. 5.3(a, b). As a result of the delayed hardening imparted by activity of tensile twinning at the initial stage of the deformation process, void growth is hindered for orientation B compared to orientation A, especially at high stress ratios.

Fig. 5.4(a, b) depict the evolution of unit cell width showing variation of $\log(\mathrm{L_o}/\mathrm{L})$ with macroscopic strain E_{22} for various stress ratios, corresponding to orientations A and B, respectively. Here, $\mathrm{L_o}$ and L represent the initial and current widths of the cell. All of the curves represented in Fig. 5.4a exhibit similar behavior. Thus, when E_{22} is increased, $\mathrm{L_o}/\mathrm{L}$ is increased, reflecting an initial reduction in cell width. Following this first stage of deformation process, for orientation A and all values of η, saturation occurs in the value of $\mathrm{L_o}/\mathrm{L}$, after which it remains nearly constant. This stage indicates that further deformation occurs in a uniaxial straining mode along the primary loading (i.e., y) direction which results in flow localization and inter necking coalescence of adjacent voids (Prasad et al., 2015). This behavior is again consistent with the response of FCC crystals in previous Chapter 4. The critical value of macroscopic strain (E_{22}^{c}) at the onset of void coalescence is defined as the magnitude of E_{22} at which the rate of change of the cell width $|\mathrm{dL}/\mathrm{dE_{22}}|$ is less than 2% of its peak magnitude and is represented by $\circ$ in the plot. Similarly, the value of peak stress is indicated by $\bullet$ as marked in Fig. 5.4a.

Corresponding to orientation B, saturation in the cell width occurs only for the large stress ratio $\eta = 0.67$, as seen in Fig. 5.4b. The curves for $\eta = 0.4$ and 0.2, on the other

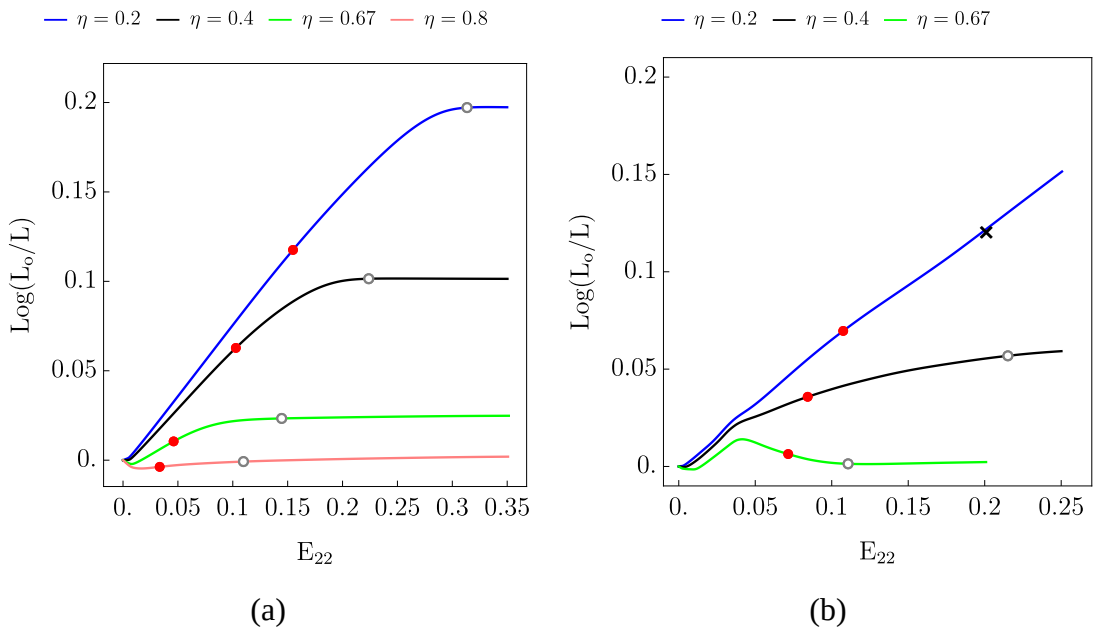

FIGURE 5.4 Evolution of normalized width of the unit cell expressed as $\log(\mathrm{L_o/L})$ versus E_{22} for (a) orientation A and (b) orientation B corresponding to initial volume fraction of 0.031. The peak stress is indicated by • where as onset of void coalescence is indicated by ∘ & ×.

hand, indicate that the cell width does not saturate but continues to decrease. These curves reveal a kink with a drastic reduction in slope around $E_{22} \approx 0.04$ (refer to Fig. 5.4b), corresponding to the phase when lattice reorientation occurs across a significant section of the cell due to tensile twinning saturation. To comprehend this behavior, it should be noted that for low stress ratios, especially for $\eta = 0.2$, void coalescence for orientation B happens through the formation of shear localization bands that connect voids across diagonally adjacent cells as it will be demonstrated in the upcoming section. When principal logarithmic strain $\log(\lambda_1^{\mathrm{p}})$ over the full length of the shear band surpasses a threshold value of 0.4, *shear localization* mode of coalescence have occurred. In Fig. 5.4b, the relevant stage is marked by × symbol on the curves for $\eta = 0.2$. The evolution plot for $\eta = 0.8$ is not presented here due to numerical convergence issues. The criteria for void coalescence, both for orientations A and B, are assumed following the work by Prasad et al. (2015).

In Fig. 5.5, the results of the cell width evolution are compared with the results of Prasad et al. (2015) for orientation A. It can be seen that there is a good agreement between both results. Nevertheless for orientation B, the results are slightly different due to the presence of twinning activity, and there are nuance differences in problem formulation and the reorientation scheme used (by comparing Fig. 8b of Prasad et al. (2015) with

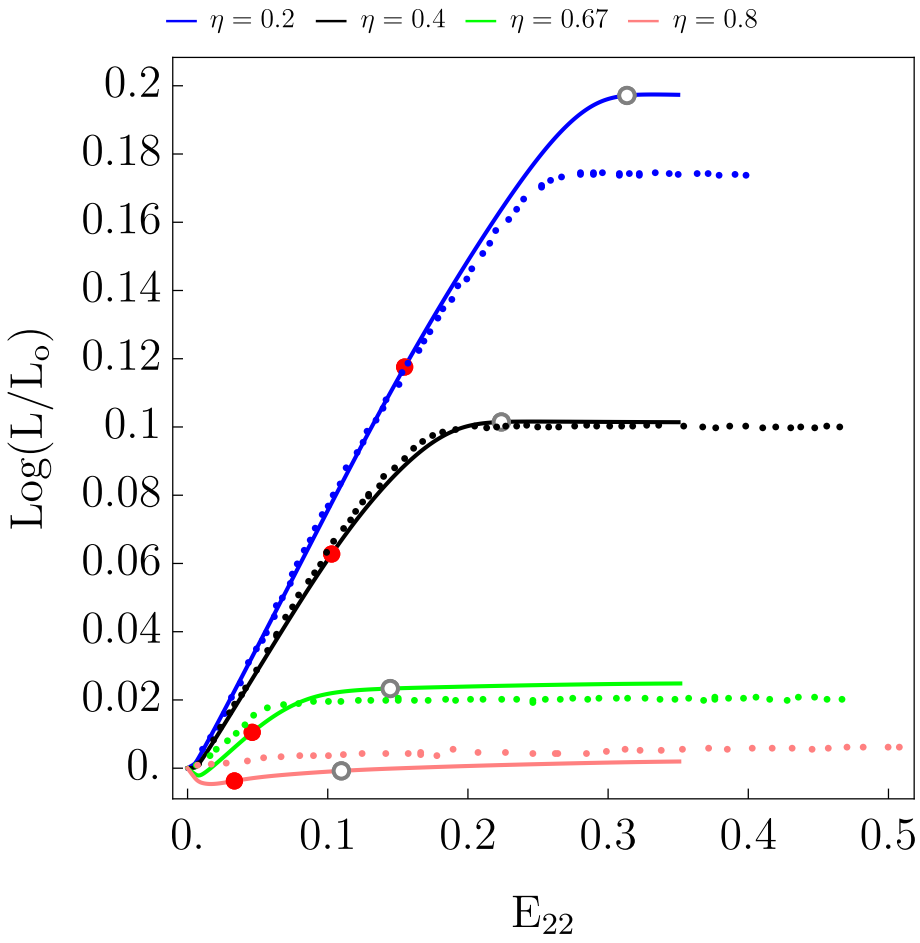

FIGURE 5.5 Comparison of the normalized width evolution of unit cell with the results of Prasad et al. (2015) for orientation A (Prismatic loading). Dotted lines represent the results of Prasad et al. (2015) whereas solid lines represent the results of crystal plasticity model used in the present work.

Fig. 5.4b).

5.1.4 Contour plots of accumulated slip for orientation A

Fig. 5.6(a, b) show the contour plots of accumulated slip (Γ^s) at the moment when the macroscopic stress reaches a maximum (i.e. a peak stress) for $\eta = 0.8$ and 0.67, respectively. For these figures, E_{22} is equal to 0.03 and 0.04, correspondingly. It should be noticed that, regardless of the level of strain E_{22}, the prismatic slip system contributes the most to plastic slip in orientation A, as indicated in the relative activity plot Fig. 5.2a. Plastic slip contours for both stress ratios are comparable, as can be seen in the contour Fig. 5.6(a, b) and considerable amounts of plastic slip accumulate around the void surface.

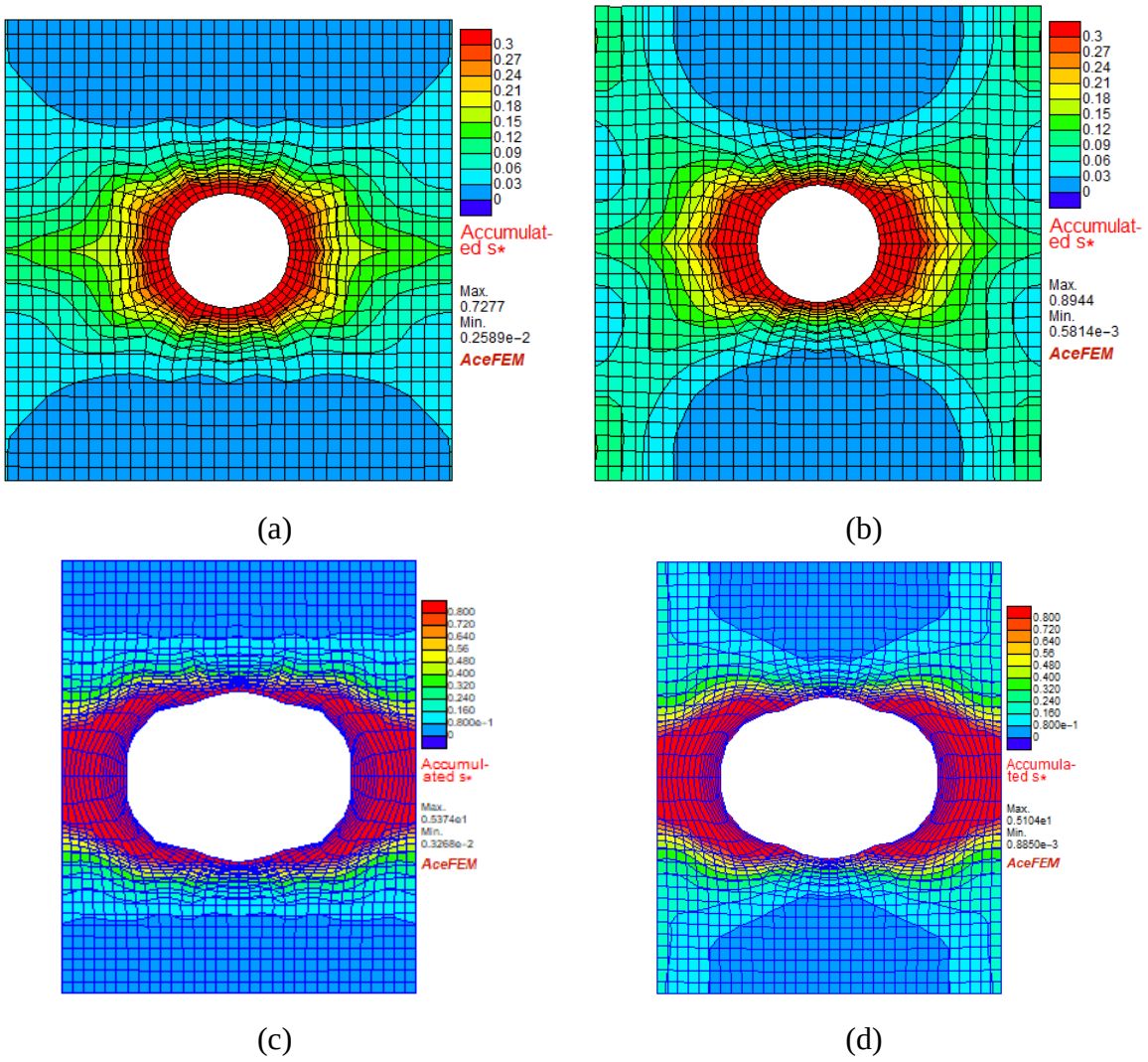

FIGURE 5.6 Contour plots of accumulated slip Γ^s, (as defined by Eq. (2.18)) for the orientation A (prismatic loading) and initial void volume fraction of 0.031 corresponding to (a) $\eta = 0.8$ at E_{22} = 0.03 (b) $\eta = 0.67$ at E_{22} = 0.04 (c) $\eta = 0.8$ at E_{22} = 0.2 (d) $\eta = 0.67$ at E_{22} = 0.2.

Also, plastic slip is beginning to accumulate in the transverse ligament normal to the major principal stress direction y. However, the void retains an almost circular shape in Fig. 5.6(a, b) and void coalescence is not seen, yet.

Fig. 5.6(c, d) illustrates the contours of accumulated slip at E_{22} = 0.2, again for η = 0.8 and 0.67, respectively. As for E_{22} = 0.03, plastic slip distributions for the two stress ratios are very similar. At the deformation stage depicted in these figures, a substantial amount of plastic slip has accumulated around the void surface as well as in the transverse ligament. Furthermore, the void has deformed into an oblate shape (i.e., it has elongated in the x direction). This is typical behavior as concerns the void growth in the presence

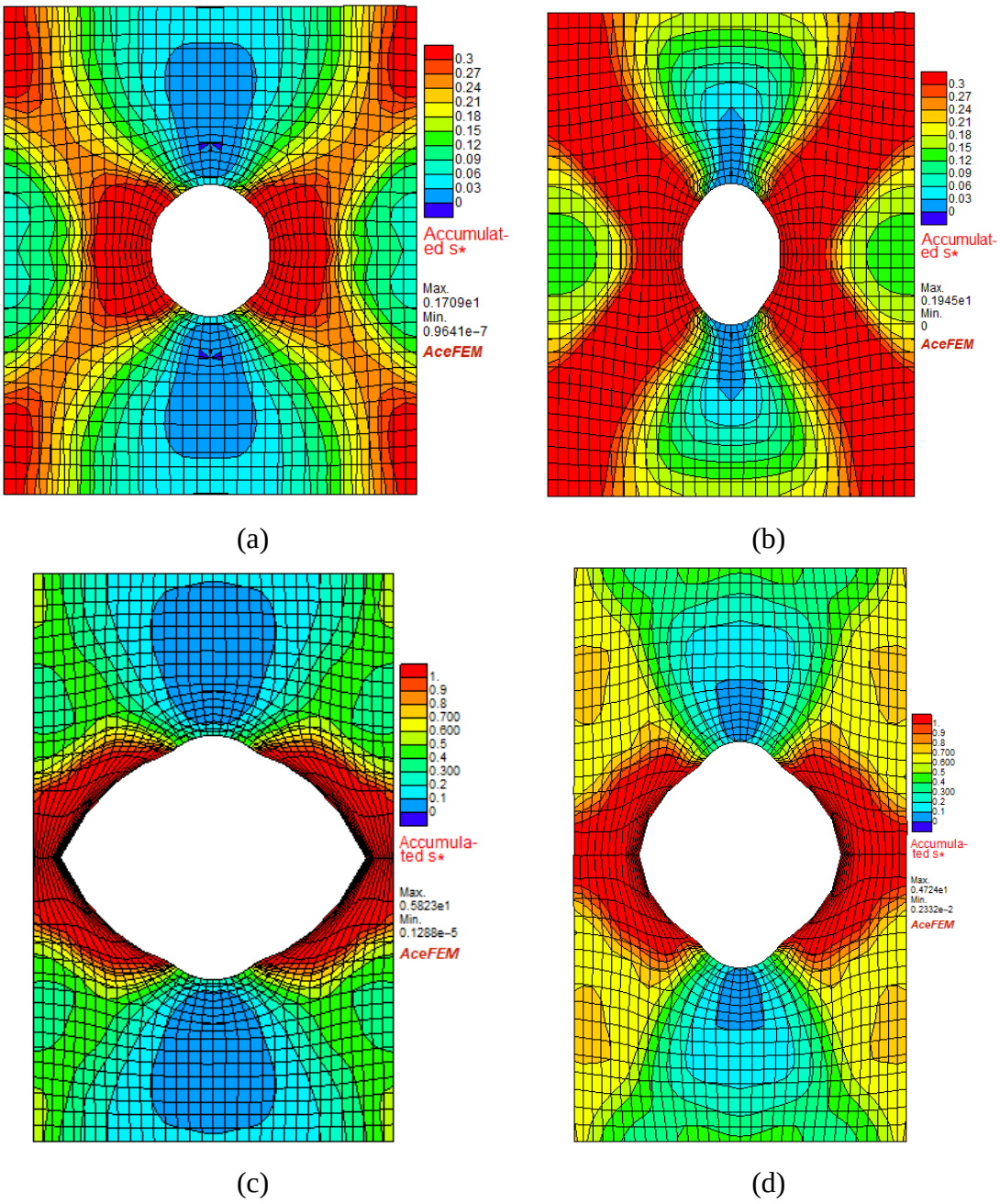

FIGURE 5.7 Contour plots of accumulated slip Γ^s, (as defined by Eq. (2.18)) for the orientation A (prismatic loading) and initial void volume fraction of 0.031 corresponding to (a) $\eta = 0.4$ at E_{22} = 0.10 (b) $\eta = 0.2$ at E_{22} = 0.15 (c) $\eta = 0.4$ at E_{22} = 0.35 (d) $\eta = 0.2$ at E_{22} = 0.35.

of high mean stress. Fig. 5.6(c, d) also reveals that the transverse ligament has shrunk significantly, indicating that the mechanism of coalescence is owing to this ligament's necking. According to Koplik and Needleman (1988), it causes a shift in overall unit cell deformation from biaxial to uniaxial straining along the y direction.

Fig. 5.7(a, b) illustrates the contour plots of accumulated plastic slip for orientation A corresponding to the low stress ratio η = 0.4 and 0.2 at the point of peak macroscopic stress. The values of E_{22} related to these figures are 0.1 and 0.15, respectively. A distinct pattern of plastic slip evolution can be seen when the stress ratio is low during the peak stress stage as compared to the one observed in Fig. 5.6(a, b) for higher stress ratios. Hence, in Fig. 5.7(a, b), high accumulated slip Γ^s can be observed just in the transverse side of the void surface, rather than all over the void surface as in Fig. 5.7(a, b). In addition, plastic slip has started to accumulate in the shape of two inclined bands at a 45° angle to the primary loading direction. The magnitude of accumulated slip Γ^s inside this domain is greater for η = 0.2 (Fig. 5.7b) than for η = 0.4 (Fig. 5.7a). Moreover, while the void preserves its circular shape at the peak stress stage for η = 0.4, it has become significantly prolate in the primary loading direction for η = 0.2.

At E_{22} = 0.35, Fig. 5.7(c, d) depicts the space distribution of accumulated slip Γ^s for η = 0.4 and η = 0.2, respectively. When comparing these results to Fig. 5.7(a, b), it can be seen that the plastic slip concentrates in the transverse ligament at greater E_{22} = 0.35. Although there is an inclination to develop an inclined strain localization band at lower E_{22} for the low stress ratio case, plastic slip accumulation in the transverse ligament predominates at later stages of loading process, leading to necking and void coalescence.

5.1.5 Contour plots of accumulated slip and tensile twin volume fraction for orientation B

The space distribution of accumulated plastic slip (Γ^s) for orientation B, under high stress biaxiality values of $\eta = 0.8$ and $\eta = 0.67$ are shown in Fig. 5.8(a, b), respectively. The contours are presented at the same $E_{22} = 0.05$, which is before the cell reaches peak macroscopic stress. This is also the moment when twinning activity is strongly decaying and twin volume fraction is close to the saturation (see Fig. 5.2b). Fig. 5.8(c, d) show the contours of accumulated twin volume fraction at the same stage under stress biaxiality values of $\eta = 0.8$ and $\eta = 0.67$, respectively. The magnitude of accumulated slip is higher for η = 0.8 when compared to stress ratio of 0.67. The prevalent contribution to accumulated slip arises from basal slip system which gets triggered at initial stage of deformation due to its low critical resolve shear stress (refer to Tab. 5.3) prior to tensile twinning. Fig. 5.8(c, d) demonstrates that the large twin volume fraction is accumulated in the outer transverse ligaments and in the middle part of the cell there is no accumulation of twin. In fact, the value of accumulated twin inside the regions encompassed by the red color contour is above 0.9, implying that lattice reorientation (in accordance with Eq. (2.3),

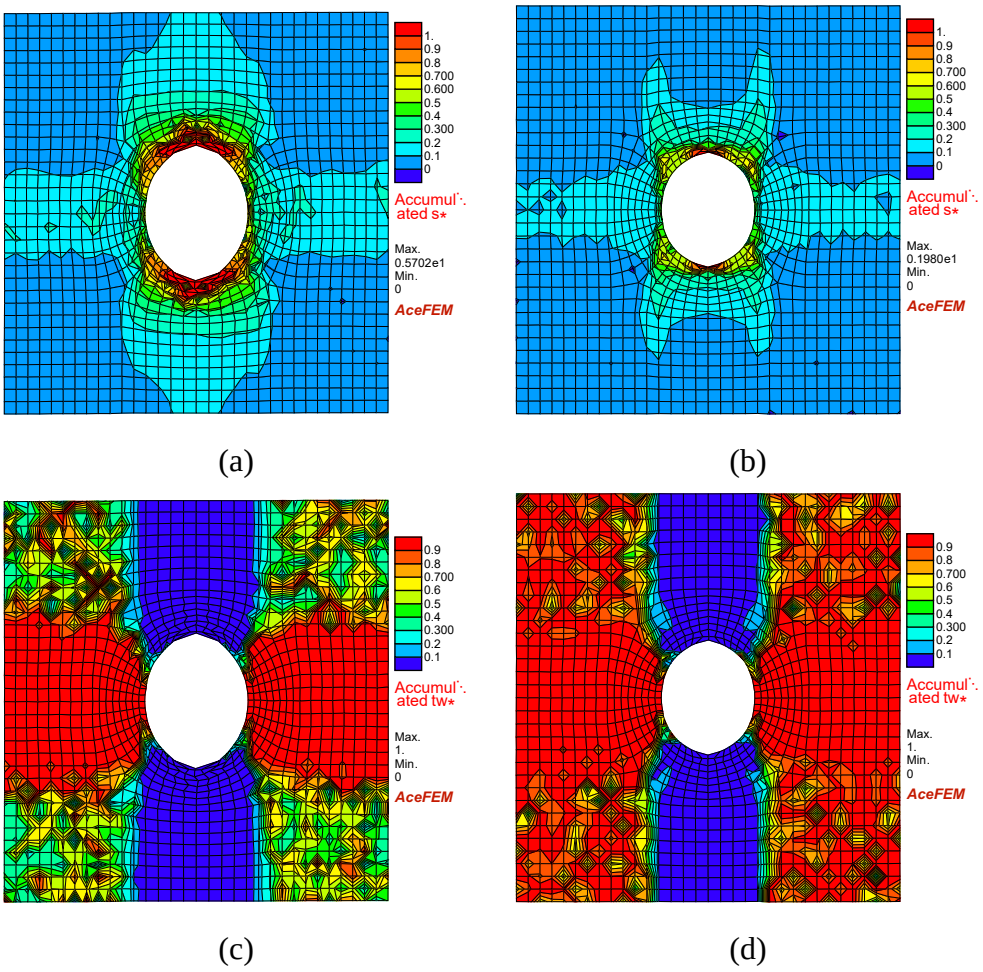

FIGURE 5.8 Contour plots of (a) accumulated slip for $\eta = 0.8$ (b) accumulated slip for $\eta = 0.67$ (c) accumulated twin for $\eta = 0.8$ (d) accumulated twin for $\eta = 0.67$ corresponding to the orientation B (c-axis loading) and initial void volume fraction of 0.031 at E_{22} = 0.05.

c axis rotates in the plane by about $86°$) has occurred as a result of tensile twinning. This observation is in accordance with literature studies concerning Mg alloys which shows that twinning once activated can quickly occupy entire grain (Frydrych et al., 2020). Thus the reorientation of the lattice causes the harder pyramidal and prismatic slip systems to be active which results in textural hardening, as observed in Fig. 5.2b. This hardening effect is associated with higher stress vital to initiate slip in the twinned region. As observed for orientation A at high stress ratio η equal to 0.8, 0.67, the same mode of void coalescence via the transverse ligament will occur for orientation B too, despite the tensile twinning is activated. Please note that the calculations were stopped before reaching the strain level $E_{22} = 0.35$ due to convergence issues associated with high local deformation, particularly for $\eta = 0.8$.

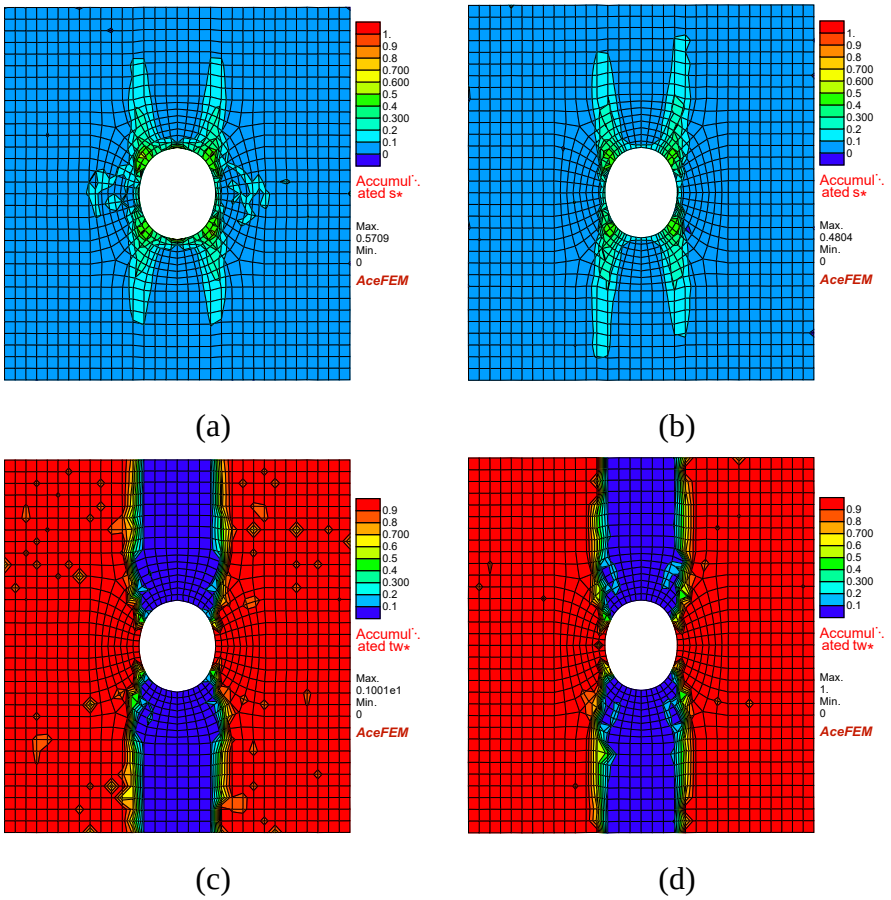

FIGURE 5.9 Contour plots of (a) accumulated shear for $\eta = 0.4$ (b) accumulated shear for $\eta = 0.2$ (c) accumulated twin f^{TW} (as defined by Eq. (2.4)) for $\eta = 0.4$ (d) accumulated twin for $\eta = 0.2$ corresponding to the orientation B (c-axis loading) and initial void volume fraction of 0.031 at E_{22} = 0.05.

Space distribution of accumulated slip Γ^s and accumulated twin volume fraction Γ^t at E_{22} = 0.05 for orientation B corresponding to lower in-plane stress ratio values of η equal to 0.4 and 0.2 are depicted in Fig. 5.9. The accumulated Γ^s, which is predominantly result of basal slip activity, as indicated in the relative activity plot (Fig. 5.2b) during initial deformation, extend out vertically in the form of bands in a slender central zone, starting from the void surface, as shown in Fig. 5.9(a, b). While comparing Fig. 5.8(a, b) with Fig. 5.9(a, b), the horizontal lobe in the plastic slip distribution around the void vanishes, and the magnitude of Γ^s reduces as η decreases. Intensive twin activity is concentrated along the whole right and left parts of the cell for η = 0.4 and 0.2 which is seen from the contours of accumulated twin volume fraction shown in Fig. 5.9(c, d). Also in Fig. 5.9(c, d), the magnitude of the accumulated twin volume fraction exceeds 0.9 over the entire right and left parts of the cell, whereas for the higher stress ratio, the twin gets

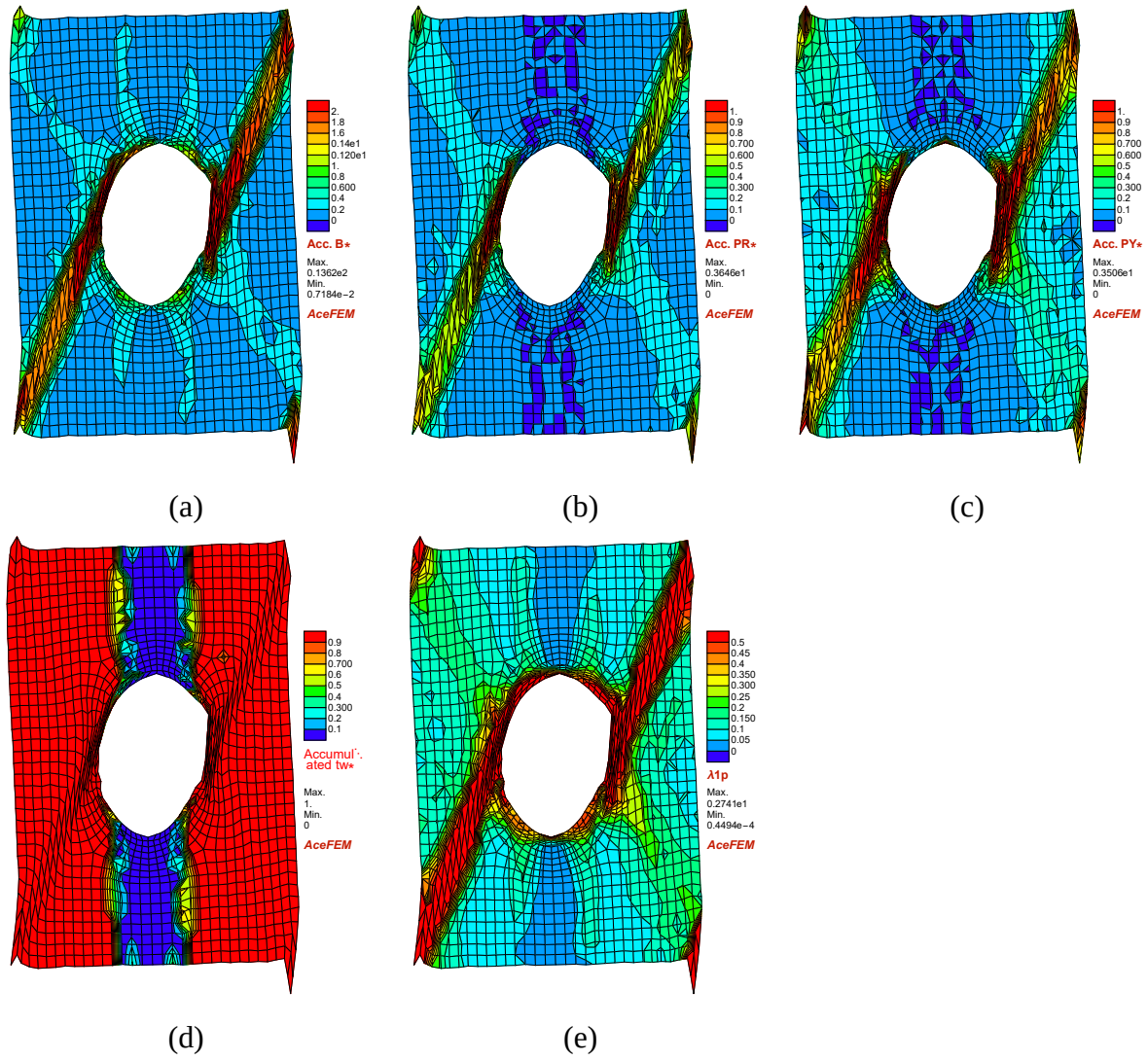

FIGURE 5.10 Contour plots of (a) accumulated basal slip (b) accumulated prismatic slip (c) accumulated pyramidal slip (d) accumulated twin (e) principal logarithmic strain corresponding to the orientation B (c-axis loading) and initial void volume fraction of 0.031 with $\eta = 0.2$ at E_{22} = 0.2.

accumulated more in the area close to the void.

In Fig. 5.10, contour plots of accumulated plastic slip subdivided into the net values for three families: basal, pyramidal and prismatic slip and accumulated twin volume fraction are presented for orientation B under η = 0.2 at E_{22} = 0.2 across the entire unit cell. At E_{22} = 0.2, significant activity of basal plastic slip is observed which accumulates around the void boundary and, to some extent, in two inclined bands connecting the voids as shown in Fig. 5.10a. From the contours in Fig. 5.10(b, c), it can be seen that the slip accumulates from the transverse side of the void to the corner of the unit cell. Additionally,

the void is slightly rotated in the primary loading direction and deformed into a prolate shape. Alternating bands of twinned and untwinned regions are depicted in Fig. 5.10d. In these twinned reorientation regions of the cell, the activity of pyramidal and prismatic slip systems has been triggered. It should be stressed that asymmetric deformation of the unit cell is observed in Fig. 5.10, in spite of the symmetry of unit cell geometry, crystal orientation and loading conditions. This is possible because of the probabilistic character of twin reorientation scheme, which breaks the symmetry of the problem. It should be underlined that such probabilistic nature of twinning behavior is closer to the physical reality.

In Fig. 5.10e, the combined influence of slip and twins on plastic deformation in the cell is illustrated by $\log(\lambda_1^{\mathrm{p}})$ (principal logarithmic strain) contours. This figure reveals the formation of two distinct inclined shear localization bands. Due to shear deformation, some cell boundaries appear distorted. As η decreases, a shift in the coalescence pattern is observed for orientation B, transitioning from internal necking of the transverse ligaments to shear localization along inclined bands that join voids diagonally across the cells. These findings suggest that at low stress ratios, plastic anisotropy and microstructure evolution induced by tensile twinning in Mg initiates this alternative failure mechanism.

5.1.6 Summary for 2D plane strain unit cell

The following are the key findings of this study:

1) For orientation A plastic deformation in the cell occurs due to dislocation slip, with the prismatic slip system playing a significant role. The behavior of the unit cell for prismatic loading is thus similar to the one seen in Chapter 4 for FCC crystals with symmetric crystal orientations. However for orientation B, during the early phases of loading, the basal slip mechanism is active along with tensile twinning in the transverse ligament. The hard deformation modes (i.e. with high critical resolved shear stress) of pyramidal and prismatic slip are triggered in the twinned area once a significant amount of the cell surrounding the transverse ligament undergoes reorientation.

2) For both orientations, void growth declines when η is reduced. However, the early phase of void formation is greatly hindered in orientation B due to twinning activity. Next, due to the activity of multiple slip systems after reorientation and resulting textural hardening of the crystal matrix, the void growth rate is increased.

3) Regardless of η, void coalescence occurs in orientation A by necking of the internal

ligament normal to the principal stress direction. This is accompanied by a change to a uniaxial straining mode along the primary principal loading direction. For orientation B at lower η, the mode of failure is by shear localization along with an inclined band that connects neighboring voids diagonally with respect to loading direction. This is because of the strong plastic anisotropy induced by tensile twinning. For higher η, the mode of coalescence is by necking of the transverse ligament normal to the principal loading direction, same as for orientation A.

4) For orientation A, the results are in good agreement with the work of Prasad et al. (2015). For orientation B due to the different problem formulation and reorientation scheme, there is slight differences in the results. Nevertheless the final observations are qualitatively the same.

5.2 Numerical analyses of a 3D unit cell with spherical void

For the analysis, a 3D unit cell with one spherical void is employed (refer to the schematic in Fig. 3.2 and the mesh in Fig. 3.4). An initial void volume fraction of $f_v = 1\%$ is considered in the calculations. Similar to the 2D case, the same deformation modes are considered (refer to Section 5.1). The same material and hardening parameters as used in the 2D case are employed in the calculations (refer to Tab. 5.2 and Tab. 5.3). Concerning loading, uniaxial tension is imposed based on the stress-controlled boundary conditions detailed in Subsection 3.2.6 and Eq. (3.17). As explained in Subsection 3.2.6, the crystal orientation is fixed, and the loading direction is varied to study the anisotropic response of the porous unit cell. The prismatic axis of a HCP crystal is directed in the y direction, whereas the c-axis is orientated in the z direction. The current study considers five uniaxial loading scenarios in the yz plane which is in the form:

$$\boldsymbol{\Sigma} = \Sigma \mathbf{n} \otimes \mathbf{n},$$

where $\mathbf{n}$ is the direction of loading and, in general, it has following components in sample frame: $[\cos[u]\sin[v],\ \sin[u]\sin[v],\ \cos[v]]$. In the present study angle u is considered as $\pi/2$ and angle v varies from 0° to 90°. 0° case corresponds to prismatic loading and 90° case corresponds to c-axis loading. Other loading scenarios include $30^\circ, 45^\circ$, and 60° cases. From now on, loading is addressed in terms of angles. The results for 0° and 90° loading are qualitatively compared to those of Selvarajou et al. (2019). Please note that the results presented here differ from those of Selvarajou et al. (2019) due to differences in the constitutive model, slip and twin systems considered (compression twinning and

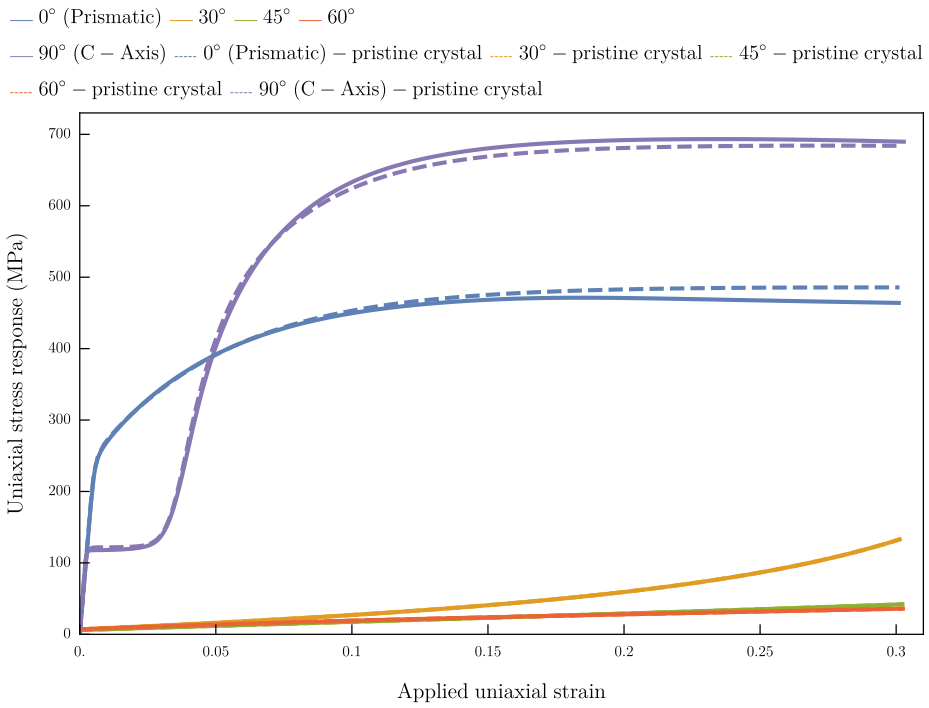

FIGURE 5.11 Uniaxial stress strain response for the porous single crystal with the void volume fraction of 1% for different orientation of loading direction with respect to crystal axes. Thick line represents response for porous crystal and dashed line represents response for pristine single crystal.

pyramidal $\langle a \rangle$ are not considered in the present study), reorientation scheme, material parameters, and applied strain level, so the quantitative comparison is not possible.

5.2.1 Stress vs strain response

First of all, the results of the uniaxial stress and strain response along the applied loading direction are reviewed. Fig. 5.11 illustrates the uniaxial stress and strain response of pristine (void-free) and porous crystals. The findings for anisotropic matrices reported here are qualitatively different from those for isotropic matrices. As observed, the responses vary depending on the loading direction. Loading at 90° exhibits a harder response, while loading at 45° and 60° produces a softer response. These findings must be interpreted in conjunction with slip system activity. The porous crystal exhibits a slightly harder response to 90° loading than its pristine equivalent. In 0° loading, the pristine crystal exhibits a slightly harder response than the porous material, particularly at higher applied strains. Due to small void volume fraction at lower strains, the difference is negligible for both loading conditions. When these results are compared to those of Selvarajou et al. (2019),

comparable responses are observed, but the difference between the responses of porous and pristine crystals is more substantial in Selvarajou et al. (2019), especially for c-axis loading. Also in that paper, the activation of tougher pyramidal slip causes the porous crystal to harden more than the pristine crystal at high strains over 0.7. In the case of present results this happens due to the reorientation of the twins and the void's induction of a local triaxial stress state for 90° loading, tougher slip systems are triggered, leading to a harder stress-strain response. Additionally, both pristine and porous crystals respond in similar ways to loading at 30°, 45°, and 60°. For 30° loading, slight hardening is observed above 0.25 strains. For 45° and 60° loading, the response is almost linear, and compared to all loading cases, they exhibit a softer response. This happens due to activation of easy basal slip for these cases.

5.2.2 Normalized void volume fraction plots

In Fig. 5.12, the porosity evolution for various loading scenarios under applied strain is presented. A substantial anisotropic response as concerns void evolution is observed, similarly to the stress-strain response. A comparable response in anisotropic crystals was reported by Prasad et al. (2015); Selvarajou et al. (2019). Under 0° loading, the void grows monotonically, whereas under 90° loading, non-monotonic void volume evolution is observed. After the initial increase the void volume decreases, and then around the strain level of 0.05 it starts to steadily increasing. The strain level of 0.05 marks the end of the regime of strong twinning activity after which the accumulated twin volume fraction reaches the saturation value. So, the regime of decreasing void volume fraction coincides with the regime of intensive reorientation due to twinning. For loading cases of 30°, 45°, and 60° under which crystal response is very soft (see Fig. 5.11), void evolution is essentially non-existent and asymptotically ceases. Similarly, a minimal void volume fraction evolution was also seen in porous isotropic materials subjected to uniaxial loading (Pardoen and Hutchinson, 2000). When compared to the results of Selvarajou et al. (2019), a similar response to prismatic loading was noted, but the response to c-axis loading differed considerably, and minimal reporting was provided in their work as void collapse was observed.

5.2.3 Relative activity plots

The aforementioned stress and void evolution responses are well characterized by respective activity of deformation mechanisms. Under 0° loading, prismatic slip is the dominant mechanism in both pristine and porous crystals, as shown in Fig. 5.13. During

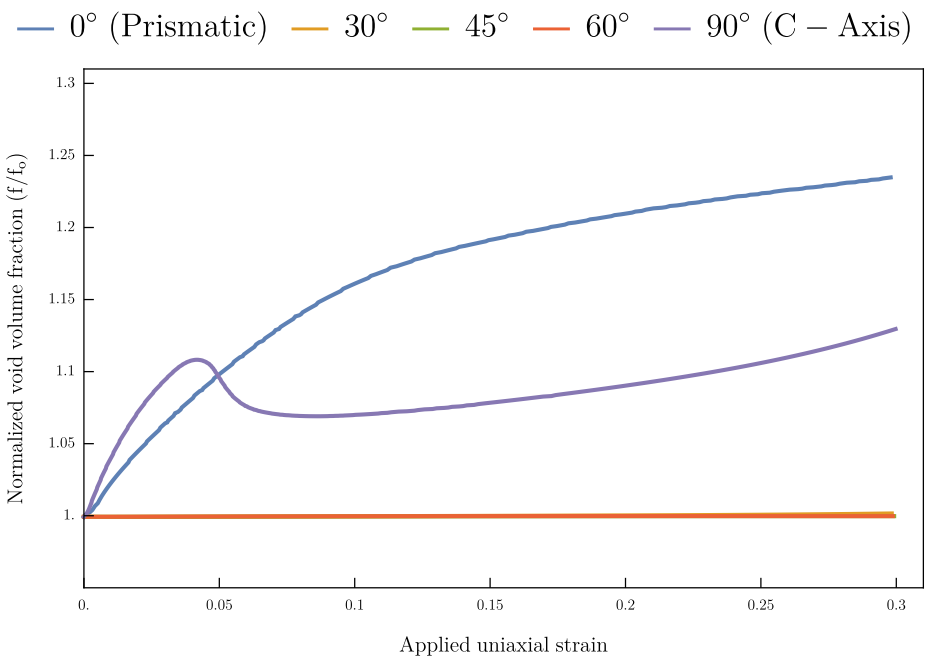

FIGURE 5.12 Evolution of normalized void volume fraction with the applied uniaxial strain corresponding to initial void volume fraction of 1%.

the early stage of $90°$ loading, twinning is activated, followed by harder prismatic and pyramidal slip systems after reorientation, resulting in a harder stress-strain response. Additionally, void-induced hardening is observed in the porous crystal under $90°$ loading. When these results are compared to those of Selvarajou et al. (2019), a similar response is noted. However, Selvarajou et al. (2019) included the additional pyramidal $\langle a \rangle$ slip mechanism, which accounts for the differences in responses between porous and pristine crystals. In Selvarajou et al. (2019), under prismatic loading, the porous crystal exhibits a harder response than the pristine crystal, particularly at higher strains due to the activity of hard pyramidal $\langle a \rangle$ slip, which is not considered in the present study. Consequently, only prismatic slip carries the deformation in the current analysis. Moreover in their work, extension twinning is activated under prismatic loading even though it is not highly favorable. In contrast, in the current simulations, the activity of twinning is not significant under $0°$ loading, as shown in Fig. 5.13. It should also be noted that the material parameters and the reorientation scheme considered in this study differ from those reported in Selvarajou et al. (2019). For the $30°$, $45°$, and $60°$ loading cases, the easy basal slip system is triggered, while the other harder slip systems remain inactive. This is evident from the geometrical nature of the slip systems. For loading directions between inclined to both prismatic direction and c-axis, basal slip serves as the easiest way for

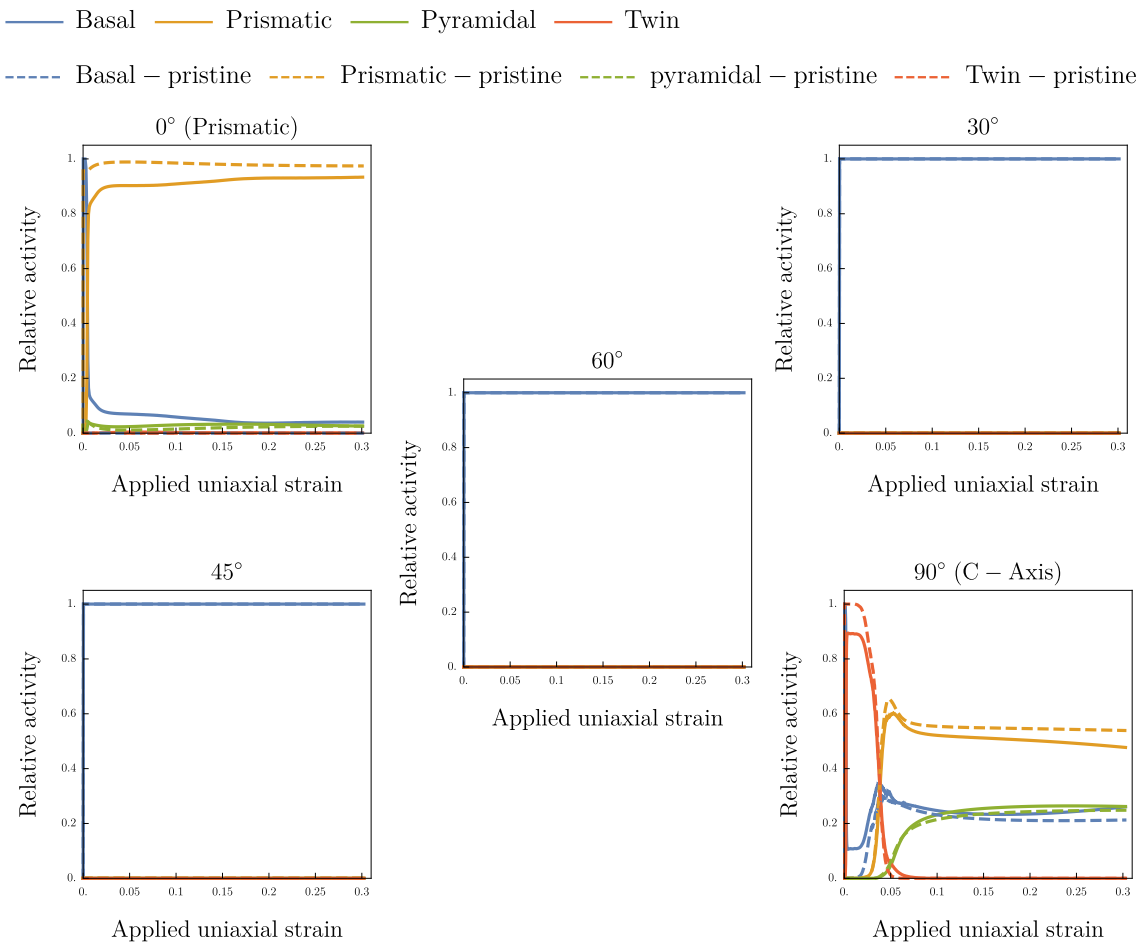

FIGURE 5.13 Relative activity plots, $\bar{\xi}$, of deformation mechanisms. Thick line represents response for porous crystal and dashed line represents response for pristine single crystal.

slip accumulation. Under these loading scenarios, void growth is almost negligible, and a much softer stress-strain response is observed.

5.2.4 Local response of a 3D unit cell

Figs. 5.15–5.21 illustrate the contours depicting key slip activities for five loading scenarios. Figs. 5.15, 5.19, 5.20, and 5.21 display three orthogonal midplane sections of the deformed cubic unit cell. These figures, specifically 5.15, 5.16a, 5.17a, and 5.19, are subdivided into four quadrants illustrating total accumulated slip (top left), basal slip (top right), prismatic slip (bottom left), and pyramidal slip (bottom right), respectively. It is important to observe that these distributions exhibit symmetry about the three planes, although symmetry may not be perfect in cases involving twinning due to the random

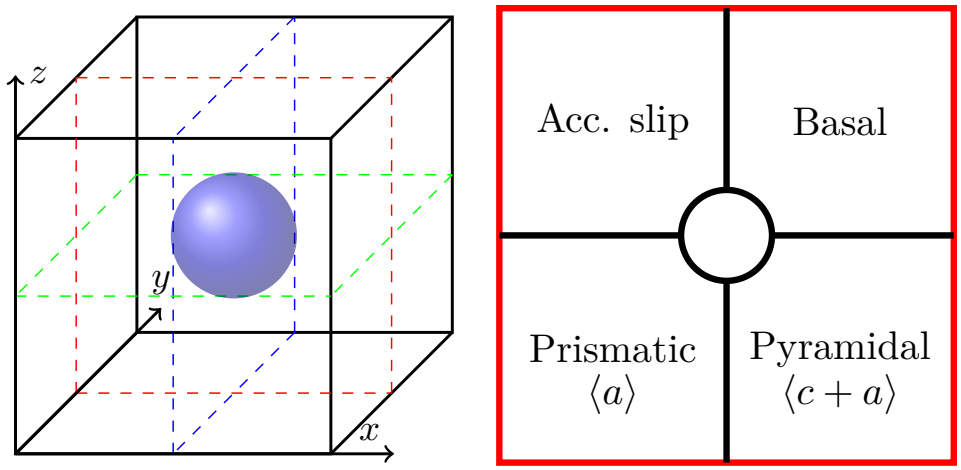

FIGURE 5.14 (a) Schematic representation of cross-sectional views of the unit cell cut along its midplanes in the deformed configuration (b) Divided compartments in the xz plane, illustrating deformation mechanisms with labeled regions corresponding to slip activities: "Acc. Slip", "Basal", "Prismatic", and "Pyramidal".

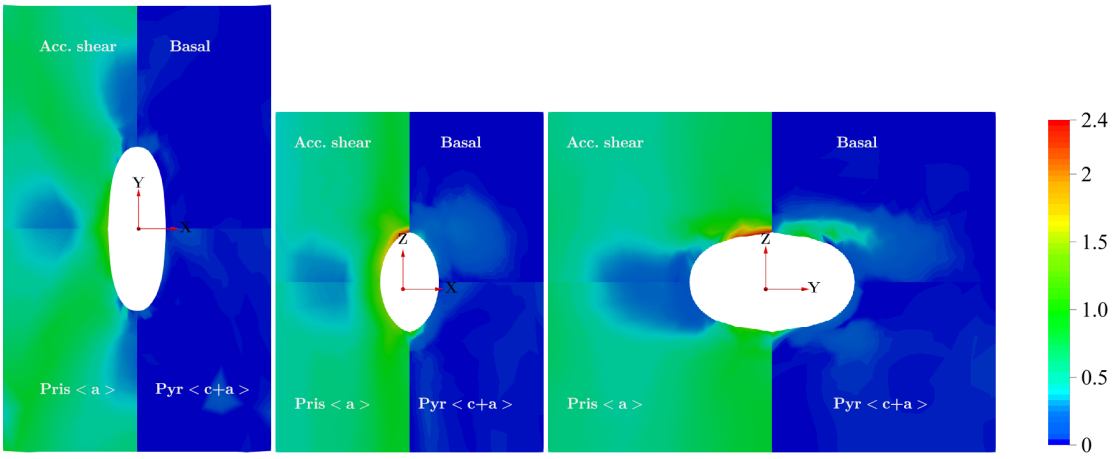

FIGURE 5.15 Contour plots of total accumulated slip, basal, prismatic and pyramidal slip in the midplanes divided into four compartments under uniaxial loading along prismatic direction ($0°$) in yz plane at the strain level of 0.3. Three figures represent the corresponding accumulated slips in the three midplanes of the deformed porous cubic unit cell.

nature of twin reorientation. For the loading scenarios at $30°$, $45°$, and $60°$ only one midplane yz is selected. The other two figures represent views along the y-y and z-z directions as marked in the left figure. Additionally, please note that the contour plots depict the final state of deformation. It is seen that for these three loading scenario the void deforms together with the surrounding material changing its shape to ellipsoidal with

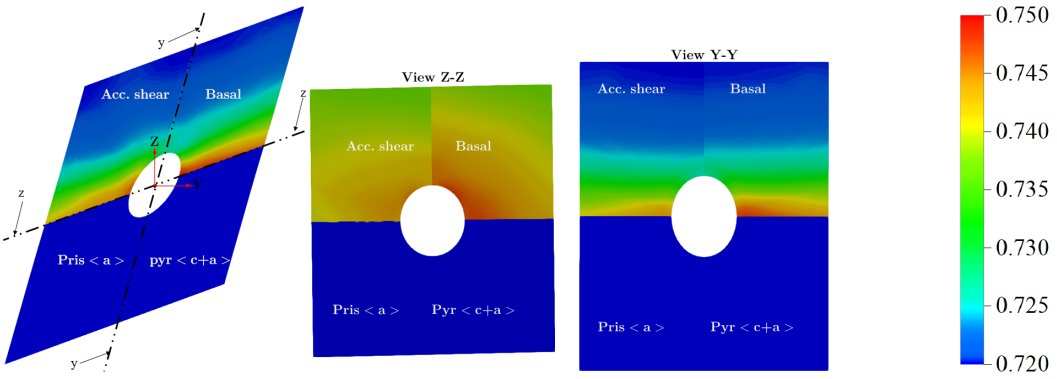

FIGURE 5.16 Contour plots of accumulated slip, basal, prismatic and pyramidal divided into four compartments under uniaxial loading along the direction inclined at an angle of 30° to the y axis in yz plane at the strain level of 0.3. First figure represent the midplane with x-axis unit normal.

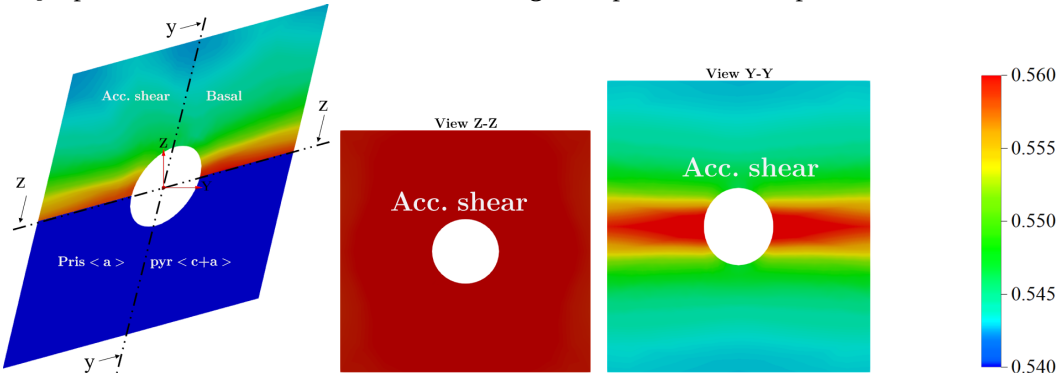

FIGURE 5.17 Contour plots of accumulated slip, basal, prismatic and pyramidal divided into four compartments under uniaxial loading along the direction inclined at an angle of 45° to the y axis in yz plane at the strain level of 0.3. First figure represent the midplane with x-axis unit normal.

almost no volume change.

Fig. 5.15 illustrates the contour plots of slip activities under 0° loading (along prismatic direction). The dominant slip activity observed across all three planes is prismatic slip, showing a highly uniform distribution. This trend is also reflected in the relative activity plots (see Fig. 5.13). Besides prismatic slip, there is minor activity of harder pyramidal and basal slips in the yz plane near the void vicinity. Similar responses have been reported in studies by Selvarajou et al. (2019). However, in the work of Selvarajou et al. (2019), extension twinning occurs at higher strain levels, resulting in reorientation around the void tip. In the current study under prismatic loading, no twinning activity is observed. Under 0° loading, void volume growth is notably pronounced, resulting in an ellipsoidal void shape.

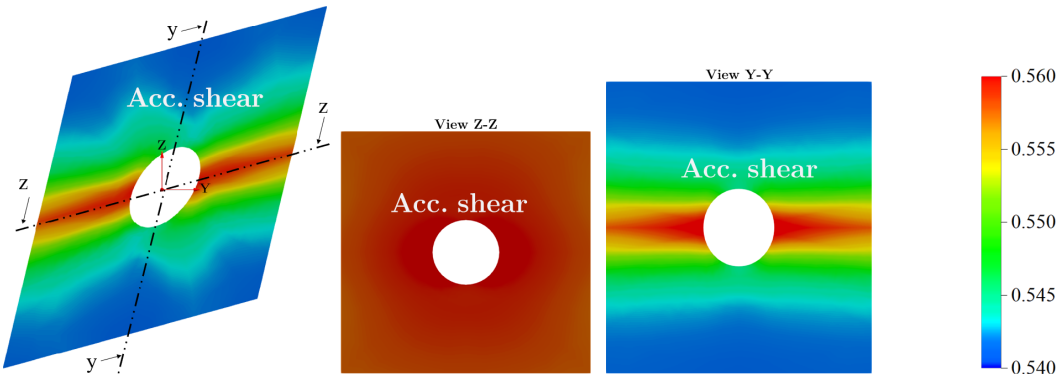

FIGURE 5.18 Contour plots of accumulated slip under uniaxial loading along the direction inclined at an angle of 60° to the y axis in yz plane at the strain level of 0.3. First figure represent the midplane with x-axis unit normal.

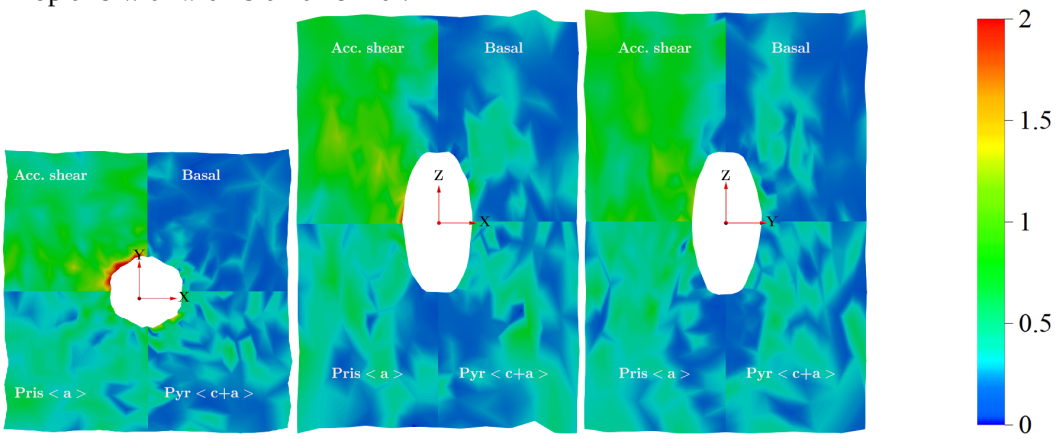

FIGURE 5.19 Contour plots of accumulated slip, basal, prismatic and pyramidal divided into four compartments under uniaxial loading along the c-axis direction(z axis) in yz plane at the strain level of 0.3. Three figures represent the corresponding accumulated slips in the midplanes of the deformed porous cubic unit cell.

The contour plot of key slip activities under 30° stress is shown in Fig. 5.16. The major slip mechanism is obviously evident to be an easy basal slip, and all other slip systems are dormant. The unit cell is sheared in the yz plane, and the void is elongated in the loading direction. An accumulated slip is uniformly distributed over the entire plane in the z-z view. Similarly, in view y-y, shear accumulates in the transverse direction close to the void. As previously stated, void growth is insignificant in this loading case.

Figs. 5.17 and 5.18 show contour plots of accumulated slip under 45° and 60° loading, respectively. Again, the same response as with 30° loading is observed, with the unit cell sheared in the yz plane. The dominant basal slip activity contributes to the accumulated

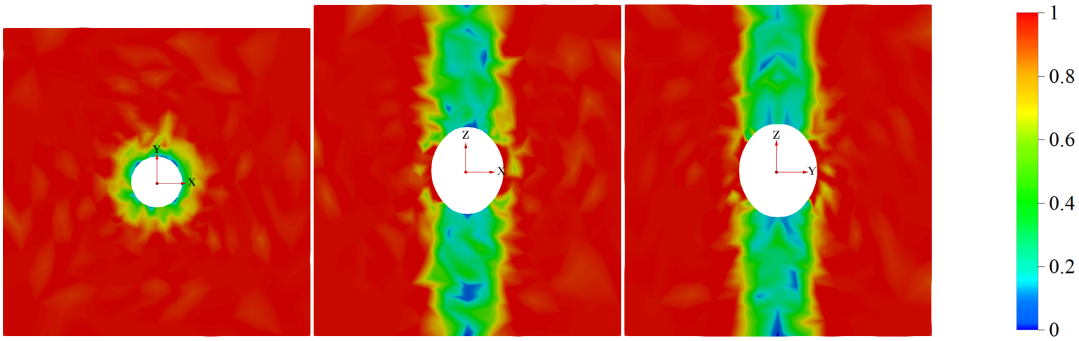

FIGURE 5.20 Contour plots of accumulated twin under uniaxial loading along the c-axis direction (z axis) in yz plane at the strain level of 0.05. Three figures represent the corresponding accumulated twin in the midplanes of the deformed porous cubic unit cell.

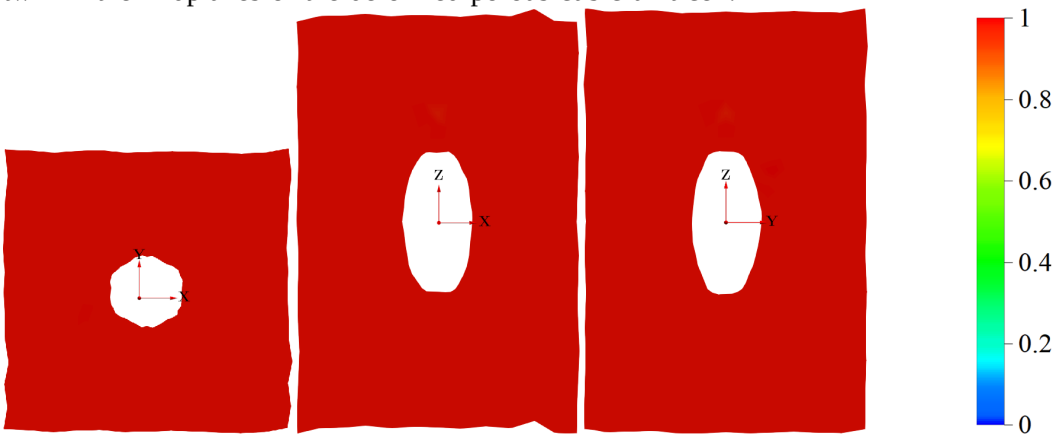

FIGURE 5.21 Contour plots of accumulated twin under uniaxial loading along the c-axis direction (z axis) in yz plane at the strain level of 0.3. Three figures represent the corresponding accumulated twin in the midplanes of the deformed porous cubic unit cell.

slip. The entire plane is uniformly distributed with accumulated slip (acc. basal) in the z-z view. Similarly, slip accumulates in the transverse direction of the void in y-y view; the similar response is observed under 30° loading.

The distribution of various slip activities under 90° loading is depicted in Fig. 5.19 showing an important activity of twinning. Due to the probabilistic twin orientation scheme, reorientation is random, and symmetry may not be observed. Initially, basal slip is triggered, followed by twinning, which causes reorientation. The activation of the tougher pyramidal and prismatic slip systems in reoriented parts of the cell results in continued accumulation of slip in these areas, leading to substantial reorientation-induced hardening. As previously noted, void growth is initially reduced during reorientation caused by twinning. Subsequently, void growth accelerates due to the activity of tougher

slip systems. This behavior contradicts the findings of Selvarajou et al. (2019) for c-axis loading. The enhanced contraction and pinching at the poles caused by twinning in c-axis loading, which resulted in the formation of a star-like shape in the transverse plane as reported by Selvarajou et al. (2019), are not observed in the current findings. Instead, a quasi-hexagonal void shape is seen in the transverse xy plane (refer to Fig. 5.19). It should be noted that the constant reorientation scheme was used by Selvarajou et al. (2019), where reorientation occurs only when the twin volume fraction exceeds 0.9 which results in perfectly symmetric deformation of the cell.

Figs. 5.20 and 5.21 display contour plots depicting the accumulation of twins at two different strain levels: 0.05 and 0.3, respectively. At the strain level of 0.05, twin accumulation is predominantly observed along the outer surfaces, forming a fiber-like pattern centrally. This distribution is evident in the xz and yz planes, while across the xy plane, accumulation occurs uniformly except in the vicinity of the void. Fig. 5.21 illustrates widespread twin accumulation across all midplanes throughout the entire region. In the xz and yz planes, the void appears rectangular hexagonal with rounded corners.

5.3 Conclusions

The evolution of spherical voids in HCP unit cell is investigated under five uniaxial loading scenarios. The following conclusions can be drawn from the presented analysis:

1) A strong anisotropy in the mechanical response of the 3D unit cell is observed, depending on the loading direction, as different deformation modes are activated. Under 90° loading, the stress response is harder due to twin reorientation and the activation of tougher prismatic and pyramidal slip systems in the reoriented areas. In contrast, under 30°, 45°, and 60° loading, the stress response is much softer, with easy basal slip as the dominant mechanism. For 0° loading, prismatic slip is the primary deformation mechanism.

2) Similarly, void growth is substantially influenced by the loading direction. Under 0° loading, the void volume increases monotonically, while no growth of the void volume is observed under 30°, 45°, and 60° loading. For 90° loading, the activity of twinning leads to non-monotonic void growth. Initially, twin reorientation reduces the void volume, but as tougher slip systems are activated by the evolving local stress conditions around the void, the void volume gradually increases.

3) The twin gets accumulated in all midplanes at a strain level of 0.3 under 90° loading.

At the strain level of 0.05, a fiber-like pattern is observed, especially in the xz and yz planes.

4) Differences are observed when comparing the results, particularly for 0° and 90° loading, with the recent work by Selvarajou et al. (2019), especially under c-axis loading most probably as a result of distinct set of potentially active mechanisms (i.e. pyramidal $\langle a \rangle$) and non-probabilistic twin reorientation procedure in the latter paper.

CHAPTER 6

Theoretical formulation of a micromechanical mean-field model of polycrystals with voids

So far, the mechanics of FCC and HCP voided single crystals deformed by slip and twinning under various loading conditions have been studied using CPFEM with the unit cell methodology. In this chapter, contrary to the calculations performed in previous chapters, the theoretical formulation of a micromechanical mean field model for porous elasto-viscoplastic polycrystals in the small strain regime is presented. A two-step homogenization procedure is proposed to determine the overall response of the porous polycrystal. In the first step of homogenization, the overall response of the porous single crystal is found using the additive Mori-Tanaka scheme. In the second step, the overall response of the porous polycrystal is predicted using the elasto-viscoplastic self consistent (EVPSC) scheme (Girard et al., 2021), which relies on the additive interaction law. Consequently, the Mori-Tanaka formulation is discussed in the first part, and the EVPSC scheme is presented in the second part.

6.1 Micromechanical mean-field formulation of porous polycrystals

The proposed two-step homogenization procedure for porous polycrystals is illustrated in Fig. 6.1. In the first step, shown in Fig. 6.2, the overall elasto-viscoplastic response of the representative porous single crystal (RPSC) is obtained using the additive Mori-Tanaka scheme. In the subsequent step, to predict the overall response for the representative volume element consisting of homogenized porous single crystals (RVE-HPSCs), the

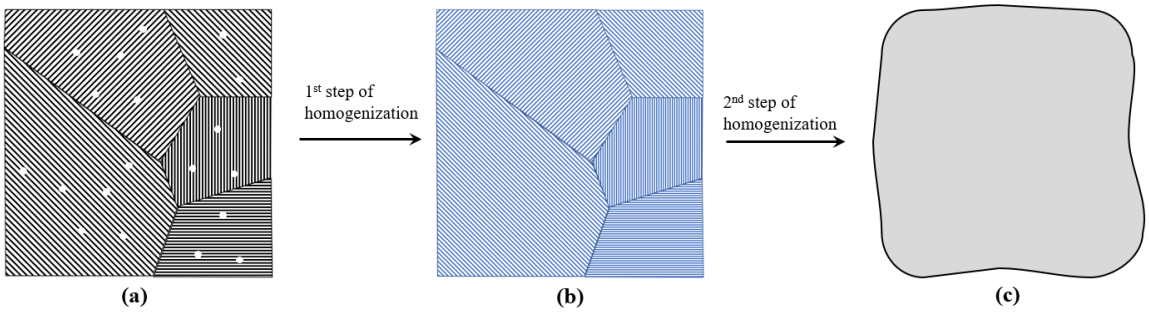

FIGURE 6.1 Schematic representation of the two-step homogenization procedure for porous polycrystal: (a) representative porous polycrystal (RPP), (b) RVE of polycrystal composed of homogenized porous single crystals (RVE-HPSC), (c) homogenized porous polycrystal (HPPC).

EVPSC scheme is applied (see Fig. 6.3). It is assumed that the RVE considered in the homogenization procedure is statistically homogeneous and it obeys ergodic hypothesis.

6.1.1 Additive Mori-Tanaka model of voided elasto-viscoplastic crystal

In this section, the framework applied for finding the effective response of the crystal with the voids of the spherical shape is presented. In this formulation, the bulk crystal plays a role of a matrix and the void is an inhomogeneity. Let us consider the representative porous polycrystal (RPP, see Fig. 6.1a) composed of many representative porous single crystals (RPSCs). The first task is to determine the overall response of an individual RPSC (see Fig. 6.2) and then apply the same approach to all RPSCs with different orientations. For convenience, the subscript g, which represents each porous single crystal (it is also referred as grain / porous grain in the description), is dropped in this section.

The local constitutive relation of the bulk crystal is of the Maxwell-type form obtained by the additive decomposition of the total strain rate into elastic and viscoplastic parts:

$$\dot{\boldsymbol{\varepsilon}}_c = \dot{\boldsymbol{\varepsilon}}_c^e + \dot{\boldsymbol{\varepsilon}}_c^v = \mathbb{M}_c^e \cdot \dot{\boldsymbol{\sigma}}_c + f(\boldsymbol{\sigma}_c), \tag{6.1}$$

where $\dot{\boldsymbol{\varepsilon}}_c$ is the strain rate in the bulk crystal. The anisotropic linear constitutive law is used for the elastic part of strain rate, where $\mathbb{M}_c^e$ refers to the elastic compliance of the bulk crystal. Regarding the viscoplastic component of the strain rate, the non-linear power law is employed (refer to Eq. (2.7)), so it is formulated as follows:

$$\dot{\boldsymbol{\varepsilon}}_c^v = f(\boldsymbol{\sigma}_c) = \dot{\gamma}_0 \sum_{r=1}^{2N+M} \left(\frac{\tau^r}{\tau_{cr}^r} \right)^n \mathbf{p}^r \,, \quad \tau^r = \langle \boldsymbol{\sigma}_c \cdot \mathbf{p}^r \rangle \,, \; \mathbf{p}^r = \frac{1}{2}(\mathbf{m}^r \otimes \mathbf{n}^r + \mathbf{n}^r \otimes \mathbf{m}^r). \tag{6.2}$$

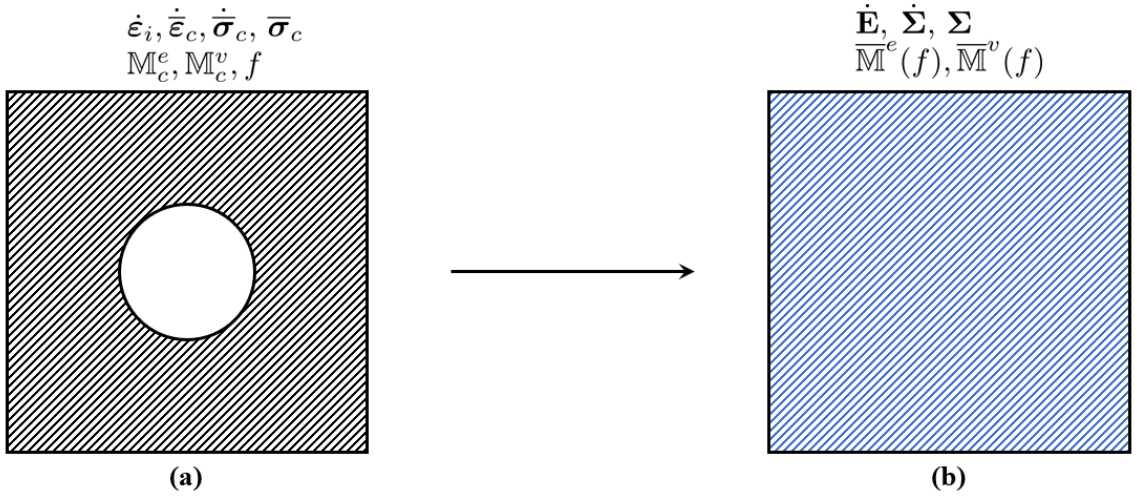

FIGURE 6.2 Schematic representation of the first step of homogenization procedure using additive Mori-Tanka scheme: (a) representative porous single crystal (RPSC), (b) homogenized porous single crystal (HPSC).

The reference strain rate on the slip or twin system is denoted by $\dot{\gamma}_0$ and the rate sensitivity exponent by n. In the above equation, slip and twinning are unified by distinguishing slip in the $\mathbf{m}$ direction from slip in the $-\mathbf{m}$ direction. The number of slip and twin systems are represented by N and M, respectively. The symmetric part of the Schmid tensor is symbolized by $\mathbf{p}^r$. The resolved shear stress, denoted as τ^r, is determined by the scalar product of stress ($\boldsymbol{\sigma}_c$) and the symmetric part of the Schmid tensor ($\mathbf{p}^r$), which is comprised of the slip plane ($\mathbf{n}$) and slip direction ($\mathbf{m}$). The Macaulay operation ($< \cdot >$) is defined as $\equiv \frac{1}{2}((\cdot) + |\cdot|)$. The model formulation is thus equivalent to the one presented in Chapter 2, however, reduced to the small strain framework. The critical resolved shear stress (CRSS) is represented by τ_{cr}^r. When hardening phenomenon is considered, its evolution in relation to the accumulation of slip or twin volume fraction has been previously presented in Chapter 2.

When $n = 1$, the following piecewise-linear law is obtained:

$$\dot{\boldsymbol{\varepsilon}}_c^v = \mathbb{M}_c^v \cdot \boldsymbol{\sigma}_c, \quad \mathbb{M}_c^v = \dot{\gamma}_0 \sum_{r=1}^{2N+M} \frac{sgn(\langle \tau^r \rangle)}{\tau_{cr}^r} \mathbf{p}^r \otimes \mathbf{p}^r. \tag{6.3}$$

The bulk crystal viscous compliance is denoted by $\mathbb{M}_c^v$. For $n > 1$, various linearization schemes, such as secant and tangent schemes, can be utilized for the nonlinear function $f(\boldsymbol{\sigma}_c)$. For more information about the linearization schemes refer to Kowalczyk-Gajewska (2011). The respective tangent and secant viscous compliances for the crystal plasticity

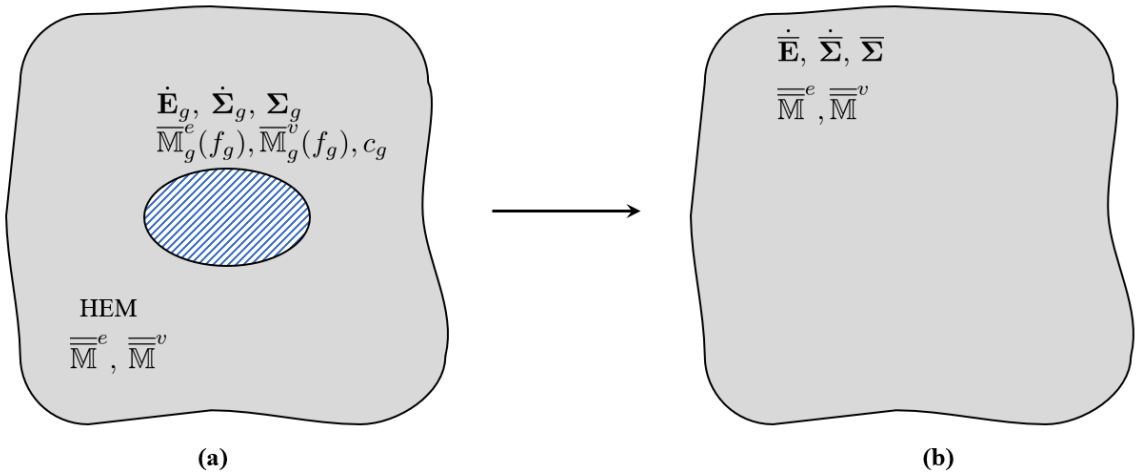

FIGURE 6.3 Schematic representation of the second step of homogenization procedure using additive self-consistent scheme: (a) HPSC embedded in homogeneous equivalent medium (HEM), (b) homogenized porous polycrystal (HPPC).

model with power law for slip and twin systems are formulated as follows:

$$\mathbb{M}_c^{v(tg)} = \frac{\partial \mathbf{f}(\boldsymbol{\sigma}_\mathbf{c})}{\partial \boldsymbol{\sigma}_c} = n\dot{\gamma}_0 \sum_{r=1}^{2N+M} \frac{sgn(\langle \tau^r \rangle)}{\tau_{cr}^r} \left(\frac{\langle \tau^r \rangle}{\tau_{cr}^r} \right)^{n-1} \mathbf{p}^r \otimes \mathbf{p}^r, \tag{6.4}$$

$$n\mathbb{M}_c^{v(sc)}(\boldsymbol{\sigma}_c) \equiv \mathbb{M}_c^{v(tg)}(\boldsymbol{\sigma}_c), \tag{6.5}$$

where $\mathbb{M}_c^{v(sc)}, \mathbb{M}_c^{v(tg)}$ refers to the secant and tangent viscous compliances of the bulk crystal, respectively. To apply the Eshelby result, the linearized properties of the crystal must be uniform. For this purpose, the mean stress ($\overline{\boldsymbol{\sigma}}_c$) in the crystal is utilized to calculate the viscous compliance. Consequently, for higher rate sensitivity exponents, the viscous strain rate in the crystal is computed as follows:

$$\dot{\boldsymbol{\varepsilon}}_c^v = \mathbb{M}_{\mathbb{c}}^{v(sc)}(\overline{\boldsymbol{\sigma}}_c) \cdot \boldsymbol{\sigma}_c. \tag{6.6}$$

From this point forward, mean quantities are predominantly utilized in the formulation. Consequently, Eq. (6.6) can be expressed in terms of mean field quantities as follows:

$$\dot{\overline{\boldsymbol{\varepsilon}}}_c^v = \mathbb{M}_{\mathbb{c}}^{v(sc)}(\overline{\boldsymbol{\sigma}}_c) \cdot \overline{\boldsymbol{\sigma}}_c. \tag{6.7}$$

For voids the stress field is zero, so

$$\dot{\boldsymbol{\sigma}}_i = \boldsymbol{\sigma}_i = 0. \tag{6.8}$$

By applying Eq. (6.8), the overall response of the voided crystal can be determined using the following averaging equations:

$$\dot{\mathbf{E}} = f\dot{\bar{\boldsymbol{\varepsilon}}}_i + (1-f)\dot{\bar{\boldsymbol{\varepsilon}}}_c, \tag{6.9}$$

$$\dot{\boldsymbol{\Sigma}} = (1-f)\dot{\overline{\boldsymbol{\sigma}}}_c, \tag{6.10}$$

$$\boldsymbol{\Sigma} = (1-f)\overline{\boldsymbol{\sigma}}_c, \tag{6.11}$$

where $\dot{\mathbf{E}}$, $\dot{\boldsymbol{\Sigma}}$, and $\boldsymbol{\Sigma}$ represent the overall (macroscopic) strain rate, stress rate, and stress, respectively. $\dot{\bar{\boldsymbol{\varepsilon}}}_c$, $\dot{\overline{\boldsymbol{\sigma}}}_c$, and $\overline{\boldsymbol{\sigma}}_c$ are the respective mean field quantities in the bulk crystal, calculated as volume averages of the form:

$$\overline{(\cdot)} \overset{def}{=} \frac{1}{V_c}\int_{V_c}(\cdot)dV \tag{6.12}$$

and 'f' refers to the volume fraction of the voids. Finally, $\dot{\bar{\boldsymbol{\varepsilon}}}_i$ is the strain rate of the void, which can be calculated based on displacements at the void boundary.

The formulation of the additive interaction law of the Mori-Tanaka type for elasto-viscoplastic materials was proposed by Molinari (2002) and was subsequently developed in Czarnota et al. (2015), as follows:

$$\dot{\bar{\boldsymbol{\varepsilon}}}_i - \dot{\bar{\boldsymbol{\varepsilon}}}_c = -\mathbb{M}^e_* \cdot (\dot{\boldsymbol{\sigma}}_i - \dot{\overline{\boldsymbol{\sigma}}}_c) - \beta\mathbb{M}^v_* \cdot (\overline{\boldsymbol{\sigma}}_i - \overline{\boldsymbol{\sigma}}_c), \tag{6.13}$$

which after substituting zero stress for void, takes the following form:

$$\dot{\bar{\boldsymbol{\varepsilon}}}_i - \dot{\bar{\boldsymbol{\varepsilon}}}_c = \mathbb{M}^e_* \cdot \dot{\overline{\boldsymbol{\sigma}}}_c + \beta\mathbb{M}^v_* \cdot \overline{\boldsymbol{\sigma}}_c, \tag{6.14}$$

where $\mathbb{M}^e_*, \mathbb{M}^v_*$ are the inverses of elastic and viscous Hill tensors $\mathbb{L}^e_*$ and $\mathbb{L}^v_*$, respectively. They are calculated using the following equation:

$$\mathbb{L}^{e/v}_* = (\mathbb{P}^{e/v})^{-1} - \mathbb{L}^{e/v}_c, \tag{6.15}$$

where $\mathbb{L}^{e/v}_c = (\mathbb{M}^{e/v}_c)^{-1}$. The polarization tensor $\mathbb{P}^{e/v}$ is determined by the shape of the ellipsoidal inhomogeneity and the linearized properties of the bulk crystal using the

following relation (Willis, 1981).

$$\mathbb{P}^{e/v} = \frac{1}{4\pi abc}\int_{|\boldsymbol{\nu}|=1} |\mathbf{a}^{-1}\cdot\boldsymbol{\nu}|^{-3}\left(\boldsymbol{\nu}\otimes(\boldsymbol{\nu}\mathbb{L}_c^{e/v}\boldsymbol{\nu})^{-1}\otimes\boldsymbol{\nu}\right)^{sym} dS\,, \tag{6.16}$$

where

$$A_{ijkl}^{sym} \equiv \frac{1}{4}\left(A_{ijkl}+A_{jikl}+A_{ijlk}+A_{klij}\right)\,, \tag{6.17}$$

and $\mathbf{a}$ is the second-order tensor of principal values a, b, c, equal to the ellipsoid semi-axes (for a spherical inhomogeneity $a = b = c$ and $\mathbf{a} = a\mathbf{I}$). The integration is over the surface of the unit sphere $|\boldsymbol{\nu}| = 1$. $\mathbb{M}_*^e$ is calculated based on the bulk crystal elastic moduli, whereas $\mathbb{M}_*^v$ is calculated based on secant viscous linearized moduli i.e, $\mathbb{M}_{\mathbb{c}}{}^{v(sc)}(\overline{\boldsymbol{\sigma}}_c)$ (refer to Eqs. (6.4)–(6.5)), which are functions of $\bar{\boldsymbol{\sigma}}_c$. Based on the value of β, two schemes can be employed for calculating linearized viscous compliance. For the secant scheme, $\beta = 1$ is used, whereas for the tangent scheme, $\beta = n$ is utilized to compute the overall viscous compliance of the porous crystal. When comparing the two schemes, the secant scheme exhibits a harder response, while the tangent scheme displays a softer response. The difference between two schemes increases with n.

The interaction Eq. (6.13) is reformulated, by multiplying the Eq. (6.13) with f and using the averaging Eqs. (6.9)–(6.11), to the following forms valid for the bulk crystal and void, respectively:

$$\dot{\mathbf{E}} - \dot{\bar{\boldsymbol{\varepsilon}}}_c = -\mathbb{M}_*^e\cdot(\dot{\boldsymbol{\Sigma}} - \dot{\overline{\boldsymbol{\sigma}}}_c) - \beta\mathbb{M}_*^v\cdot(\boldsymbol{\Sigma} - \overline{\boldsymbol{\sigma}}_c), \tag{6.18}$$

$$\dot{\mathbf{E}} - \dot{\bar{\boldsymbol{\varepsilon}}}_i = -\mathbb{M}_*^e\cdot\dot{\boldsymbol{\Sigma}} - \beta\mathbb{M}_*^v\cdot\boldsymbol{\Sigma}. \tag{6.19}$$

Let us assume that the overall constitutive relation has the following form:

$$\dot{\mathbf{E}} = \overline{\mathbb{M}}^e\cdot\dot{\boldsymbol{\Sigma}} + \dot{\mathbf{E}}^v \text{ (or) } \dot{\boldsymbol{\Sigma}} = \overline{\mathbb{L}}^e\cdot(\dot{\mathbf{E}} - \dot{\mathbf{E}}^v), \tag{6.20}$$

where $\overline{\mathbb{M}}^e$ is the overall (homogenized) elastic compliance of the voided crystal and $\dot{\mathbf{E}}^v$ is the overall (homogenized) viscous strain rate of the voided crystal. To specify the quantities $\overline{\mathbb{M}}^e$ and $\dot{\mathbf{E}}^v$ we express the linearized local constitutive law for bulk crystal in terms of mean stress and strain rate:

$$\dot{\bar{\boldsymbol{\varepsilon}}}_c = \mathbb{M}_c^e\cdot\dot{\overline{\boldsymbol{\sigma}}}_c + \mathbb{M}_{\mathrm{c}}^{v(sc)}(\overline{\boldsymbol{\sigma}}_c)\cdot\overline{\boldsymbol{\sigma}}_c. \tag{6.21}$$

Now substituting Eq. (6.21) into Eq. (6.9) and using Eqs. (6.10)–(6.11) the following relation is obtained:

$$\dot{\mathbf{E}} = f\dot{\bar{\boldsymbol{\varepsilon}}}_i + \mathbb{M}^e \cdot \dot{\boldsymbol{\Sigma}} + \mathbb{M}_c^{v(sc)}(\overline{\boldsymbol{\sigma}}_c) \cdot \boldsymbol{\Sigma}. \tag{6.22}$$

Finally, substituting Equation (6.22) into (6.19), the following overall relation is obtained:

$$\dot{\mathbf{E}} = \left(\frac{1}{1-f}\mathbb{M}_c^e + \frac{f}{1-f}\mathbb{M}_*^e\right) \cdot \dot{\boldsymbol{\Sigma}} + \left(\frac{1}{1-f}\mathbb{M}_c^{v(sc)}(\overline{\boldsymbol{\sigma}}_c) + \frac{f}{1-f}\beta\mathbb{M}_*^v\right) \cdot \boldsymbol{\Sigma}. \tag{6.23}$$

By comparing Eq. (6.23) with Eq. (6.20) we identify that

$$\overline{\mathbb{M}}^e = \frac{1}{1-f}\mathbb{M}^e + \frac{f}{1-f}\mathbb{M}_*^e, \tag{6.24}$$

$$\dot{\mathbf{E}}^v = \overline{\mathbb{M}}^v \cdot \boldsymbol{\Sigma}, \quad \text{where } \overline{\mathbb{M}}^v = \frac{1}{1-f}\mathbb{M}_c^{v(sc)}\left(\frac{\boldsymbol{\Sigma}}{1-f}\right) + \frac{f}{1-f}\beta\mathbb{M}_*^v. \tag{6.25}$$

It is emphasized that assuming relation (6.20) is not necessary to derive Eq. (6.23) above; however, it facilitates the interpretation of elastic and viscoplastic component of Eq. (6.23). Using the overall relations (6.24) and (6.25), the effective response of RPSCs with different orientations can be determined. Consequently, we obtain an RVE composed of HPSCs, to which the next step of the homogenization procedure can be applied.

6.1.2 Micromechanical Model of RVE Composed of HPSCs Using EVPSC Scheme

In the next step, to predict the overall response for RVE-HPSC (Fig. 6.1b), the elasto-viscoplastic self-consistent scheme (EVPSC) is considered (see Fig. 6.3). Numerous self-consistent schemes devoted to elasto-viscoplastic heterogeneous materials are documented in the literature, such as those in Wang et al. (2010); Kowalczyk-Gajewska and Petryk (2011); Mareau and Berbenni (2015). The EVPSC scheme developed in the present thesis is based on the tangent additive interaction law introduced by Molinari et al. (1997); Molinari (2002) and adopted, combined with the tangent linearization, for non-porous polycrystalline materials in Girard et al. (2021). In the current formulation similarly to Girard et al. (2021), tangent linearization is applied to the viscous component in bulk crystal (i.e. $\beta = n$ is used in Eq. (6.27) below). As concerns the viscous component of HPSC, the overall $\overline{\mathbb{M}}_g^v$ in relation (6.27) obtained based on the Mori-Tanaka scheme (refer to Eq. (6.25)) can be identified as the secant compliance of the porous grain and it will be used to calculate the overall viscous properties of the homogeneous equivalent medium (HEM).

Let c_g be the volume fraction of HPSC in RVE-HPSC with porosity f_g and orientation

ϕ_g, where subscript g denotes the index of HPSC. Overall relations (6.20) and (6.24)–(6.25) can be used in the second step of homogenization as local compliances. These relations are as follows (refer to Fig. 6.3a):

$$\dot{\mathbf{E}}_g = \overline{\mathbb{M}}^e_g \cdot \dot{\mathbf{\Sigma}}_g + \dot{\mathbf{E}}^v_g, \quad \text{where} \quad \overline{\mathbb{M}}^e_g = \frac{1}{1-f_g}\mathbb{M}^e_{c,g} + \frac{f_g}{1-f_g}\mathbb{M}^e_{*,g}, \tag{6.26}$$

$$\dot{\mathbf{E}}^v_g = \overline{\mathbb{M}}^v_g \cdot \mathbf{\Sigma}_g, \quad \text{where} \quad \overline{\mathbb{M}}^v_g = \frac{1}{1-f_g}\mathbb{M}^{v(sc)}_{c,g}\left(\frac{\mathbf{\Sigma_g}}{1-f_g}\right) + \frac{f_g}{1-f_g}\beta\mathbb{M}^v_{*,g}. \tag{6.27}$$

All tensorial quantities are already explained in the previous section. Eq. (6.27) resembles Eq. (6.7), indicating that the viscous compliance of the porous crystal is calculated by means of secant linearization. The interaction law is as follows for secant linearization:

$$\dot{\mathbf{E}}_g - \dot{\overline{\mathbf{E}}} = -\overline{\mathbb{M}}^e_* \cdot (\dot{\mathbf{\Sigma}}_g - \dot{\overline{\mathbf{\Sigma}}}) - \overline{\mathbb{M}}^v_* \cdot (\mathbf{\Sigma}_g - \overline{\mathbf{\Sigma}}), \tag{6.28}$$

where $\dot{\overline{\mathbf{E}}}$, $\dot{\overline{\mathbf{\Sigma}}}$, and $\overline{\mathbf{\Sigma}}$ denote the overall strain, stress rate and stress in the HPPC, respectively. All HPSCs treated as inclusions embedded in the HEM are considered spherical in the current scenario. In the above equation, $\overline{\mathbb{M}}^e_*, \overline{\mathbb{M}}^v_*$ are fourth order inverse elastic and viscous Hill tensor, respectively. The tensor $\overline{\mathbb{M}}^v_*$ is calculated using the overall effective viscous stiffness $\overline{\overline{\mathbb{L}}}^v = \left(\overline{\overline{\mathbb{M}}}^v\right)^{-1}$ in Eqs. (6.15)–(6.16). Similarly, $\overline{\mathbb{M}}^e_*$ is calculated using the overall effective elastic stiffness, $\overline{\overline{\mathbb{L}}}^e = \left(\overline{\overline{\mathbb{M}}}^e\right)^{-1}$ in Eqs. (6.15)–(6.16).

According to the self-consistent scale transition, $\overline{\overline{\mathbb{M}}}^v$ is given by the following formula:

$$\overline{\overline{\mathbb{M}}}^v = \left\langle \overline{\mathbb{M}}^v_g \circ \overline{\mathbb{B}}^v_g \right\rangle, \tag{6.29}$$

where the secant local viscous compliance, $\overline{\mathbb{M}}^v_g$ provided in the Eq. (6.27), depends on the grain orientation and current values of the mechanical fields in the HPSC. It must be updated at each step of the calculation. $\langle\bullet\rangle$ denotes the volume averaging over the RVE-HPSC and $\circ$ stands for the double contraction of two fourth order tensors (see Section 2.1). $\overline{\mathbb{B}}^v_g$ is the representative stress localization tensor calculated as:

$$\overline{\mathbb{B}}^v_g = \left(\overline{\mathbb{M}}^v_* + \overline{\mathbb{M}}^v_g\right)^{-1} \circ \left(\overline{\mathbb{M}}^v_* + \overline{\overline{\mathbb{M}}}^v\right). \tag{6.30}$$

Similarly to $\overline{\overline{\mathbb{M}}}^v$, the overall elastic compliance $\overline{\overline{\mathbb{M}}}^e$ and $\overline{\mathbb{B}}^e_g$ are obtained by Eqs. (6.29) and (6.30) where the superscript v is replaced by e (for corresponding elastic quantities). Contrary to the non-porous polycrystal considered in Girard et al. (2021), where $\overline{\overline{\mathbb{M}}}^e$ was calculated

once, in this study, because f_g evolves during the process, the quantities $\overline{\mathbb{M}}^e_g$, $\overline{\mathbb{B}}^e_g$, and $\overline{\overline{\mathbb{M}}}^e$ have to be updated at every time step.
Similarly to the proposals applied to the elasto-viscoplastic voided single crystal formulation, the EVPSC model is completed by the following averaging relations:

$$\dot{\overline{\mathbf{E}}} = \langle \dot{\mathbf{E}}_g \rangle, \quad \dot{\overline{\mathbf{\Sigma}}} = \langle \dot{\mathbf{\Sigma}}_g \rangle, \quad \overline{\mathbf{\Sigma}} = \langle \mathbf{\Sigma}_g \rangle. \tag{6.31}$$

Using the interaction law (6.28), averaging relations (6.31), and the relations (6.26)–(6.27), the macroscopic response is obtained in the same way as the overall elasto-viscoplastic single crystal response as follows:

$$\dot{\overline{\mathbf{E}}} = \overline{\overline{\mathbb{M}}}^e \cdot \dot{\overline{\mathbf{\Sigma}}} + \dot{\overline{\mathbf{E}}}^v, \quad \text{where } \overline{\overline{\mathbb{M}}}^e = \left\langle \overline{\mathbb{M}}^e_g \circ \overline{\mathbb{B}}^e_g \right\rangle, \; \dot{\overline{\mathbf{E}}}^v = \left\langle \left(\overline{\mathbb{B}}^e_g\right)^T . \left[\dot{\mathbf{E}}^v_g + \overline{\mathbb{M}}^v_* . (\mathbf{\Sigma}_g - \overline{\mathbf{\Sigma}})\right] \right\rangle. \tag{6.32}$$

This closed-form expression for the macroscopic response of the HPPC is novel. The derivation of overall relation (6.32) for polycrystals is clearly explained in Appendix **B** of Girard et al. (2021).

6.1.3 Evolution of local and overall porosities in the RVE-HPSC

In the preceding section, the formulation for the overall elasto-viscoplastic response of RVE-HPSC was presented. The subsequent stage involves formulating relations for void evolution within each HPSC, followed by updating the overall porosity in RVE-HPSC.

6.1.3.1 Evolution of local porosity

Since a mean-field model is utilized, the volume fraction of void (f_g) in grain g, which is defined as the ratio of void volume ($V_{i,g}$) to the overall volume of HPSC (V_g), namely:

$$f_g = \frac{V_{i,g}}{V_g}. \tag{6.33}$$

Then, the relationships describing the evolution of void volume and overall volume of HPSC can be analogously calculated according to the relation valid for infinitesimal quantities:

$$\dot{V}_{i,g} = (\mathrm{Tr}\, \dot{\bar{\boldsymbol{\varepsilon}}}_{i,g}) V_{i,g}, \quad \dot{V}_g = (\mathrm{Tr}\, \dot{\mathbf{E}}_g) V_g, \tag{6.34}$$

where $\dot{\bar{\boldsymbol{\varepsilon}}}_{i,g}$ is the strain rate in the void of the given HPSC (g), and it can be found by the averaging relation:

$$\dot{\bar{\boldsymbol{\varepsilon}}}_{i,g} = \frac{1}{f_g}[\dot{\mathbf{E}}_g - (1 - f_g)\dot{\bar{\boldsymbol{\varepsilon}}}_{c,g}]. \tag{6.35}$$

Such relation can be used for two phase medium, so considering only single crystal with void. In general for n phase material one can find this quantity by using concentration tensors ($\mathbb{A}_{i,g}, \boldsymbol{\alpha}_{i,g}$) and the overall strain in the given HPSC ($\dot{\mathbf{E}}_g$) by the following relation:

$$\dot{\bar{\boldsymbol{\varepsilon}}}_{i,g} = \mathbb{A}_{i,g} \cdot \dot{\mathbf{E}}_g + \boldsymbol{\alpha}_{i,g}. \tag{6.36}$$

By taking the material derivative of the Eq. (6.33) and using the relation (6.34) after some manipulations, the following evolution equation for local porosity is obtained:

$$\dot{f}_g = (\operatorname{Tr} \dot{\bar{\boldsymbol{\varepsilon}}}_{i,g} - \operatorname{Tr} \dot{\mathbf{E}}_g) f_g. \tag{6.37}$$

For incompressible matrix, as is the case for rigid plastic material, this equation reduces to:

$$\dot{f}_g = (1 - f_g) \operatorname{Tr} \dot{\mathbf{E}}_g, \tag{6.38}$$

which is the formula used for void evolution in classical GTN model (Li and Wang, 2018).

6.1.3.2 Overall porosity

As outlined earlier, the volume fraction of HPSC (c_g) refers to the ratio between the volume of HPSC (V_g) and the overall volume of RVE-HPSC (V). It is important to note that the collective volume fractions of all HPSCs sum up to one.

$$c_g = \frac{V_g}{V}, \quad \sum_g c_g = 1, \quad V_g = V_{i,g} + V_{c,g}, \tag{6.39}$$

where $V_{i,g}, V_{c,g}$ refer to the volume of void and crystal respectively in the given HPSC. Analogously to Eq. (6.37), the following evolution equation is employed for grain volume fraction evolution ($\dot{c}_g$):

$$\dot{c}_g = (\operatorname{Tr} \dot{\mathbf{E}}_g - \operatorname{Tr} \dot{\bar{\mathbf{E}}}) c_g. \tag{6.40}$$

By using the Eq. (6.39) and after doing some manipulations the following overall porosity is obtained in terms of f_g and c_g:

$$\bar{f} = \frac{\sum_g V_{i,g}}{V} = \langle f_g \rangle = \sum_g c_g f_g. \tag{6.41}$$

In the above relation, $\bar{f}$ is updated based on the current value of f_g and c_g, which is calculated based on volume fraction evolution equation for the pore, Eq. (6.37), and for the grain, Eq. (6.40). It should be mentioned that during the current deformation step,

all volume fractions are kept constant and they are updated after the deformation step is performed, together with mechanical properties like critical resolved shear stress (τ_{cr}) if necessary.

6.2 Summary

In this chapter the mean-field model for porous elasto-viscoplastic polycrystal has been formulated. The model employs two-step homogenization procedure. In the first step using the additive Mori-Tanaka scheme a single grain with voids is homogenized, while in the second step the additive self-consistent scheme is used to find the effective response of RVE-HPSC. Additionally, the evolution equations for local and overall porosity are formulated. In the next chapter, the numerical implementation and preliminary validation for FCC polycrystals will be presented.

CHAPTER 7

Numerical verification of the mean field model for FCC crystals

In this chapter, the numerical implementation of the mean field model formulation, as introduced in the previous chapter for both single and polycrystals, is discussed. The model's estimates for both single and polycrystals are next compared with unit cell calculations for FCC crystals.

Throughout the discussion of numerical procedure below, the following terminology is employed:

- Superscripts e and v denote the elastic and viscous components, respectively.
- The subscript g indicates the porous grain, while i, g specifies the void within the porous grain, and c, g identifies the crystal within the porous grain.
- The notations $\overline{\mathbb{L}}$ and $\overline{\mathbb{M}}$ represent the overall stiffness and compliance tensors of the porous grain, whereas $\overline{\overline{\mathbb{L}}}$ and $\overline{\overline{\mathbb{M}}}$ correspond to the overall stiffness and compliance tensors of the porous polycrystal.
- $\mathbb{M}_*$ and $\overline{\mathbb{M}}_*$ refer to the inverse Hill tensors of the porous grain and the porous polycrystal, respectively.
- The symbols $\mathbf{E}$ and $\overline{\mathbf{E}}$ denote the overall strain in the porous grain and the porous polycrystal, respectively.
- Similarly, $\boldsymbol{\Sigma}$ and $\overline{\boldsymbol{\Sigma}}$ represent the overall stress in the porous grain and the porous polycrystal, respectively.
- $\overline{\boldsymbol{\varepsilon}}$ and $\overline{\boldsymbol{\sigma}}$ indicate the local average strain and stress for the constituent phases of a homogenized porous grain.

- $\mathbb{A}$ and $\overline{\mathbb{A}}$ refer to the strain concentration tensors for the constituent phases of the porous grain and porous polycrystal, respectively, while $\mathbb{B}$ and $\overline{\mathbb{B}}$ refer to the corresponding stress concentration tensors.
- Regarding rate quantities of stress and strain, a similar notation is employed to maintain consistency across the formulation.
- Subscript g is dropped when overall response of porous single crystal is considered, especially in the following section.

7.1 Numerical implementation of the micromechanical model for a porous elasto-viscoplastic FCC single crystal

This section comprehensively details the numerical implementation of the proposed micromechanical model for elasto-viscoplastic porous single crystals, based on the additive Mori-Tanaka scheme. The numerical scheme is implemented using the symbolic and algebraic system, Wolfram Mathematica. Before delving into the primary procedure, a brief explanation of the prerequisites is provided.

1) To facilitate straightforward tensorial operations, all tensor quantities are represented in the Kelvin-Rychlewski-Cowin (KRC) and deviatoric bases. In these bases, symmetric second-order tensors are represented as 6-dimensional vectors and fourth-order tensors are represented as 6x6 second-order tensors. To express tensor components in different bases, relevant transformations rules are employed. The utilization of the deviatoric basis allows for a straightforward splitting of the tensor into its hydrostatic and deviatoric parts. For further information regarding these bases, please refer to Kowalczyk-Gajewska (2011).

2) In addition to the basis transformations, the tensorial quantities represented in the crystal frame are also rotated to the sample frame and vice versa, utilizing Euler angles.

3) The polarization tensor (Eq. (6.16)) for both the elastic and viscoplastic components is computed using numerical integration with n Gauss points through an external FORTRAN procedure based on the crystal anisotropic elastic and viscous stiffness tensor as an input. The Hill tensor and its inverse are determined using the polarization tensor. Regarding the viscoplastic part, the bulk modulus of the Hill tensor is calculated through the isotropization (refer next chapter for more details). In

the case where one of the eigenvalues of the secant viscous compliance tensor ($\mathbb{M}_{\mathrm{c}}^{v(sc)}$) is found to be zero, the compliance tensor undergoes a necessary modification to stabilize numerical calculations in the transient elastic-plastic regime. This involves replacing the zero eigenvalue with the minimum remaining eigenvalue of the compliance tensor. By making this adjustment, the inversion of the compliance tensor becomes feasible, thereby enabling the straightforward calculation of the viscous inverse Hill tensor using an external FORTRAN procedure.

4) Once the elastic Hill tensor ($\mathbb{L}_*^e$) is computed using an external FORTRAN procedure, using the crystal elastic stiffness tensor($\mathbb{L}_c^e$) as an input, the determination of the overall elastic stiffness and compliance ($\overline{\mathbb{L}}^e, \overline{\mathbb{M}}^e$) for the porous crystal is carried out using the additive Mori-Tanka scheme. Furthermore, the calculation of elastic strain concentration tensors is performed. The corresponding equations are provided below:

$$\overline{\mathbb{M}}^e = \frac{1}{1-f}\mathbb{M}^e + \frac{f}{1-f}\mathbb{M}_*^e, \quad \overline{\mathbb{L}}^e = (\overline{\mathbb{M}}^e)^{-1}, \tag{7.1}$$

$$\mathbb{A}_j^e = (\mathbb{L}_j^e + \mathbb{L}_*^e)^{-1} \circ (\overline{\mathbb{L}}^e + \mathbb{L}_*^e), \tag{7.2}$$

where f is the void volume fraction within the grain and the above equations are recalculated at each time step if the evolution of f is considered. Otherwise the above equations are calculated only once during the initial step. Concerning elastic strain concentration tensors ($\mathbb{A}_j^e$), the subscript j denotes the index of void ($j = i$) and crystal ($j = c$). These concentration tensors are used in the calculation of the local strain rates in the void, crystal and in turn, these are used in the calculation of void evolution. Also, it is important to note that the stiffness of the void is set to zero.

5) The forward Euler explicit integration method is utilized to update the quantities at $t + \Delta t$ based on the rate equations calculated at time t. Since the explicit method is conditionally stable, small time increments are considered to ensure stability.

6) The subsequent stage involves defining the input data for the main procedure. The input data is divided into three parts, and each part is elaborated as follows:

   a) The first part primarily consists of the process control parameters (time (t), time increment (Δt), overall strain rate ($\dot{\mathbf{E}}$), overall initial strain ($\mathbf{E}(0)$, if considered, otherwise assumed as $\mathbf{0}$) and the stress direction $\mathbf{N}$ in terms of triaxiality and Lode parameter or stress ratios), the initial void volume fraction (f_0), and the Euler angles responsible for rotating the crystal to the sample

frame and vice versa. In the current approach, the process can be either fully strain rate controlled or controlled by one of the strain rate components and the stress direction.

b) The second part consists of the elastic Hill tensor ($\mathbb{M}^e_*$), the overall elastic stiffness ($\overline{\mathbb{L}}^e$), its inverse ($\overline{\mathbb{M}}^e$), and the elastic strain concentration tensors, all of which have been discussed previously.

c) The third part includes the viscoplastic data, such as the reference shear rate ($\dot{\gamma}_0$), dyads of the symmetric Schmid tensor ($\mathbf{p}^r \otimes \mathbf{p}^r$) in the deviatoric basis for calculating the secant viscous compliance, predefined formulas for the resolved shear stress (τ^r) for all slip and twin systems, hardening parameters, rate sensitivity exponent, and β parameter (where $\beta = 1$ for secant linearization and n for tangent linearization). Additionally, symmetric Schmid tensors are represented as 5-dimensional vectors in the deviatoric basis for computing the viscous strain rate in the crystal.

Main procedure. Up to this point, the essential prerequisites for the main module have been outlined. The next step presents the main procedure for the additive Mori-Tanaka scheme, specifically for crystals with a spherical void, in comprehensive detail. Initially, all the input data described earlier are imported into the module to facilitate the necessary calculations.

Step 1: The analysis begins at $t = 0$ with the assumption of a purely elastic solution. If not given, the overall strain rate is computed using the provided stress direction and the component of the imposed strain e.g. $\dot{\mathrm{E}}_{11}$ in the following manner:

$$\dot{\mathbf{E}} = \alpha(t)(\overline{\mathbb{M}}^e \cdot \mathbf{N})(\because \dot{\mathbf{E}}^v = 0, \dot{\boldsymbol{\Sigma}} = \alpha(t)\mathbf{N}), \tag{7.3}$$

$$\alpha(t) = \frac{\dot{\mathrm{E}}_{11}}{\overline{\mathrm{M}}^e_{11ij}\mathrm{N}_{ij}}. \tag{7.4}$$

Developed procedure allows also for using the imposed equivalent strain rate $\dot{\mathbf{E}}_{eq} = \sqrt{\frac{2}{3}\dot{\mathbf{E}}' \cdot \dot{\mathbf{E}}'}$, where $\dot{\mathbf{E}}'$ is the deviatoric part of macroscopic strain rate to calculate $\alpha(t)$. However, in the calculations presented later, one of the strain rate components is usually assumed in accordance with the reference unit cell calculations.

Step 2: If the initial overall strain ($\mathbf{E}$) is zero, all local quantities, including strain ($\boldsymbol{\varepsilon}_i, \boldsymbol{\varepsilon}_c$), stress ($\boldsymbol{\sigma}_i, \boldsymbol{\sigma}_c$, **stress in the void is always zero**), viscous strain ($\boldsymbol{\varepsilon}^v_i, \boldsymbol{\varepsilon}^v_c$), equivalent viscous strain ($\boldsymbol{\varepsilon}^v_{eq}$) in both void and crystal, overall viscous strain ($\mathbf{E}^v$), and overall

stress ($\boldsymbol{\Sigma}$, calculated based on overall relation), are initialized to zero.
Otherwise, for the given initial strain, the local strains in both void and crystal are updated using the strain concentration tensors and assuming an elastic step. The viscous quantities are set to zero. The equations are as follows:

$$\boldsymbol{\varepsilon}_j = \mathbb{A}_j^e \cdot \mathbf{E}, \tag{7.5}$$

$$\boldsymbol{\sigma}_c = \mathbb{L}_c \cdot \boldsymbol{\varepsilon}_c, \quad \boldsymbol{\sigma}_i = \mathbf{0}, \quad \boldsymbol{\Sigma} = \overline{\mathbb{L}}^e \cdot \mathbf{E}. \tag{7.6}$$

Step 3: Next, the initial secant viscous compliance in the crystal ($\mathbb{M}_c^{v(sc)}$) is initialized using the local stresses within the crystal ($\boldsymbol{\sigma}_c$) and the known local quantities from the elastic step.
For power law exponent $n > 1$:

$$\mathbb{M}_c^{v(sc)} = \dot{\gamma}_0 \sum_r \frac{1}{\tau_{cr}^r} \left(\frac{|\tau^r|}{\tau_{cr}^r} \right)^{n-1} \mathbf{p}^r \otimes \mathbf{p}^r, \quad \text{where } \tau^r = \overline{\boldsymbol{\sigma}}_c \cdot \mathbf{p}^r. \tag{7.7}$$

For $n = 1$:

$$\mathbb{M}_c^{v(secant)} = \nu_0 \sum_r \frac{1}{\tau_{cr}^r} \mathbf{p}^r \otimes \mathbf{p}^r, \tag{7.8}$$

where $\mathbf{p}^r$ is the symmetric part of the Schmid tensor (Eq. (6.2)), τ^r is the resolved shear stress, $\dot{\gamma}_0$ is the reference shear rate and τ_{cr}^r is the critical resolved shear stress, and it will be updated at each time step based on the accumulated strain. Note that in the above formulas we assumed deformation by slip only. They need to be modified when twinning is incorporated. Similarly to the large strain formulation discussed in Chapter 2, the rate of shear is given by the *rate-dependent* viscoplastic power law (Asaro and Needleman, 1985):

$$\dot{\gamma}^r = \dot{\gamma}_0 \text{sign}(\tau^r) \left| \frac{\tau^r}{\tau_{cr}^r} \right|^n, \tag{7.9}$$

where $\dot{\gamma}_0$ is the material parameter, n is a rate-sensitivity parameter.
Now, based on the initial secant viscous compliance the viscous inverse Hill tensor is calculated, employing an external FORTRAN procedure. With this, the initialization steps are completed, and all the global and local quantities are exported to their respective output vectors.
The following steps are executed in a while loop until the maximum imposed time is reached.

Step 4: The viscous strain rate in the crystal is calculated based on the rate of shear on the slip systems obtained during the previous step:

$$\dot{\bar{\boldsymbol{\varepsilon}}}_c^v = \sum_r \dot{\gamma}^r \mathbf{p}^r. \tag{7.10}$$

The viscous part of the strain rate in the void is assumed to be zero. The overall viscous strain rate is calculated using the Eq. (6.25):

$$\dot{\mathbf{E}}^v = \overline{\mathbb{M}}^v \cdot \boldsymbol{\Sigma} \;\text{ where }\; \overline{\mathbb{M}}^v = \frac{1}{1-f}\mathbb{M}_c^{v(sc)}\left(\frac{\boldsymbol{\Sigma}}{1-f}\right) + \frac{f}{1-f}\beta\mathbb{M}_*^v, \tag{7.11}$$

where f refers to the current void volume fraction, $\mathbb{M}_*^v$ is the viscous inverse Hill tensor calculated based on the secant viscous compliance in the crystal($\mathbb{M}_c^{v(sc)}$) as discussed before. For secant linearization, β is considered to be equal to 1, whereas, for tangent linearization, β is considered to be equal to n.

Step 5: After determining the overall viscous strain rate, if not imposed, the overall strain rate is then calculated based on imposing one of the strain rate component, e.g. $\dot{\mathrm{E}}_{11}$, and the stress direction ($\mathbf{N}$) as follows:

$$\alpha(t) = \frac{\dot{E}_{11} - \dot{E}_{11}^v}{\overline{M}_{11ij}^e N_{ij}}, \quad \dot{\boldsymbol{\Sigma}} = \alpha(t)\mathbf{N}, \quad \dot{\mathbf{E}} = \overline{\mathbb{M}}^e \cdot \dot{\boldsymbol{\Sigma}} + \dot{\mathbf{E}}^v. \tag{7.12}$$

Once the overall strain rate is known, the overall stress rate is updated using the overall relation (Eq. (7.12)).

Step 6: All local quantities are computed using the relations:

$$\begin{aligned}
\dot{\boldsymbol{\sigma}}_i &= \mathbf{0}\ (\text{for void}),\\
\dot{\bar{\boldsymbol{\sigma}}}_c &= \frac{1}{1-f}\dot{\boldsymbol{\Sigma}}\ (\text{for bulk crystal}),\\
\dot{\bar{\boldsymbol{\varepsilon}}}_i &= \frac{1}{f}(\dot{\mathbf{E}} - (1-f)\dot{\bar{\boldsymbol{\varepsilon}}}_c)(\text{for void}),\\
\dot{\bar{\boldsymbol{\varepsilon}}}_c &= \mathbb{M}_c^e \cdot \dot{\bar{\boldsymbol{\sigma}}}_c + \dot{\bar{\boldsymbol{\varepsilon}}}_c^v(\text{for bulk crystal}).
\end{aligned} \tag{7.13}$$

Step 7: After determining the strain rate in the void, the next step is to calculate void evolution and explicitly update the void volume fraction using the following equations:

$$\dot{f} = (\operatorname{Tr}\dot{\bar{\boldsymbol{\varepsilon}}}_i - \operatorname{Tr}\dot{\mathbf{E}})f_{old}, \quad f = f_{old} + \dot{f}\Delta t. \tag{7.14}$$

Step 8: After obtaining the local rate quantities, the succeeding step involves explicitly updating the current local quantities in the following manner:

$$\begin{aligned}
\boldsymbol{\sigma}_j &= \boldsymbol{\sigma}_{j,old} + \dot{\boldsymbol{\sigma}}_j \Delta t, \\
\boldsymbol{\varepsilon}_j &= \boldsymbol{\varepsilon}_{j,old} + \dot{\boldsymbol{\varepsilon}}_j \Delta t, \\
\boldsymbol{\varepsilon}^v_j &= \boldsymbol{\varepsilon}^v_{j,old} + \dot{\boldsymbol{\varepsilon}}^v_j \Delta t, \\
\boldsymbol{\varepsilon}^v_{eq,j} &= \boldsymbol{\varepsilon}^v_{eq,j,old} + \dot{\boldsymbol{\varepsilon}}^v_{eq,j} \Delta t, \quad \text{where } \dot{\boldsymbol{\varepsilon}}^v_{eq,j} = \sqrt{\frac{2}{3} \dot{\boldsymbol{\varepsilon}}^v_j \cdot \dot{\boldsymbol{\varepsilon}}^v_j}.
\end{aligned} \tag{7.15}$$

An essential point to remember is that the viscous strain ($\boldsymbol{\varepsilon}^v_i$), stress ($\boldsymbol{\sigma}_i$), and stress rate ($\dot{\boldsymbol{\sigma}}_i$) in the void are all zero.

Step 9: Once the local quantities are updated, the following step is to update the critical resolved shear stress based on its evolution equation. This can be achieved using various hardening laws, for instance, as described in Girard et al. (2021); Virupakshi and Kowalczyk-Gajewska (2023).

Step 10: In the next step, the overall stress, strain, and viscous strain are explicitly updated using the rate equations in the following manner:

$$\begin{aligned}
\boldsymbol{\Sigma} &= \boldsymbol{\Sigma}_{old} + \dot{\boldsymbol{\Sigma}} \Delta t, \\
\mathbf{E} &= \mathbf{E}_{old} + \dot{\mathbf{E}} \Delta t, \\
\mathbf{E}^v &= \mathbf{E}^v_{old} + \dot{\mathbf{E}}^v \Delta t.
\end{aligned} \tag{7.16}$$

Step 11: The final step of the loop involves calculating the secant viscous compliance and the viscous inverse Hill tensor using Eq. (7.7), based on the updated local quantities. These results will be applied in the subsequent time increment. Lastly, the overall elastic stiffness tensor, compliance tensor, and elastic strain concentration tensors are computed, taking into account the updated void volume fraction. At the end of the loop all the current quantities are exported as an output for a given time step.

7.2 Numerical implementation of the two-step homogenized micromechanical model for porous elasto-viscoplastic FCC polycrystals

In this section, the numerical implementation of the two-step homogenization procedure, as formulated in Subsections 6.1.1 and 6.1.2 of the previous Chapter 6, is elucidated. As

outlined earlier, the Mori-Tanaka scheme is employed at the porous single crystal level for homogenization, while a self-consistent scheme is utilized in the second step to determine the overall response for the RVE-HPSC. Numerical algorithm for the Mori-Tanaka scheme was outlined in previous section. Before the main procedure for the self consistent scheme is addressed, some necessary initializations need to be made, which will lay the foundation for subsequent calculations.

1) As explained in the previous section, the same prerequisites and input parameters will be employed in this numerical implementation; only the new additions will be presented here. In the numerical procedure tensorial quantities are represented using the KRC and deviatoric basis.

2) The primary difference is that, unlike the previous case where only one porous grain with void volume fraction of f_g was homogenized, here each grain with volume fraction (c_g), having different orientations relative to the sample axes and represented by Euler angles (ϕ_g), needs to be homogenized. Further, each HPSC will be treated as an inclusion in a homogeneous equivalent medium (HEM) to determine the overall response of the RVE-HPSC.

3) The inverse elastic and viscous Hill tensors ($\mathbb{M}^e_{*,g}, \mathbb{M}^v_{*,g}$) for each single porous grain, based on crystal properties, and for the RVE-HPSC ($\overline{\mathbb{M}}^e_{*,g}, \overline{\mathbb{M}}^v_{*,g}$), based on the properties of HEM, are calculated using the respective polarization tensors (Eq. (6.16)) through an external FORTRAN procedure.

4) Once the elastic Hill tensor ($\mathbb{M}^e_{*,g}$), based on the crystal property for each porous grain, has been calculated, the effective properties (stiffness or compliance tensors, $\overline{\mathbb{L}}^e_g/\overline{\mathbb{M}}^e_g$) of the porous crystals in the sample frame are determined. This calculation is based on the initial void volume fraction in each grain and the given orientation of the porous crystals, using the overall relation from the Mori-Tanaka scheme (Eq. (6.26)). In the present implementation, the elastic/viscous compliance tensor is predominantly utilized at both the single crystal and polycrystal levels; consequently, most of the equations are expressed in terms of stress localization and compliance tensors. These effective properties then serve as the local compliance for the HPSCs. Subsequently, the overall elastic compliance ($\overline{\overline{\mathbb{M}}}^e$) is determined using the self-consistent scale transition rule, as outlined below:

$$\begin{aligned} \overline{\overline{\mathbb{M}}}^e &= \left\langle \overline{\mathbb{M}}^e_g \circ \overline{\mathbb{B}}^e_g \right\rangle, \\ \overline{\mathbb{B}}^e_g &= \left(\overline{\mathbb{M}}^e_* + \overline{\mathbb{M}}^e_g\right)^{-1} \circ \left(\overline{\mathbb{M}}^e_* + \overline{\overline{\mathbb{M}}}^e\right), \quad \text{where} \quad \overline{\mathbb{M}}^e_*(\overline{\overline{\mathbb{M}}}^e) \end{aligned} \tag{7.17}$$

where overall elastic compliance of the porous grain ($\overline{\mathbb{M}}_g^e$) is calculated using Eq. (6.26), $\overline{\mathbb{B}}_g^e$ is the elastic strain concentration tensor. The self-consistent scale transition rule Eq. (7.17) is an implicit equation, and it can be solved iteratively by assuming an initial guess for the overall elastic compliance of the HEM. The averaging is performed based on the volume fraction of the HPSC (c_g). Another important point is that the Hill tensor ($\overline{\mathbb{M}}_*^e$) must be updated during each iteration. The overall viscous compliance ($\overline{\overline{\mathbb{M}}}^v$) of the HEM is calculated using a similar procedure.

5) The next step consists of defining the input data, which is then provided to the main procedure. The input data is categorized into three parts, as was outlined in the previous section.

   a) The first part includes process control parameters and Euler angles (ϕ_g) . The new additions with respect to the Mori-Tanaka model discussed in the previous section, include the volume fraction of each porous crystal (c_g) and the void volume fraction (f_g) within each crystal.

   b) The second part consists of the elastic Hill tensors, overall elastic stiffness, its inverse, and the strain concentration tensors for each porous grain (g). These are calculated based on the porous grain orientation (ϕ_g) with respect to sample axes and initial void volume fraction (f_g) in each porous grain. Additionally, the overall compliance, Hill, and concentration tensors for the elastic part, calculated using the self-consistent scheme, are provided as input for the initial elastic step.

   c) The third part consists of the viscoplastic data, as detailed in the previous section.

Main procedure. In this section, the main procedure for the two-step homogenization process is outlined. Initially, all the input data is loaded as described in the previous section.

Step 1: At the initial time step $t = 0$, a purely elastic solution is assumed. Initially, the overall strain rate ($\dot{\overline{\mathbf{E}}}$) is determined based on the specified stress direction ($\mathbf{N}$) and the component of the applied strain, as follows:

$$\dot{\overline{\mathbf{E}}} = \overline{\overline{\mathbb{M}}}^e \cdot \dot{\overline{\mathbf{\Sigma}}} + \dot{\overline{\mathbf{E}}}^v, \quad \dot{\overline{\mathbf{\Sigma}}} = \alpha(t)\mathbf{N}, \quad \dot{\overline{\mathbf{E}}} = \alpha(t)(\overline{\overline{\mathbb{M}}}^e \cdot \mathbf{N})(\because \dot{\overline{\mathbf{E}}}^v = 0) \tag{7.18}$$

where $\alpha(t)$ can be calculated as follows:

$$\alpha(t) = \frac{\dot{\overline{E}}_{11}}{\overline{\overline{M}}^{e}_{11ij} N_{ij}}. \tag{7.19}$$

Step 2: If the initial overall strain is zero, all global and local quantities remain zero. Otherwise, the overall and local stresses and strains are determined using the following equations:

$$\begin{aligned}
\mathbf{E}_g = \overline{\mathbb{A}}^{e}_{g} \cdot \overline{\mathbf{E}} \implies & \boldsymbol{\varepsilon}_{i,g} = \mathbb{A}^{e}_{i,g} \cdot \mathbf{E}_g \\
& \overline{\boldsymbol{\varepsilon}}_{c,g} = \mathbb{A}^{e}_{c,g} \cdot \mathbf{E}_g \\
\boldsymbol{\Sigma}_g = \overline{\mathbb{L}}^{e}_{g} \cdot \mathbf{E}_g \implies & \overline{\boldsymbol{\sigma}}_{c,g} = \frac{1}{1 - f_g} \boldsymbol{\Sigma}_g \\
& \boldsymbol{\sigma}_{i,g} = 0 \text{ (stress in void)} \\
\overline{\boldsymbol{\Sigma}} = \overline{\overline{\mathbb{L}}}^{e} \cdot \overline{\mathbf{E}} & \text{ (based on overall relation).}
\end{aligned} \tag{7.20}$$

Step 3: Next, based on the local and global quantities determined above, the following step involves calculating the resolved shear stress, rate of shear and the viscous compliance of the bulk crystal (refer to Eqs. (7.7) and (7.9)). Utilizing the viscous compliance of the bulk crystal ($\mathbb{M}^{v}_{c,g}$), the inverse viscous Hill tensor of the porous grain ($\mathbb{M}^{v}_{*,g}$) is determined (refer to Section 7.1, prerequisites point 3), which is then used to compute the overall compliance of the porous grain ($\overline{\mathbb{M}}^{v}_{g}$) based on Mori-Tanka scheme (Eq. (6.27)). This procedure is repeated for each porous grain, considering the specified Euler angles (ϕ_g) to transform and represent the quantities in the sample frame. After determining the overall viscous compliance ($\overline{\mathbb{M}}^{v}_{g}$), the overall viscous strain rate ($\dot{\mathbf{E}}^{v}_{g}$) in the porous grain is calculated using Eq. (6.27).

Step 4: With the overall viscous compliance of all the grains now determined, the subsequent step involves calculating the overall compliance of the porous polycrystal ($\overline{\overline{\mathbb{M}}}^{v}$) using the self-consistent scheme as outlined below.

$$\begin{aligned}
\overline{\overline{\mathbb{M}}}^{v} &= \left\langle \overline{\mathbb{M}}^{v}_{g} \circ \overline{\mathbb{B}}^{v}_{g} \right\rangle \\
\overline{\mathbb{B}}^{v}_{g} &= \left(\overline{\mathbb{M}}^{v}_{*} + \overline{\mathbb{M}}^{v}_{g} \right)^{-1} \circ \left(\overline{\mathbb{M}}^{v}_{*} + \overline{\overline{\mathbb{M}}}^{v} \right), \quad \text{where} \quad \overline{\mathbb{M}}^{v}_{*}(\overline{\overline{\mathbb{M}}}^{v}).
\end{aligned} \tag{7.21}$$

The procedure for determining $\overline{\overline{\mathbb{M}}}^{v}$ was already explained in the initialization step, specifically in point 4 for the elastic part. The same method applies to the viscous

part as well. With this, the elastic step is completed, and all global and local quantities are exported to their respective output vectors.

The steps below are executed in each iteration of a while loop until the maximum imposed time is reached. In each iteration of the loop based on the stress and strains at time t, first, their rates are found, and next used to update these quantities for $t + \Delta t$.

Step 5: The viscoplastic strain rate ($\dot{\bar{\boldsymbol{\varepsilon}}}^v_{c,g}$) for each bulk crystal within the porous grains is calculated based on the rate of shear and the symmetric Schmid tensors ($\mathbf{P}^r$) using the Eq. (7.10).

Subsequently, the overall viscous strain rate of the porous polycrystal ($\dot{\overline{\mathbf{E}}}^v$) is determined. This is calculated by using the overall viscous strain rate of the porous grains ($\dot{\mathbf{E}}^v_g$), the inverse Hill tensor obtained from the prior self-consistent step ($\overline{\mathbb{M}}^v_*$), and the elastic strain concentration tensor for porous polycrystal based on self consistent scheme ($\overline{\mathbb{B}}^e_g$) as shown below (refer to Eq. (6.32)):

$$\begin{aligned} \dot{\tilde{\mathbf{E}}}^v_g &= \dot{\mathbf{E}}^v_g + \overline{\mathbb{M}}^v_* \left(\boldsymbol{\Sigma}_g - \overline{\boldsymbol{\Sigma}} \right) \\ \dot{\overline{\mathbf{E}}}^v &= \left\langle (\overline{\mathbb{B}}^e_g)^T \cdot \dot{\tilde{\mathbf{E}}}^v_g \right\rangle . \end{aligned} \tag{7.22}$$

Step 6: Following the determination of the overall viscous strain rate, the overall stress and strain rate is subsequently calculated by imposing one of the strain rate components e.g. $\dot{\overline{\mathrm{E}}}_{11}$ and specifying the stress direction (in terms of triaxiality and Lode angle), as shown below:

$$\begin{aligned} \alpha(t) = \frac{\dot{\overline{\mathrm{E}}}_{11} - \dot{\overline{\mathrm{E}}}^v_{11}}{\overline{\overline{\mathrm{M}}}^e_{11ij} \mathrm{N}_{ij}}, \quad \dot{\overline{\mathbf{E}}} = \alpha(t)(\overline{\overline{\mathbb{M}}}^e \cdot \mathbf{N}) + \dot{\overline{\mathbf{E}}}^v \\ \dot{\overline{\boldsymbol{\Sigma}}} = \overline{\overline{\mathbb{L}}}^e \cdot (\dot{\overline{\mathbf{E}}} - \dot{\overline{\mathbf{E}}}^v). \end{aligned} \tag{7.23}$$

Step 7: Once the overall stress and strain rates in the porous crystals are determined, the local rate quantities in the porous grains are calculated using the following localization and closure relations:

$$\begin{aligned} &\dot{\boldsymbol{\Sigma}}_g = \overline{\mathbb{B}}^e_g \cdot \dot{\overline{\boldsymbol{\Sigma}}} + (\overline{\mathbb{M}}^e_* + \overline{\mathbb{M}}^e_g)^{-1} \cdot (\dot{\overline{\mathbf{E}}}^v - \dot{\tilde{\mathbf{E}}}^v_g) \text{ (overall stress rate in the porous grain)} \\ &\dot{\mathbf{E}}_g = \overline{\mathbb{M}}^e_g \cdot \dot{\boldsymbol{\Sigma}}_g + \dot{\mathbf{E}}^v_g \text{ (overall strain rate in the porous grain)} \end{aligned} \tag{7.24}$$

$$
\begin{aligned}
\dot{\boldsymbol{\sigma}}_{i,g} &= \mathbf{0} \text{ (for void)} \\
\dot{\overline{\boldsymbol{\sigma}}}_{c,g} &= \frac{1}{1-f_g}\dot{\boldsymbol{\Sigma}}_g \text{ (for bulk crystal)} \\
\dot{\overline{\boldsymbol{\varepsilon}}}_{c,g} &= \mathbb{M}^e_{c,g} \cdot \dot{\overline{\boldsymbol{\sigma}}}_{c,g} + \dot{\overline{\boldsymbol{\varepsilon}}}^v_{c,g} \text{(for bulk crystal)} \\
\dot{\overline{\boldsymbol{\varepsilon}}}_{i,g} &= \frac{1}{f_g}(\dot{\mathbf{E}}_g - (1-f_g)\dot{\overline{\boldsymbol{\varepsilon}}}_{c,g}) \text{(for void)}.
\end{aligned}
\tag{7.25}
$$

Step 8: After the strain rate in the void and the porous grain has been determined, the subsequent step involves calculating the evolution of the void and grain volume fractions. The void and grain volume fractions are then explicitly updated using the following equations:

$$
\begin{aligned}
\dot{f}_g &= (\operatorname{Tr}\dot{\overline{\boldsymbol{\varepsilon}}}_{i,g} - \operatorname{Tr}\dot{\mathbf{E}})f_{old,g}, \quad f_g = f_{old,g} + \dot{f}_g \Delta t \\
\dot{c}_g &= (\operatorname{Tr}\dot{\mathbf{E}}_g - \operatorname{Tr}\dot{\overline{\mathbf{E}}})c_{old,g}, \quad c_g = c_{old,g} + \dot{c}_g \Delta t.
\end{aligned}
\tag{7.26}
$$

Step 9: After determining the local rate quantities in the porous grains, crystals, and voids, the subsequent step involves explicitly updating the current local quantities at $t + \Delta t$ using a similar approach as outlined in Eq. (7.15). Once the local quantities are updated, the next step is to update the critical resolved shear stress using its evolution equation (refer to Girard et al. (2021); Virupakshi and Kowalczyk-Gajewska (2023)).

Step 10: In the final step, based on the updated volume fractions, the overall compliances, stress concentration tensors, and inverse Hill tensors for the elastic components of the porous grains and overall porous polycrystal are updated as outlined in the initialization procedure, point 4 in this section and also Section 7.1. Similarly, based on the updated local stresses at both the grain and bulk crystal levels, the overall viscous compliance, concentration, and inverse Hill tensors are computed for both the porous grain and the overall porous polycrystal, as detailed in Eq. (7.21). These quantities will be utilized in the subsequent step to calculate the rate equations. Finally, all the updated quantities are exported to the global and local output vectors, and this loop will continue to execute until the maximum imposed time is reached.

7.3 Numerical verification of mean field model for FCC porous single crystal

Preliminaries. In this section, the results of the numerical analyses for the FCC porous single crystal, based on unit cell methodology, are compared with the predictions of the additive Mori-Tanaka mean field model, discussed in Chapter 6, Subsection 6.1.1. A finite strain CPFEM formulation, detailed in Chapter 2 (see Section 2.4 for the formulation and Subsection 2.4.4 for the hardening laws, Eq. (2.15)), has been implemented. For comparison with the small strain additive Mori-Tanaka mean field model for porous crystals, the FE model is considered under small strains. A 3D unit cell with a spherical void, as described in Chapter 3 with an initial volume fraction of $f_0 = 1\%$, is considered (refer to Section 3.4). The mesh, generated using ABAQUS, is subsequently exported to the AceFEM package for further analysis. To control the overall triaxiality and Lode parameter, stress-controlled boundary conditions are imposed, as detailed in Chapter 3, Subsection 3.2.6. In this study, the x-direction is designated as the primary loading direction, and the boundary conditions specified in Eq. (3.15) are applied. Additionally, periodic boundary conditions are implemented. The parameters of the hardening model, the elastic constants of the material, and the rate sensitivity coefficient used in the both FE analyses and the MFM model are presented in Tab. 7.1. The triaxialities T = $\frac{1}{3}$ and T = 1, along with the Lode parameter L = -1 and three crystal orientations A, B, and C, as described in Chapter 4 (refer Tab. 4.2), were considered.

TABLE 7.1 Elastic constants (C_{11}, C_{12}, C_{44}), initial critical resolved shear stress (τ_0), hardening model parameters (τ_{sat}, h_0, h_1), latent hardening on non-coplanar and coplanar systems (q, q_0), exponent in the power law (n), and reference shear rate ($\dot{\gamma}_0$).

C_{11} GPa	C_{12} GPa	C_{44} GPa	τ_0 GPa	τ_{sat} GPa	h_0 GPa	h_1 GPa	q	q_0	n	$\dot{\gamma}_0$
170.2	30.5	114.9	0.0384	0.05	0.0581	20.5×10^{-3}	1.4	1.4	20	0.001

Results and Discussion. Fig. 7.1a depicts a comparison of the overall stress vs. strain response, which is computed using both CPFEM and a micromechanical model, for three different crystal orientations. This comparison is carried out within the context of a uniaxial loading scenario, where the triaxiality is set to 1/3, and the Lode parameter is set to -1. When comparing the three orientations, it is evident that the asymmetric orientation A exhibits a stiffer stress response in both the numerical and mean field models. Specifically, the mean field model with secant linearization predicts higher stress values compared to

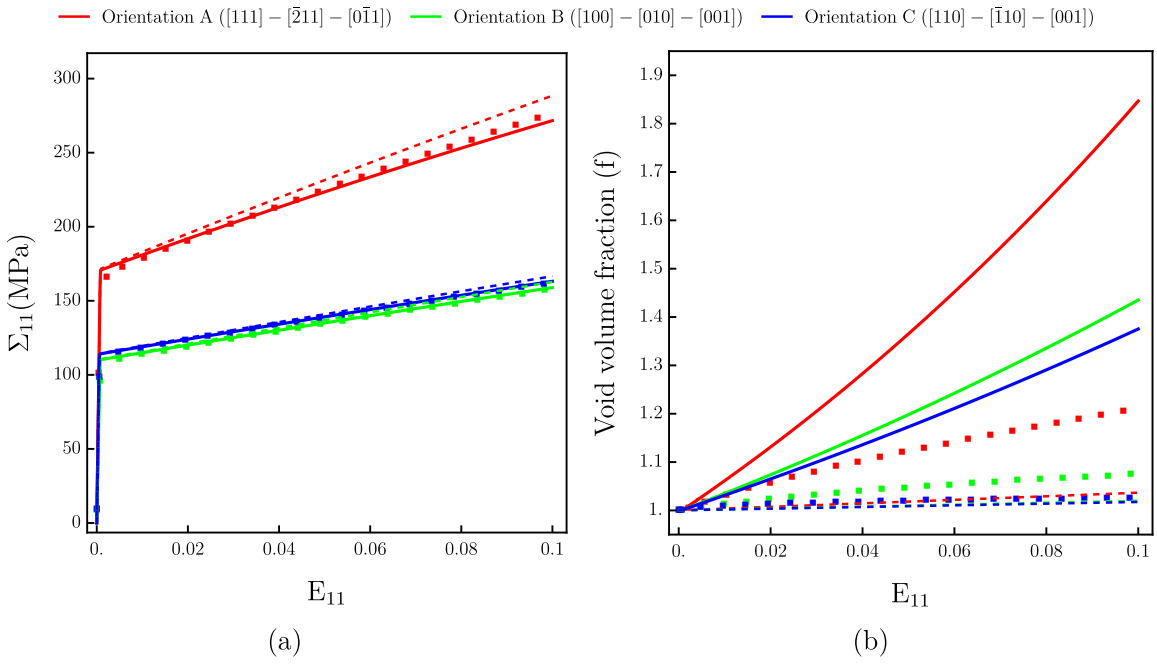

FIGURE 7.1 Comparison of a) overall stress response, b) void volume fraction evolution for FCC porous single crystal using CPFEM and additive Mori-Tanaka scheme with Lode parameter equal -1, triaxiality equal to 1/3 and the initial void volume fraction of 1%. The thick line represents tangent linearization with $\beta = n$, the dashed line represents secant linearization and ■ represents the CPFEM results.

both the tangent linearization and the numerical analyses. In contrast, for the symmetric orientations B and C, the stress response appears to be quite similar. It is evident that the numerical results and the mean field model results are in good agreement, especially tangent linearization and CPFEM results almost coincide.

Fig. 7.1b shows the comparison of void evolution for three crystallographic orientations, calculated using CPFEM and the additive Mori-Tanaka scheme, under a uniaxial loading scenario (Lode parameter = -1 & triaxiality = 1/3). In the context of asymmetric orientation A, void growth is notably more pronounced compared to the symmetric orientations B and C. This holds true for both CPFEM and the micromechanical model. Comparing numerical results and those obtained from the mean field model, it is evident that the tangent linearization tends to overestimate the void growth due to high compliance of the matrix, while the secant linearization results in nearly negligible void expansion. To harmonize the mean field results with the numerical data, the value of β (generalized linearization exponent) must be adjusted to fall within the range of 1 to n.

Fig. 7.2a illustrates the comparison of the overall stress vs. strain response between the

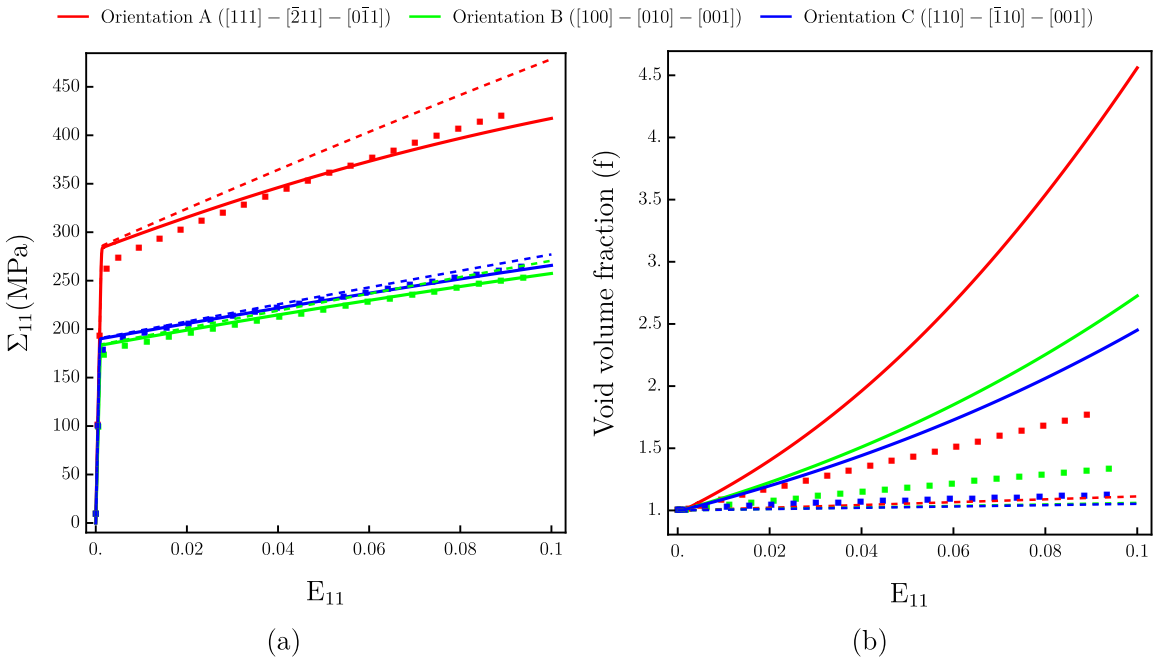

FIGURE 7.2 Comparison of a) overall stress response, b) void volume fraction evolution for FCC porous single crystal using CPFEM and additive Mori-Tanaka scheme with Lode parameter equal to -1, triaxiality equal to 1 and the initial void volume fraction of 1%. The thick line represents tangent linearization with $\beta = n$, the dashed line represents secant linearization and ■ represents the CPFEM results.

mean field model and CPFEM for three crystal orientations under higher triaxiality of 1 and a Lode parameter of -1. Similar to Fig. 7.1a, orientation A displays a more pronounced hard stress response in contrast to the symmetric orientations B and C. When the overall stress response between uniaxial loading (Fig. 7.1a) and triaxiality equal to 1 is compared, it becomes apparent that the stress levels along the principal loading direction are higher for the higher triaxiality loading as compared to uniaxial loading. In the case of orientation A, the response from secant linearization significantly deviates and overestimates the numerical response, primarily due to the low compliance of the matrix when compared to the tangent linearization. Conversely, for symmetric orientations B and C, the disparity between the numerical and mean field results is less conspicuous.

Fig. 7.2b presents a comparison of void evolution between mean field model and CPFEM for three crystal orientations under higher triaxiality of 1 and a Lode parameter of -1. Due to the higher triaxiality, significant void growth is observed when compared to Fig. 7.1b. Similarly to uniaxial loading in Fig. 7.1b, pronounced void growth is seen for hard orientation A when compared to soft and symmetric orientations B and C. The soft

TABLE 7.2 Elastic constants (C_{11}, C_{12}, C_{44}), initial critical resolved shear stress (τ_0), hardening model parameters (τ_{sat}, h_0, h_1), latent hardening on non-coplanar and coplanar systems (q, q_0), exponent in the power law (n), and reference shear rate ($\dot{\gamma}_0$).

C_{11} GPa	C_{12} GPa	C_{44} GPa	τ_0 GPa	τ_{sat} GPa	h_0 GPa	h_1 GPa	q	q_0	n	$\dot{\gamma}_0$
150	75	37.5	0.06	0.097	0.0	0.0×10^{-3}	1.4	1.4	10	0.001

compliance of the matrix in the tangent linearization results in an over prediction of void evolution when compared to numerical analyses, whereas almost negligible void growth is observed for secant linearization due to the high stiffness of the matrix similarly to results presented in Fig. 7.1b. As previously discussed, one possibility can be to adjust the value of the generalized linearization exponent (β), to match the mean field response with that of the numerical results. Another possibility is to incorporate second moment of stress to calculate linearized viscous compliance as proposed in Lebensohn et al. (2011); Bieniek et al. (2024).

7.4 Numerical verification of homogenized mean field model results for FCC porous polycrystals

In this section, the results of numerical analyses of FCC porous polycrystals based on the unit cell methodology are compared with the predictions of the two-step mean field micromechanical model, as discussed in Chapter 6, Subsection 6.1.2. First, all the details concerning the full-field FE analyses are elaborated, followed by the implementation of the MFM model. A finite strain rate-dependent crystal plasticity model is implemented for FCC crystals, even though small strains are considered for the analyses, as explained in Chapter 2 (refer to Section 2.4 for the formulation and Subsection 2.4.4 for the hardening laws). The parameters of the hardening model, the elastic constants of the material, and the value of the rate sensitivity coefficient used in the FE analyses are shown in Tab. 7.2. The FE implementation is explained in Chapter 3, Section 3.1.

7.4.1 Finite element mesh and boundary conditions

As explained in Chapter 3, Section 3.3, a 3D unit cell geometry with a spherical void is generated using the commercial FE package ABAQUS (Version 6.13) (Fig. 3.4). This unit cell represents a single crystal containing a spherical void. In the present

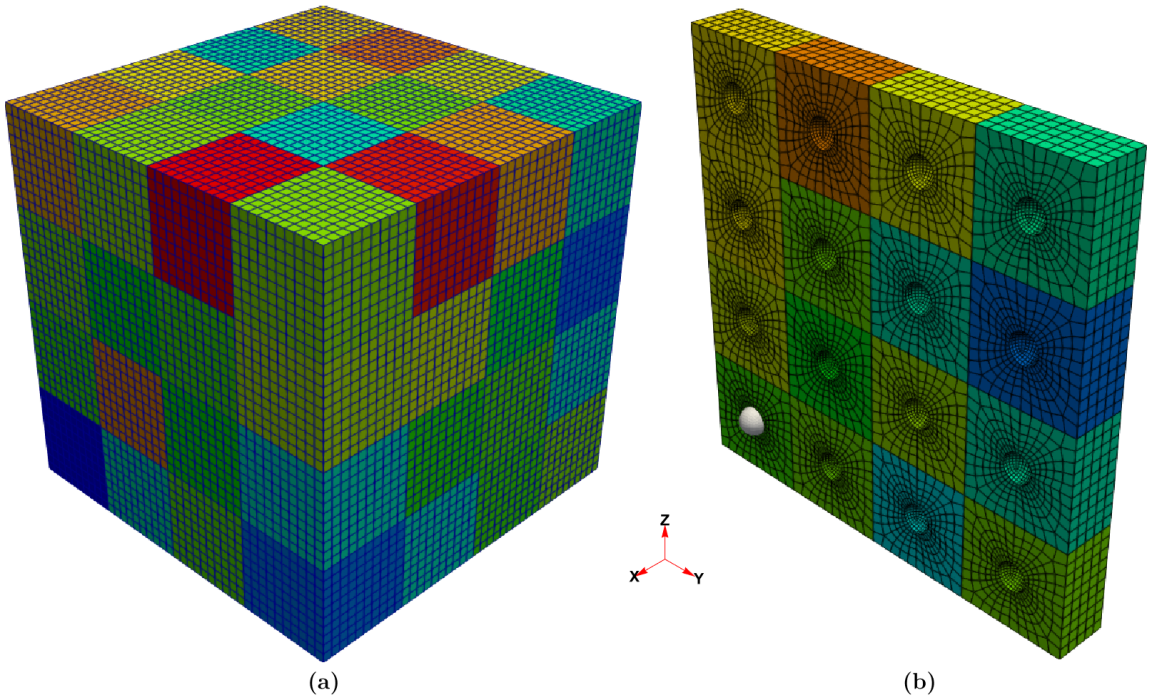

FIGURE 7.3 a) Finite element mesh of 3D porous polycrystal with spherical voids of same overall and local initial volume fraction ($\bar{f}_0 = f_0 = 1\%, 3\%$), b) cross sectional view of the porous polycrystal unit cell ($f_0 = 1\%$) cut at $x = 0.5$, gray spherical ball represents the contact surface elements in one of the voids.

analysis, two initial void volume fractions of $f_0 = 1\%$ and 3% are considered. The mesh data is then imported into Wolfram Mathematica for further preprocessing, analysis, and post-processing.

The resultant mesh data, representing a porous single crystal unit cell, serves as the building block for generating a porous polycrystal. Through additional preprocessing in Mathematica, the single unit cell is replicated within a 4x4x4 cube, resulting in 64 porous unit cells. Each unit cell is then randomly assigned with orientations in terms of Euler angles, which define the unit cell orientations relative to the sample axes. Fig. 7.3a shows the 3D porous polycrystal with "H1" element topology, following the AceGen convention. Each color represents different orientation of the crystal relative to the sample axes. Fig. 7.3b presents the cross-sectional view of the unit cell with $f_0 = 1\%$, cut at $x = 0.5$. A special contact surface elements are attached to the void surface to track the current volume of each void, based on the average deformation gradient of the void, defined as follows:

$$\overline{\mathbf{F}}_{\text{void}} = \frac{1}{V_0}\int_{\partial V} \mathbf{x} \otimes \mathbf{N}\, dS = \frac{1}{V_0}\sum_{ig} \mathbf{x}_{ig} \otimes \mathbf{N}_{ig} w_{ig}, \tag{7.27}$$

where V_0 is the initial void volume, $\mathbf{x}_{ig}$ is the current coordinate of the integration point ig, $\mathbf{N}_{ig}$ is the normal to the contact elements at ig in the initial configuration and w_{ig} is a Gauss weight defining the area corresponding to ig in the initial configuration. In the FE analyses, the numerical integration is carried out at each integration point ig of the contact surface elements corresponding to a given void.

Concerning boundary conditions, to study the overall and local behavior of the porous polycrystal, different values of the constant Lode parameter and stress triaxialities are imposed. For this purpose, stress-controlled boundary conditions are utilized, as explained in Chapter 3, Subsection 3.2.6. In the present study, the x-direction is considered as the primary loading direction, and the boundary conditions specified in Eq. (3.15) are applied. Depending on the given Lode parameter and triaxiality, the stress direction, which is a function of η_1 and η_2, is defined. In addition to the stress-controlled boundary conditions, periodic boundary conditions, as discussed in Chapter 3, Subsection 3.2.2, are also implemented.

The numerical implementation of the two-step homogenized mean field model for porous polycrystals, as explained in Section 7.2, is executed in Wolfram Mathematica. The same material parameters presented in Tab. 7.2 and the same Euler angles used in the unit cell computations are applied. Concerning the boundary conditions, similarly to the full-field model, the overall stress direction is imposed in terms of the stress ratios η_1 and η_2, and the overall strain rate component in the x-direction is applied, as explained in Eq. (7.23).

7.4.2 Results and Discussion

In the current study, both the crystal plasticity finite element method (CPFEM) and the mean field model (MFM) were applied using a combination of Lode parameters, triaxialities, and initial void volume fractions. Specifically, Lode parameters of $L = -1$, representing axisymmetric loading, and $L = 0$, representing pure shear non-axisymmetric loading, were considered. Additionally, low and high triaxialities of $\frac{1}{3}$ and 3 were imposed to examine the overall and local responses of the FCC porous polycrystal. Furthermore, two initial void volume fractions, $f_0 = 1\%$ and $f_0 = 3\%$, were considered in the analysis. Since the MFM is formulated within a small strain framework, an overall strain of 5% was imposed in both the CPFEM and MFM calculations. Although the main objective is to compare the global and local responses of the CPFEM and MFM models, full field results in terms of the space distribution of equivalent Huber-Mises stress are also presented.

In CPFEM, both first and second moment of Huber-Mises equivalent stress are

calculated, they are defined as follows:

$$\overline{\Sigma}_{\text{eq}} = \sqrt{\frac{3}{2}\langle \mathbf{s} \rangle \cdot \langle \mathbf{s} \rangle}$$
$$\overline{\overline{\Sigma}}_{\text{eq}} = \sqrt{\frac{3}{2}\langle \mathbf{s} \cdot \mathbf{s} \rangle}, \tag{7.28}$$

where $\mathbf{s}$ is the deviatoric part of Cauchy stress tensor and the average ($\langle \cdot \rangle$) is performed over all the Gauss points. $\overline{\Sigma}_{\text{eq}}$ is the overall first moment of stress and it is calculated based on average stress tensor over all Gauss points, whereas $\overline{\overline{\Sigma}}_{\text{eq}}$ is the overall second moment of stress, in which square root of the average of square of equivalent stress (i.e, σ^2_{eq}) is performed over all Gauss points.

Fig. 7.4 illustrates the space distribution of equivalent stress for axisymmetric loading $L = -1$ with an imposed triaxiality of $T = 3$ at a overall strain level of 5%. Each slice represents the cross-sectional views cut along the x-direction. The first notable observation is that, across all cross-sections large differences between voids growth are observed, some voids exhibit rapid growth, while in few unit cells, the voids do not grow at all, even though overall high triaxiality is being imposed. Additionally, the distribution of equivalent stress is heterogeneous, being predominantly localized around the voids and exhibiting distinctive patterns. Furthermore, the voids are not only rotating but also evolving into various shapes, particularly polygonal shapes with rounded corners. This shows that one additional aspect yet to be studied is the influence of the orientations of neighboring crystals on void growth. In Fig. 7.4c, it can be observed that voids in the second row are experiencing significant growth and the stress is localized between the grains. This will lead to onset of intervoid necking-based failure. Similar experimental observations were reported by Naragani et al. (2020).

7.4.2.1 Macroscopic response

Normalized volume fraction evolution plots. Fig. 7.5(a, b) compares the overall normalized void volume fraction between two Lode parameters of -1 and 0, with imposed triaxialities of 1/3 and 3, and initial overall void volume fractions ($\bar{f}_0$) of 1% and 3%. The comparison is made between the results from CPFEM and the porous polycrystal (MFM). For Lode parameters of $L = -1$ and 0, it is observed that void growth is more pronounced in CPFEM compared to the mean field model (MFM). CPFEM predictions are closer to reality due to its full-field nature. When triaxiality is higher ($T = 3$), void growth is significantly more pronounced than at $T = 1/3$ for both Lode cases of $L = -1$ and 0. Under the higher triaxiality ($T = 3$), comparing the Lode cases in MFM shows that

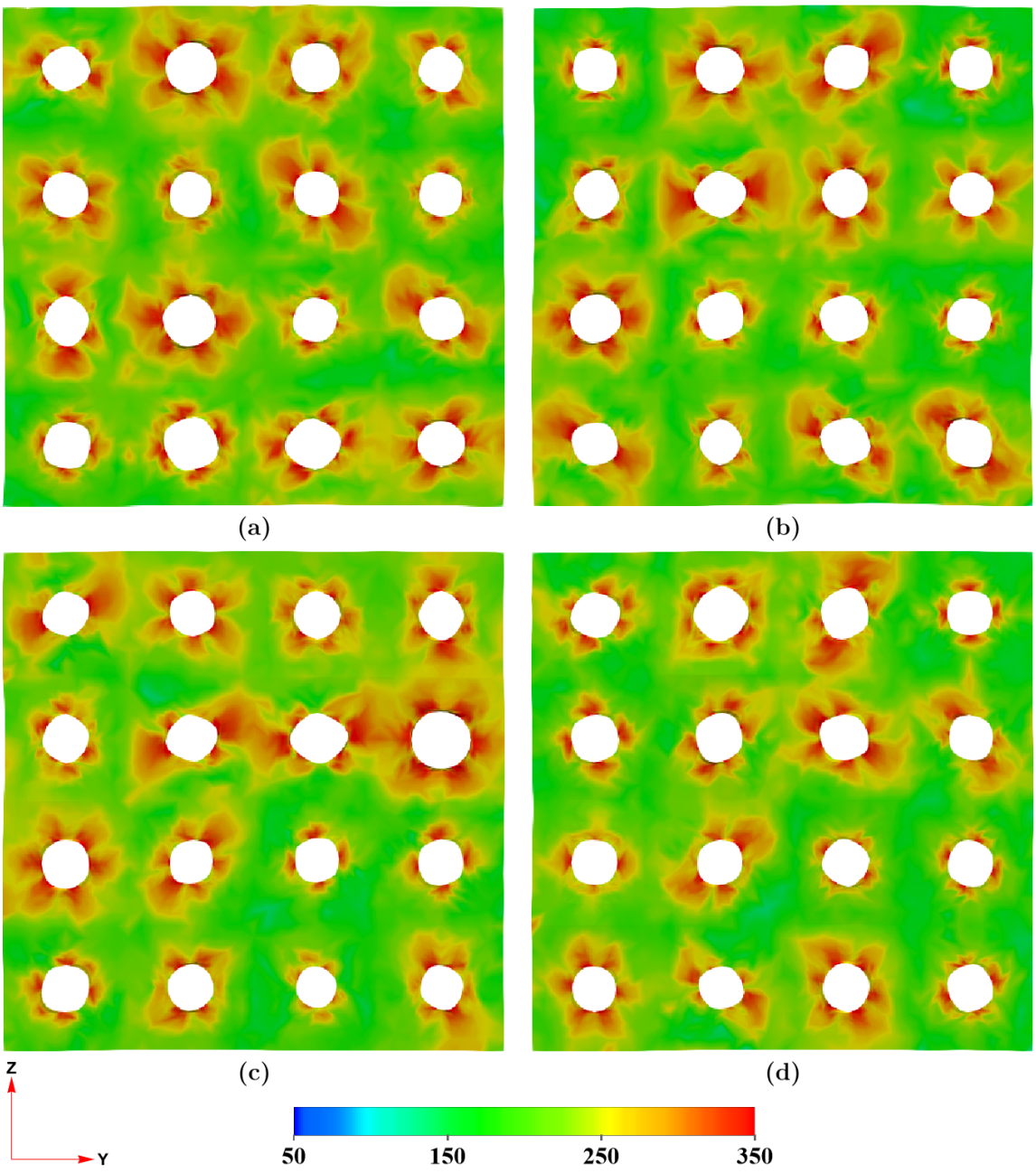

FIGURE 7.4 Space distribution of equivalent stress (in MPa) for axisymmetric loading ($L = -1$), under high triaxiality ($T = 3$) at a strain level of 5%, with an initial void volume fraction $f_0 = 1\%$ (in each grain), cross-sectional view at: a) $x = 0.5$, b) $x = 1.5$, c) $x = 2.5$, d) $x = 3.5$.

$L = -1$ (the axisymmetric case) results in greater void evolution for both initial volume fractions of $\bar{f}_0$ = 1% and 3%. In contrast, for CPFEM, at an initial volume fraction of 1%, both $L = -1$ and 0 exhibit similar high void evolution. However, at 3% void volume fraction, $L = 0$ shows slightly higher void evolution than $L = -1$, although both are

lower than the 1% case. Therefore, void growth is more rapid in the axisymmetric case ($L = -1$) and is particularly pronounced when the initial volume fraction is lower, i.e, 1%. Fig. 7.6(a, b) compares the overall normalized void volume fraction plots for Lode

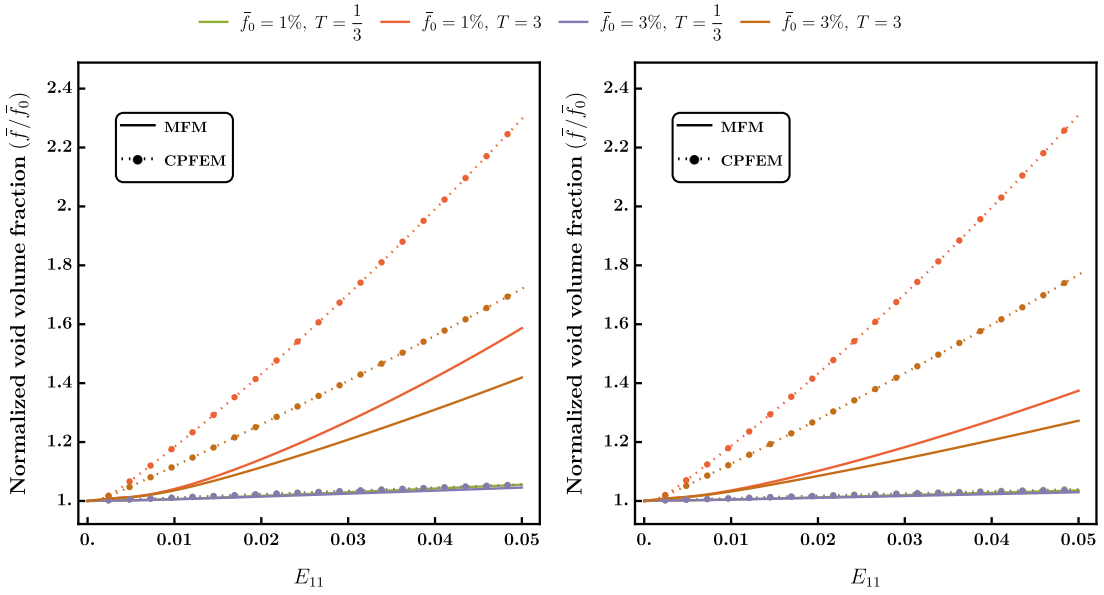

(a) $L = -1$ (b) $L = 0$

FIGURE 7.5 Overall normalized void evolution plots with imposed triaxialities of 1/3 and 3 for Lode parameter a) $L = -1$, b) $L = 0$.

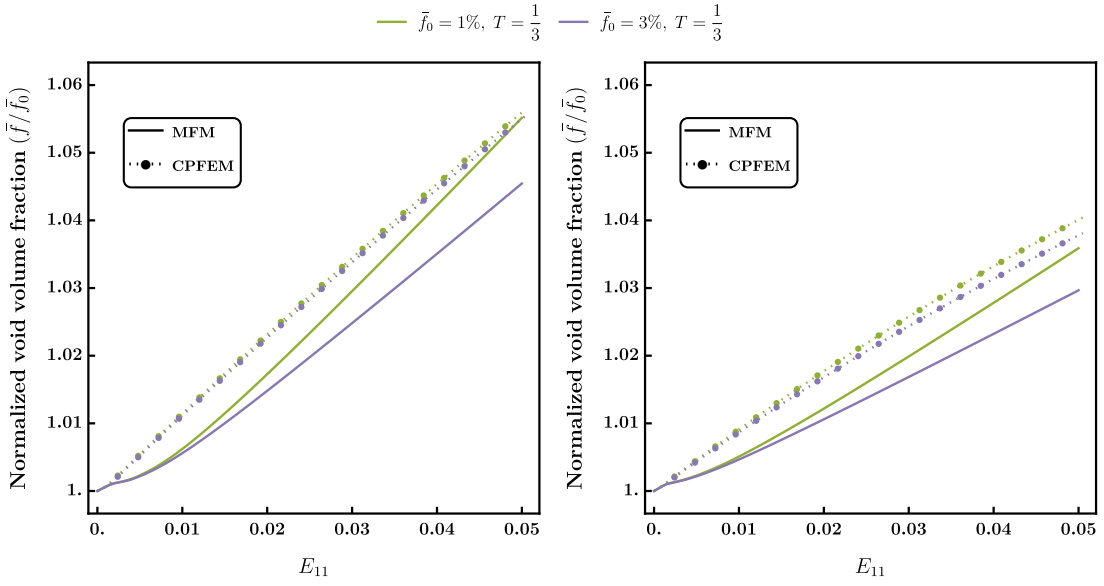

(a) $L = -1$ (b) $L = 0$

FIGURE 7.6 Overall normalized void evolution plots with imposed triaxiality of 1/3 for Lode parameter a) $L = -1$, b) $L = 0$.

parameters $L = -1$ and 0, with an imposed triaxiality of $T = 1/3$, and initial volume fractions of 1% and 3% for both the mean field model and CPFEM. Similar to the case of higher triaxiality $T = 3$, it is clearly seen that void evolution is greater for CPFEM compared to the mean field model for both Lode cases 0 and -1. Nevertheless, for both models, greater void growth is observed under axisymmetric loading conditions ($L = -1$) with an initial overall volume fraction of 1%. In contrast, void evolution is less pronounced for L = 0 and $\bar{f}_0 = 3\%$.

Equivalent stress plots. Fig. 7.7 compares the overall first moment equivalent stress between the mean field and CPFEM models, focusing on Lode parameters $L = -1$ and $L = 0$ under triaxialities $T = 1/3$ and 3 with overall initial volume fractions of 1% and 3%. Additionally, a pristine case is included for $L = -1$ for verification purpose. A higher magnitude of equivalent stress is predicted by the mean field model compared to CPFEM in all scenarios. This difference is also seen for the pristine polycrystal case, contrary to the porous single crystal analysis in previous section, due to the heterogeneity of the polycrystalline RVE. It should be reminded that the secant linearization is used for the self-consistent homogenization of grain aggregate within the second step of MFM procedure, so this observation is consistent with the literature results showing overly stiff predictions of secant scheme as compared to full-field results, cf. (Tome and Lebensohn, 2023). When the pristine polycrystal is compared to the polycrystal with an initial overall void volume fraction of 1% in both MFM and CPFEM, a harder stress response is observed in the pristine case under triaxialities $T = 1/3$ and $T = 3$, with results nearly coinciding. In contrast, a noticeable difference in equivalent stress levels is observed for $\bar{f}_0 = 1\%$ with triaxiality $T = 3$, exhibiting a lower magnitude. Under triaxiality $T = 1/3$, for the given initial void volume fraction, $L = -1$ shows a higher stress magnitude compared to $L = 0$. Additionally, for $T = 1/3$ in both MFM and CPFEM models, a harder stress response is noted for $L = -1$ and $\bar{f}_0 = 1\%$, while a lower magnitude is observed for $L = 0$ and $\bar{f}_0 = 3\%$. A similar response is observed under triaxiality $T = 3$ as well for mean field model. Furthermore, significant void growth is observed in the CPFEM plots under $T = 3$, leading to a softening stress response for $L = 1$ and $L = 0$, whereas no such softening is observed in the mean field model plots. Another important observation is that under high triaxiality ($T = 3$), the influence of the Lode parameter is negligible in the CPFEM. Similar observations were reported by Barsoum and Faleskog (2011); Nahshon and Hutchinson (2008). Moreover, the softest response is observed for $\bar{f}_0 = 3\%$ compared to $\bar{f}_0 = 1\%$. In the elastic range, CPFEM predictions closely align with the mean field model, but they begin to deviate in the viscoplastic range. It is also important to note that, the differences between the $T = 1/3$ and $T = 3$ cases is larger when the overall mean

stress value is considered.

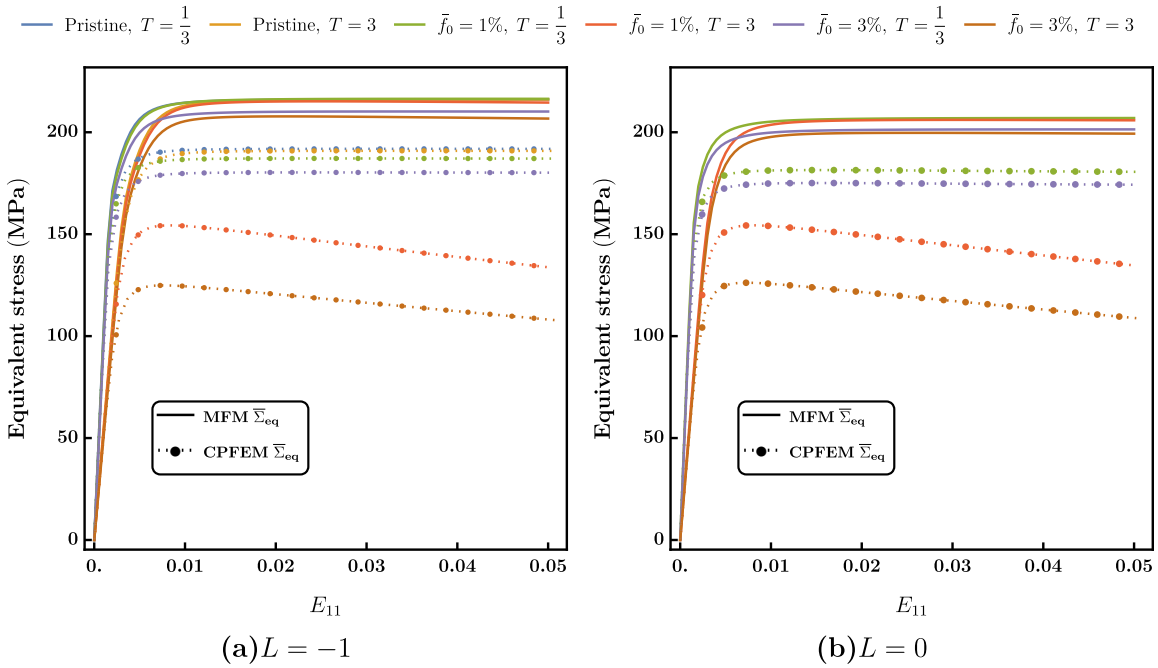

FIGURE 7.7 Overall first moment equivalent stress plots with imposed triaxialities of 1/3 and 3 for Lode parameter a) $L = -1$, b) $L = 0$.

Fig. 7.8 compares the overall equivalent stress plots with parameters similar to those in Fig. 7.7. The key difference is that the overall first moment equivalent stress from the mean field model is compared with the overall second moment equivalent stress from CPFEM. It is important to note that the second moment equivalent stresses are computed only for CPFEM. When the magnitudes of the first moment equivalent stresses are compared with the second moment equivalent stresses of the CPFEM, higher values are predicted for the second moment stresses. This is due to the second moments ability to capture the local plasticity effects, even under imposed hydrostatic stress state. Additionally, it is interesting to observe that the predictions of the first moment stresses from the mean field model are closely aligned with the predictions of the second moment stresses from CPFEM. When the second moment equivalent stresses are compared between a pristine polycrystal and a polycrystal with initial void volume fractions of 1% and 3%, under imposed triaxialities of 1/3 and 3, $L = -1$, it is observed that the pristine polycrystal exhibits a harder response for both triaxialities. As explained before, the overall mean stress values provide clearer distinctions between the high and low triaxiality cases than the equivalent stress. For both cases of $L = -1$ and $L = 0$, and for the given triaxiality, only minimal differences are observed in the magnitude of the second moment equivalent stresses between the initial

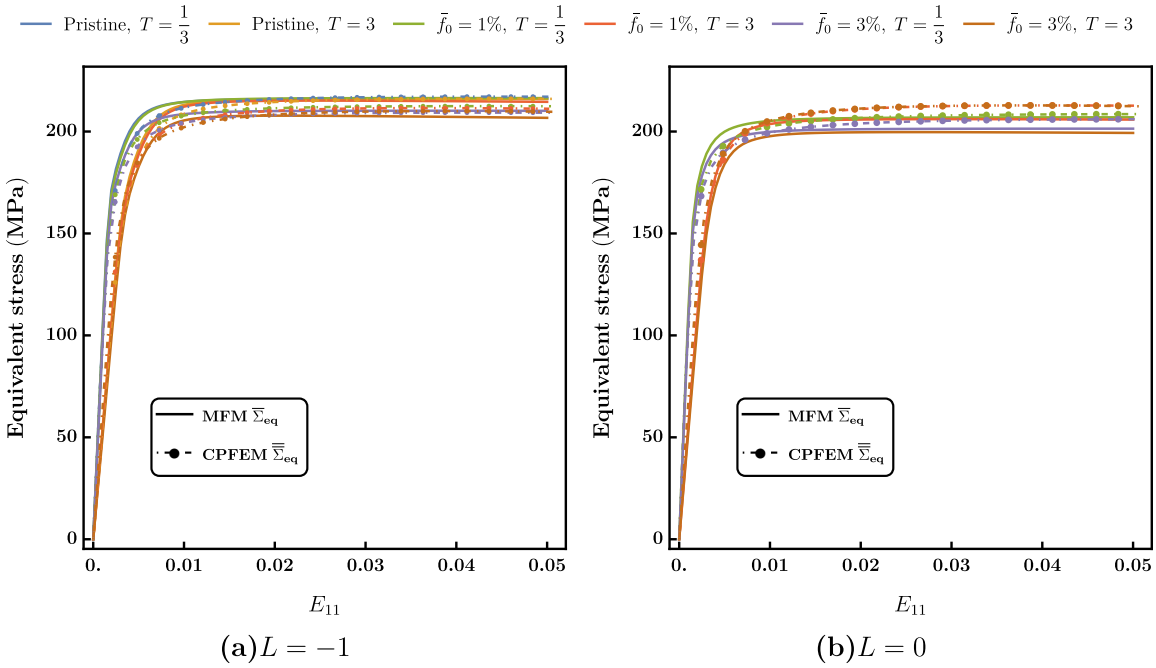

FIGURE 7.8 Comparison of overall first moment equivalent stress from the mean field model with the overall second moment equivalent stress from CPFEM under imposed triaxiality of 1/3 , 3 for Lode parameter a) $L = -1$, b) $L = 0$.

volume fractions of 1% and 3%. When comparing the second moment stresses of the CPFEM model with the first moment stresses of the MFM across both triaxialities and Lode cases, the mean field model with $L = -1$ and $\bar{f}_0 = 1\%$ predicts the stiffest response. As shown in Fig. 7.8b, a harder response is evident for $T = 3$ and $\bar{f}_0 = 1, 3\%$ in the second moment equivalent stress from the CPFEM.

7.4.2.2 Local responses of porous grains

Normalized void volume fraction. Figs. 7.9 and 7.10 illustrate the local normalized void volume fraction plots (i.e. for each grain) for the MFM and CPFEM, respectively, as a function of the porous grain orientation under an imposed triaxiality of $T = 3$ and a macroscopic strain of $E_{11} = 5\%$. The position of each dot in the inverse pole figure indicates the orientation of the primary loading axis (i.e., the x-axis) relative to the local crystal axes of the porous grain g. For the whole discussion of local responses, dots depicted in blue will be referred to as "cold spots", while those in red will be referred to as "hot spots" as representing high and low values of a shown quantity, respectively. The legend for all local plots is generated based on the minimum and maximum values of the

respective quantities.

For the MFM with a Lode parameter $L = 0$, the influence of orientation on void evolution is less significant than with $L = -1$. For both initial void volume fractions, $f_0 = 1\%$ and $f_0 = 3\%$, only selected orientations exhibit void growth, and these orientations are predominantly located in the same spots in the inverse pole figure (IPF) for both volume fractions. In contrast, with $L = -1$, void growth is observed in specific orientations, particularly near the $[\bar{1}11]$ direction[1], and it happens at the same spot for both $f_0 = 1\%$ and $f_0 = 3\%$. Additionally, the trend of void growth for the given orientation is similar for $L = -1$ across both volume fractions. A significant amount of void evolution is shown by groups of orientations near the $[\bar{1}11]$ and $[011]$ directions (see the footnote), compared to other orientations, when the Lode parameter is $L = -1$.

In the CPFEM, significantly more void growth and variability are observed between the orientations, particularly for $f_0 = 1\%$ (with a maximum of 3.71 and a minimum of 1.57 for $L = 0$). For $f_0 = 3\%$, this variability decreases. In all cases, when the magnitude is ignored, the positions of the hot and cold spots in the IPF remain almost the same. Not much difference between $L = 0$ and $L = -1$ for both volume fractions is observed. When the hot spots for both CPFEM and MFM are compared, some deviations are observed. These differences arise due to neighboring orientation effects, which are absent in MFM, and it is clearly visible in CPFEM. The influence of the Lode parameter is less pronounced in CPFEM compared to MFM. When comparing the minimum magnitude of the normalized void volume fraction between MFM and CPFEM, it is found to be smaller in MFM, consistently with the overall void volume fraction evolution presented in Figs. 7.5 and 7.6. Similarly, CPFEM exhibits a higher maximum magnitude than MFM (as indicated in the IPF legend). Among all the cases, the scenario with $L = 0$ and $f_0 = 1\%$ shows the highest maximum magnitude for both CPFEM and MFM.

Equivalent stress plots. Figs. 7.11 and 7.12 depict the local first moment equivalent stress plots for porous grains on the IPF for both MFM and CPFEM, respectively. These plots use the same representation as the normalized void volume fraction plots, under an imposed triaxiality $T = 3$ and a macroscopic strain of $E_{11} = 5\%$. For the MFM with a Lode parameter $L = -1$, the stiff orientations are located near the $[\bar{1}11]$ and $[011]$ directions, while the soft orientations are found near the $[001]$ direction, with the void volume fraction having no influence on these distributions. When the magnitudes for $f_0 = 1\%$ and $f_0 = 3\%$ are ignored, the distributions remain same for $L = -1$. For $L = 0$ and $f_0 = 1\%$ and 3%, the loading is not axisymmetric, which causes the orientation of the secondary axis to play a significant role. This asymmetry leads to the observation of

[1]Note that this observation applies to all symmetrically equivalent directions $\langle 111 \rangle$.

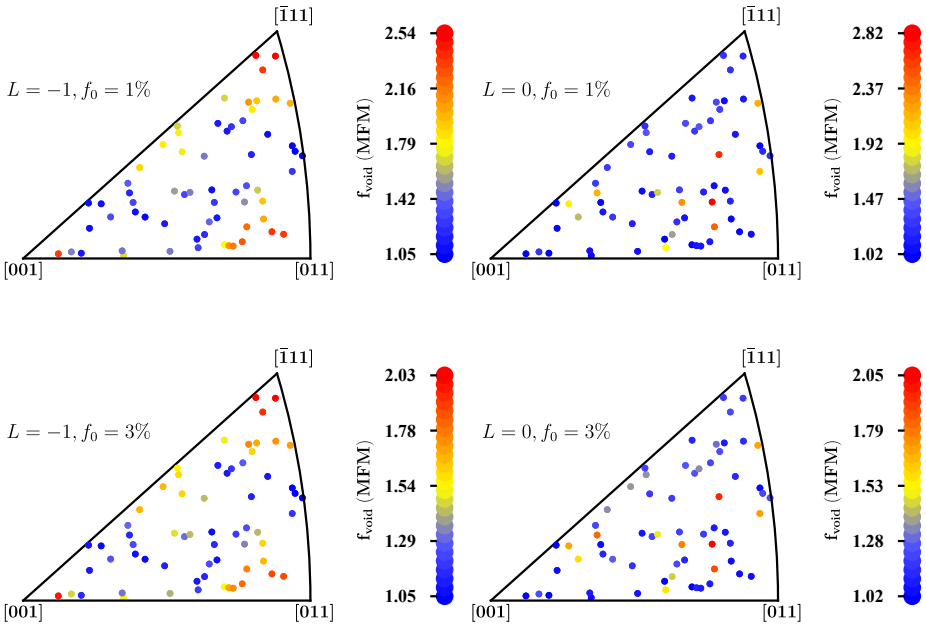

FIGURE 7.9 Local normalized void evolution for the mean field model (MFM) on the inverse pole figure (IPF) under triaxiality $T = 3$ and macroscopic strain $E_{11} = 5\%$, showing void growth across different grain orientations.

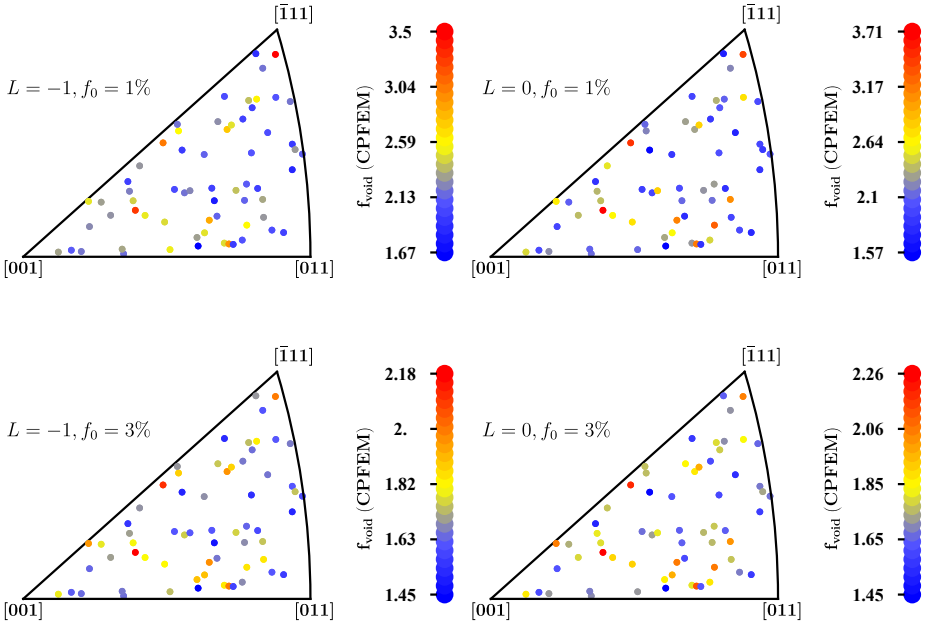

FIGURE 7.10 Local normalized void evolution for the CPFEM on the inverse pole figure (IPF) under triaxiality $T = 3$ and macroscopic strain $E_{11} = 5\%$, showing void growth across different grain orientations.

cold spots within the hot spots. Among all the cases, the spread of equivalent stress is the highest for $L = 0$ and $f_0 = 1\%$. Although some grains exhibit a locally stiffer response (refer hot spots) for $L = 0$ and $f_0 = 1\%$, when comparing it with the global plots, the scenario with $L = -1$ and $f_0 = 1\%$ demonstrates the stiffest overall response.

In the CPFEM model, similar to the MFM, the stiffer orientations are located near the $[\bar{1}11]$ and $[011]$ directions, while the softer orientations are found near the $[001]$ direction. When the magnitude is neglected for $L = -1$, $f_0 = 1\%$ and 3% cases exhibit a similar trend of distribution of spots, with no significant effect of void volume fraction on the cold and hot spots. Like in the MFM, the non-axisymmetric loading causes the secondary orientation to play a role, resulting in the observation of cold spots within hot spots. The highest spread of equivalent stress is observed for $L = 0$, $f_0 = 1\%$. For CPFEM with $f_0 = 3\%$, the spread is similar for $L = 0$ and $L = -1$; however, differences are observed in the MFM for the same case.

CPFEM generally exhibits a softer response than MFM, leading to more pronounced void evolution in CPFEM. While there is a good correlation of hot and cold spots between the CPFEM and MFM models, some discrepancies in magnitude are observed between the two. This suggests that MFM predictions tend to be harder, indicating a need to modify the formulation to achieve a softer response for better alignment with CPFEM results, especially for first moment equivalent stress. Fig. 7.13 outlines the local second moment equivalent stress plot for porous grains on the IPF for the CPFEM model, under an imposed triaxiality T = 3 and a macroscopic strain of $E_{11} = 5\%$. When the first moments of the CPFEM model are compared with the second moments, a strong correlation is observed in the locations of the spots across all cases. However, in certain orientations, the order of magnitude between the first and second moments is reversed i.e., if we take two orientations A & B, orientation A has larger first moment than orientation B but smaller second moment than orientation B. It is also noticed that the magnitude of the second moments in the CPFEM model is greater than that of the first moments in all cases, although the spread of the second moments is smaller compared to the spread of the first moments in the CPFEM model. Mathematically, the first moment equivalent stress should always be less than the second moment equivalent stress (as shown in Eq. (7.28)). Despite some differences observed between the first moments of MFM and the second moments of CPFEM locally, it is surprising that the first moments of MFM are nearly equal to the second moments of the CPFEM model on average across all cases (as indicated by the global plots). Under a hydrostatic stress state, the first moment may lose the effect of local plasticity, whereas the second moment will still capture this effect.

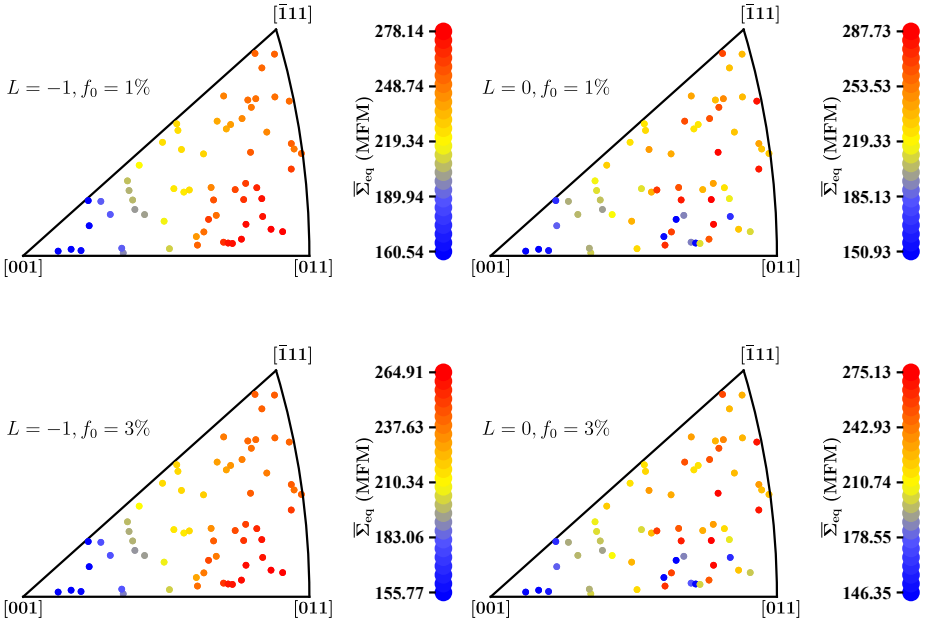

FIGURE 7.11 Local first moment equivalent stress plot for the mean field model (MFM) on the inverse pole figure (IPF) under triaxiality $T = 3$ and macroscopic strain $E_{11} = 5\%$, showing void growth across different grain orientations.

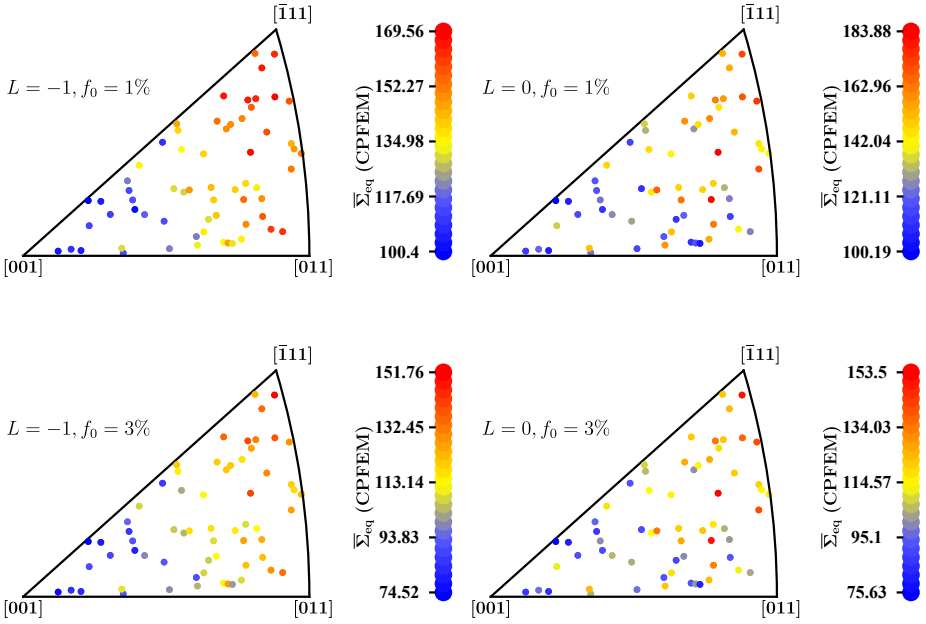

FIGURE 7.12 Local first moment equivalent stress plot for the CPFEM on the inverse pole figure (IPF) under triaxiality $T = 3$ and macroscopic strain $E_{11} = 5\%$, showing void growth across different grain orientations.

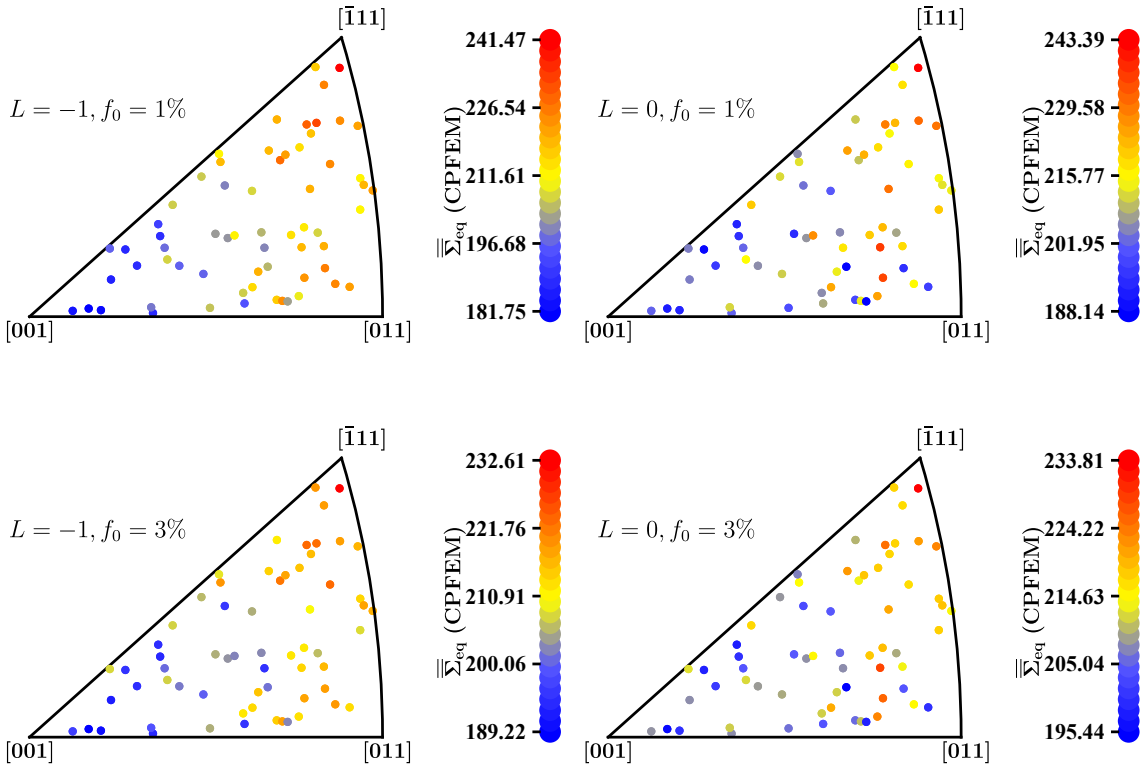

FIGURE 7.13 Local second moment equivalent stress for the CPFEM on the inverse pole figure (IPF) under triaxiality $T = 3$ and macroscopic strain $E_{11} = 5\%$, showing void growth across different grain orientations.

7.5 Summary and conclusions

The numerical implementation for both of the two-scale micromechanical model for porous single crystals, based on the additive Mori-Tanaka scheme, and the three-scale model, which incorporates transition rules at both scales using the additive interaction law developed in the previous chapter, is thoroughly explained. The presented scheme for both porous single and polycrystals can be easily followed and implemented in any computational program. Finally, mean field model predictions were validated with respect to the CPFEM calculations for FCC crystals and polycrystals. The following important conclusions are drawn:

- In FCC porous single crystals, the mean field model with tangent linearization over-predict void evolution due to the soft matrix compliance, while secant linearization shows minimal void growth because of the high stiffness of the matrix.

- In porous polycrystal unit cells, the numerical calculations predicts heterogeneous responses across all cross-sections due to the different orientations of the crystals. Consequently, some voids are observed to exhibit growth, while others are found to remain unchanged, despite the imposition of high triaxiality.

- In unit cell numerical calculations, distribution of stress is heterogeneous being predominantly localized between the voids, leading to intervoid necking failure. This is in agreement with experimental observations were reported by Naragani et al. (2020).

- The mean field model of porous polycrystal underestimates the overall void volume fraction compared to CPFEM, while overestimating the overall equivalent stress levels. This happens mainly due to neglecting local heterogeneities of plastic flow and use of the secant linearization.

- Regarding the local equivalent stress response, a strong correlation is observed, as the orientations on the inverse pole figure with high equivalent stress magnitude (hot spots) and those with low magnitude (cold spots) match closely between the CPFEM and mean field models.

- It is observed in the literature that mean field models incorporating second moments, as seen for instance in Bieniek et al. (2024), produce a softer response compared to models that rely solely on first moment mean values. Therefore, in the future incorporating the second moment of stress to enhance mean field model predictions seems to be necessary.

CHAPTER 8

Phenomenological yield criterion for porous single crystals

In this chapter, the physically-based yield criteria for porous single crystals are discussed. First, two GTN-type yield surfaces for porous single crystals, proposed by Han et al. (2013) and Paux et al. (2018) and already discussed in Chapter 1 (State of the Art), are briefly revisited alongside the constitutive relations. Then, a new yield surface for porous single crystals, derived using a micro-mechanical approach as outlined in Chapter 6, is presented in detail. Following this presentation, the calibration of tuning or fitting parameters is conducted using unit cell calculations for HCP porous single crystals deforming by slip and twinning. Finally, the predictions of the proposed yield criterion are compared with existing models proposed by Han et al. (2013) and Paux et al. (2018) for FCC porous single crystals undergoing deformation by slip.

8.1 GTN-type plastic yield criteria for porous single crystals

Han et al. (2013) multi-surface yield criterion. The formulation proposed by Han et al. (2013) is based on the classical Schmid condition for slip initiation and results in a multi-surface formulation of crystal plasticity. However, this yield criterion has issues related to the non-unique selection of active slip systems, so some energy-based criterion is added to select such systems. As demonstrated in Han et al. (2013), the initiation of plastic slip in FCC porous single crystals is proposed to be governed by the following multi-criterion:

$$\left(\frac{\tau^{\alpha}}{\tau^{\alpha}_{cr}}\right)^2 + a\frac{2}{45}f\left(\frac{\Sigma_{eqv}}{\tau^{\alpha}_{cr}}\right)^2 + 2q_1 f\cosh\left[q_2\sqrt{\frac{3}{20}}\frac{\Sigma_h}{\tau^{\alpha}_{cr}}\right] - (q_1 f)^2 - 1 \leq 0, \quad \alpha = 1,\ldots,12, \tag{8.1}$$

where f is the volume fraction of voids, τ^α is the resolved shear stress, τ^α_{cr} - its critical value, Σ_{eqv} and Σ_h - equivalent Huber-Mises and mean stress, respectively. Tuning parameters: $a = 6.456$, $q_1 = 1.471$, $q_2 = 1.325$ have been identified by Han et al. (2013) by means of unit cell calculations for FCC porous single crystals. The criterion was developed based on the micromechanical variational homogenization method of Ponte Castañeda and Suquet (1998). It should be noted that the initial result of this method is the quadratic criterion which depends on the void volume fraction as shown below:

$$\left(\frac{\tau^\alpha}{\tau^\alpha_{cr}}\right)^2 + \frac{2}{45} f \left(\frac{\Sigma_{eqv}}{\tau^\alpha_{cr}}\right)^2 + f\frac{3}{20}\left(\frac{\Sigma_h}{\tau^\alpha_{cr}}\right)^2 - (1-f)^2 \leq 0, \quad \alpha = 1, \ldots, 12 \tag{8.2}$$

and which is next modified towards the Gurson-type model (for which $q_1 = q_2 = a = 1$ in Eq. (8.1)), relaying on the power expansion of the function $\cosh(x) \sim 1 + 1/2x^2$. Finally, similarly to the classical GTN approach tuning parameters a, q_1, q_2 are introduced. This crystal plasticity GTN-type model was incorporated into the large strain constitutive model and implemented into the finite element code in (Ling et al., 2016). Recently, Khadyko et al. (2021) modified this porous crystal plasticity model through regularization by using KS-function (Kreisselmeier and Steinhauser, 1980) which replaces multi surface condition by a smooth envelope and used it to study ductile fracture in polycrystalline materials.

Paux et al. (2018) yield criterion. The second formulation is based on the regularized Schmid law (Arminjon and Bacroix, 1991; Gambin, 1991) and results in a single yield surface, which enables to avoid the problem of non-unique selection of active slip systems. The corresponding yield criterion takes the form (cited after Paux et al. (2018) in which slightly modified relation as compared to (Paux et al., 2015) was used),

$$\left(\sum_\alpha \left|\frac{\tau^\alpha}{\tau^\alpha_{cr}}\right|^n\right)^{2/n} + 2qf\cosh\left[\kappa'\Sigma_h\right] - (qf)^2 - 1 \leq 0, \tag{8.3}$$

where q, κ' are fitting parameters (q plays a similar role as a q_1 parameter in the first formulation and all other GTN-type approaches, so that it modifies the volume fraction of voids: $f \to qf$). This model is a phenomenological extension of the anisotropic Benzerga-Besson porous yield criterion Benzerga and Besson (2001), which was developed on the basis of the quadratic orthotropic yield criterion due to Hill. For hydrostatic loading, it employs the limit analysis calculation for a hollow sphere whose matrix presents the original (multi-surface and non-porous) Schmid yield locus. More details of the model are to be found in Paux et al. (2018). The proposed model is applicable to crystals of any symmetry; for example, it is used in this thesis for both FCC and HCP porous single crystals.

New proposed criterion based on micromechanical homogenization. The overall viscous compliance of the elasto-viscoplastic porous single crystal has already been formulated in Chapter 6, relaying on the micromechanical model based on the additive Mori-Tanaka scheme. With the use of Eqs. (6.11) and (6.25), the corresponding overall equation for the viscous strain rate takes the form provided below:

$$\dot{\mathbf{E}}^v = \overline{\mathbb{M}}^v \cdot \boldsymbol{\Sigma}, \quad \text{where} \quad \overline{\mathbb{M}}^v = \frac{1}{1-f}\mathbb{M}_c^{v(sc)}\left(\frac{\boldsymbol{\Sigma}}{1-f}\right) + \frac{f}{1-f}\beta\mathbb{M}_*^v, \tag{8.4}$$

where all the quantities have already been defined in Chapter 6. Consider the limit creep-like scenario where $\dot{\boldsymbol{\Sigma}} = \mathbf{0}$, which implies that $\dot{\mathbf{E}} = \dot{\mathbf{E}}^v$. Let's calculate the stress power at this stage of the loading using the formula $\boldsymbol{\Sigma} \cdot \dot{\mathbf{E}} = \boldsymbol{\Sigma} \cdot \dot{\mathbf{E}}^v$, where $\dot{\mathbf{E}}^v = \overline{\mathbb{M}}^v \cdot \boldsymbol{\Sigma}$, so the stress power will be $\boldsymbol{\Sigma} \cdot \overline{\mathbb{M}}^v \cdot \boldsymbol{\Sigma}$. Employing this quantity as indicator of material effort, the following yield surface is proposed:

$$\frac{\boldsymbol{\Sigma} \cdot \overline{\mathbb{M}}^v \cdot \boldsymbol{\Sigma}}{(1-f)\dot{\gamma}_0\tau_0} \overset{\text{def}}{=} 1. \tag{8.5}$$

Note that the denominator includes a local reference stress power for bulk crystal. Here, $\dot{\gamma}_0$ represents the reference shear rate, τ_0 denotes the minimum critical resolved shear stress chosen from the provided CRSS of slip and twin systems, $\boldsymbol{\Sigma}$ is the overall macroscopic stress imposed.

The quadratic like form $\boldsymbol{\Sigma} \cdot \overline{\mathbb{M}}^v \cdot \boldsymbol{\Sigma}$ is to be expanded for a macroscopic stress defined as $\boldsymbol{\Sigma} = \alpha\mathbf{N}$, where α represents the magnitude of the overall stress and $\mathbf{N}$ denotes the stress direction. By considering N slip systems and M twin systems separately, the following form for $\mathbb{M}_c^{v(sc)}$ is adopted (see Eq. (6.4)):

$$\mathbb{M}_c^{v(sc)} = \dot{\gamma}_0 \sum_{r=1}^{N} \frac{1}{\tau_{cr}^r}\left(\frac{|\tau^r|}{\tau_{cr}^r}\right)^{n-1} \mathbf{p}^r \otimes \mathbf{p}^r + \dot{\gamma}_0 \sum_{r=1}^{M} \frac{1}{\tau_{cr}^r}\left(\frac{\langle\tau^r\rangle}{\tau_{cr}^r}\right)^{n-1} sgn(\langle\tau^r\rangle)\mathbf{p}^r \otimes \mathbf{p}^r. \tag{8.6}$$

For the considered stress direction, utilizing the resolved shear stress relation $\boldsymbol{\tau}^r = \overline{\boldsymbol{\sigma}}_c \cdot \mathbf{p}^r = \frac{\boldsymbol{\Sigma}\cdot\mathbf{p}^r}{1-f} = \frac{\alpha\mathbf{N}\cdot\mathbf{p}^r}{1-f}$, and by defining the critical resolved shear stress (CRSS) in terms of the CRSS ratio (β^r) as $\tau_{cr}^r = \beta^r\tau_0$, Eq. (8.6) can be expanded as follows:

$$\mathbb{M}_c^{v(sc)} = \frac{\dot{\gamma}_0(\frac{\alpha}{\tau_0})^{n-1}}{\tau_0(1-f)^{n-1}} \Bigg(\underbrace{\sum_{r=1}^{N}\left(\frac{|\mathbf{N}\cdot\mathbf{p}^r|}{\beta^r}\right)^{n-1}\frac{\mathbf{p}^r\otimes\mathbf{p}^r}{\beta^r} + \sum_{r=1}^{N}\left(\frac{\langle\mathbf{N}\cdot\mathbf{p}^r\rangle}{\beta^r}\right)^{n-1} sgn(\langle\mathbf{N}\cdot\mathbf{p}^r\rangle)\frac{\mathbf{p}^r\otimes\mathbf{p}^r}{\beta^r}}_{\widetilde{\mathbb{M}}_c^v} \Bigg). \tag{8.7}$$

Similarly, by using the fact that $\mathbb{M}_*^v$ is a linear function of $\overline{\mathbb{M}}_c^v$, we may write that

$$\mathbb{M}_*^v = \frac{\dot{\gamma}_0(\frac{\alpha}{\tau_0})^{n-1}}{\tau_0(1-f)^{n-1}}\tilde{\mathbb{M}}_*^v(\tilde{\mathbb{M}}_c^v). \tag{8.8}$$

Using Eqs. (8.7) and (8.8), the overall viscous compliance in Eq. (8.4) can be calculated as:

$$\overline{\mathbb{M}}^v = \frac{\dot{\gamma}_0(\frac{\alpha}{\tau_0})^{n-1}}{\tau_0(1-f)^{n}}[\tilde{\mathbb{M}}_c^v + \beta f\tilde{\mathbb{M}}_*^v(\tilde{\mathbb{M}}_c^v)]. \tag{8.9}$$

In general, $\tilde{\mathbb{M}}_c^v$ is anisotropic, so the Hill tensor $\tilde{\mathbb{M}}_*^v$ must be obtained performing numerical integration of respective polarization tensor (see Eq. (6.16)). At this stage, to simplify the calculations, $\tilde{\mathbb{M}}_*^v$ will be obtained by performing isotropization of $\tilde{\mathbb{M}}_c^v$, assuming spherical shape of the void and using the closed form result (8.10) of Eq. (6.16) for such case.

For isotropic $\tilde{\mathbb{M}}_c^v$, the inverse Hill tensor ($\tilde{\mathbb{M}}_*^v$) written in terms of hydrostatic and deviatoric projectors ($\mathbb{I}^P, \mathbb{I}^D$) is:

$$\tilde{\mathbb{M}}_*^v = (h_*^P)^{-1}\mathbb{I}^P + (h_*^D)^{-1}\mathbb{I}^D, \tag{8.10}$$

where $h_*^{P^{-1}}, h_*^{D^{-1}}$ can be calculated as follows :

$$h_0^{D^{-1}} = \mathrm{Tr}[\tilde{\mathbb{M}}_c^v \cdot \mathbb{I}^{\mathbb{D}}]/5,\ h_*^{P^{-1}} = \frac{h_0^{D^{-1}}}{2},\ \ h_*^{D^{-1}} = \frac{2}{3}h_0^{D^{-1}}. \tag{8.11}$$

In the case of FCC crystals for which only slip systems are active, the $\overline{\mathbb{M}}_c^v$ calculated for $n = 1$ is not influenced by the stress direction, thereby exhibiting cubic symmetry. For the $n = 1$ case in HCP crystals, the twin contribution is influenced by the stress direction through the factor $sgn(\langle \mathbf{N} \cdot \mathbf{p}^r \rangle)$ in the second term in Eq. (8.7). The inactivity of certain twin systems may result in a loss of hexagonal symmetry. On the other hand, since the slip mechanism remains unaffected by the stress direction, transverse isotropy is retained for the slip component in Eq. (8.7).

Finally, by substituting all terms into the proposed yield surface (Eq. (8.5)), and applying the binomial expansion for $(1-x)^n$ as well as the hyperbolic cosine expansion into a power series ($\cosh x \sim 1 + \frac{x^2}{2}$), the following Gurson-type yield criterion in terms of the equivalent stress (Σ_{eq}) and the mean stress (Σ_m) is obtained:

$$\left(\frac{\alpha}{\tau_0}\right)^{n-1}\left[\frac{\boldsymbol{\Sigma}\cdot\overline{\mathbb{M}}_c^v\cdot\boldsymbol{\Sigma}}{\tau_0^2} + \frac{2f\beta\Sigma_{eq}^2}{3h_*^D\tau_0^2}\right] + (n+1)f\cosh\left(\sqrt{\left(\frac{\alpha}{\tau_0}\right)^{n-1}\frac{6\beta}{h_*^P(n+1)}}\frac{\Sigma_m}{\tau_0}\right) - 1 - \frac{n(n+1)}{2}f^2 \overset{\text{def}}{=} 0. \tag{8.12}$$

By substituting $n = 1$ and $\beta = 1$, the following quadratic form is recovered:

$$\frac{\boldsymbol{\Sigma} \cdot \overline{\mathbb{M}}_c^v \cdot \boldsymbol{\Sigma}}{\tau_0^2} + \frac{2f\Sigma_{eq}^2}{3h_*^D\tau_0^2} + 2f\cosh\left(\sqrt{\frac{3}{h_*^P}}\frac{\Sigma_m}{\tau_0}\right) - 1 - f^2 \overset{\text{def}}{=} 0. \tag{8.13}$$

It should be reminded that $\tilde{\mathbb{M}}_c^v$ is independent of $\boldsymbol{\Sigma}$ when only slip is considered. By comparing the cosine hyperbolic term in Eqs. (8.12) and (8.13), it was decided to replace non-linear coefficient $\sqrt{\left(\frac{\alpha}{\tau_0}\right)^{n-1}\frac{2\beta}{n+1}}$ by a single scalar parameter q_2. Then Eq. (8.12) simplifies to:

$$\left(\frac{\alpha}{\tau_0}\right)^{n-1}\left[\frac{\boldsymbol{\Sigma} \cdot \overline{\mathbb{M}}_c^v \cdot \boldsymbol{\Sigma}}{\tau_0^2} + \frac{2f\beta\Sigma_{eq}^2}{3h_*^D\tau_0^2}\right] + 2f\cosh\left(\sqrt{\frac{3}{h_*^P}}\frac{q_2\Sigma_m}{\tau_0}\right) - 1 - f^2 \overset{\text{def}}{=} 0. \tag{8.14}$$

Note that similar form of cosine hyperbolic term was obtained by Paux et al. (2018) when generalizing the non-linear regularized Schmid law for porous polycrystals. Moreover, similar to the previous works of Tvergaard and Needleman (1984); Han et al. (2013); Paux et al. (2018) to obtain an agreement with the unit cell numerical calculations, it is proposed to introduce two additional tuning parameters q_1 and κ as follows:

$$\left(\frac{\alpha}{\tau_0}\right)^{n-1}\left[\frac{\boldsymbol{\Sigma} \cdot \overline{\mathbb{M}}_c^v \cdot \boldsymbol{\Sigma}}{\tau_0^2} + \frac{2\kappa f\Sigma_{eq}^2}{3h_*^D\tau_0^2}\right] + 2fq_1\cosh\left(\sqrt{\frac{3}{h_*^P}}\frac{q_2\Sigma_m}{\tau_0}\right) - 1 - (q_1 f)^2 \overset{\text{def}}{=} 0, \tag{8.15}$$

where q_1 modifies volume fraction (porosity enhancement), q_2 is related to the anisotropic parameter and modifies the volumetric term, and κ is controlling the impact of deviatoric term stemming from the interaction between the bulk crystal and the void. One important remark is that the effect of β which is constant depending on the linearization scheme used in the Mori-Tanaka additive model, is incorporated into the tuning parameter κ, and thus, it is not explicitly included in the above equation.

The GTN-type yield criterion proposed above is generally applicable to anisotropic porous crystals with various lattice symmetries deforming by both slip and twinning. However, in the present study, the proposed criterion has been verified only for FCC single porous crystals, focusing solely on deformation by slip mechanism.

8.2 Yield surface of HCP porous crystals deforming by slip and twinning

In the present study, the yield criterion for HCP porous single crystals, as proposed by Paux et al. (2018), is considered. While Paux et al. (2018) considered only slip systems for

the calibration of the yield surface for HCP crystals, the current work incorporated both slip and twinning in Eq. (8.3) to calibrate tuning parameters $\kappa' = \kappa\tau_{cr}^0$ (where $\tau_{cr}^0 = min_k(\tau_{cr}^k)$) and q using unit cell CPFEM calculations.

Again, the rate-dependent crystal plasticity model, which accounts for both slip and twinning as detailed in Chapter 2, is employed to determine the yield point under varying overall stress ratios based on unit cell computations. The elastic constants as outlined in Chapter 5, Tab. 5.2 and the CRSS ratios $\frac{\tau_{cr}^{Pris}}{\tau_{cr}^{Bas}} = 38.6\,, \frac{\tau_{cr}^{Pyr}}{\tau_{cr}^{Bas}} = 46.5\,, \frac{\tau_{cr}^{Twin}}{\tau_{cr}^{Bas}} = 22.3$ with $\tau_{cr}^{Bas} = 2.9$MPa, were applied in the computations. To ensure a perfectly plastic behavior, hardening was suppressed. Furthermore, as the initial plastic strain regime was considered for assessing the yield stress, reorientation due to twinning were also suppressed in the model. Slip and twin systems, as mentioned in Chapter 2, Tab. 2.3, were considered as the primary deformation mechanisms for HCP crystals. In the calculations, overall strain of 2% is imposed along the primary loading direction (i.e, along z direction). To achieve nearly rate-independent behavior, a relatively high value of n (rate exponent) was selected. Additionally, the reference shear rate on the slip systems and an overall imposed strain rate of 0.001 were chosen. When the plastic strain along the principal loading direction reaches 0.2%, the corresponding yield stress values are determined from unit cell calculations for various loading conditions, volume fractions and crystal orientations with respective sample axes. These yield stress values are then used to calibrate the tuning parameters in the yield criterion.

A 3D unit cell with a spherical void was considered. The initial void volume fraction was defined as the ratio of the spherical void volume to the cubic unit cell volume. A finite element model utilizing 3D hexahedral elements, as described in Chapter 3, Fig. 3.4, was employed. Two initial void volume fractions of 1 and 5% were considered. The crystallographic orientations considered in this study are presented in Tab. 8.1. Two crystal orientations are used for calibration, while the third orientation is used for validation of yield surface.

TABLE 8.1 Crystal orientations along with Euler angles (z axes as primary loading direction).

Crystal orientation with respect to global sample axes	Euler angles		
	ϕ_1	Φ	ϕ_2
Orientation 1 (c-axis loading)	0°	0°	0°
Orientation 2 (Prismatic loading)	0°	90°	0°
Orientation 3 ($45°$ loading)	0°	45°	0°

As mentioned in Chapter 3, Subsection 3.2.6, stress-controlled boundary conditions are imposed using stress ratios η_1 and η_2, implemented through a spring element (refer to

the schematic in Fig. 3.2). Consequently, the overall macroscopic Cauchy stress in terms of these stress ratios and the overall macroscopic displacement gradient are represented in Eq. (3.16). By varying the stress ratios, i.e., by imposing different triaxialities, corresponding yield values are obtained from the unit cell computations. Both η_1 and η_2 range from -0.5 to 1. Two cases are considered in this study: one with axisymmetric loading where $\eta_1 = \eta_2$, and the other with $\eta_1 = 0.4$ and η_2 varying. Note that when $\eta_1 = \eta_2 = 1$ for the axisymmetric loading case, purely hydrostatic stress state is imposed on the unit cell. The z-direction is defined as the primary loading direction, and periodic boundary conditions are imposed, as described in Eq. (3.3).

8.2.1 Identification of tuning parameters

The unit cell computations are carried out using the AceFEM package, as described in Chapter 3, Section 3.1. A total of 85 unit cell calculations were performed based on different combinations of crystal orientations, volume fractions, and stress ratios, covering a wide range of stress triaxiality ratios. Out of the 85 unit cell calculations, 65 are used for calibration and the remaining 25 are used to test the model using the obtained tuning parameters. Based on the obtained yield points, the tuning parameters in the yield criterion can be determined using various methods, such as the evolutionary algorithm (e.g., as utilized in Frydrych et al. (2021)) or the Levenberg-Marquardt method. In the present scenario, a non-linear least square error cost function with unknown tuning parameters is constructed using the yield stress values obtained from unit cell calculations, along with the corresponding stress ratios, volume fractions, and crystallographic orientations. The tuning parameters are calculated by minimizing the following cost function:

$$\text{Cost function} = (F_{predicted} - F_{actual})^2 = \sum_{i=1}^{n} \left(F(\sigma_{y_i}, \kappa', q, f_i, \eta_{1_i}, \eta_{2_i}, \phi_{1_i}, \Phi_i, \phi_{2_i}) - 0\right)^2 .$$

This approach is similar to solving a regression problem, where the objective is to reduce the discrepancy between the model results and FE unit cell yield stress values through parameter optimization. In Wolfram Mathematica, the ”NMinimize” function is utilized with the Differential Evolution algorithm to minimize the cost function, thereby identifying the optimal tuning parameters for the yield function. The optimized tuning parameters obtained in this way are presented in Tab. 8.2.

The anisotropic parameter κ' is also alternatively determined by performing a numerical limit-analysis calculation on a single crystal hollow sphere. This process involves the numerical integration of plastic dissipation over all the vertices of the Schmid polyhedron.

TABLE 8.2 Calibrated values of tuning parameters.

κ'	q
0.022	2.224

The set of vertices, which is required for the integration, depends on the crystal structure (here: HCP) and the ratio of the CRSS, i.e. $\frac{\tau_{cr}^{Pris}}{\tau_{cr}^{Bas}}$, $\frac{\tau_{cr}^{Pyr}}{\tau_{cr}^{Bas}}$, $\frac{\tau_{cr}^{Twin}}{\tau_{cr}^{Bas}}$. More details regarding the limit analysis under hydrostatic loading can be found in Paux et al. (2018). While Paux et al. (2018) considered only slip systems, twinning has also been included in the present work to perform the numerical integration. It is significant that the anisotropic parameter κ' value of 0.023, obtained through the analytical method, is found to be close to the value obtained from finite element calibration (0.022). This serves as additional verification of the tuning parameters obtained through unit cell FE computations.

8.2.2 Results and discussion

In this section, the yield stress predicted by the extended Paux et al. (2018) criterion (Eq. (8.3)) are compared with FE unit cell calculations for two loading cases to investigate the effects of crystallographic orientation and porosity on the resulting yield surface. As discussed earlier, nearly perfectly plastic behavior is maintained in the unit cell calculations, and the yield point is extracted. Finally, the physical interpretation of the tuning parameters is discussed and compared with the results of Paux et al. (2018).

In contrast to the multi surface yield criterion for porous single crystals proposed by Han et al. (2013), the Paux et al. (2018) model is based on the regularized Schmid criterion to benefit from a single yield surface for porous single crystals and to avoid non-uniqueness problem. The macroscopic stress in the primary loading direction, as a function of the stress ratios η_1 and η_2, will serve as a representation of the yield surface:

$$\sigma_{33} = F(\eta_1, \eta_2). \tag{8.16}$$

The macroscopic stress is simply a function of η ($\eta_1 = \eta_2 = \eta$) in the case of axisymmetric loading:

$$\sigma_{33} = F(\eta). \tag{8.17}$$

The above relations (8.16) and (8.17) are obtained by substituting the stress tensor given by Eq. (3.16) to the yield function (8.3) and finding σ_{33} as fulfilling the yield conditions. The results of unit cell calculations and predictions of the proposed yield surface for

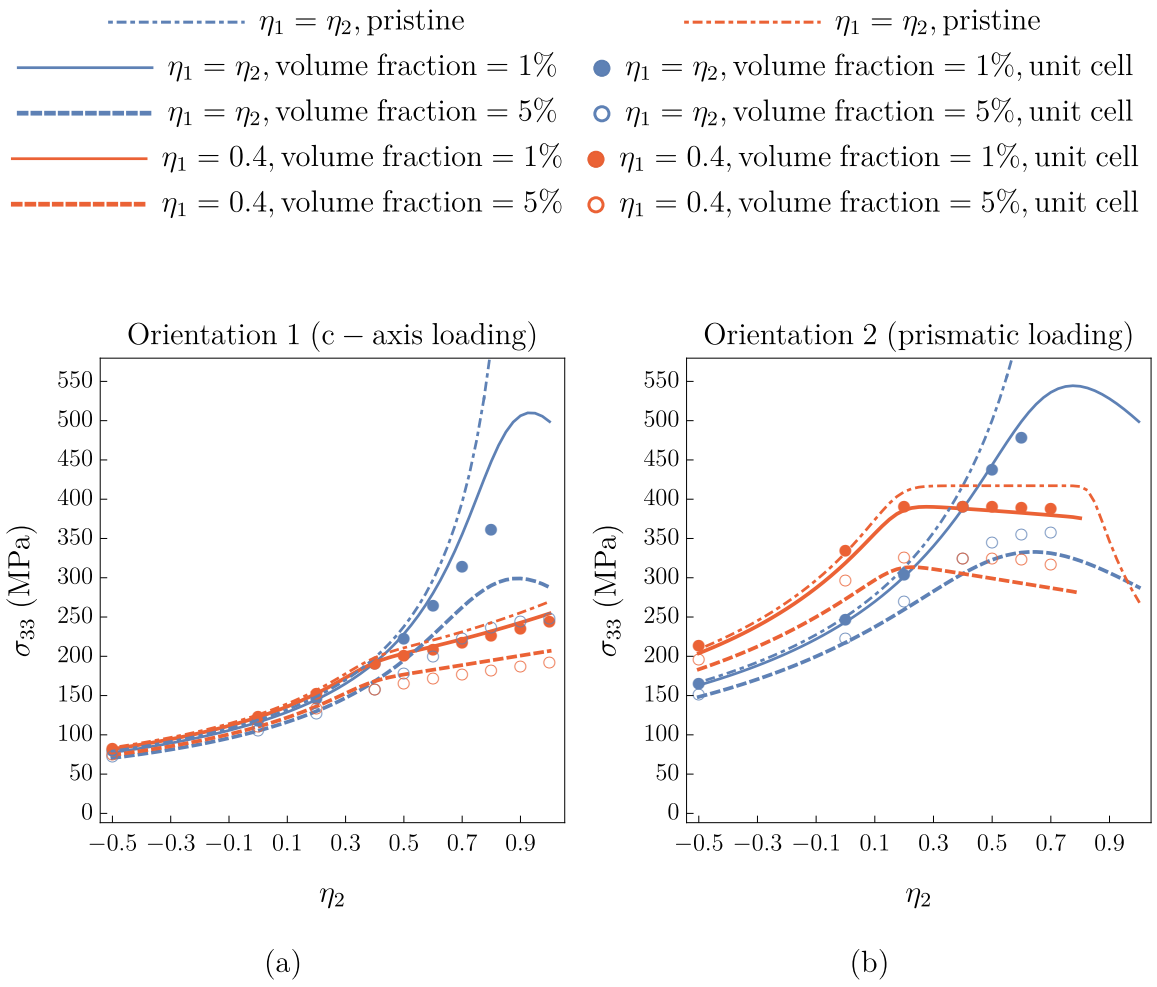

FIGURE 8.1 Yield surfaces for HCP porous single crystals with f = 1% and 5% under loading cases with $\eta_1 = \eta_2$ and $\eta_1 = 0.4$ for a) orientation 1 b) orientation 2. The finite element unit cell calculations are represented by closed and open circles, while the model predictions are represented by thick and dashed lines.

orientations 1 and 2 under axisymmetric loading and η_1 = 0.4 with volume fractions of 1% and 5% are shown in Fig. 8.1. An anisotropic response is observed for different crystallographic orientations due to strong plastic anisotropy of HCP crystals. The yield surface for the model is plotted based on the tuning parameters found (refer to Tab. 8.2). A fairly good fit between the model and unit cell results is evident for both orientations. In orientation 1, the c-axis is aligned along the primary loading direction, z, which makes this orientation more favorable for twinning activity. The yield surface is observed to be smooth, continuous, and differentiable under axisymmetric loading for both 1% and 5%

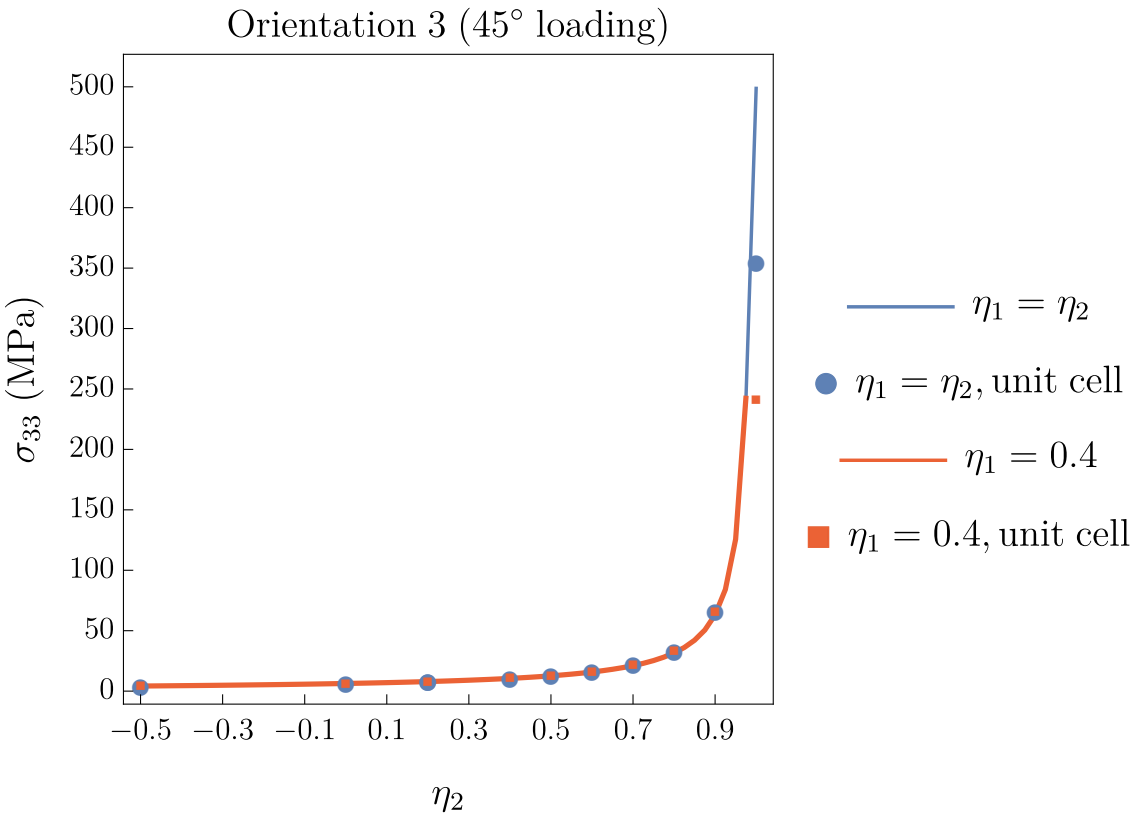

FIGURE 8.2 Yield surfaces for HCP porous single crystals with f = 1 % under loading cases with $\eta_1 = \eta_2$ and $\eta_1 = 0.4$ for orientation 3. The finite element unit cell calculations are represented by closed circles, while the model predictions are represented by thick line. The lines representing the pristine crystal response coincide with those of the new model in the plot (except of infinite value for hydrostatic stress state).

volume fractions. Under $\eta_1 = 0.4$ loading, a rounded-off kink is observed at $\eta_2 = 0.4$. In the multi-surface description of Han et al. (2013) for FCC crystals, the model yield surface is not differentiable at $\eta_2 = 0.4$ under similar loading conditions. In contrast, since the proposed criterion is based on the regularized Schmid law with an exponent n linked to the approximation of the yield surface, the yield surface remains differentiable, even though a kink is still observed at this point. This kink marks the loading case under which the set of active systems changes. In both the model and unit cell calculations, the yield stress is observed to decrease as porosity increases. Importantly, while the yield stress tends to approach infinity in bulk crystals at higher values of η i.e., approaching hydrostatic loading, it remains finite in porous single crystals under the same loading conditions.

In orientation 2 the prismatic axis is oriented along the primary loading direction z. Prismatic slip is the primary slip activity for this orientation. A good fit between model

and unit cell calculations is observed, as in orientation 1. The yield curve remains smooth under axisymmetric loading for both 1% and 5% volume fractions, whereas a rounded-off kink is observed under $\eta_1 = 0.4$ loading, similarly to c-axis loading. As previously, this point physically corresponds to a change in the predominant activity of slip and twin systems. Additionally, as porosity increases, the yield stress value decreases.

The yield surface plots for orientation 3 with a volume fraction of 1% are presented in Fig. 8.2. In this orientation, the primary loading axis is oriented at 45° between the prismatic and c-axis. The primary deformation activity for this orientation is easy basal slip (refer to Chapter 5, Fig. 5.13). This orientation is referred to as the soft orientation. It is observed that the response is similar to that of the bulk crystal in both the model and unit cell calculations. The results from both axisymmetric and $\eta_1 = 0.4$ loading cases are similar for both the unit cell and model calculations. Since the analyzed orientation is a soft one, and the anisotropic parameter (κ') is low, the hyperbolic cosine term in the yield function becomes insignificant over a large range of η, resulting in behavior similar to that of bulk crystals. The hyperbolic cosine term only becomes significant as η approaches the hydrostatic stress state.

The physical significance of the κ' parameter is that as single crystal anisotropy increases, κ' decreases. Consequently, greater plastic anisotropy is associated with higher yield strength under hydrostatic loading, resulting in porous crystals being nearly incompressible (Mbiakop et al. (2015b)). Furthermore, it has been demonstrated that this property is present in low lattice symmetry crystals, such as HCP crystals, which lack five independent slip systems. Orientation 3 demonstrates that for large scope of loading conditions the yield stress is much lower than for the hydrostatic loading conditions, so Mg crystal exhibits similar behavior.

The calculated κ' value for Mg crystals, as reported by Paux et al. (2018), is 0.14. They used CRSS ratios of $\frac{\tau_{cr}^{Pris}}{\tau_{cr}^{Bas}} = 5.5$ and $\frac{\tau_{cr}^{Pyr}}{\tau_{cr}^{Bas}} = 6$, which differ from the values used in the current work. This indicates a higher anisotropy in the current study and accounts for the inclusion of twinning in the calculations. Furthermore, the predicted q value in Paux et al. (2018) is of the order of 2, which is consistent with the findings of the current work.

8.3 Comparison of proposed model predictions with existing proposals for FCC porous crystals

In this section, the proposed yield criterion is compared with the existing proposals of Han et al. (2013) and Paux et al. (2018) for FCC porous crystals deformed by slip. First,

some verification studies on the quality of CPFEM unit cell calculations are reported. The data points obtained from unit cell calculations using H1 elements with linear shape functions and H2S 20-node serendipity elements with quadratic shape functions, following the AceGen convention, are compared. Subsequently, the data points calculated using CPFEM are compared with the unit cell calculations of Han et al. (2013). In next part the impact of individual terms in the proposed criterion is briefly discussed, along with a comparison of the three models for a particular crystal orientation with CPFEM results.

The crystal plasticity model and its implementation, the unit cell model, as well as the stress-controlled and periodic boundary conditions for FCC crystals deformed by slip, have already been explained in Chapters 2–4. Additionally, the method for extracting yield points has been described in the previous section. The elastic constants are the same as those considered by Han et al. (2013) whereas the hardening parameters are mentioned in Chapter 4, Tab. 4.1.

In the unit cell computations, the x axis is taken as the primary loading direction (refer to Chapter 3, Eq. (3.15)). Combinations of three loading cases in terms of stress ratios $\eta_2 = \eta_3$, $\eta_2 = 0.4$, and $\eta_2 = 0.727$ with three crystallographic orientations (A, B, and C, as outlined in Chapter 4, Tab. 4.2) and five void volume fractions (1%, 3%, 5%, 7%, and 10%) were analyzed. For calibration purposes, last four volume fractions were applied only to crystal orientation B under axisymmetric loading ($\eta_2 = \eta_3$). This allowed for a comprehensive evaluation of the interactions between crystallographic orientation, loading conditions, and porosity.

8.3.1 Verification of unit cell calculations

Han et al. (2013) used 20-node quadratic serendipity elements with reduced integration for their unit cell calculations on FCC single crystals. Similar elements with reduced integration were used in current CPFEM calculations, and the results of these calculations are presented. The same boundary conditions and material parameters as for the linear H1 element were used. Figs. 8.3a and 8.3b depict the yield stress plots for a 1% volume fraction under various loading conditions for both H1 and H2S elements. The yield stress is represented by macroscopic stress component at yielding along the primary loading direction normalized by the initial CRSS. These plots show two crystal orientations, with [100] and [111] crystallographic directions along the main loading direction, respectively. In addition, Fig. 8.4 illustrates the yield stress plot for different volume fractions under axisymmetric loading (where η_2 = η_3) for both H1 and H2S elements. This plot specifically showcases the [100] crystal direction along the main loading direction. By observing the

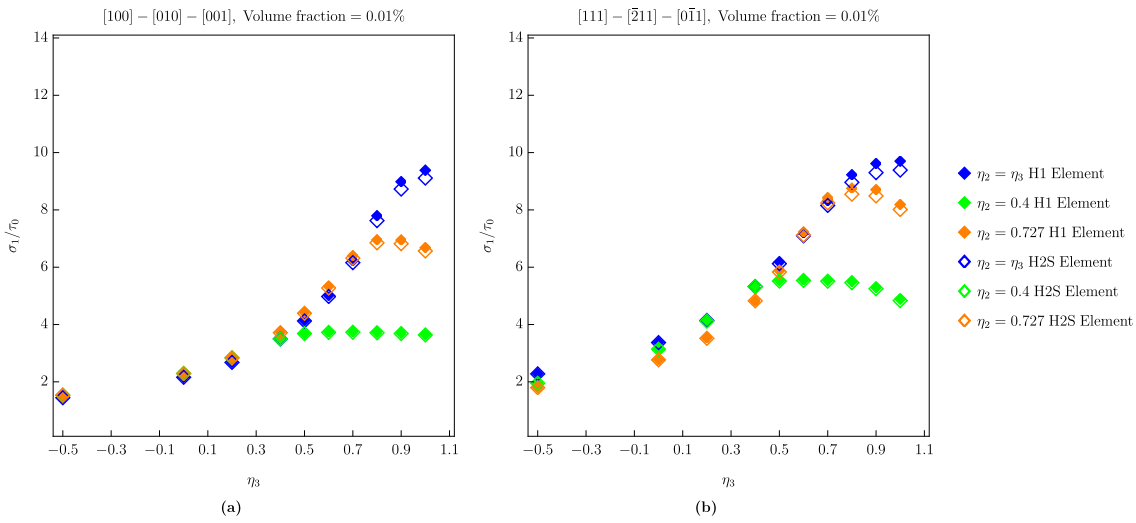

FIGURE 8.3 Yield stress for FCC porous single crystal based on unit cell calculations with f = 1% under different loading cases for two crystal orientations (a) [100] main loading direction, (b) [111] main loading direction.

results, it is evident that there is minimal deviation between the outcomes of H1 and H2S elements. However, in Fig. 8.4, a minor difference is noticeable for a higher volume fraction of 10%, especially for η values exceeding 0.7. As there is minimal deviation observed with the data points obtained using H2S element, the tuning parameters were calibrated using data points acquired from unit cell calculations with the H1 element.

In this section, a comparison is made between the unit cell calculations performed in this work and those by Han et al. (2013) for various volume fractions and loading cases. The data points are used to calibrate the tuning parameters in the proposed yield criterion. The elasto-viscoplastic crystal plasticity model, based on Schmid law with a plasticity threshold value, was employed by Han et al. (2013). The elastic moduli are chosen for 300 series stainless steel. Han et al. (2013) provide more information about the model and the parameters considered for analysis. Unlike Han et al. (2013), the elasto-viscoplastic crystal plasticity model, which is based on the rate dependent visco-plastic power law was used in this work. As already mentioned, the elastic constants are the same as those considered by Han et al. (2013). In the model, hardening is suppressed to achieve perfect creep-like behavior, and a plastic strain level of 0.2% is selected to identify the yield stress. Additionally, the same strain rate and reference shear rate in the power law are selected. In contrast, Han et al. (2013) achieved nearly perfectly plastic behavior by ensuring the viscous stress is less than 1% of the critical resolved shear stress. This was accomplished by selecting a very large reference shear rate value in their model. Figs. 8.5a and 8.5b show yield stress plots for 1% volume fraction under various loading cases for two crystal

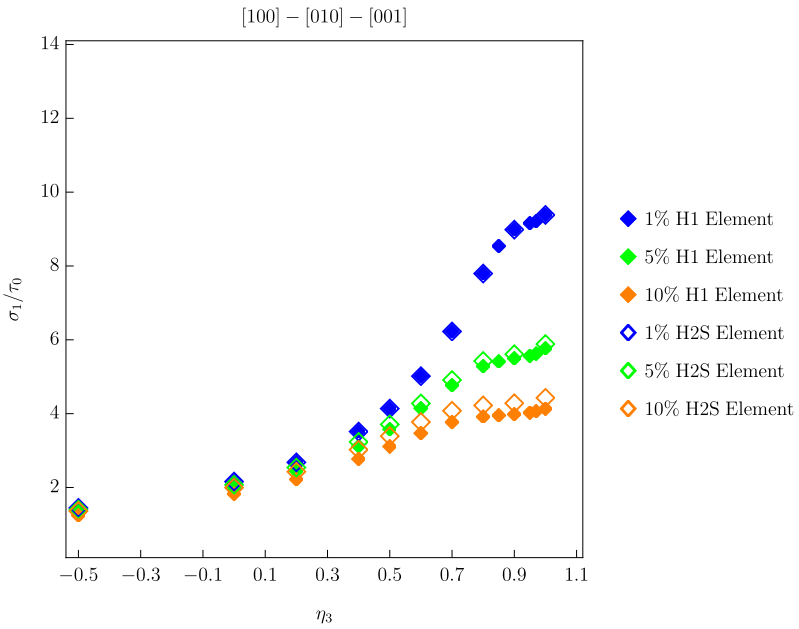

FIGURE 8.4 Yield stress for FCC porous single crystals based on unit cell calculations with different volume fractions f = 1, 5, 10% under loading case with $\eta_2 = \eta_3$ for crystal orientation [100] along main loading direction.

orientations with [100] and [111] along the main loading direction, respectively. Fig. 8.6 shows the yield stress plot for various volume fractions under axisymmetric loading ($\eta_2 = \eta_3$) with [100] crystal direction along the main loading direction. At low values of η_3, less than 0.5, both unit cell calculations agree well, but at higher values of η_3, slight deviations between the two data points are observed. The data points obtained from our unit cell calculations are found to be higher than those reported by Han et al. (2013), particularly for higher η_3 values under axisymmetric loading. A similar trend is observed for crystal orientation A ([111]) under non-axisymmetric loading conditions. The slight differences between the data points are likely attributed to the use of different constitutive models and boundary conditions in the unit cell calculations. It should be mentioned that the similar mesh density was applied in both cases. In general, good agreement is observed between both sets of data points.

8.3.2 Comparison of proposed model predictions with the existing models and unit cell results

The predictions of the newly proposed yield criterion for different loading cases and volume fractions are compared to the existing models of Han et al. (2013), and Paux et al. (2018), particularly for symmetric orientation B ([100]). Moreover, the significance of

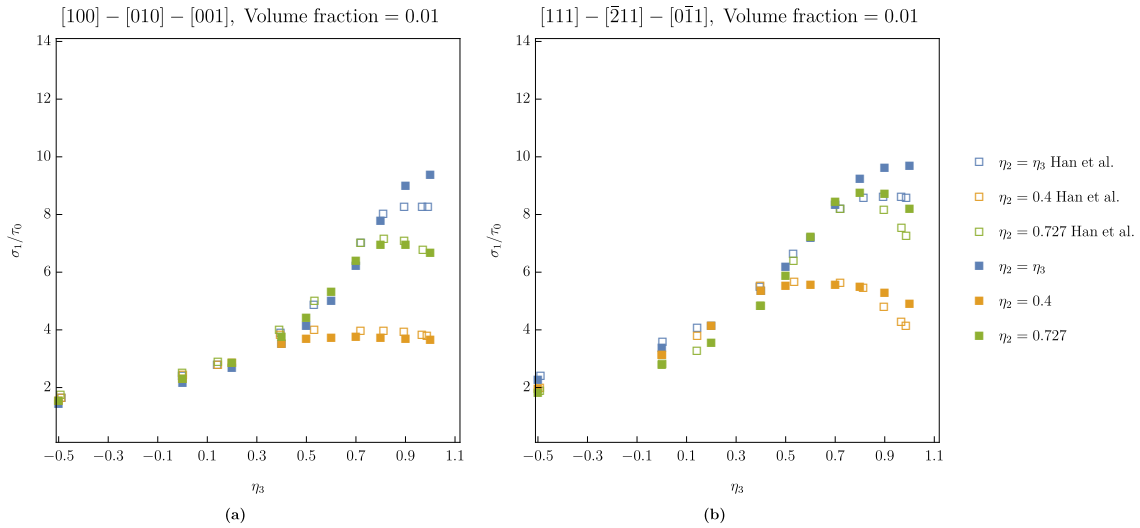

FIGURE 8.5 Yield stress for FCC porous single crystal with f = 1% under different loading cases for two crystal orientations: a) orientation B with [100] as main loading direction, b) orientation A with [111] as main loading direction (■ - model).

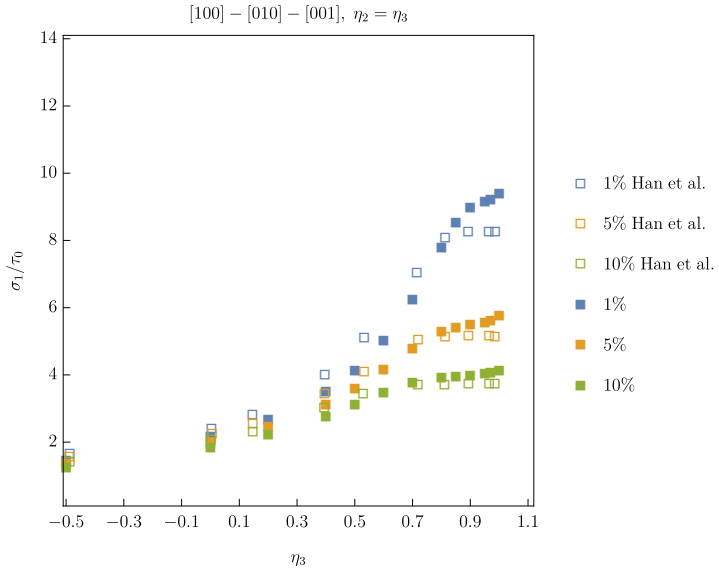

FIGURE 8.6 Yield stress for FCC porous single crystals with different volume fractions f = 1, 5, 10% under loading case with $\eta_2 = \eta_3$ for crystal orientation B with [100] along main loading direction (■ - model).

individual terms in the proposed yield criterion is also discussed briefly in this section. The tuning parameters in the proposed criterion are determined using the numerical data presented in the previous section. For the yield functions of Han et al. (2013), and Paux et al. (2018), the tuning parameters are taken from their respective works. The differential evolution algorithm, available in Mathematica, is employed for calibration of the proposed

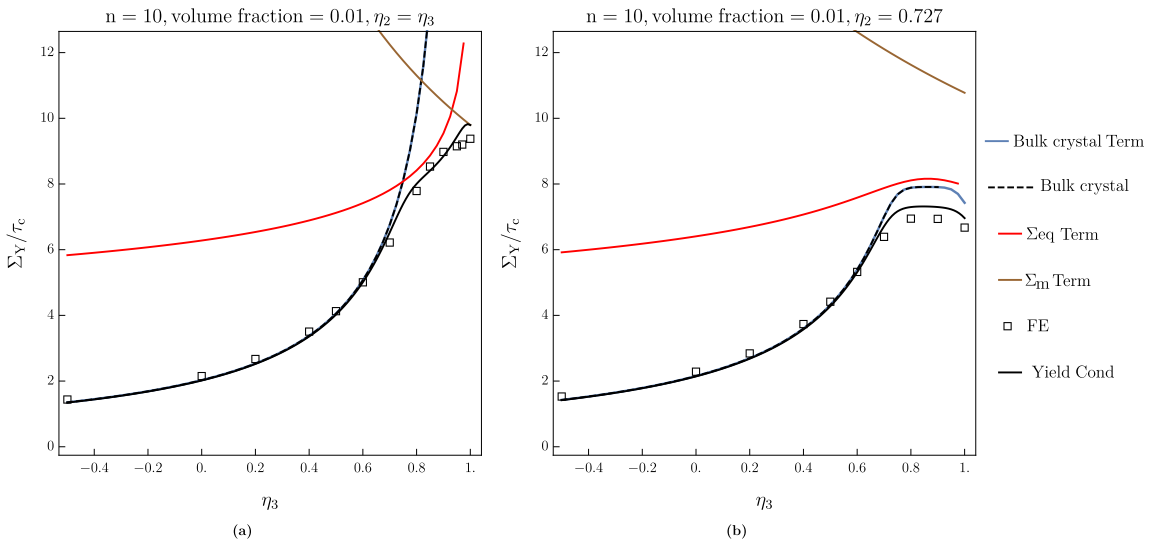

FIGURE 8.7 Significance of different terms in the proposed model under loading cases of (a) $\eta_2 = \eta_3$, (b) $\eta_2 = 0.727$.

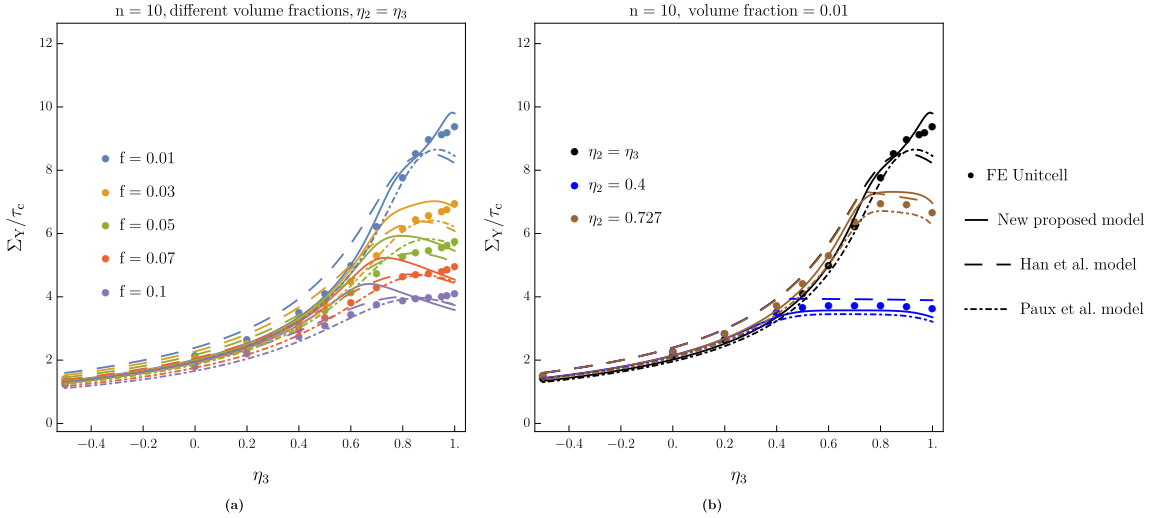

FIGURE 8.8 Comparison of three yield surface models for FCC porous single crystals with (a) Different volume fractions f = 1, 3, 5, 10% under loading case with $\eta_2 = \eta_3$ for crystal orientation [100] along main loading direction, (b) different loading cases for volume fraction of 1%.

condition (Eq. (8.15)). Additionally, only the symmetric orientation B ([100]) with varying η loading cases and volume fractions is selected for yield function calibration. The tuned values of three tuning parameters are $q_1 = 2.651, q_2 = 0.2762$, and $\kappa = 3.137 \times 10^{-7}$, respectively.

Three terms can be distinguished in the proposed yield criterion Eq. (8.15): the so-called

bulk crystal term which remains even when the void volume fraction is zero (f=0), the Σ_{eq} term depending on the macroscopic equivalent stress, and the Σ_m term which through cosh function depends on the macroscopic mean stress. Their relative importance has been studied by considering separately three trial yield functions:

$$\begin{aligned}
\left(\frac{\alpha}{\tau_0}\right)^{n-1}\left[\frac{\boldsymbol{\Sigma}\cdot\overline{\mathbb{M}}_c^v\cdot\boldsymbol{\Sigma}}{\tau_0^2}\right]-1-(q_1 f)^2 &\overset{\text{def}}{=} 0,\\
\left(\frac{\alpha}{\tau_0}\right)^{n-1}\left[\frac{2\kappa f\Sigma_{eq}^2}{3h_*^D\tau_0^2}\right]-1-(q_1 f)^2 &\overset{\text{def}}{=} 0,\\
2fq_1\cosh\left(\sqrt{\frac{3}{h_*^P}}\frac{q_2\Sigma_m}{\tau_0}\right)-1-(q_1 f)^2 &\overset{\text{def}}{=} 0.
\end{aligned} \tag{8.18}$$

Fig. 8.7 illustrates the regimes of η_3 where the subsequent terms in the proposed yield criterion become decisive for crystal yielding. It is observed that for η_3 values ranging from -0.5 to 0.5, only the bulk crystal term is relevant. The term Σ_{eq} becomes important for η_3 values between 0.5 and 0.9, while the Cosh term determines the yield stress value under hydrostatic loading. For axisymmetric loading (Fig. 8.7a), the bulk term approaches infinity as the η_3 value tends toward one, corresponding to the hydrostatic loading case. In the case of $\eta_2 = 0.727$ (Fig. 8.7b), the response differs at higher η_3 values compared to the axisymmetric loading scenario.

In Fig. 8.8, the predictions of the newly proposed yield criterion are compared to those of Han et al. (2013), and Paux et al. (2018) for various volume fractions under axisymmetric loading ($\eta_2 = \eta_3$). Additionally, comparisons are made for different loading cases at the 1% volume fraction for symmetric orientation B [100]. At low η_3 values, below 0.5, all models nearly coincide, with the response of the Han et al. (2013) model being slightly higher. The bulk crystal response is observed in this range, but deviations begin to appear at higher η_3 values. When referring to FE calculations, the model by Han et al. (2013) is delivering higher values than our calculations at low η_3, with the trend reversing at higher triaxialities. To fit present numerical data, the proposed yield criterion predicts larger values for $\eta_2 = \eta_3$ loading at high η_3 values compared to the models of Han et al. (2013), and Paux et al. (2018). Under the $\eta_2 = 0.4$ loading case, predictions of new model are lower than those of Han et al. (2013). Furthermore, for $\eta_2 = 0.4$, they are very close to Paux et al. (2018). This is because only the term related to bulk crystal response plays a role in predicting the yielding of porous crystals for this case.

Fig. 8.9 depicts the yield stress based on the proposed model and its comparison with present unit cell data points and those of Han et al. (2013) for the asymmetric orientation A [111] under different loading scenarios at the 1% volume fraction. It is evident that

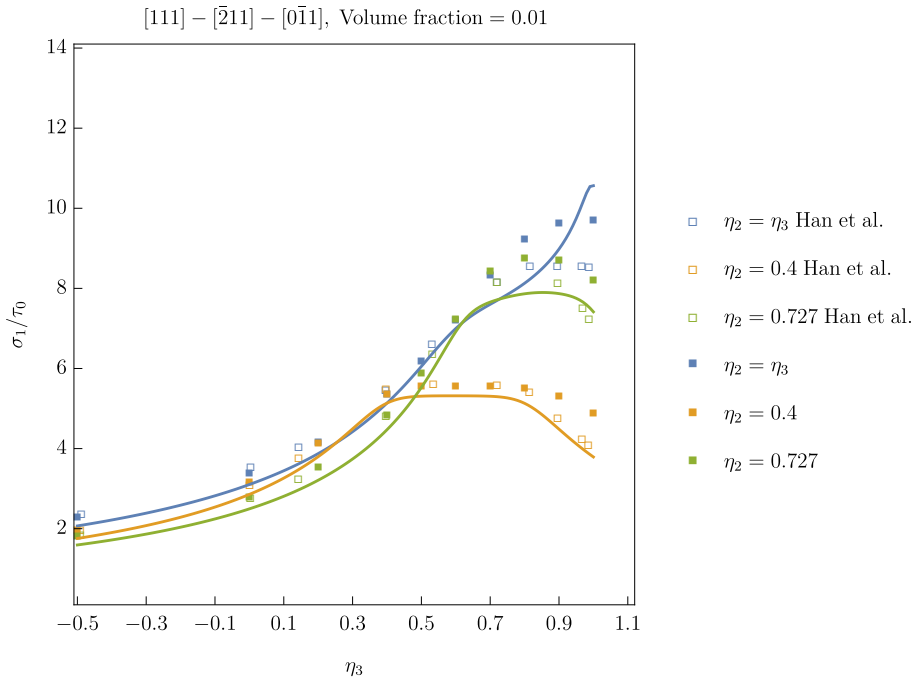

FIGURE 8.9 Yield stress for the proposed model for asymmetric orientation A[111] with 1% volume fraction under different loading scenarios (■ present unit cell model results, □ Han et al. unit cell model results).

for different orientations of loading directions, the proposed model predicts an anisotropic response. The model closely matches the unit cell model results, using only the calibrated parameters based on crystal orientation B [100]. The cases dominated by a deviatoric part of stress, i.e., low η_3 values across all loading scenarios, are well captured by the model. However, at high η_3 values, some deviations are observed due to the influence of the Σ_{eq} term. For the $\eta_2 = 0.4$ and $\eta_2 = 0.727$ loading cases, the model results are closer to the unit cell data points of Han et al. (2013), particularly at high η_3 values with an increased hydrostatic part, compared to our unit cell model results.

8.4 Summary

In this chapter, a new yield criterion based on a micromechanical approach has been formulated for porous single crystals. The criterion is applicable to porous crystals with arbitrary lattice symmetry. Additionally, the Paux et al. (2018) yield criterion is extended to account for twinning and calibrated using CPFEM unit cell calculations for HCP porous crystals of high anisotropy. Note that Paux et al. (2018) considered only slip systems and calibrated the tuning parameters using FFT-based unit cell computations. Additionally,

the calibrated anisotropic parameter is verified through both CPFEM-based optimization and a kinematic limit analysis approach for hydrostatic loading. Finally, the proposed yield criterion is analyzed, and compared with other existing proposals and validated with respect to unit cell calculations for the set of orientations and loading conditions, on the example of FCC porous crystal.

CHAPTER 9

Summary and future works

In this thesis, numerical analyses and a micromechanical approach were employed to unravel the mechanisms governing the ductile failure and its impact on the macroscopic response of porous single and polycrystals with FCC and HCP lattice symmetries. In the performed analyses relevant deformation mechanisms at the local level were considered, and appropriate micro-macro transition schemes were applied. A rate-dependent crystal plasticity constitutive model was employed, incorporating slip and twin mechanisms. In the model the evolution of the critical resolved shear stress (CRSS), influenced by the interaction between various slip and twin systems, and crystal reorientation scheme due to twinning were accounted for. Detailed results from numerical simulations on single and polycrystal unit cell models, conducted using the crystal plasticity finite element method (CPFEM), are presented, analyzing how plastic anisotropy, stress state, and boundary conditions affect void growth, coalescence, and collapse in porous FCC and HCP single and polycrystals.

The work also explores the possibility of describing the macroscopic responses of porous crystals and polycrystals through micromechanical mean field models. The formulated mean field model uses the additive Mori-Tanaka scheme for porous single crystals and a three-scale model based on the additive self-consistent scheme for porous polycrystals. They are both validated against full-field numerical analyses. Additionally, using the proposed micromechanical model, a GTN-like yield criterion for porous crystals was formulated, and its predictions were compared with existing models and validated with respect to numerical unit cell results. This newly proposed yield condition is well suited for the implementation into the finite element framework, following similar implementations by Ling et al. (2016) to predict damage in porous crystals. The results demonstrate that the numerical analyses and micromechanical approach are effective tools for understanding the relation between material microstructure, including the crystal lattice symmetry, and the developed scenarios of void growth and related changes in macroscopic response of

metallic materials. Key findings and conclusions from each chapter are outlined below. Numerical analyses reported in chapters 4 and 5 demonstrated that:

- In FCC crystals with cylindrical voids, analyzed using 2D unit cells under plane strain condition, softening is observed at higher stress and displacement biaxiality ratios, induced by significant void growth and coalescence, with the impact of crystallographic orientation becoming less pronounced.

- However, at lower stress and displacement biaxiality values, an anisotropic response is observed, where the strain-stress behavior remains strongly dependent on crystallographic orientation. Especially, crystals with the main lattice directions inclined with respect to the loading axes (i.e. non-symmetric orientations) show the greatest plastic heterogeneity, resulting in noticeable lattice rotation and grain fragmentation induced by the presence of void across different loading conditions.

- In HCP crystals with cylindrical voids, analyzed using 2D unit cells under plane strain condition strongly anisotropic void growth is observed depending if twinning mechanisms is activated or remains inactive, namely:

  a) under low stress biaxiality with loading along the c-axis of the crystal, alternating bands of twinned and untwinned regions are observed. In the twinned regions the activity of pyramidal and prismatic slip systems has been triggered. The void experiences slight rotation in the primary loading direction and deforms into a prolate shape. Failure occurs through shear localization, with an inclined band connecting neighboring voided cells diagonally. For higher stress biaxiality, following the predicted stress-strain response, evolution of porosity is non-monotonous, with the accelerated growth once the twinning is completed within the unit cell.

  b) On the other hand, irrespective of stress biaxiality, under loading along prismatic direction, with no twinning being active, void coalescence occurs by necking of the internal ligament normal to the principal stress direction, similarly to FCC crystals deforming by slip.

- Similarly, in HCP 3D unit cells, a harder stress response is observed under uniaxial loading along the c-axis due to twin reorientation, while a much softer response is observed when the loading axis is inclined between the prismatic plane and the c-axis.

- It was observed that for hard orientations at 0° and 90° loading, void evolution was more significant as compared to soft orientations (30°, 45°, 60°), where negligible void growth was observed. Furthermore, in cases where twinning was active, the void growth exhibited a non-monotonic behavior.

Micro-mechanical modeling performed in Chapters 6–8 demonstrated that:

- In FCC porous single crystals, the mean-field model using tangent linearization tends to overestimate void evolution due to the relatively high compliance of the matrix. In contrast, the secant linearization approach demonstrates minimal void growth, due to the relatively high stiffness.

- In FCC porous polycrystals, the mean-field model tends to under predict the overall void volume fraction when compared to CPFEM results, while simultaneously overestimating the equivalent stress levels. However, a strong correlation is found in terms of the local equivalent stress response, where orientations with high and low stress magnitudes on the inverse pole figure align closely between both CPFEM and mean-field models.

- The comparison of the newly calculated anisotropic parameter with that of Paux et al. (2018) reveals that the parameter decreases as anisotropy increases. Consequently, higher plastic anisotropy corresponds to greater yield strength under hydrostatic loading, leading to nearly incompressible response of porous crystal. A similar behavior is noted for these cases where the loading axis is inclined between the prismatic and c-axis in HCP crystals.

- The predictions of newly proposed yield criterion is compared with the existing proposals of Han et al. (2013) and Paux et al. (2018) for FCC crystals. The model correctly predicts an anisotropic response for different orientations across various loading scenarios, exhibiting strong agreement with the unit cell data points.

Key contributions. The following points highlight the key novel contributions of the thesis:

- The effect of crystallographic orientation and different boundary conditions on void growth and coalescence, along with related microstructural evolution due to heterogeneous lattice rotation, has been thoroughly examined employing full-field large strain CPFEM for 2D plane strain unit cell model of FCC crystal.

- The impact of twinning activity and insufficient number of easy slip modes on the void growth and possible ductile failure scenario in HCP crystals have been investigated using large strain CPFEM equipped with a PTVC reorientation scheme and employing a unit cell methodology. Both a 2D plane strain unit cell with a cylindrical void and a 3D unit cell with a spherical void have been considered in this analysis. The influence of active deformation mechanisms, stress heterogeneity, and twinning-induced lattice rotation have also been examined, highlighting critical role of strong crystal anisotropy in void behavior.

- A new micromechanical mean-field model for porous elasto-viscoplastic polycrystals has been formulated in small strain format. The closed-form of macroscopic constitutive law for porous polycrystals has been obtained from the proposed three-scale micro-macro transition scheme.

- The predictions of the proposed mean-field model have been validated with respect to the corresponding full-field unit cell CPFEM computations for both FCC crystals and polycrystals in terms of the overall and per-grain stress-strain responses.

- The extension of the yield criterion proposed by Paux et al. (2018), enabling its application to crystals deforming by slip and twinning, has been formulated. The tuning parameters in the extended Paux et al. (2018) yield surface have been calibrated by considering both slip and twinning in HCP crystals of high plastic anisotropy independently employing two methods: numerical one based on CPFEM analysis of 3D unit cell and analytical one through kinematic limit analysis. For the application of the latter method a new numerical scheme has been developed to determine the so-called anisotropy parameter in the yield surface. Parameters obtained by two methods were in very good agreement.

- Additionally, a new GTN-type yield criterion has been formulated based on the proposed micromechanical approach for voided elasto-viscoplastic crystals, with the tuning parameters calibrated using full-field finite element analyses. The predictions of the proposed criterion have been compared with existing models of Han et al. (2013) and Paux et al. (2018) for FCC crystals.

Future works. Building on the novel micromechanical mean-field model and the analysis of the results, there is clear potential for future research. It can be pursued in the following direction:

- The proposed yield criterion for porous crystals can be further enhanced and incorporated into a finite element framework with the large strain crystal plasticity,

enabling accurate predictions of damage in single crystal and polycrystal models that exhibit both HCP and FCC symmetry.

- In the context of the micromechanical mean field model, depending on the relation between void and grain size, the reverse order of homogenization steps can be employed. Accordingly, if the void size is much larger than the grain size, this approach will involve applying a self-consistent scheme for grain aggregate without voids, and next the obtained effective properties of the polycrystal will be used as a matrix material, into which voids are incorporated. Next, the Mori-Tanaka scheme will be employed to compute the effective properties of the resulting porous material. Finally, if voids are of similar size as grains then the one-step homogenization with the self-consistent scheme can be applied.

- It has been noted in the literature that mean field models incorporating second moments of stress yield a softer response compared to those relying solely on first moment of stress (i.e. mean values) and enable to predict yielding under purely hydrostatic loading. Consequently, attention should be directed toward incorporating the second moment of stress in the proposed mean field models to improve their predictions.

- In the context of porous polycrystal unit cells analyzed by full-field methods, like CPFEM, RVEs can be developed using Voronoi tessellations instead of regular cubic unit cells. This allows for a more accurate representation of actual microstructures and facilitating the study of the local mechanics of porous evolution in polycrystal materials.

- It is also interesting to analyze the macroscopic response of porous crystals under cyclic and non proportional loading using both, proposed micromechanical models, and full-field unit cell computations.

- As our study focuses on micro-scale problems, it is crucial to consider length scales. Incorporating the gradient effects of field quantities will facilitate the development of non-local crystal plasticity models incorporating damage.

Bibliography

Agnew, S., Yoo, M., and Tome, C. (2001). Application of texture simulation to understanding mechanical behavior of Mg and solid solution alloys containing Li or Y. *Acta Materialia*, 49(20):4277–4289.

Agoras, M. and Ponte Castañeda, P. (2013). Iterated linear comparison bounds for viscoplastic porous materials with "ellipsoidal" microstructures. *Journal of the Mechanics and Physics of Solids*, 61(3):701–725.

Agoras, M. and Ponte Castañeda, P. (2014). Anisotropic finite-strain models for porous viscoplastic materials with microstructure evolution. *International Journal of Solids and Structures*, 51(5):981–1002.

Alharbi, K., Ghadbeigi, H., Efthymiadis, P., Zanganeh, M., Celotto, S., Dashwood, R., and Pinna, C. (2015). Damage in dual phase steel dp1000 investigated using digital image correlation and microstructure simulation. *Modelling and Simulation in Materials Science and Engineering*, 23(8):085005.

Appel, F. and Wagner, R. (1998). Microstructure and deformation of two-phase γ-titanium aluminides. *Materials science and engineering: r: reports*, 22(5):187–268.

Argon, A., Im, J., and Safoglu, R. (1975). Cavity formation from inclusions in ductile fracture. *Metallurgical transactions A*, 6:825–837.

Arminjon, M. and Bacroix, B. (1991). On plastic potentials for anisotropic metals and their derivation from the texture function. *Acta Mechanica*, 88(3):219–243.

Asaro, R. and Needleman, A. (1985). Texture development and strain hardening in rate dependent polycrystals. *Acta Metallurgica*, 33(6):923–953.

Asaro, R. and Rice, J. (1977). Strain localization in ductile single crystals. *Journal of the Mechanics and Physics of Solids*, 25(5):309–338.

Asgari, S., El-Danaf, E., Kalidindi, S. R., Doherty, R. D., and Necker, C. (1997). Strain hardening regimes and microstructural evolution during large strain compression of low stacking fault energy fcc alloys that form deformation twins. *Metallurgical and*

Materials Transactions A, 28:1781–1795.

Barrioz, P., Hure, J., and Tanguy, B. (2019). Effect of dislocation channeling on void growth to coalescence in fcc crystals. *Materials Science and Engineering: A*, 749:255–270.

Barsoum, I. and Faleskog, J. (2011). Micromechanical analysis on the influence of the lode parameter on void growth and coalescence. *International Journal of Solids and Structures*, 48(6):925–938.

Basinski, Z., Szczerba, M., Niewczas, M., Embury, J., and Basinski, S. (1997). The transformation of slip dislocations during twinning of copper-aluminum alloy crystals. *Revue de Metallurgie. Cahiers D'Informations Techniques*, 94(9):1037–1044.

Basu, S., Dogan, E., Kondori, B., Karaman, I., and Benzerga, A. (2017). Towards designing anisotropy for ductility enhancement: A theory-driven investigation in mg-alloys. *Acta Materialia*, 131:349–362.

Benzerga, A. and Keralavarma, S. (2009). Finite–element analyses of combined void shape and plastic anisotropy effects in ductile fracture. In *12th International Conference on Fracture. National Research Council of Canada*, page 10.

Benzerga, A. A. and Besson, J. (2001). Plastic potentials for anisotropic porous solids. *European Journal of Mechanics - A/Solids*, 20(3):397 – 434.

Bieniek, K., Majewski, M., Hołobut, P., and Kowalczyk-Gajewska, K. (2024). Anisotropic effect of regular particle distribution in elastic–plastic composites: The modified tangent cluster model and numerical homogenization. *International Journal of Engineering Science*, 203:104118.

Bluhm, J. I. and Morrissey, R. J. (1965). Fracture in a tensile specimen. In *Proceedings of the First Conference on Fracture*, volume 3, pages 1739–1780.

Bonfoh, N., Lipinski, P., Carmasol, A., and Tiem, S. (2004). Micromechanical modeling of ductile damage of polycrystalline materials with heterogeneous particles. *International Journal of Plasticity*, 20(1):85–106.

Bringa, E. M., Traiviratana, S., and Meyers, M. A. (2010). Void initiation in fcc metals: effect of loading orientation and nanocrystalline effects. *Acta Materialia*, 58(13):4458–4477.

Chan, K. S. and Davidson, D. L. (1999). Evidence of void nucleation and growth on planar slip bands in a nb-cr-ti alloy. *Metallurgical and Materials Transactions A*, 30:579–585.

Chang, H.-J., Segurado, J., and LLorca, J. (2015). Three-dimensional dislocation dynamics analysis of size effects on void growth. *Scripta Materialia*, 95:11–14.

Chen, D., Zhang, X., Meng, X., Ma, R., Li, R., Wang, Z., Su, B., Lang, D., Yang, T., and Meng, D. (2018). Mechanisms of void formation during uniaxial tensile testing in a low-temperature-aged u-nb alloy. *Materials Science and Engineering: A*, 723:182–193.

Chin, G. Y., Hosford, W. F., Mendorf, D. R., and Taylor, G. I. (1969). Accommodation of constrained deformation in f. c. c. metals by slip and twinning. *Proceedings of the Royal Society of London. A. Mathematical and Physical Sciences*, 309(1499):433–456.

Cox, T. and Low, J. R. (1974). An investigation of the plastic fracture of AISI 4340 and 18 Nickel-200 grade maraging steels. *Metallurgical and Materials Transactions B*, 5:1457–1470.

Cui, B., Kacher, J., McMurtrey, M., Was, G., and Robertson, I. (2014). Influence of irradiation damage on slip transfer across grain boundaries. *Acta materialia*, 65:150–160.

Czarnota, C., Kowalczyk-Gajewska, K., Salahouelhadj, A., Martiny, M., and Mercier, S. (2015). Modeling of the cyclic behavior of elastic–viscoplastic composites by the additive tangent mori–tanaka approach and validation by finite element calculations. *International Journal of Solids and Structures*, 56-57:96–117.

Dakshinamurthy, M., Kowalczyk-Gajewska, K., and Vadillo, G. (2021). Influence of crystallographic orientation on the void growth at the grain boundaries in bi-crystals. *International Journal of Solids and Structures*, 212:61–79.

Danas, K. and Aravas, N. (2012). Numerical modeling of elasto-plastic porous materials with void shape effects at finite deformations. *Composites Part B: Engineering*, 43(6):2544–2559.

Das, A. (2021). Stress/strain induced void? *Archives of Computational Methods in Engineering*, 28(3):1795–1852.

Das, S., Song, D., and Ponte Castañeda, P. (2021). Macroscopic response and microstructure evolution in viscoplastic polycrystals with pressurized pores. *International Journal of Fracture*, pages 1–28.

de Souza Neto, E., Perić, D., Dutko, M., and Owen, D. (1996). Design of simple low order finite elements for large strain analysis of nearly incompressible solids. *International Journal of Solids and Structures*, 33(20):3277–3296.

DeBotton, G. and Ponte Castañeda, P. (1995). Variational estimates for the creep behaviour of polycrystals. *Proceedings of the Royal Society of London. Series A: Mathematical and Physical Sciences*, 448(1932):121–142.

El Ghezal, M. and Doghri, I. (2018). Porous plasticity: Predictive second moment homogenization models coupled with Gurson's single cavity stress-strain solution. *International Journal of Plasticity*, 108:201–221.

Fadida, R., Shirizly, A., and Rittel, D. (2020). Static and dynamic shear-compression response of additively manufactured Ti6Al4V specimens with embedded voids. *Mechanics of Materials*, 147:103413.

Faleskog, J., Gao, X., and Shih, C. F. (1998). Cell model for nonlinear fracture analysis–I. micromechanics calibration. *International Journal of Fracture*, 89:355–373.

Fischer, F., Schaden, T., Appel, F., and Clemens, H. (2003). Mechanical twins, their development and growth. *European Journal of Mechanics - A/Solids*, 22(5):709–726. General and plenary lectures from the 5th EUROMECH Solid Mechanics Conference.

Fourmeau, M., Børvik, T., Benallal, A., and Hopperstad, O. S. (2013). Anisotropic failure modes of high-strength aluminium alloy under various stress states. *International Journal of Plasticity*, 48:34–53.

Fressengeas, C. and Molinari, A. (1985). Inertia and thermal effects on the localization of plastic flow. *Acta Metallurgica*, 33(3):387–396.

Frodal, B. H., Lodgaard, L., Langsrud, Y., Børvik, T., and Hopperstad, O. S. (2023). Inuence of local microstructural variations on the bendability of aluminium extrusions: experiments and crystal plasticity analyses. *Journal of Applied Mechanics*, pages 1–21.

Frodal, B. H., Thomesen, S., Børvik, T., and Hopperstad, O. S. (2021). On the coupling of damage and single crystal plasticity for ductile polycrystalline materials. *International Journal of Plasticity*, 142:102996.

Frydrych, K. (2017). *Modelling of microstructure evolution of high specific strength metals subjected to severe plastic deformation processes*. PhD thesis, Institute of Fundamental Technological Research, Polish.

Frydrych, K., Jarzębska, A., Virupakshi, S., Kowalczyk-Gajewska, K., Bieda, M., Chulist, R., Skorupska, M., Schell, N., and Sztwiertnia, K. (2021). Texture-based optimization of crystal plasticity parameters: application to zinc and its alloy. *Metallurgical and Materials Transactions A*, 52(8):3257–3273.

Frydrych, K. and Kowalczyk-Gajewska, K. (2018). Microstructure evolution in cold-rolled pure titanium: modeling by the three-scale crystal plasticity approach accounting for twinning. *Metallurgical and Materials Transactions A*, 49(8):3610–3623.

Frydrych, K., Maj, M., Urbański, L., and Kowalczyk-Gajewska, K. (2020). Twinning-induced anisotropy of mechanical response of AZ31B extruded rods. *Materials Science and Engineering: A*, 771:138610.

Furukimi, O., Kiattisaksri, C., Takeda, Y., Aramaki, M., Oue, S., Munetoh, S., and Tanaka, M. (2017). Void nucleation behavior of single-crystal high-purity iron specimens subjected to tensile deformation. *Materials Science and Engineering: A*, 701:221–225.

Gambin, W. (1991). Plasticity of crystals with interacting slip systems. *Engineering Transactions*, 39(3-4):303–324.

Gan, Y. X., Kysar, J. W., and Morse, T. L. (2006). Cylindrical void in a rigid-ideally

plastic single crystal II: experiments and simulations. *International Journal of Plasticity*, 22(1):39–72.

Gardner, R. N., Pollock, T., and Wilsdorf, H. (1977). Crack initiation at dislocation cell boundaries in the ductile fracture of metals. *Materials Science and Engineering*, 29(2):169–174.

Girard, G., Frydrych, K., Kowalczyk-Gajewska, K., Martiny, M., and Mercier, S. (2021). Cyclic response of electrodeposited copper films. experiments and elastic–viscoplastic mean-field modeling. *Mechanics of Materials*, 153:103685.

Gladman, T., Holmes, B., and McIvor, I. (1971). Effects of second-phase particles on strength, toughness and ductility. In *Iron and Steel Institute Conference on Effect of Second-Phase Particles on the Mechanical Properties of Steel, 1971, 68-78*.

Gologanu, M., Leblond, J.-B., and Devaux, J. (1993). Approximate models for ductile metals containing non-spherical voids—case of axisymmetric prolate ellipsoidal cavities. *Journal of the Mechanics and Physics of Solids*, 41(11):1723–1754.

Gologanu, M., Leblond, J.-B., and Devaux, J. (1994). Approximate Models for Ductile Metals Containing Nonspherical Voids—Case of Axisymmetric Oblate Ellipsoidal Cavities. *Journal of Engineering Materials and Technology*, 116(3):290–297.

Gologanu, M., Leblond, J.-B., Perrin, G., and Devaux, J. (1997). Recent extensions of Gurson's model for porous ductile metals. In *Continuum micromechanics*, pages 61–130. Springer.

Guo, T. and Wong, W. (2018). Void-sheet analysis on macroscopic strain localization and void coalescence. *Journal of the Mechanics and Physics of Solids*, 118:172–203.

Gurland, J. (1972). Observations on the fracture of cementite particles in a spheroidized 1.05% C steel deformed at room temperature. *Acta Metallurgica*, 20(5):735–741.

Gurland, J. and Plateau, J. (1963). The mechanism of ductile rupture of metals containing inclusions. Technical report, Brown Univ., Providence; Institut de Recherches de la Siderugie, St.-Germain.

Gurson, A. L. (1977). Continuum Theory of Ductile Rupture by Void Nucleation and Growth: Part I—Yield Criteria and Flow Rules for Porous Ductile Media. *Journal of Engineering Materials and Technology*, 99(1):2–15.

Ha, S. and Kim, K. (2010). Void growth and coalescence in FCC single crystals. *International Journal of Mechanical Sciences*, 52(7):863–873.

Han, S., Chang, Y., Wang, C., Han, Y., and Dong, H. (2022). Experimental and numerical investigations on the damage induced in the shearing process for QP980 steel. *Materials*, 15(9):3254.

Han, X., Besson, J., Forest, S., Tanguy, B., and Bugat, S. (2013). A yield function for single crystals containing voids. *International Journal of Solids and Structures*, 50(14):2115–2131.

Hill, R. and Rice, J. (1972). Constitutive analysis of elastic-plastic crystals at arbitrary strain. *Journal of the Mechanics and Physics of Solids*, 20(6):401–413.

Hure, J. (2019). A coalescence criterion for porous single crystals. *Journal of the Mechanics and Physics of Solids*, 124:505–525.

Hutchinson, J. W. (1976). Bounds and self-consistent estimates for creep of polycrystalline materials. *Proceedings of the Royal Society London A*, 348:101–127.

Idiart, M. I. and Ponte Castañeda, P. (2007). Variational linear comparison bounds for nonlinear composites with anisotropic phases. II. crystalline materials. *Proceedings of the Royal Society A: Mathematical, Physical and Engineering Sciences*, 463(2080):925–943.

Jeong, W., Lee, C.-H., Moon, J., Jang, D., and Lee, M.-G. (2018). Grain scale representative volume element simulation to investigate the effect of crystal orientation on void growth in single and multi-crystals. *Metals*, 8(6):436.

Joëssel, L., Vincent, P.-G., Gărăjeu, M., and Idiart, M. I. (2018). Viscoplasticity of voided cubic crystals under hydrostatic loading. *International Journal of Solids and Structures*, 147:156–165.

Kalidindi, S., Bronkhorst, C., and Anand, L. (1992). Crystallographic texture evolution in bulk deformation processing of FCC metals. *Journal of the Mechanics and Physics of Solids*, 40(3):537–569.

Kalidindi, S. R. (1998). Incorporation of deformation twinning in crystal plasticity models. *Journal of the Mechanics and Physics of Solids*, 46(2):267 – 290.

Kanouté, P., Boso, D., Chaboche, J. L., and Schrefler, B. (2009). Multiscale methods for composites: A review. *Archives of Computational Methods in Engineering*, 16:31–75.

Karaman, I., Sehitoglu, H., Beaudoin, A., Chumlyakov, Y., Maier, H., and Tomé, C. (2000). Modeling the deformation behavior of Hadfield steel single and polycrystals due to twinning and slip. *Acta Materialia*, 48(9):2031 – 2047.

Keralavarma, S. and Benzerga, A. (2010). A constitutive model for plastically anisotropic solids with non-spherical voids. *Journal of the Mechanics and Physics of Solids*, 58(6):874–901.

Keralavarma, S., Reddi, D., and Benzerga, A. (2020). Ductile failure as a constitutive instability in porous plastic solids. *Journal of the Mechanics and Physics of Solids*, 139:103917.

Khadyko, M., Frodal, B. H., and Hopperstad, O. S. (2021). Finite element simulation of

ductile fracture in polycrystalline materials using a regularized porous crystal plasticity model. *International Journal of Fracture*, 228:15–31.

Kocks, U. F., Tomé, C. N., and Wenk, H.-R. (2000). *Texture and Anisotropy*. Cambridge University Press, II edition.

Kondori, B. and Benzerga, A. A. (2014). Effect of stress triaxiality on the flow and fracture of Mg alloy AZ31. *Metallurgical and Materials Transactions A*, 45:3292–3307.

Kondori, B., Morgeneyer, T. F., Helfen, L., and Benzerga, A. A. (2018). Void growth and coalescence in a magnesium alloy studied by synchrotron radiation laminography. *Acta Materialia*, 155:80–94.

Kong, X., Morgeneyer, T. F., Missoum-Benziane, D., and Rousselier, G. (2023). A polycrystalline damage model applied to an anisotropic aluminum alloy 2198 under non-proportional load path changes. *International Journal of Plasticity*, 168:103674.

Koplik, J. and Needleman, A. (1988). Void growth and coalescence in porous plastic solids. *International Journal of Solids and Structures*, 24(8):835–853.

Korelc, J. (2002). Multi-language and multi-environment generation of nonlinear finite element codes. *Engineering with computers*, 18:312–327.

Kowalczyk, K. and Gambin, W. (2004). Model of plastic anisotropy evolution with texture-dependent yield surface. *International Journal of Plasticity*, 20(1):19–54.

Kowalczyk-Gajewska, K. (2010). Modelling of texture evolution in metals accounting for lattice reorientation due to twinning. *European Journal of Mechanics - A/Solids*, 29(1):28 – 41.

Kowalczyk-Gajewska, K. (2011). Micromechanical modelling of metals and alloys of high specific strength. Habilitation Thesis 1/2011, IFTR Reports.

Kowalczyk-Gajewska, K. (2013). Crystal plasticity models accounting for twinning. *Computer Methods in Materials Science*, 13:436–451.

Kowalczyk-Gajewska, K. and Petryk, H. (2011). Sequential linearization method for viscous/elastic heterogeneous materials. *European Journal of Mechanics - A/Solids*, 30(5):650–664.

Kreisselmeier, G. and Steinhauser, R. (1980). Systematic control design by optimizing a vector performance index. In CUENOD, M., editor, *Computer Aided Design of Control Systems*, pages 113–117. Pergamon.

Kysar, J. W., Gan, Y. X., and Mendez-Arzuza, G. (2005). Cylindrical void in a rigid-ideally plastic single crystal. Part I: Anisotropic slip line theory solution for face-centered cubic crystals. *International Journal of Plasticity*, 21(8):1481–1520.

Lebensohn, R. and Tomé, C. (1993). A self-consistent anisotropic approach for the

simulation of plastic deformation and texture development of polycrystals: Application to zirconium alloys. *Acta Metallurgica et Materialia*, 41(9):2611 – 2624.

Lebensohn, R. A. and Cazacu, O. (2012). Effect of single-crystal plastic deformation mechanisms on the dilatational plastic response of porous polycrystals. *International Journal of Solids and Structures*, 49(26):3838–3852.

Lebensohn, R. A., Escobedo, J. P., Cerreta, E. K., Dennis-Koller, D., Bronkhorst, C. A., and Bingert, J. F. (2013). Modeling void growth in polycrystalline materials. *Acta Materialia*, 61(18):6918–6932.

Lebensohn, R. A., Idiart, M. I., and Ponte Castañeda, P. (2012). Modeling microstructural effects in dilatational plasticity of polycrystalline materials. *Procedia IUTAM*, 3:314–330.

Lebensohn, R. A., Idiart, M. I., Ponte Castañeda, P., and Vincent, P.-G. (2011). Dilatational viscoplasticity of polycrystalline solids with intergranular cavities. *Philosophical Magazine*, 91(22):3038–3067.

Leblond, J., Perrin, G., and Suquet, P. (1994). Exact results and approximate models for porous viscoplastic solids. *International Journal of Plasticity*, 10(3):213–235.

Lecarme, L., Tekog, C., Pardoen, T., et al. (2011). Void growth and coalescence in ductile solids with stage III and stage IV strain hardening. *International Journal of Plasticity*, 27(8):1203–1223.

León-García, O., Petrov, R., and Kestens, L. A. (2010). Void initiation at tin precipitates in if steels during tensile deformation. *Materials Science and Engineering: A*, 527(16):4202–4209.

Li, S. and Wang, G. (2018). *Introduction to Micromechanics and Nanomechanics*. WORLD SCIENTIFIC, 2nd edition.

Ling, C., Besson, J., Forest, S., Tanguy, B., Latourte, F., and Bosso, E. (2016). An elastoviscoplastic model for porous single crystals at finite strains and its assessment based on unit cell simulations. *International Journal of Plasticity*, 84:58–87.

Ling, C., Forest, S., Besson, J., Tanguy, B., and Latourte, F. (2018). A reduced micromorphic single crystal plasticity model at finite deformations. application to strain localization and void growth in ductile metals. *International Journal of Solids and Structures*, 134:43–69.

Liu, W., Zhang, X., and Tang, J. (2009). Study on the growth behavior of voids located at the grain boundary. *Mechanics of materials*, 41(7):799–809.

Liu, W., Zhang, X., Tang, J., and Du, Y. (2007). Simulation of void growth and coalescence behavior with 3d crystal plasticity theory. *Computational materials science*, 40(1):130–139.

Liu, Z., Wong, W., and Guo, T. (2016). Void behaviors from low to high triaxialities: Transition from void collapse to void coalescence. *International Journal of Plasticity*, 84:183–202.

Madou, K. and Leblond, J.-B. (2012a). A Gurson-type criterion for porous ductile solids containing arbitrary ellipsoidal voids—I: Limit-analysis of some representative cell. *Journal of the Mechanics and Physics of Solids*, 60(5):1020–1036.

Madou, K. and Leblond, J.-B. (2012b). A Gurson-type criterion for porous ductile solids containing arbitrary ellipsoidal voids—II: Determination of yield criterion parameters. *Journal of the Mechanics and Physics of Solids*, 60(5):1037–1058.

Mahajan, S. and Chin, G. (1973). Twin-slip, twin-twin and slip-twin interactions in Co-8 wt.% Fe alloy single crystals. *Acta Metallurgica*, 21(2):173–179.

Mareau, C. and Berbenni, S. (2015). An affine formulation for the self-consistent modeling of elasto-viscoplastic heterogeneous materials based on the translated field method. *International Journal of Plasticity*, 64:134–150.

Mbiakop, A., Constantinescu, A., and Danas, K. (2015a). An analytical model for porous single crystals with ellipsoidal voids. *Journal of the Mechanics and Physics of Solids*, 84:436–467.

Mbiakop, A., Constantinescu, A., and Danas, K. (2015b). A model for porous single crystals with cylindrical voids of elliptical cross-section. *International Journal of Solids and Structures*, 64:100–119.

McClintock, F. A. (1968). A Criterion for Ductile Fracture by the Growth of Holes. *Journal of Applied Mechanics*, 35(2):363–371.

Mercier, S., Kowalczyk-Gajewska, K., and Czarnota, C. (2019). Effective behavior of composites with combined kinematic and isotropic hardening based on additive tangent mori–tanaka scheme. *Composites Part B: Engineering*, 174:107052.

Molinari, A. (2002). Averaging models for heterogeneous viscoplastic and elastic viscoplastic materials. *Journal of Engineering Materials and Technology*, 124:62–70.

Molinari, A., Ahzi, S., and Kouddane, R. (1997). On the self-consistent modeling of elastic-plastic behavior of polycrystals. *Mechanics of Materials*, 26:43–62.

Monchiet, V., Cazacu, O., Charkaluk, E., and Kondo, D. (2008). Macroscopic yield criteria for plastic anisotropic materials containing spheroidal voids. *International Journal of Plasticity*, 24(7):1158–1189.

Morin, L., Leblond, J.-B., and Kondo, D. (2015). A Gurson-type criterion for plastically anisotropic solids containing arbitrary ellipsoidal voids. *International Journal of Solids and Structures*, 77:86–101.

Morin, L., Michel, J.-C., and Leblond, J.-B. (2017). A Gurson-type layer model for ductile porous solids with isotropic and kinematic hardening. *International Journal of Solids and Structures*, 118:167–178.

Mróz, Z. (2006). State of the art report on knowledge-based multicomponent materials. *Intermetallics: Properties, Modelling and Applications. KMM*.

Nahshon, K. and Hutchinson, J. (2008). Modification of the Gurson model for shear failure. *European Journal of Mechanics-A/Solids*, 27(1):1–17.

Naragani, D. P., Park, J.-S., Kenesei, P., and Sangid, M. D. (2020). Void coalescence and ductile failure in IN718 investigated via high-energy synchrotron X-ray tomography and diffraction. *Journal of the Mechanics and Physics of Solids*, 145:104155.

Needleman, A. (1972). Void Growth in an Elastic-Plastic Medium. *Journal of Applied Mechanics*, 39(4):964–970.

Needleman, A. and Rice, J. R. (1978). *Limits to Ductility Set by Plastic Flow Localization*, pages 237–267. Springer US, Boston, MA.

Nemat-Nasser, S. (1999). Averaging theorems in finite deformation plasticity. *Mechanics of Materials*, 31(8):493–523.

Nemat-Nasser, S. and Hori, M. (1999). *Micromechanics: overall properties of heterogeneous materials*. North-Holland Elsevier.

Nemcko, M. J., Li, J., and Wilkinson, D. S. (2016). Effects of void band orientation and crystallographic anisotropy on void growth and coalescence. *Journal of the Mechanics and Physics of Solids*, 95:270–283.

Nemcko, M. J. and Wilkinson, D. S. (2016). On the damage and fracture of commercially pure magnesium using x-ray microtomography. *Materials Science and Engineering: A*, 676:146–155.

Noell, P. J., Sabisch, J. E., Medlin, D. L., and Boyce, B. L. (2020). Nanoscale conditions for ductile void nucleation in copper: Vacancy condensation and the growth-limited microstructural state. *Acta Materialia*, 184:211–224.

O'Regan, T., Quinn, D., Howe, M., and McHugh, P. (1997). Void growth simulations in single crystals. *Computational mechanics*, 20(1-2):115–121.

Pala, R. and Dzioba, I. (2018). Influence of delamination on the parameters of triaxial state of stress before the front of the main crack. In *AIP Conference Proceedings*. AIP Publishing.

Pardoen, T. and Hutchinson, J. (2000). An extended model for void growth and coalescence. *Journal of the Mechanics and Physics of Solids*, 48(12):2467–2512.

Pathak, N., Adrien, J., Butcher, C., Maire, E., and Worswick, M. (2020). Experimental stress

state-dependent void nucleation behavior for advanced high strength steels. *International Journal of Mechanical Sciences*, 179:105661.

Paux, J., Brenner, R., and Kondo, D. (2018). Plastic yield criterion and hardening of porous single crystals. *International Journal of Solids and Structures*, 132-133:80–95.

Paux, J., Morin, L., Brenner, R., and Kondo, D. (2015). An approximate yield criterion for porous single crystals. *European Journal of Mechanics - A/Solids*, 51:1–10.

Perez-Bergquist, A., Cerreta, E. K., Trujillo, C. P., Cao, F., and Gray III, G. (2011). Orientation dependence of void formation and substructure deformation in a spalled copper bicrystal. *Scripta Materialia*, 65(12):1069–1072.

Pineau, A., Benzerga, A. A., and Pardoen, T. (2016). Failure of metals I: Brittle and ductile fracture. *Acta Materialia*, 107:424–483.

Ponte Castañeda, P. and Suquet, P. (1998). Nonlinear composites. *Advances in Applied Mechanics*, 34:171–302.

Ponte Castañenda, P. (1991). The effective mechanical properties of nonlinear isotropic composites. *Journal of the Mechanics and Physics of Solids*, 39:45–71.

Ponte Castañeda, P. (2015). Fully optimized second-order variational estimates for the macroscopic response and field statistics in viscoplastic crystalline composites. *Proceedings of the Royal Society A: Mathematical, Physical and Engineering Sciences*, 471(2184):20150665.

Poole, W. and Charras, N. (2005). An experimental study on the effect of damage on the stress–strain behaviour for Al–Si model composites. *Materials Science and Engineering: A*, 406(1-2):300–308.

Potirniche, G., Hearndon, J., Horstemeyer, M., and Ling, X. (2006). Lattice orientation effects on void growth and coalescence in fcc single crystals. *International Journal of Plasticity*, 22(5):921–942.

Prasad, N. S., Narasimhan, R., and Suwas, S. (2015). Numerical simulations of cylindrical void growth in mg single crystals. *International Journal of Fracture*, 200:159–183.

Proust, G., Tomé, C., and Kaschner, G. (2007). Modeling texture, twinning and hardening evolution during deformation of hexagonal materials. *Acta Materialia*, 55(6):2137 – 2148.

Proust, G., Tomé, C. N., Jain, A., and Agnew, S. R. (2009). Modeling the effect of twinning and detwinning during strain-path changes of magnesium alloy AZ31. *International Journal of Plasticity*, 25(5):861 – 880.

Reboul, J., Srivastava, A., Osovski, S., and Vadillo, G. (2020). Influence of strain rate sensitivity on localization and void coalescence. *International Journal of Plasticity*,

125:265–279.

Rezaee-Hajidehi, M., Sadowski, P., and Stupkiewicz, S. (2022). Deformation twinning as a displacive transformation: Finite-strain phase-field model of coupled twinning and crystal plasticity. *Journal of the Mechanics and Physics of Solids*, 163:104855.

Rice, J. and Tracey, D. (1969). On the ductile enlargement of voids in triaxial stress fields. *Journal of the Mechanics and Physics of Solids*, 17(3):201–217.

Rogers, H. (1960). The tensile fracture of ductile metals. *Metallurgical Society of AIME*, 218:498–506.

Rousselier, G. (1981). Finite deformation constitutive equations including ductile fracture damage. *Three Dimensional Constitutive Relations and Ductile Fracture, Ed. S. Nemat-Nasser, North-Holland*, 331.

Rousselier, G. (2021). Porous plasticity revisited: Macroscopic and multiscale modeling. *International Journal of Plasticity*, 136:102881.

Sahoo, S. K., Toth, L. S., and Biswas, S. (2019). An analytical model to predict strain-hardening behaviour and twin volume fraction in a profoundly twinning magnesium alloy. *International Journal of Plasticity*, 119:273 – 290.

Salem, A., Kalidindi, S., Doherty, R., and Semiatin, S. (2006). Strain hardening due to deformation twinning in α-titanium: Mechanisms. *Metallurgical and Materials Transactions A: Physical Metallurgy and Materials Science*, 37(1):259–268.

Santos, R. O., da Silveira, L. B., Moreira, L. P., Cardoso, M. C., da Silva, F. R. F., dos Santos Paula, A., and Albertacci, D. A. (2019). Damage identification parameters of dual-phase 600–800 steels based on experimental void analysis and finite element simulations. *Journal of Materials Research and Technology*, 8(1):644–659.

Sartori, C., Mercier, S., and Molinari, A. (2019). Analytical expression of mechanical fields for Gurson type porous models. *International Journal of Solids and Structures*, 163:25–39.

Schacht, T., Untermann, N., and Steck, E. (2003). The influence of crystallographic orientation on the deformation behaviour of single crystals containing microvoids. *International Journal of Plasticity*, 19(10):1605–1626.

Scherer, J.-M., Besson, J., Forest, S., Hure, J., and Tanguy, B. (2019). Strain gradient crystal plasticity with evolving length scale: Application to voided irradiated materials. *European Journal of Mechanics-A/Solids*, 77:103768.

Selvarajou, B., Joshi, S. P., and Benzerga, A. A. (2019). Void growth and coalescence in hexagonal close packed crystals. *Journal of the Mechanics and Physics of Solids*, 125:198–224.

Shanthraj, P. and Zikry, M. (2012). Dislocation-density mechanisms for void interactions in crystalline materials. *International Journal of Plasticity*, 34:154–163.

Siddiq, A. (2019). A porous crystal plasticity constitutive model for ductile deformation and failure in porous single crystals. *International Journal of Damage Mechanics*, 28(2):233–248.

Simo, J. C. and Hughes, T. J. R. (1998). *Computational Inelasticity*. Springer.

Song, D. and Ponte Castañeda, P. (2017a). A finite-strain homogenization model for viscoplastic porous single crystals: I–theory. *Journal of the Mechanics and Physics of Solids*, 107:560–579.

Song, D. and Ponte Castañeda, P. (2017b). Macroscopic response of strongly anisotropic porous viscoplastic single crystals and applications to ice. *Extreme Mechanics Letters*, 10:41–49.

Song, D. and Ponte Castañeda, P. (2018a). A multi-scale homogenization model for fine-grained porous viscoplastic polycrystals: I–finite-strain theory. *Journal of the Mechanics and Physics of Solids*, 115:102–122.

Song, D. and Ponte Castañeda, P. (2018b). A multi-scale homogenization model for fine-grained porous viscoplastic polycrystals: II–applications to FCC and HCP materials. *Journal of the Mechanics and Physics of Solids*, 115:77–101.

Srivastava, A. and Needleman, A. (2013). Void growth versus void collapse in a creeping single crystal. *Journal of the Mechanics and Physics of Solids*, 61(5):1169–1184.

Srivastava, A. and Needleman, A. (2015). Effect of crystal orientation on porosity evolution in a creeping single crystal. *Mechanics of Materials*, 90:10–29. Proceedings of the IUTAM Symposium on Micromechanics of Defects in Solids.

Srivastava, A., Revil-Baudard, B., Cazacu, O., and Needleman, A. (2017). A model for creep of porous crystals with cubic symmetry. *International Journal of Solids and Structures*, 110:67–79.

Staroselsky, A. and Anand, L. (1998). Inelastic deformation of polycrystalline face centered cubic materials by slip and twinning. *Journal of the Mechanics and Physics of Solids*, 46(4):671 – 696.

Stewart, J. B. and Cazacu, O. (2011). Analytical yield criterion for an anisotropic material containing spherical voids and exhibiting tension–compression asymmetry. *International Journal of Solids and Structures*, 48(2):357–373.

Tancogne-Dejean, T., Roth, C. C., Morgeneyer, T. F., Helfen, L., and Mohr, D. (2021). Ductile damage of AA2024-T3 under shear loading: Mechanism analysis through in-situ laminography. *Acta Materialia*, 205:116556.

Tekoğlu, C., Hutchinson, J., and Pardoen, T. (2015). On localization and void coalescence as a precursor to ductile fracture. *Philosophical Transactions of the Royal Society A: Mathematical, Physical and Engineering Sciences*, 373(2038):20140121.

Thomason, P. (1985). A three-dimensional model for ductile fracture by the growth and coalescence of microvoids. *Acta Metallurgica*, 33(6):1087–1095.

Thompson, A. W. and Williams, J. C. (1977). Nuclei for ductile fracture in titanium. *In: FOURTH INTERNATIONAL CONFERENCE ON FRACTURE*, 2:343–348.

Tipper, C. (1949). The fracture of metals. *Metallurgia*, 39(231):133–137.

Tome, C. and Lebensohn, R. (2023). *Material modelling with the visco-plastic self-consistent (VPSC) approach. Theory and practical applications*. Elsevier.

Tomé, C., Lebensohn, R., and Kocks, U. (1991). A model for texture development dominated by deformation twinning: Application to zirconium alloys. *Acta Metallurgica et Materialia*, 39(11):2667 – 2680.

Torki, M., Keralavarma, S., and Benzerga, A. (2021). An analysis of lode effects in ductile failure. *Journal of the Mechanics and Physics of Solids*, 153:104468.

Torki, M. E. (2019). A unified criterion for void growth and coalescence under combined tension and shear. *International Journal of Plasticity*, 119:57–84.

Trejo Navas, V. M., Bernacki, M., and Bouchard, P.-O. (2018). Void growth and coalescence in a three-dimensional non-periodic void cluster. *International Journal of Solids and Structures*, 139-140:65–78.

Tvergaard, V. (1981). Influence of voids on shear band instabilities under plane strain conditions. *International Journal of fracture*, 17:389–407.

Tvergaard, V. (1982). On localization in ductile materials containing spherical voids. *International Journal of fracture*, 18:237–252.

Tvergaard, V. and Needleman, A. (1984). Analysis of the cup-cone fracture in a round tensile bar. *Acta Metallurgica*, 32(1):157 – 169.

Van Houtte, P. (1978). Simulation of the rolling and shear texture of brass by the Taylor theory adapted for mechanical twinning. *Acta Metallurgica*, 26(4):591 – 604.

Van Stone, R. H., Low, J. R., and Shannon, J. L. (1978). Investigation of the fracture mechanism of Ti-5Al-2.5Sn at cryogenic temperatures. *Metallurgical Transactions A*, 9(4):539–552.

Virupakshi, S. and Kowalczyk-Gajewska, K. (2023). Cylindrical void growth vs. grain fragmentation in FCC single crystals: CPFEM study for two types of loading conditions. *International Journal of Solids and Structures*, 280:112397.

Wang, H., Wu, P. D., Tomé, C. N., and Huang, Y. (2010). A finite strain elastic-viscoplastic

self-consistent model for polycrystalline materials. *Journal of the Mechanics and Physics of Solids*, 58:594–612.

Wciślik, W. and Lipiec, S. (2022). Void-induced ductile fracture of metals: Experimental observations. *Materials*, 15(18):6473.

Willis, J. R. (1981). Variational and related methods for the overall properties of composites. *Advances in applied mechanics*, 21:1–78.

Wong, W. and Guo, T. (2015). On the energetics of tensile and shear void coalescences. *Journal of the Mechanics and Physics of Solids*, 82:259–286.

Yerra, S., Tekog, C., Scheyvaerts, F., Delannay, L., Van Houtte, P., Pardoen, T., et al. (2010). Void growth and coalescence in single crystals. *International Journal of Solids and Structures*, 47(7-8):1016–1029.

Zhang, F., Bower, A., Mishra, R., and Boyle, K. (2009). Numerical simulations of necking during tensile deformation of aluminum single crystals. *International Journal of Plasticity*, 25(1):49–69.

Zhang, J. and Joshi, S. P. (2012). Phenomenological crystal plasticity modeling and detailed micromechanical investigations of pure magnesium. *Journal of the Mechanics and Physics of Solids*, 60:945–972.